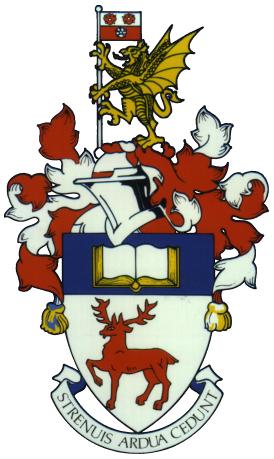

UNIVERSITY OF SOUTHAMPTON

Faculty of Natural and Environmental Sciences

School of Ocean and Earth Science

On the role of the Southern Ocean in the global carbon cycle and atmospheric CO_2 change

by

Jonathan Maitland Lauderdale

A thesis submitted for the degree of Doctor of Philosophy

November 2010

Declaration of Authorship

I, Jonathan Maitland Lauderdale, declare that this thesis titled, "On the role of the Southern Ocean in the carbon cycle and atmospheric CO_2 change" and the work presented within are my own original research. I confirm that:

- This work was done wholly or mainly while in candidature for a research degree at this University.
- Where any part of this thesis has previously been submitted for a degree or any other qualification at this University or any other institution, this has been clearly stated.
- Where I have consulted the published work of others, this is always clearly attributed.
- Where I have quoted from the work of others, the source is always given. With the exception of such quotations, this thesis is entirely my own work.
- I have acknowledged all main sources of help.
- Where the thesis is based on work done by myself jointly with others, I have made clear exactly what was done by others and what I have contributed myself.
- None of this work has been published before submission.

Signed: _____

Date: _____

"We ourselves feel that what we are doing is just a drop in the ocean. But the ocean would be less because of that missing drop."

Mother Teresa of Calcutta (Founder, Missionary)

UNIVERSITY OF SOUTHAMPTON

Abstract

FACULTY OF NATURAL AND ENVIRONMENTAL SCIENCES
SCHOOL OF OCEAN AND EARTH SCIENCE

Doctor of Philosophy

ON THE ROLE OF THE SOUTHERN OCEAN IN THE GLOBAL CARBON CYCLE AND ATMOSPHERIC CO_2 CHANGE

by Jonathan Maitland Lauderdale

Uncertainty about the causes of glacial-interglacial CO_2 variations demonstrates our incomplete grasp of fundamental processes that govern our climate and thus one of the foremost problems in palaeoceanography and Earth System Science regards the mechanism(s) responsible for natural changes in atmospheric CO_2 concentration. It is becoming clear that the Southern Ocean overturning circulation plays an important role in the global carbon cycle because altered communication between the atmosphere and abyss in the Southern Ocean is relatively well documented and often implicated in explanations of past and future climate changes, but the ambiguity of the paleoceanographic record defies interpretation of the mechanisms involved.

Using a coarse resolution ocean general circulation model and coupled biogeochemistry code, an ensemble of idealised perturbations to external forcing and internal physics of the Southern Ocean is examined to explain the processes that link ocean circulation, nutrient distributions and biological productivity, and determine the extent to which the Southern Ocean governs the partitioning of CO_2. Strengthened or northward-shifted winds result in oceanic outgassing and increased atmospheric carbon dioxide levels, while weakened or southward-shifted winds cause oceanic carbon uptake and reduced atmospheric carbon dioxide concentration. Driven by the work done on the ocean by the winds, changes in the rate or spatial pattern of the Southern Ocean residual overturning circulation lead to alteration of upper ocean stratification and the rate and depth from which carbon and nutrient-rich deep waters are upwelled to the surface. These surface waters, imprinted with the pattern of air-sea gas exchange, are subducted to intermediate depths in the ocean interior, not the abyss as previous suggested.

These results are robust to significant alterations to surface heat and freshwater boundary conditions, mesoscale eddy activity and rates of air-sea gas exchange and represent a significant proportion of the change in glacial-interglacial CO_2 that can be currently generated by altered ocean circulation in a variety of models, revealing that the upper limb of the Southern Ocean overturning circulation is important in determining atmospheric CO_2 levels.

Acknowledgements

Firstly my thanks go to my supervisors Alberto Naveira Garabato, Kevin Oliver and David Smeed and my advisory panel chair Harry Bryden for their support, guidance and mentorship. Thank you for your enthusiasm, attention to detail and countless helpful discussions, ideas and suggestions without which this project would not have been successful. I also thank Joel Hirschi, Stephanie Dutkiewicz, Mick Follows, Gael Forget, Patrick Heimbach and Andreas Oschlies for advice, assistance, technical expertise and hospitality during my visits to MIT and IFM-GEOMAR. I am also grateful to Sheldon Bacon for letting me join his scientific party for a cruise to the Southern Ocean aboard *RRS James Cook*, and giving me the opportunity to see the scenic highlights of South Georgia and the Falkland Isles. Thank you to the scientists and crew of JC30. I thank the University of Southampton, the National Oceanography Centre, Southampton and the Natural Environment Research Council for financial support during this project and for providing a stimulating environment in which to carry out my research.

My office-mates, Alex Brearley, Chris Atkinson and Lorna McLean, fellow modeller Maria Broadbridge, my extended postgrad family and my parents provided support and encouragement that were essential ingredients that permeate every page of this thesis and I am eternally grateful that I have such good friends and family around me. I also owe my continuing sanity to Jorge Cham for reminding me that Ph.D. students everywhere go through the same experiences and Douglas Adams for his words of wisdom *DON'T PANIC*.

I am indebted to all my past teachers who inspired me to pursue my interest in science and my undergraduate lecturers and supervisors at the University of Southampton who fuelled my interest in oceanography, gave me a real taste of ocean research and encouraged me to challenge myself. Finally, I thank Sally Close for making this time truly special and for everything.

Contents

List of Figures

List of Tables

Part I

Introduction

Chapter 1

Introduction

The last one million years is punctuated by a series of ~100,000 year cycles of glacial and interglacial periods documented by complementary climate records contained in deep-sea sediments, continental assemblages of flora and fauna and loess (fine-grained wind-blown deposits) [e.g. *Imbrie et al.*, 1992]. Cores of ice drilled from the Antarctic and Greenland ice caps are particularly important since trapped air bubbles provide a direct record of previous atmospheric trace gas composition, revealing coherent cycles of greenhouse gases highly correlated with changes in atmospheric temperature.

The Vostok ice core from East Antarctica records the previous four glacial–interglacial cycles over a period of approximately 420,000 years (Figure 1.1). Minimum temperatures are remarkably similar to within 1 °C [*Petit et al.*, 1999], while the maximum temperatures were only slightly warmer than the Holocene (the current period of unusually stable climate). The cycles of the greenhouse gases carbon dioxide (CO_2) and methane (CH_4) measured throughout the core show that the largest changes are associated with the transition from glacial to interglacial state, occurring between values of 180 to 280–300 ppm for CO_2 and 350 to 650–770 ppb for CH_4. Each cycle shows a characteristic saw-tooth sequence beginning with warm interglacial conditions becoming increasingly cooler, superimposed with high frequency fluctuations, ending in a glacial maximum period followed by rapid return towards the warm conditions of the next interglacial.

Much of this variability occurs with periodicities that correspond to the Milankovitch cycles of precession, obliquity and eccentricity of the Earths orbit, particularly on 100 and 41 kyr timescales. The total energy received from the sun is relatively insensitive to

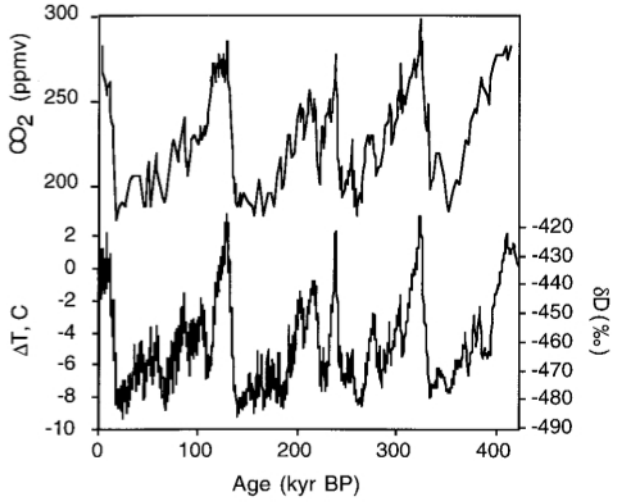

Figure 1.1: Atmospheric carbon dioxide concentration (top) and Temperature change (bottom) over the last 420 kyr from the Vostok ice core [*Petit et al.*, 1999].

these changes in orbit, whereas significant variations occur seasonally and with latitude due to changes in the distribution of solar energy over the course of one year. The growth of large ice sheets appears to be sensitive to Northern Hemisphere summer because: (1) The Northern Hemisphere is where most of the large ice sheets were located, and (2) Summer is the critical season for survival of the previous winter's ice to allow ice sheet expansion. This line of reasoning indicates that the CO_2 signal recorded in the Vostok core is a secondary amplifier of the glacial cycles because of the obvious link between insolation and ice volume [*Archer et al.*, 2000]. However, if atmospheric Oxygen-18 isotope anomaly ($\delta^{18}O_{atm}$) is a reliable indicator of global ice volume, which is directly related to sea level, then the rise in atmospheric CO_2 may have preceded the rise in sea level, that is the melting of the Northern Hemisphere ice sheets, by as much as 2–4 kyr [*Broecker and Henderson*, 1998]. Antarctic palaeo-temperatures recovered from Deuterium isotope anomaly (δ^2H or δD) in the Vostok ice core are also highly correlated (0.71) with pCO_2 [*Petit et al.*, 1999] and this correlation increases when a lag of 600–800 years is applied to bring the change in temperature in line with the CO_2 record [*Fischer et al.*, 1999]. This is also true of higher resolution results obtained from Dome Concordia 500 km north east of Lake Vostok since the Last Glacial Maximum (LGM), about 22,000 years ago where the correlation between CO_2 and palaeo-temperatures is as high as 0.85 [*Monnin*, 2001]. These data suggest that CO_2 is a primary driver of the glacial–interglacial transitions, with small initial increases in temperature magnified by increased greenhouse gas concentration [*Caillon et al.*, 2003] that then act to melt the ice caps. However, the $\delta^{18}O_{atm}$ data is only conclusive for the last two glacial terminations

while error bars on the temperature lag are of a similar order as the lag itself due to the uncertainty in the ice-air age difference and could be larger if the error in the age model of the ice core is included.

Our uncertainty about the causes of glacial-interglacial CO_2 variations and its role in the waxing and waning of continental ice sheets and global climate change, even after more than 20 years of research, demonstrates our incomplete grasp of fundamental processes that govern our climate. Coupled with the threat of anthropogenic greenhouse gas emissions which have very likely caused most of the observed global warming over the last fifty years [*Hegerl et al.*, 2007], one of the foremost problems in palaeoceanography and Earth System Science regards the mechanism(s) responsible for natural changes in atmospheric CO_2 concentration over millennial timescales.

There is general agreement that oceanic processes are primarily involved [e.g. *Schmittner and Galbraith*, 2008], since the oceanic reservoir of CO_2 is about 60 times greater than that for the atmosphere, while the residence time of carbon stored in calcite rock is orders of magnitude too large to affect geologically rapid changes in either ocean or atmospheric pCO_2. Furthermore, it is estimated that roughly 40%, or ~171±28 Gt C, of the anthropogenic carbon dioxide emitted since approximately 1750 has been taken up by the ocean [42±7% between 1750–1994 falling to 37±7% between 1980–2005 *Bindoff et al.*, 2007]. The key to unlocking the "glacial-interglacial problem" and understanding the future development of anthropogenic climate change may therefore be found in the fact that approximately 75% of the world ocean's volume is connected, via polar regions, to 2% of the ocean's surface area, and these cold waters can hold a larger concentration of dissolved gases than warmer regions. A particular region of interest is the Southern Ocean and the associated physical processes surrounding the Antarctic Circumpolar Current (ACC). Comparing ice core temperature proxies between Antarctica and Greenland reveals contrasting behaviour with the Southern Hemisphere exhibits milennial scale temperature variability of only 1–3 °C that correlates well with atmospheric CO_2 levels whilst the Northern Hemisphere experienced rapid, decadal scale shifts of 8–16 °C (Dansgaard-Oeschger events) with no concurrent changes in atmospheric CO_2, hinting at a central role for the Southern Ocean in modulating the glacial-interglacial cycles.

The ACC is the strongest and longest current system in the ocean and permits interbasin transfer of heat, salt and passive tracers, which determine important aspects of the global climate. Roughly 40% of anthropogenic carbon taken up by the ocean may be found at intermediate depths between 50°S and 14°S due to uptake and export in the

Southern Ocean and without the global ocean carbon sink, atmospheric CO_2 would be ~55 ppm higher than observed [*Caldeira and Duffy*, 2000; *Sabine et al.*, 2004]. The unique geometry of the Southern Ocean and dynamics of the ACC leads to steeply sloping meridional density surfaces that rise toward surface near the Antarctic continent. Consequently, there is a direct connection between the deep ocean and atmosphere through which rapid variations in atmospheric composition may be realised. The aim of the work presented in this thesis is to explore the sensitivity of atmospheric CO_2 to processes that influence the ACC and Southern Ocean overturning and to investigate the role of the Southern Ocean on the global carbon cycle as a whole.

This introductory chapter will review the current understanding of Southern Ocean physics and how the ACC might be implicated in altering atmospheric CO_2 levels in the past and in the future. Section 1.1 will introduce the circulation, dynamics and driving mechanisms of the ACC and the Southern Ocean meridional overturning circulation. Section 1.2 will explore the development of the "glacial-interglacial CO_2 problem", describing the evolution of the most widely endorsed biogeochemical and physical theories to explain these changes and assessing their skill against paleoceanographic proxy evidence. This section deviates initially from the key region of interest, but as conjecture rapidly converges to current theories of glacial-interglacial climate change, the Southern Ocean emerges as the foremost focus of research. Section 1.3 will examine observations and model studies of current, anthropogenic climate change in the Southern Ocean and how these results may be used to interpret the glacial–interglacial behaviour of the climate system. Finally, Section 1.4 outlines the specific aims of the thesis and provides a summary of this manuscript's structure.

1.1 The Antarctic Circumpolar Current and Southern Ocean Overturning Circulation

The formation of the Southern Ocean and establishment of the Antarctic Circumpolar Current (ACC) between 20–40 million years ago had a profound effect on the distribution of water masses in the global ocean, not only because of the transport of heat, salt, carbon and nutrients between the Atlantic, Indian and Pacific basins on its continuous circuit of the globe but also because the swift, deep-reaching, zonally orientated ACC acts as a meridional barrier that impedes oceanic heat transport from the tropics towards Antarctica [e.g. *Cox*, 1989]. This isolation helped initiate the growth of glaciers

on the previously temperate Antarctic continent and the expansion of sea ice leading to the production of cold, dense Antarctic Bottom Water (AABW) exported to the north. The ubiquitous presence of AABW is thought to have increased the vertical temperature gradient in equatorial regions from 4 °C with a closed Drake Passage, between the southern tip of South America (55°S) and the Antarctica Peninsula (63°S), to 26 °C today [*Olbers et al.*, 2004], but also as a result of increased sub-thermocline temperatures when Drake Passage is opened [*Cox*, 1989].

Through Drake Passage the ACC transports 130–140 Sv ($1\,\mathrm{Sv} \equiv 1 \times 10^6\,\mathrm{m^3\,s^{-1}}$) based on hydrographic sections and moored current metre arrays[*Cunningham et al.*, 2003; *Ganachaud and Wunsch*, 2000; *Nowlin and Klinck*, 1986; *Sloyan and Rintoul*, 2001]. This is particularly large, compared to other major current systems due to the deep reaching geostrophic zonal velocity structure supported through even vertical distribution of the pressure gradient force created by the sea surface slope of ~1.5 m across the Southern Ocean [*Tomczak and Godfrey*, 2005]. The flow is concentrated into several fronts that are defined by rapid meridional changes in density [*Orsi et al.*, 1995], particularly the Subantarctic and Polar Fronts, highlighted in the context of other major flows in the Southern Hemisphere in Figure 1.2.

1.1.1 Controlling mechanisms of the Antarctic Circumpolar Current

The unique geometry of the Southern Ocean, with a circumpolar band that passes through Drake Passage with no zonal boundaries, has confounded application of common physical oceanographic paradigms such as Sverdrup balance that are well understood in closed basins to explain ACC transports and associated dynamics [e.g. *Olbers et al.*, 2004; *Rintoul et al.*, 2001]. The first issue is that to conserve the mass of the ocean to the south of the ACC in the range of latitudes of Drake Passage, there can be no net northward transport but the curl of the westerly wind stress does not usually integrate to zero, hence Sverdrup balance fails. This situation cannot be recovered by implication of a western boundary current to return the mass flux south because the absence of zonal boundaries precludes establishment of a zonal pressure gradient to support such a meridional current in geostrophic balance. Also, Sverdrup balance at the latitude of Cape Horn (55°S) actually reveals a southward net flow between South America and South Georgia, which also cannot be compensated by the northward deflection of the

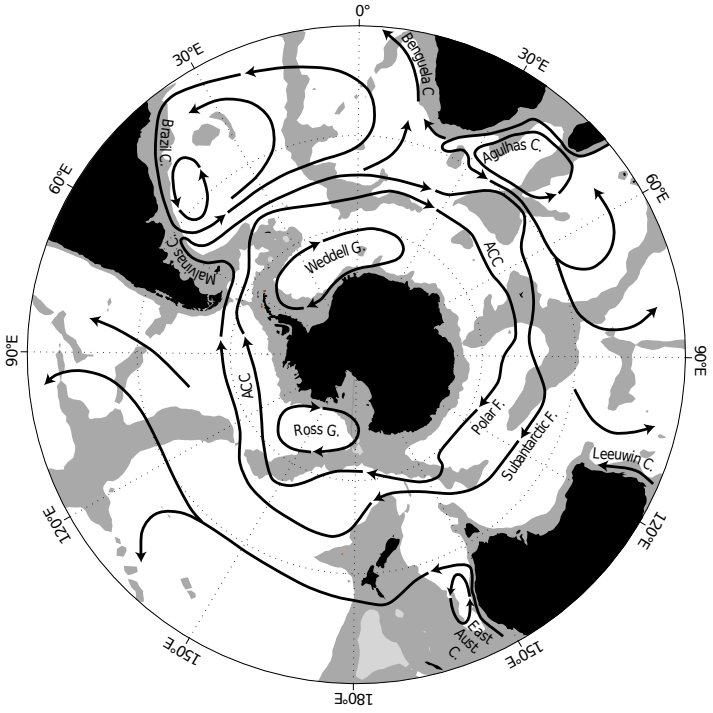

Figure 1.2: Schematic illustration of the horizontal circulation in the Southern Hemisphere south of 20°S showing the Antarctic Circumpolar Current (ACC), the Southern Hemisphere subtropical currents (initialed "C") and the subpolar gyres (initialed "G") [from *Rintoul et al.*, 2001]. The mean positions of the Subantarctic and Polar Fronts (initialed "F") are marked and topography that is less than 3500 m deep is shaded. This is the depth at which there are no continuous flow streamlines through Drake Passage and therefore the interbasin connection between the Atlantic and Pacific Oceans is severed.

ACC in the Falkland/Malvinas Current because this current need not be of the same magnitude [*Gent et al.*, 2001]. The second issue is that the great vertical penetration of the ACC, in all likelihood, introduces interactions with the complex topography in the Southern Ocean that Sverdrup balance neglects, assuming vanishing vertical motion at depth and no change in thickness of the total water column to conserve vorticity, which are reasonable assumptions for shallow gyre circulations.

Munk and Palmén [1951] recognised the importance of topographic interactions in dissipating the eastward momentum imparted by strong midlatitude westerly winds at the surface. Reynolds stresses and viscous dissipation were subsequently found to be insignificant using a variety of methods such as satellite altimetry [see *Rintoul et al.*, 2001] therefore the eastward momentum is likely transferred through the water column by perturbations in the density field caused by the passing of energetic mesoscale eddies, creating eddy-induced interfacial form stress [*Bryden and Cunningham*, 2003; *Johnson and Bryden*, 1989] before the final transfer of momentum from ocean to solid earth by

bottom form stress due to pressure differences across submarine topographical features (note that form stress, interfacial or topographic, is the difference in eastward pressure force between an upper and lower interface).

However, the Southern Ocean density field may play an especially active role in setting the strength of the ACC, so much so that the influence of eastward wind stress forcing may actually be via an indirect effect of altered stratification. Simply by decreasing the depth of the sill across Drake Passage to half the depth of the surrounding ocean, *Gill and Bryan* [1971] tripled the transport of the circumpolar current in a numerical model by trapping colder, denser water on the Atlantic side than the Pacific side. This established a pressure gradient but the associated force was in the same direction as, and larger than, the wind stress force [c.f. *Munk and Palmén*, 1951] and therefore acted to drive the circulation, not retard it. This may be reconciled by considering barotropic and baroclinic bottom pressure separately: the total bottom form stress does balance the momentum imparted by the westerlies driven by a barotropic pressure gradient across a bathymetric feature, however acting against this is a baroclinic pressure gradient due to differences in density either side of topographic features that acts to accelerate the current [*Olbers et al.*, 2004; *Stevens and Ivchenko*, 1997, see also Figure 1.3]. *Johnson and Bryden* [1989] derive a square-root relationship between ACC shear transport and the eastward wind stress at Drake Passage on long timescales, but validation of such a relationship has proven difficult possibly due to assumptions of prescribed stratification and adiabatic interior flow [e.g. *Gent et al.*, 2001; *Gnanadesikan and Hallberg*, 2000].

The effects of wind and thermohaline forcing on ACC transport has been considered in ocean general circulation models (OGCMs), both as a combined set of forcings and individually. In a homogenous ocean forced with zonal winds, *Cai and Baines* [1996] found a diminutive circumpolar transport of 7.6 Sv with the ACC confined to geostrophic contours (f/H, where f is the Coriolis parameter and H is ocean depth) only passing through Drake Passage in jets at the continental margins [see also *Borowski et al.*, 2002; *Krupitsky and Cane*, 1994; *Wang and Huang*, 1995]. The path of the ACC is somewhat tied to the distribution of topography, requiring additional driving mechanisms to enable the current to cross geostrophic contours that are blocked by meridional ridges (shaded grey in Figure 1.2), which prevents significant ACC transports being achieved with wind forcing alone, such as across Drake Passage and between Australia and Antarctica in order to conserve vorticity.

Buoyancy forcing alone in an ocean without bathymetry also compares poorly to observations, with an ACC transport of near zero [*Cai and Baines*, 1996; *Gill and Bryan*,

1971]. However, with topographical features - even a one grid point shoaling of the topography in Drake Passage [*Cai and Baines*, 1996] - a substantial circumpolar transport of 40–110 Sv is established [*Cai and Baines*, 1996; *Saenko et al.*, 2002] as well as qualitatively recreating the observed distribution of water masses in the global ocean [*Cai and Baines*, 1996; *Cox*, 1989]. This is the Joint Effect of Baroclinicity and Relief (JEBAR) that evaluates the difference between the calculated bottom pressure torque and the resulting torque if bottom pressure gradients were equal to depth averaged pressure gradients. *Borowski et al.* [2002] demonstrated that cross-contour ACC transport is supported by JEBAR, driven by the distribution of baroclinic potential energy, or simply the meridional density gradient. This gradient is particularly influenced by the production of dense AABW due to brine rejection from sea ice adjacent to the Antarctic continent. *Cai and Baines* [1996] switched off bottom water production in their thermohaline-driven model resulting in a ~30 Sv reduction in ACC transport. Furthermore, their relationship between thermohaline driving and ACC transport is enhanced with increased vertical mixing due to greater bottom water production in the Weddell Sea. *Gent et al.* [2001] also find a strong correlation between transport and bottom water circulation near Antarctica, particularly when their OGCM is coupled to a sea ice model and brine rejection is explicitly captured. They find a similar value of 30 Sv for the thermohaline-driven component of Drake Passage transport, with an additional 7 Sv for each 1 Sv increase in AABW formation.

When wind- and thermohaline forcing are considered in unison, interaction between the forcings take place and therefore the resultant circulation is not simply the superposition of the two individual flows [*Cai and Baines*, 1996]. The indirect effects of the wind, in particular northward Ekman transport and Ekman pumping at the surface, establish further meridional gradients in density and therefore create a more vigorous ACC. The indirect effects of the wind are considered of prime importance by many authors [*Borowski et al.*, 2002; *Cai and Baines*, 1996; *Gent et al.*, 2001; *Gnanadesikan and Hallberg*, 2000], with estimates of up to 100 Sv due to these processes alone.

1.1.2 The Southern Ocean meridional overturning circulation

Due to the likely dependence of the zonal circulation of the ACC on meridional density structure, it is intimately tied to the Southern Ocean meridional overturning circulation [*Rintoul et al.*, 2001]. Northward Ekman transport driven by the westerly winds creates surface divergence to the south that draws deeper waters to the surface along isopycnals

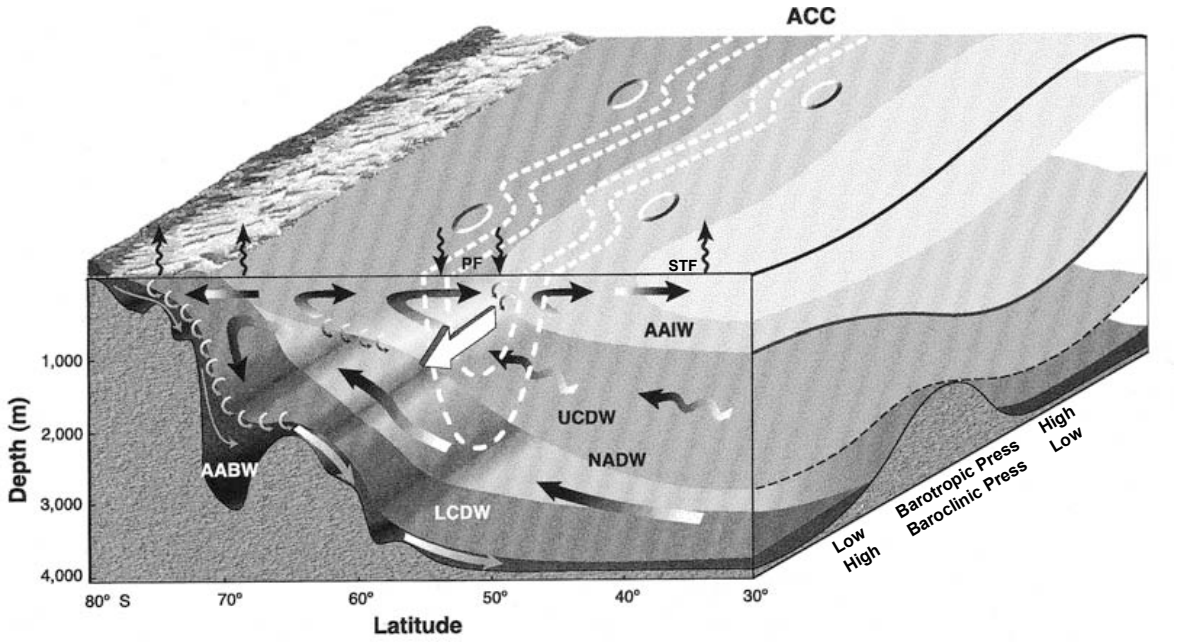

Figure 1.3: Schematic view of the zonal flow and meridional overturning circulation in the Southern Ocean [from *Olbers et al.*, 2004; *Speer et al.*, 2000]. The east-west (side) section shows isopycnal and sea surface gradients in relation to submarine features that support baroclinic (hydrostatic) and barotropic (surface) pressure gradients and associated bottom form stresses that act on the circumpolar current and almost balance, counteracting wind stress. Note that form stress is the difference in eastward pressure force between an upper and lower interface (topography for bottom form stress or isopycnals for interfacial form stress). The north-south (front) section illustrates two Southern Ocean meridional overturning circulation cells and the water masses involved. The upper cell is formed by northward Ekman transport beneath strong westerly winds and subduction of Antarctic Intermediate Water (AAIW) and Subantarctic Mode Waters (SAMW), with compensating southward eddy transports in the Upper Circumpolar Deep Water (UCDW) layer. The lower cell is driven by formation of dense Antarctic Bottom Water (AABW) and by compensating geostrophic southward flow of Lower Circumpolar Deep Water (LCDW) and North Atlantic Deep Water (NADW) below the depth of the Drake Passage sill. Surface fluxes add buoyancy around the Polar Front (PF) and buoyancy is lost from the Subtropical Front (STF) to the north and by cooling and brine rejection to south. Arrows attached to isopycnals represent turbulent mixing.

that shoal towards the surface. These waters gain buoyancy and are advected across mean density contours in the Ekman layer and are eventually subducted to intermediate depths and exported to lower latitudes. The dense to intermediate water transformation associated with this limb of the Southern Ocean meridional overturning circulation relaxes the need for uniform interior upwelling to close the global overturning circulation associated with deep water formation in the Northern Hemisphere [*Gnanadesikan*, 1999].

Integration of the zonal momentum balance with depth and longitude reveals that this northward Ekman transport is almost completely balanced by a southward flow at depth

and these Eulerian components form the Southern Ocean "Deacon Cell" [*Döös and Webb*, 1994]. Denser varieties of deep water also upwell further south where heat loss to the atmosphere and brine rejection due to sea ice formation, make the surface waters increasingly dense. Production of Bottom Waters near Antarctica feed the sinking branch of the Southern Ocean overturning circulation and are also exported to the northern basins (Figure 1.3). The water mass present at this depth is Lower Circumpolar Deep Water (LCDW) that has a high salinity signature indicating an input of North Atlantic Deep Water (NADW) [*Rintoul et al.*, 2001]. Exactly how this deep/bottom water circulation is closed remains uncertain. Diapycnal mixing appears to raise AABW into lighter density classes (~2000 m), particularly in the deep Southern Ocean [e.g. *Watson and Naveira Garabato*, 2006], but also further north. These waters can then be returned towards Antarctica in the upper limb as Upper Circumpolar Deep Water (UCDW), exported again as intermediate and mode waters before being returned to the deep ocean in the North Atlantic as NADW [e.g. *Schmitz*, 1996b].

The denser southward flow needed to sustain these overturning cells can be achieved by geostrophy in the deeper layers through east-west pressure gradients supported beneath the peaks of submarine topography. However, observations of southward flow across 30–40°S imply significant transport along isopycnals shallower than Drake Passage, particularly in UCDW layers. The mesoscale eddy field is highly important in this respect, acting to smooth gradients in potential vorticity, resulting in a southward volume flux within density intervals [*Speer et al.*, 2000]. The accompanying poleward heat flux is also important in balancing the heat lost to the atmosphere at the surface and in the process of downward flux of eastward momentum from the surface to seafloor [*Bryden and Cunningham*, 2003; *Johnson and Bryden*, 1989].

The effect of mesoscale eddies in the Southern Ocean has been investigated by applying residual-mean theory [e.g. *Karsten and Marshall*, 2002; *Marshall*, 1997; *Marshall and Radko*, 2003]: Westerly winds induce northward surface Ekman transport and establish an Eulerian meridional circulation, $\bar{\Psi}$, equivalent to the Deacon cell [*Döös and Webb*, 1994] with upwelling of dense waters to the south that stores potential energy in the steeply sloping isopycnals and enhancing the buoyancy gradients maintained by air-sea fluxes. Tracer-inferred water mass subduction rates are not consistent with this overturning circulation alone [*Marshall*, 1997; *Marshall and Radko*, 2003]. Baroclinic instability in the ACC creates transient, mesoscale eddies that transport mass southward via an advective "bolus" velocity and establish an opposing overturning circulation, Ψ^*,

by extracting potential energy from the large-scale baroclinic field and restoring isopycnals to the horizontal. This assumes that below the mixed layer, the eddy transport is adiabatic, implying negligible diapycnal eddy mixing in the ocean interior, which is a fair assumption away from continents and rough topography where low values of vertical diffusivity are observed [e.g. *Gregg*, 1987; *Ledwell et al.*, 1993; *Polzin et al.*, 1997]. However in non-quiescent regions such as locations of complex topography, widespread in the deep Southern Ocean, where high rates of diapycnal mixing are observed this assumption may not be valid [*Heywood et al.*, 2002; *Naveira Garabato et al.*, 2004, 2007].

Nevertheless, with this assumption, the eddy circulation can be considered in terms of horizontal buoyancy fluxes, which can be simply parameterised with an eddy transfer coefficient and the slope of isopycnals following *Gent and McWilliams* [1990]. The balance between the two opposing circulations (in the Southern Ocean), determined by the net buoyancy forcing [*Marshall*, 1997], results in a "residual", or "transport" circulation, $\Psi_{res} = \bar{\Psi} + \Psi^*$, that advects buoyancy and passive oceanographic tracers, sets the water mass formation rate and determines Southern Ocean stratification (see also Figure 1.4). This framework allows a concise representation of two important and competing circulations and therefore provides useful insight to interpret perturbations of surface forcing and internal physics of the Southern Ocean. By evaluating these eddy-induced bolus velocities in a coarse resolution OGCM, using the *Gent and McWilliams* [1990] eddy closure scheme and advecting tracers with the residual circulation rather than the Eulerian-mean circulation, *Danabasoglu and McWilliams* [1995] found a marked improvement of their simulations compared to results with traditional horizontal diffusion and observations, particularly in the Southern Ocean where the Deacon cell was greatly reduced due to compensation by eddy advection.

1.1.3 Interhemispheric connections and the Southern Ocean's effect on climate

The unique circulation in the Southern Ocean with associated sloping isopycnals that outcrop at the surface provides a direct connection between the deep ocean and atmosphere through which rapid variations in atmospheric composition may be realised. Unlike the Nordic Seas, for example, the Southern Ocean is not only a region of water mass subduction but also a large upwelling system [*Heinze*, 2002].

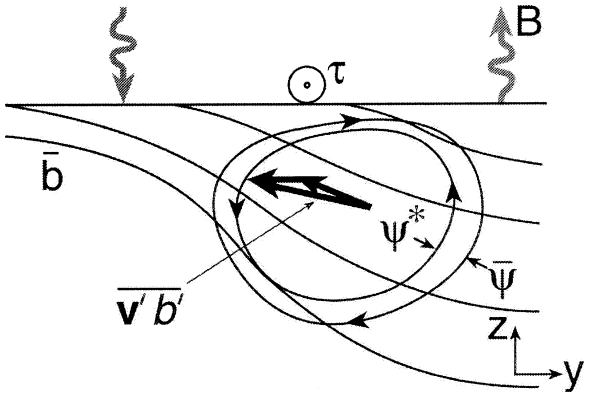

Figure 1.4: Application of residual mean theory to the meridional overturning circulation in the Southern Ocean. The "residual" circulation is decomposed into an Eulerian mean ($\bar{\Psi}$) circulation, driven by surface wind stress (τ) and buoyancy (B) fluxes that tilts isopycnals ($\bar{b}$) and an eddy-induced (Ψ^*) circulation that acts flattens them. The mesoscale eddy field drives a southward buoyancy flux ($\overline{v'b'}$) [*Marshall and Radko*, 2003].

Figure 1.5 shows that via water mass transformations, the Southern Ocean is at the heart of a global overturning circulation [*Lumpkin and Speer*, 2007; *Schmitz*, 1995, 1996a,b] and may play an important role in influencing the climate of the Northern Hemisphere through variation in poleward heat transport determined by the rate of the Atlantic meridional overturning circulation (AMOC) [e.g. *Kuhlbrodt et al.*, 2007]. The traditional mechanism for this circulation is the reduction of NADW density in the ocean interior by downward diapycnal mixing of heat causing widespread upwelling at low latitudes [*Munk*, 1966; *Munk and Wunsch*, 1998]. These waters are transported to the North Atlantic in the upper ocean where buoyancy loss and subsequent convection replenishes NADW. However, divergence of Ekman transport, driven by the Southern Hemisphere westerlies, causes upwelling of deep waters that flow south at or below the Drake Passage sill depth (see Figures 1.3 or 1.4). *Toggweiler and Samuels* [1995, 1998] suggest that given the difference in densities of the two water masses involved, the only place where the deep waters can be replenished is in the North Atlantic, therefore, NADW is simply the closing branch of the Southern Ocean wind-driven upwelling circulation. This has become known as the "Drake Passage effect", because of the dynamical constraints discussed above that prevent net southward flow in the unbounded latitudes thus determining the great depth from which the upwelled waters must originate. The AMOC is indeed sensitive to the magnitude of the Southern Hemisphere westerlies in coarse resolution OGCMs [e.g. *McDermott*, 1996; *Toggweiler and Samuels*, 1995], however the use of restoring boundary conditions may prevent North Atlantic surface temperatures responding to ocean circulation changes causing negative feedback, which

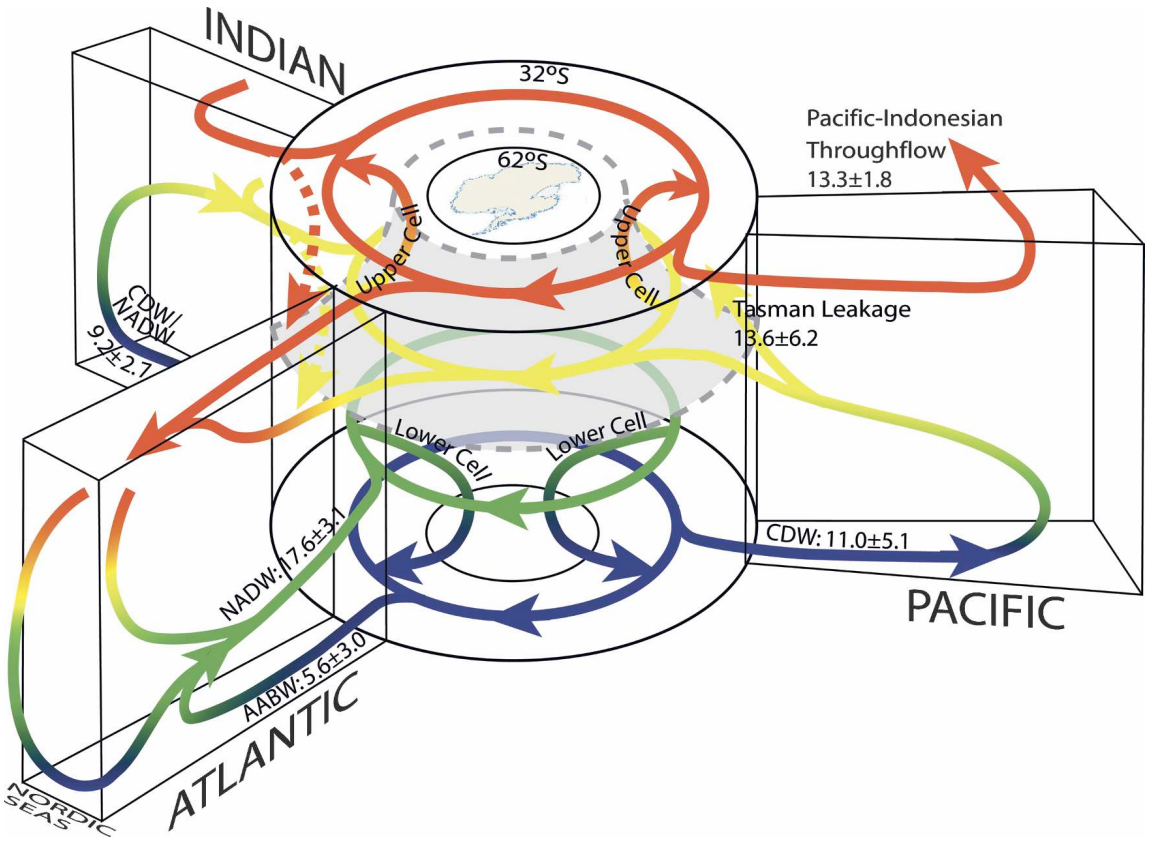

Figure 1.5: Schematic view of the Southern Ocean meridional overturning circulation and water masses in context with the global ocean overturning circulation [*Lumpkin and Speer*, 2007; *Schmitz*, 1996a,b] showing the central role of the Antarctic Circumpolar Current (ACC) and water masses formed in the Southern Ocean in the circulation of the global ocean. Coloured lines indicate approximate neutral density ranges: red/upper ocean ($\gamma^n \leq 27.0$), yellow/ intermediate ($27.0 \leq \gamma^n \leq 27.6$), green/deep ($27.6 \leq \gamma^n \leq 28.15$), and blue/bottom ($\gamma^n \geq 28.15$).

may reduce the sensitivity of the AMOC to the Drake Passage effect [*Rahmstorf and England*, 1997]. Also, observations of northward flow at 40°S [*Schmitz*, 1995, 1996b] are smaller than the Ekman transport, suggesting substantial return flow occurs above the sill depth of Drake Passage, probably associated with mesoscale eddies [*Hallberg and Gnanadesikan*, 2006; *Rintoul et al.*, 2001; *Speer et al.*, 2000]. Nevertheless, paleoceanographic modelling indicates that there is a strong interhemispheric link between Southern Ocean and North Atlantic water mass formation, with a freshwater input to the formation regions of AAIW able to reconcile the warm northern hemisphere climate during the Bølling-Allerød with a strong AMOC [*Weaver et al.*, 2003].

Linked with the circulation in Figure 1.5 and the dynamics associated with the ACC and

the "Drake Passage effect" is the density structure of the global ocean [e.g. *Gnanadesikan*, 1999; *Gnanadesikan and Hallberg*, 2000; *Levermann and Fürst*, 2010]. The pycnocline delineates the boundary between light surface waters at low latitudes and dense abyssal waters formed at high-latitude often defined as σ_0 = 27.4–27.5 kg m^{-3} [*Gnanadesikan and Hallberg*, 2000]. If diapycnal mixing and the southward eddy flow that may balance northward wind-driven Ekman transport are small, then *Gnanadesikan* [1999]'s simple model of the global pycnocline reproduces the tight linkage between North Atlantic sinking and Southern Ocean Ekman transport with the former reducing the depth of the pycnocline and the latter deepening it. However, the degree of compensation of the northward Ekman flow by southward eddy compensation, as suggested above, can alter the North-South balance with larger eddy fluxes leading to reduced export of water from the Southern Ocean and a shallower pycnocline with reduced NADW formation. A further relationship suggests that low latitude upwelling across the pycnocline is directly proportional to Southern Ocean eddy-induced transport and inversely proportional to pycnocline depth [*Gnanadesikan*, 1999; *Levermann and Fürst*, 2010].

The Southern Ocean is also a critical area for setting the rates of global ocean primary production and biogeochemical cycling [e.g. *Marinov et al.*, 2006; *Sarmiento et al.*, 2004]. In surface waters, photosynthetic organisms utilise energy from the sun to fix dissolved inorganic nutrients such as phosphate (PO_4^{3-}), nitrate (NO_3^-) and dissolved inorganic carbon (DIC) into particulate (and dissolved) organic matter. This biogenic matter is advected in oceanic currents and recirculated locally before a fraction is eventually exported out of the surface layer into the deep ocean where dissolution and remineralisation occur, releasing the inorganic nutrients back into the water column. The age of a water mass also contributes to the level of nutrients it acquires through nutrient regeneration, with low concentrations in newly formed deep waters in the North Atlantic, increasing concentrations as these waters are advected around the Southern Hemisphere and high concentrations in the oldest waters of the deep North Pacific. This is the integrated effect of what is known as the biological pump [*Volk and Hoffert*, 1985]. Simultaneously, sinking cold polar waters associated with the meridional overturning circulation are enriched with CO_2 because of their high solubility. This is termed the "solubility pump" and through their combined effects, vertical gradients are established with low concentrations of nutrients at the surface and high concentrations in the deep ocean [e.g. *Gruber and Sarmiento*, 2002].

Upwelling of Circumpolar Deep Waters (CDW) in the Southern Ocean provides the

main conduit to return exported and remineralised nutrients to the surface [e.g. *Marinov et al.*, 2006] and if no such return flow occurred then the surface waters would become completely exhausted and primary production would cease. Despite the high surface concentrations of major nutrients the level of biological activity and concentrations of Chlorophyll *a*, the major photosynthetic pigment in phytoplankton, are low. In these so-called High Nutrient Low Chlorophyll (HNLC) regions such as the Southern Ocean and upwelling regions of the north and equatorial Pacific, numerous *in vitro* (bottle incubation) and *in situ* experiments [reviewed by *de Baar et al.*, 2005] have indicated that addition of dissolved iron (Fe) stimulates the growth of phytoplankton, but this theory does not take into account other factors that could be limiting primary production in the Southern Ocean, such as light limitation due to the high-latitude and deep mixed layers found in the region [*Dutkiewicz et al.*, 2006; *van Oijen et al.*, 2004], iron/light colimitation or grazing pressure, because often the control experiments of Fe enrichment studies would also show increased chlorophyll *a* concentration, suggesting iron limitation is not the only restricting factor [*de Baar et al.*, 2005]. Additionally, self shading of phytoplankton may restrict the effects of additional Fe and cap the maximum productivity attainable [*Boyd et al.*, 2000]. Because productivity is inefficient in this region, upwelling of carbon-rich deep waters causes net outgassing of carbon dioxide into the atmosphere [e.g. *Mikaloff Fletcher et al.*, 2007]. The remaining elevated concentrations of nutrients in Antarctic surface waters are mostly carried north, driven by the wind and either delivered laterally in the Ekman layer to neighbouring oligotrophic gyres [*Williams and Follows*, 1998] or subducted into the ocean interior in Antarctic Intermediate Water (AAIW) and Subantarctic Mode Waters (SAMW), which forms an important pathway for nutrient supply, controlling approximately 75% of biological productivity north of 30°S [*Sarmiento et al.*, 2004]. Furthermore, formation of AAIW and SAMW sequesters heat, freshwater and CO_2 at the northern flank of the ACC [*Rintoul*, 2006] since their formation is driven by air-sea interactions so perturbations to the injection of these water masses into the ocean interior could dramatically affect marine productivity and the atmospheric concentration of carbon dioxide. Yet, *Marinov et al.* [2006] suggest that, while AAIW and SAMW formation sets global thermocline nutrient budget and thus biological production rates, it is nutrient utilisation in upwelled waters (LCDW, Figure 1.3) that eventually form AABW adjacent to Antarctica that determines the concentration of atmospheric CO_2.

As will be shown below, different regions of the Southern Ocean have responded in different ways to changes in climate and a salient question concerns the linkages between ocean circulation and phytoplankton productivity, the key players in the global

carbon cycle. Variations in the rate of CDW upwelling that occurs relatively rapidly under modern conditions due to high abyssal mixing rates, air-sea-ice buoyancy fluxes [*Watson and Naveira Garabato*, 2006] and surface northward Ekman transport due to westerly wind stress over the ACC [*Toggweiler et al.*, 2006] may induce rapid variations in atmospheric composition. On the one hand, correlation between increased Southern Hemisphere winds (itself a likely result of human induced changes in climate [e.g. *Gillet and Thompson*, 2003; *Thompson and Solomon*, 2002]) and reduced Southern Ocean carbon sink suggest that future atmospheric pCO_2 may stabilise at a higher level than predicted by carbon chemistry alone because those estimates do not take into account the physical responses of the carbon cycle to changes in forcing [*Gille*, 2002; *Le Quéré et al.*, 2007]. On the other hand slowing this upward flux and subsequent carbon dioxide escape during the Last Glacial Maximum (LGM) may have effectively increased the deep ocean's ability to store biologically partitioned carbon for an extended period of time, isolating it from the surface ocean and atmospheric carbon reservoirs. Alternatively, an increase in primary production in the Southern Ocean may halt the evasion of CO_2 from upwelled CDW to the atmosphere stimulated by relieving dissolved iron stress by increased atmospheric dust supply at the LGM, which is a source of iron [*Martin*, 1990]. These issues, the development of which are charted below, have been at the heart of the debate surrounding the mechanism(s) responsible for natural changes in atmospheric CO_2 concentration associated with changes between glacial (cold) and interglacial (warm) climates.

1.2 Past Evidence of the Role of the Southern Ocean in Global Climate

1.2.1 Early hypotheses for glacial-interglacial climate change

Alteration of oceanic bulk properties associated with building/destroying large ice sheets cannot explain the differences in glacial–interglacial CO_2 through physical chemistry alone. Altering the temperature and salinity of the ocean have conflicting effects on the solubility of carbon dioxide: CO_2 is more soluble in cold water (the glacial ocean temperature was ~3–5 °C cooler than today), but less soluble in salty water (the glacial ocean was ~ 3% more saline due to storage of freshwater as ice on land). These combined effects could lower pCO_2 by 10–20 ppm [*Archer et al.*, 2000], which is an order of

magnitude too small to explain the glacial–interglacial CO_2 change. Other controls on solubility such as inorganic carbon and acid/base chemistry are more complex in their action and depend on a variety of other processes, such as biological productivity and ocean circulation.

Terrestrial biosphere carbon is also available on glacial–interglacial timescales although its size would need to more than double to account for the total change in atmospheric pCO_2. Indeed, depleted $\delta^{13}C$ from deep-sea calcium carbonate deposits during glacials suggests that the terrestrial biosphere actually released approximately 300–700 Gt C [*Archer et al.*, 2000; *Curry et al.*, 1988; *Duplessy et al.*, 1988], while ecosystem reconstructions suggest an even greater release [*Jansen et al.*, 2007]. This equates to an atmospheric increase of CO_2 of approximately 17 ppm after sediment interactions due to acidifying the ocean are taken into account [*Archer et al.*, 2000]

An early idea suggested a global increase in nutrient concentration that stimulated biological productivity in the macronutrient limited, oligotrophic, low latitude gyres achieved by erosion of organic rich sediments deposited on the continental shelf during interglacial sea level maxima that are then exposed by glacial sea level minima [*Broecker*, 1982]. The increase in primary production would result in a drawdown of atmospheric carbon dioxide and the accumulation of light isotopic carbon in the deep ocean. However, the "shelf hypothesis" now appears unlikely to be a major driver of CO_2 glacial-interglacial variability based on the possible lead in atmospheric pCO_2 over $\delta^{18}O_{atm}$ isotope anomaly as an indicator of global ice volume and sea level [*Broecker and Henderson*, 1998] and the fact that deposition and erosion of shelf sediments is a slow process bound by these changes in sea level [*Siegenthaler and Wenk*, 1984] and so therefore may not be able to explain the relatively rapid changes in the CO_2 record found in the ice cores. Additionally, the large volume of sediment required to be deposited and eroded on timescales of the order of 100 kyr is probably far greater than observations suggest [*Peacock et al.*, 2006], while export of such quantities of organic carbon might have led to deep ocean anoxia, which is not recorded [*François et al.*, 1997].

Box models were first used to address the sensitivity of atmospheric CO_2 concentration to high-latitude, particularly Southern Ocean, processes. *Sarmiento and Toggweiler* [1984] recognised that a change in high-latitude productivity or thermohaline circulation rate could lead to large changes in atmospheric CO_2, while *Siegenthaler and Wenk* [1984] suggested changes in ocean circulation that affect surface biogeochemical distributions, could affect atmospheric CO_2 concentration. *Knox and McElroy* [1984] also suggest circulation could be important. All three articles, the "Harvardton Bears"

(named after the three hosting institutions: Harvard, Princeton and Bern), based their conjecture on the Southern Ocean where macronutrients at the surface are present at high concentrations. Thus biological productivity in this region is not limited by these nutrients, as is the case elsewhere in the ocean, so changes in circulation and/or productivity here could ultimately lead to variations in pCO_2 by altering the strength of the biological pump.

Since the atmosphere can only "see" the surface ocean, the effect of the biological pump exporting carbon and nutrients to the deep ocean is to lower the pCO_2 of the atmosphere below what would be found in an abiotic "Strangelove" ocean. Considering the HNLC regions, if all the surface nutrients were consumed then the biological pump would be at full efficiency and a greater amount of CO_2 would be stored at depth, whereas if nutrients remained unused and returned to the deep ocean, the pump would operate inefficiently and CO_2 would leak back to the atmosphere. Atmospheric pCO_2 could vary by a factor of 3 if the biological pump were to vary over its extreme range of efficiency [*Knox and McElroy*, 1984].

1.2.2 Biological productivity explanations for lower glacial CO_2

The high nutrient low chlorophyll situation may be ameliorated by the addition of dissolved iron [e.g. *de Baar et al.*, 2005]. In an extension of this, *Martin* [1990] suggested glacial pCO_2 may have been lower due to a 50-fold increase in atmospheric dust supply (a source of iron) to the Southern Ocean (2-5× globally) during the LGM [*Mahowald et al.*, 2006b; *Petit et al.*, 1999]. By relieving the Fe limitation, phytoplankton growth may have been greatly enhanced and larger amounts of upwelled nutrients may have been utilised causing CO_2 drawdown, that is the biological pump would have operated more efficiently. While direct Southern Ocean iron fertilisation of phytoplankton is an attractive mechanism given the sensitivity of atmospheric pCO_2 to changes in production there [*Knox and McElroy*, 1984; *Sarmiento and Toggweiler*, 1984; *Siegenthaler and Wenk*, 1984], this theory does not take into account other factors that could be limiting [e.g. *Dutkiewicz et al.*, 2006; *van Oijen et al.*, 2004].

Proxy evidence also suggests a more complicated account of events, not least the suggestion that the majority of CO_2 changes occurred somewhat independently of dust variability [*Wolff et al.*, 2006]. An obvious sedimentary indicator of increased export production would be increased deposition, particularly of diatomaceous remains composed of silicate. Indeed the global signal of increased export production at the last

ice age coincides with the timing of the maximum in the dust record [*Kohfeld et al.*, 2005]. In the subantarctic zone (~ 40–50°S), increased importance of diatoms and evidence for increased export production from multiple proxies can be seen (Figure 1.6), however, the accumulation of diatom tests in sediments south of the modern Polar Front was clearly lower [*Kohfeld et al.*, 2005; *Sigman and Boyle*, 2000], probably due to reduction in upwelling supply of silicate [*Anderson et al.*, 2009]. It is still possible that productivity was elevated during ice ages but that it occurred in a form that was poorly preserved. However, measurements of a biogenic compound dimethylsulphide (DMS), mainly produced by phytoplankton such as *phaeocystis* which leave no fossil record, in an ice core suggest that this was not the case [*Wolff et al.*, 2006].

The ratio of $^{14}N/^{15}N$ may be used to estimate nutrient utilisation of overlying waters which could imply enhanced productivity: Uptake of nitrate by phytoplankton is associated with preferential uptake of lighter $^{14}NO_3^-$ which results in a 2.5‰ enrichment of the heavier isotope in the nitrate pool, that is an increase in $\delta^{15}N$, of the surrounding water and higher levels of the light isotope in the organic tissue formed, or a decrease of $\delta^{15}N$. This gradient is maintained by the biological pump, however any long term changes in nutrient utilisation may alter this balance. For example, an increase in nutrient uptake would decrease levels of the light isotope available and increase the use of the remaining heavier isotope. The sediment would record an increase in the $\delta^{15}N$ of the organic tissue. Similarly, the ratio of other nutrients may be used such as the ratio of $^{29}Si/^{30}Si$ of the silicate tests of diatoms, the ratio of $^{12}C/^{13}C$ in dissolved inorganic carbon (DIC), with the added complication of fractionation during air-sea exchange and collapse of the terrestrial biosphere, and the ratio of cadmium to calcium (Cd/Ca) of the surface water, which varies predictably with its nutrient (especially phosphate) content [*Elderfield and Rickaby*, 2000]. Although interpretation of proxies is complicated because the biological processes and export of organic tissue from the surface is dependent on multiple other processes and environmental factors [*Kohfeld et al.*, 2005], most studies agree that glacial $\delta^{15}N$ and $\delta^{13}C$ of the Southern Ocean did increase suggesting an increase in nutrient utilisation of a factor of two or more [*François et al.*, 1997; *Sigman and Boyle*, 2000] (although values from the equatorial Pacific, another HNLC region, show lower nutrient utilisation [*Archer et al.*, 2000]). This is at odds with the export production findings so likely represents a decrease in nutrient supply to the surface, causing more complete nutrient consumption than today and indicating decreased ventilation of deep waters at the surface of the Southern Ocean [*François et al.*, 1997]. Also, $\delta^{30}Si$ suggest lower silicate uptake, consistent with the export production patterns south of the Polar

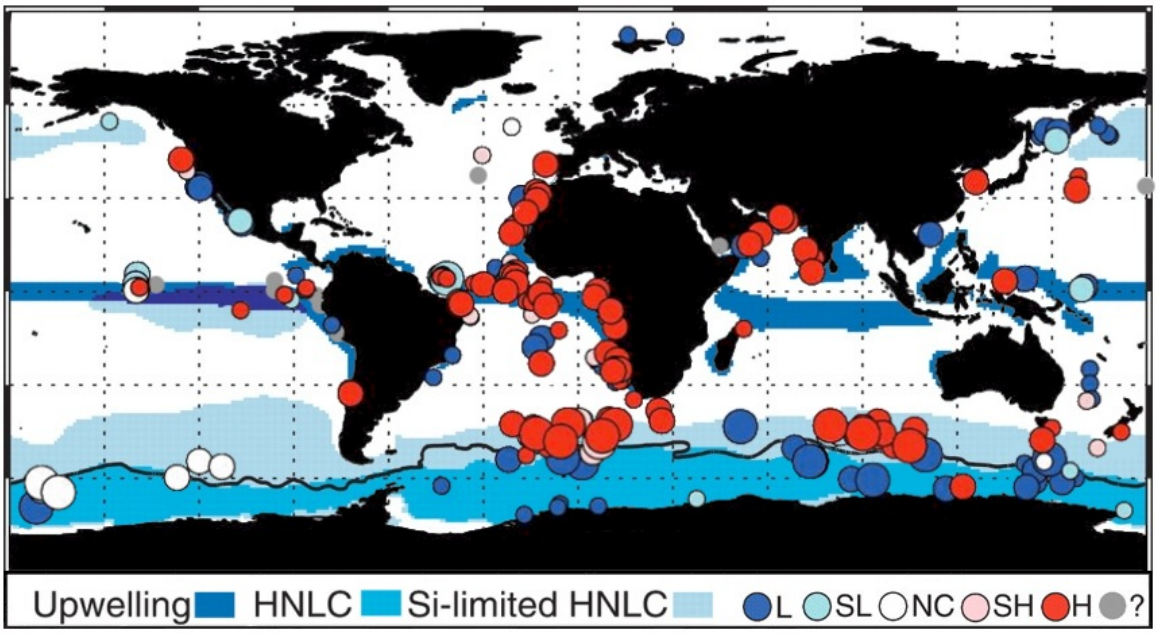

Figure 1.6: Relative changes in export production between the late Holocene (0-5000 years ago) and LGM (18–22 kyr ago). Dark and pale blue circles indicate lower (L) and slightly lower (SL) export production, respectively; dark and pale red circles indicate higher (H) and slightly higher (SH) export, respectively. White circles indicate no change (NC) between the two time periods. Grey circles represent sites where there is no unambiguous consensus between the different types of data. The size of the circle indicates the level of confidence (with small circles indicating low and large circles high confidence) in the assessment of the change in export production. The thick black line is the approximate position of the Antarctic Polar Front. Shaded areas of ocean are the most critical for controlling CO_2 uptake, including wind-induced upwelling (dark blue), HNLC regions where ratios of N or P to Chlorophyll-*a* concentration are above 20 µmol kg^{-1} per mg Chla m^{-2} (intermediate blue) and HNLC regions with Silica concentrations of less than 20 µmol kg^{-1} per mg Chla m^{-2} (light blue) [adapted from *Kohfeld et al.*, 2005].

Front in Figure 1.6. North of the Polar Front, nitrate utilisation appears to decrease slightly and therefore to remain consistent with export proxies suggests an increase in nutrient supply from below [*François et al.*, 1997]. Widespread foraminiferal Cd/Ca ratios also increase, suggesting an increase in phosphate concentration (or decrease in utilisation). The majority of the evidence does not support the idea that nutrient utilisation south of the modern Polar Front, stimulated by increased aeolian Fe deposition (whose importance and magnitude has recently been called into question [*Meskhidze et al.*, 2007; *Wagener et al.*, 2008]) can be used to explain entire glacial–interglacial change in atmospheric CO_2, although the enhancement seen in the sub-Antarctic region may help to explain some of the difference. It has been suggested that at the most this is may account for ~30 ppm [*Bopp et al.*, 2003]. Interestingly, this pattern of nutrient supply, biological activity and atmospheric CO_2 change is reminiscent of *Marinov*

et al. [2006]'s "biogeochemical divide" with decreased ventilation of the deep-limb of the Southern Ocean meridional overturning circulation regulating CO_2 concentrations while increased vigour of the intermediate limb controls net primary production. Although export production opposes this pattern because productivity might have been reduced in the region where atmospheric CO_2 is supposed to be removed to the deep ocean, it may be reconciled by considering the efficiency of nutrient utilisation.

Indirect effects of increased iron availability at the glacial maxima could help explain some of the discrepancies between proxy data. There is debate over which nutrient ultimately limits primary production [*Tyrrell*, 1999] due to the fact that PO_4^{-3} has a very long residence time while NO_3^- can be generated fairly rapidly by biological processes yet in oligotrophic regions of the ocean, there remains a small residual concentration of phosphate even when nitrate has been totally exhausted, furthermore, additions of nitrate to these waters stimulates extra primary production, while addition of phosphate does not. Nitrate is thought to be the proximate limiting nutrient in surface waters, that is, the most limiting to instantaneous growth while phosphate can be seen as the ultimate limiting nutrient, whose rate of supply regulates total ocean productivity.

Nitrogen fixation (diazotrophy) has a large metabolic iron requirement [100× that of photoautotrophy, *Falkowski*, 1997] and the distributions of nitrate and phosphate suggest that this process occurs mainly in tropical sea surface areas with abundant dust deposition such as the tropical East Atlantic. The increased dustiness during glacial periods (particularly of the Southern Ocean) could promote nitrogen fixation, release the surface ocean from nitrate limitation and increase primary production until it becomes phosphate-limited or, if not used locally, millennial-scale ocean circulation would redistribute excess nitrate to productive regions where it would increase carbon fixation. This is the equivalent of increasing the global pool of nutrients by 4–10% [*Archer et al.*, 2000]. If iron-stimulated diazotrophy were to increase the N:P ratio of the ocean to the point at which phosphate becomes absolutely limiting then the global nutrient pool could increase by a factor of ~ 2 [*Archer et al.*, 2000]. Indeed, phytoplankton under nutrient replete laboratory culture do exhibit a wide range of N:P ratios [*Geider and La Roche*, 2002]. A decrease in phosphate dependence in this way might explain the conflicting $\delta^{15}N$ and Cd/Ca data which point to increased nitrate, but decreased phosphate utilisation.

Possible changes in the rate of denitrification may also be important since an active biological pump might increase the volume of low-oxygen waters, while increased ventilation of intermediate layers of the ocean could decrease denitrification rates, perhaps

by formation of glacial intermediate water in the north Atlantic [*Keeling and Stephens*, 2001] and Pacific, or decreased tropical stratification because of lower sea-surface temperatures.

By carefully picking the location of sites for isotope/proxy studies, details of the nitrogen cycle can be discerned. Denitrification has a strong signal in δ^{15}N of −30‰ (that is the unused nitrate pool becomes progressively enriched in ^{15}N) [*Devol*, 2002]. Sediment-based denitrification often utilises the entire sedimentary pool of nitrate and therefore leaves none behind to carry an isotopic signal whereas water-column denitrification is only partially completed leaving behind an isotopic signal that can be detected. Oligotrophic regions where surface nitrate is completely utilised does not include the fractionation effect of biological uptake in the deep nitrate pool and therefore provides an insight into the balance of denitrification since the bulk δ^{15}N should be a balance between its sources (~0‰) and sinks (−30‰ for watercolumn and 0‰ for sediment denitrification)[*Archer et al.*, 2000]. The glacial δ^{15}N of 5–6‰ is similar to today's value, suggesting that the balance between sedimentary to water column denitrification was also similar, although, cyclical variations in sediment δ^{15}N with interglacial enrichments of >8‰ [*Altabet et al.*, 2002; *Ganeshram et al.*, 2000, 2002] suggest that denitrification as a whole may have decreased during glacial times by as much as 50%.

Ganeshram et al. [2002] also argue for decreased diazotrophy during glacials, not higher as has been suggested [e.g. *Broecker and Henderson*, 1998; *Falkowski*, 1997]. Nitrogen fixation is independent of nitrate concentration but still depends on the concentration of phosphate. If nitrate is scarce or absent (low N:P ratio) then diazotrophs enjoy competitive advantage over other types of phytoplankton, however, if nitrate is more abundant then they are at a disadvantage because of the extra metabolic cost of using otherwise unavailable N_2 [*Tyrrell*, 1999]. Linked to a possible decline in denitrification, *Ganeshram et al.* [2002] find an accompanying decrease in phopshorite formation, an important sedimentary sink for phosphate, probably due to the decline in the area of suboxic waters off northwest Mexico and in the Arabian Sea which together account for more than one-third of denitrification and 90% of phosphogenesis. These concurrent changes, a modest (~10%) increase in phosphate concentration and a possible large increase in nitrate concentration, alter the glacial ocean's N:P ratio beyond Redfield stoichiometry, effectively depleting phosphate relative to nitrate. The model of *Tyrrell* [1999] predicts that this change would reduce nitrogen fixation, despite increases in aeolian iron input, thus restoring the Redfield ratio. These findings fuel skepticism that

the Redfield ratio is negotiable and therefore cast some doubt over the effectiveness of these mechanisms for generating glacial–interglacial changes in atmospheric CO_2.

One feature of the Southern Ocean proxy data discussed remains to be explained. The $\delta^{15}N$ and $\delta^{13}C$ of Southern Ocean sediments both increase while their $\delta^{30}Si$ decreases [*Sigman and Boyle*, 2000], despite a probable increase in siliceous diatom importance as shown in *in situ* iron fertilisation experiments [*de Baar et al.*, 2005]. Even if the nitrogen isotope signal is due to higher nutrient usage because of increased stratification [*Ganeshram*, 2002], the shift from carbonate secreting to silicate secreting phytoplankton should increase Si uptake. However, during SOIREE [the Southern Ocean Iron Release Experiment, *Boyd et al.*, 2000] enhanced iron supply to diatoms within the "patch" resulted in a 50% decrease in Si:C uptake ratios [*Watson et al.*, 2000] and therefore Si:N ratios from 2:1 in the modern Southern Ocean to 1:1 [*Brzezinski et al.*, 2002; *Matsumoto et al.*, 2002]. More efficient use of silicate by diatoms in response to iron fertilisation could reconcile the $\delta^{15}N$ and $\delta^{30}Si$ proxies and could affect glacial–interglacial atmospheric CO_2. Modern nutrient distributions [*Brzezinski et al.*, 2002] show that silicic acid depleted waters formed in the Southern Ocean are transported northward across the Antarctic Polar Front and combined into AAIW and SAMW that penetrate at thermocline depths at least as far as the subtropics. Figure 1.6 shows that a large part of the subantarctic zone is Si-limited, as well as parts of the equatorial and northern Pacific. If the waters that carry the underutilised silicic acid signal were advected in a similar way as the present [*Matsumoto et al.*, 2001], then upwelling of high silica low nitrate waters could have driven changes in phytoplankton community structure from coccolithophorids to diatoms [*Archer et al.*, 2000], supported by lower glacial opal accumulation rates in the Antarctic and higher opal accumulation rates near the equator [*Brzezinski et al.*, 2002; *Matsumoto et al.*, 2002] and specific molecular biomarkers [*Kohfeld et al.*, 2005], and productivity. This floral shift has two implications. Firstly, diatoms are heavier and therefore sink faster through the water-column and are also less prone to grazing which increases the efficiency of particle (and nutrient) export to the deep ocean. This can partially decouple export production from primary production due to increased carbon export and increased area of oligotrophic gyres as is partially suggested by Figure 1.6. There is evidence for increased export production north of the modern position of the Antarctic Polar Front, yet primary production is thought to be more or less constant [*Bopp et al.*, 2003]. Secondly, reduction in the export ratio of inorganic calcium carbonate to organic carbon associated with the shift from calcarious secreting to opal secreting phytoplankton affects the alkalinity of the surface waters which has a large effect on the ocean's capacity to absorb CO_2 [*Archer et al.*,

2000]. The effect of decreasing the "rain ratio" in this way is discussed below, however the important results for the deep ocean are an increase in carbonate ion concentration and deepening of the calcite lysocline, the depth above which the calcium carbonate in sediments is preserved and below which it is dissolved, causing increased carbonate sediment preservation, while at the surface, excess alkalinity due to the reduced export of calcium carbonate increases CO_2 solubility.

It is hard to tell if this leakage of silicic acid from the Southern Ocean actually occurred because opal accumulation rates are not uniformly high in sediment records [*Ganeshram*, 2002], there is no increase in export production south of the Polar Front (Figure 1.6) where the underutilised silicic acid pool should be created and, as described below, there is little evidence for the predicted increase of deep ocean carbonate ion concentration [*Kohfeld et al.*, 2005] or a large shift in the lysocline [*Archer et al.*, 2000; *Broecker and Henderson*, 1998; *Sigman and Boyle*, 2000], which is often cited as this theory's "fatal flaw". Nevertheless, the different sensitivities of box models and GCMs leave this result open because atmospheric CO_2 in OGCMs is more sensitive to changes in $CaCO_3$ production and simulated shifts in the lysocline may be reduced by 50% [*Archer et al.*, 2000].

1.2.3 The effect of ocean chemistry and carbonate compensation

The solubility of carbon dioxide not only depends on the preexisting concentration of DIC, whose major constituents are dissolved CO_2, bicarbonate (HCO_3^-) and carbonate (CO_3^{2-}), but also the alkalinity, which is a measure of the ocean's acid buffering capacity, determining the extent of equilibriation between the components of DIC. One family of hypotheses regarding low glacial atmospheric CO_2 invokes an increase or redistribution in ocean alkalinity. An increase in mean ocean alkalinity causes a greater quantity of DIC to exist as carbonate ions, which reduces concentrations of dissolved CO_2, the ocean becomes more basic and therefore lowers atmospheric CO_2. However, if alkalinity is constant and DIC increases (as with addition of anthropogenic CO_2) then the ocean becomes more acidic, which prohibits CO_2 hydrolysis into carbonate. Therefore, the concentration of dissolved CO_2 tends to increase, as does atmospheric CO_2 [e.g. *Archer et al.*, 2000; *Sigman and Boyle*, 2000].

Alkalinity is added to the ocean mainly by rivers carrying the products of carbonate weathering on land and forms a balance with alkalinity removal by precipitation of calcium carbonate ($CaCO_3$) by phytoplankton and burial in deep sea sediments and *in situ* precipitation in shallow water coral reefs. This balance is achieved by altering the preservation of carbonate sediments in the deep ocean through variations in the carbonate compensation depth (CCD), the level above which $CaCO_3$ is preserved and below which $CaCO_3$ sediments dissolve. An increase in glacial carbonate weathering would deepen the CCD in order to increase the removal of alkalinity from the ocean. For every 1 km deepening of the CCD, atmospheric CO_2 decreases by 25 ppm. Similarly, a decrease of coral reef growth in the shallow ocean caused by falling glacial sea level would cause a similar response as carbonate burial shifts to the deep ocean.

Changes in the export ratio of $CaCO_3$ and organic material to the deep ocean can also invoke a carbonate compensation response. Decreasing the ratio, i.e. more organic carbon is exported or the particles sink faster so organic carbon remineralisation is reduced (see above), has a two-fold impact. Firstly, there is a reduced export of alkalinity from the surface to the deep ocean, which enables a larger concentration of CO_2 to dissolve at the sea surface and causes a reduction in alkalinity removal at the sea floor. Secondly, the greater remineralisation of organic carbon at the sea floor creates acidic conditions that dissolve carbonate sediments and therefore shoal the depth of the CCD, causing reduced carbonate burial and an increase in the mean ocean alkalinity.

However, these mechanisms require large changes in the deposition pattern of $CaCO_3$ and large changes in the depth of the CCD to explain the full amplitude of the glacial-interglacial CO_2 difference that paleoceanographic evidence does not support and furthermore, the timescale for carbonate compensation is of the order of 5-10 kyr and therefore may only explain slow variations in atmospheric CO_2 between glacial and interglacial periods [*Archer et al.*, 2000; *Jansen et al.*, 2007; *Sigman et al.*, 2010].

1.2.4 The Southern Ocean ventilation hypothesis for lower glacial CO_2

Upwelling around the Antarctic continent exposes carbon dioxide rich deep waters to the atmosphere and occurs relatively rapidly under modern conditions due to high abyssal mixing rates, air-sea-ice buoyancy fluxes [*Watson and Naveira Garabato*, 2006] and surface northward Ekman transport due to westerly wind stress over the ACC [*Toggweiler*

et al., 2006]. Slowing this upward flux and carbon dioxide escape might effectively increase the deep ocean's ability to store biologically partitioned carbon for an extended period of time, isolating it from the surface ocean and atmospheric carbon reservoirs. This reduced Southern Ocean ventilation could be realised via several mechanisms, all of which act to modulate different parts of the residual overturning circulation in the Southern Ocean [e.g. *Keeling and Visbeck*, 2001] and thus the residence time of deep ocean CO_2:

1. Increased sea-ice cover limiting gas exchange [*Keeling and Stephens*, 2001; *Stephens and Keeling*, 2000].

2. Increased stratification due to reduced/reversed buoyancy fluxes and/or reduced deep mixing [*Toggweiler*, 1999; *Watson and Naveira Garabato*, 2006].

3. Reduced Ekman transport induced upwelling due to variation in southern hemisphere winds [*Anderson et al.*, 2009; *Sigman and Boyle*, 2000; *Toggweiler*, 2008; *Toggweiler et al.*, 2006].

Reduced supply of deep water to the surface, or increased Southern Ocean stratification [e.g. *François et al.*, 1997; *Schmittner and Galbraith*, 2008; *Toggweiler*, 1999] has already been suggested by evidence that implies increased nutrient utilisation efficiency and because of this, even lower export production than presently found south of the modern position of the Polar Front (Figure 1.6) could suppress CO_2 outgassing to the atmosphere. Furthermore, there is evidence of reduced (but non-zero) Southern Ocean sourced intermediate and bottom water oxygen concentrations [*François et al.*, 1997; *Govin et al.*, 2009]. This implies both reduced ventilation during periods of low atmospheric CO_2 and restarting or strengthening of the Southern Ocean meridional overturning upon deglaciation. Several paleoceanographic studies support such a sequence of events, however a hydrographic reconstruction in the Southern Ocean based on $\delta^{18}O$ measurements suggests that in fact, vertical circulation, stratification and upwelling fluxes were probably similar during the LGM and Holocene [*Matsumoto et al.*, 2001] with continued upwelling of CDW, northward surface Ekman transport and intermediate and mode water formation [*Pahnke and Zahn*, 2005; *Pahnke et al.*, 2008, albeit at a reduced rate].

Spero and Lea [2002] explained the presence of low bulk $\delta^{13}C$ of intermediate dwelling foraminifera during the most recent deglaciation at low latitudes as the signal of a reinvigorated Southern Ocean circulation. They postulated that the low carbon isotope

signal originated in deep CDW was isolated from the surface ocean and atmosphere, but as Antarctica warmed, and ventilation of the deep ocean strengthened then these waters were drawn to the surface. Here, partial outgassing of low $\delta^{13}CO_2$ may have occurred (recorded in the atmospheric CO_2 record [*Spero and Lea*, 2002, and references therein]) before these waters were subducted into the ocean interior as low-isotopic-carbon AAIW and SAMW, exported to the north and the signal recorded.

A similar sequence of events is proposed to explain the drops in the ratio of ^{14}C to ^{12}C during these periods [*Marchitto et al.*, 2007; *Skinner et al.*, 2010]. Isolation of abyssal water masses causes depletion in ^{14}C by radioactive decay, therefore should the Southern Ocean stratification become weakened and upwelling of these depleted water masses initiated, then their reintroduction to the surface would release low $\delta^{14}CO_2$ into the surface ocean/atmosphere, causing the observed reduced atmospheric isotopic signal. Again, subduction and northward advection of low-isotopic-carbon AAIW and SAMW is found [*Marchitto et al.*, 2007], although possibly not as widely as the low $\delta^{13}C$ [e.g. *De Pol-Holz et al.*, 2010]. Also, the existence of an isolated, low ^{14}C reservoir is inconclusive, at least in the Pacific Ocean [*Anderson and Carr*, 2010; *Broecker and Clark*, 2010].

Finally, *Anderson et al.* [2009] find periods of likely elevated opal production by diatoms just to the south of the Polar Front (lower during the LGM than today, Figure 1.6) concurrent with periods of increasing atmospheric CO_2. The total amount of biogenic opal accumulated in sediments is limited by the supply of dissolved silicon (Si) contained within upwelling nutrient (and carbon) rich deep waters. For this reason, these results might conclusively link deglacial ventilation of the deep Southern Ocean, inferred from increased opal fluxes, with the rise in carbon dioxide in the atmosphere. Moreover, widespread accumulation of biogenic opal fed by nutrients carried to low latitudes by AAIW and SAMW then upwelled to the surface also increases [*Anderson et al.*, 2009].

The cause of such changes in Southern Ocean overturning is still under debate [*Stephens and Keeling*, 2000; *Toggweiler et al.*, 2006; *Watson and Naveira Garabato*, 2006]. Antarctic sea ice is highly seasonal with low coverage during southern hemisphere summer ($\sim 3.5 \times 10^6\,km^2$) increasing to $\sim 18 \times 10^6\,km^2$ and extending to between 60–65°S in the winter [*Tomczak and Godfrey*, 2005]. Ice rafted debris and paleo-phytoplankton assemblages suggest that winter sea ice extent was greater during the LGM and could have reached as far north as the modern position of the Polar Front [*Crosta et al.*, 1998]. However, summer ice extent is poorly constrained and may have been similar to the modern summer or winter limit. Not only would sea ice cover physically prevent air-sea

gas exchange when present, thus locking respired CO_2 into the water masses formed in the Southern Ocean when they are subducted into the interior, but the stored freshwater would have been released during summer melting south of the Polar Front to form a highly stratified surface layer, especially since the colder glacial ocean is easier to stabilise by surface freshening due to the non-linearity of the equation of state. Furthermore, sea ice formation and shielding of the outcropping deep water from net precipitation and heat flux inhibits northward surface flow in the Ekman layer as the density change that allows crossing of mean surface isopycnals is prevented [*Keeling and Stephens*, 2001; *Watson and Naveira Garabato*, 2006] causing a decrease in Antarctic upwelling. However, *Keeling and Visbeck* [2001] indicate that deep upwelling may actually increase in response to stratified conditions that suppress southward eddy transport from the Polar Front thus altering the balance of the residual circulation, yet if only the shallowest 30–50 m are affected, and the remainder of the density structure remains similar to present conditions [*Matsumoto et al.*, 2001], then there may have been no change in eddy, or residual circulation induced [*Sigman and Boyle*, 2001]. Reduced overturning may result in a reduced volume of intermediate and mode waters exported northward [*Pahnke and Zahn*, 2005; *Pahnke et al.*, 2008]. Although this is uncertain [*Fischer et al.*, 2010; *Muratli et al.*, 2010], an increase in AAIW extent is seen during the last deglaciation and may contribute to or cause observed AMOC collapses due to increase in freshwater supply to the North Atlantic [*Pahnke et al.*, 2008; *Weaver et al.*, 2003].

Altering deep stratification is related to changing abyssal diapycnal mixing rates. Evidence for greater glacial stratification in the deep ocean due to near freezing AABW temperatures, increased salinity and non-linearity in the equation of state suggests that the density anomaly between glacial AABW and overlying waters could have been three times larger [*Adkins et al.*, 2002] thus inhibiting abyssal diapycnal mixing [*Watson and Naveira Garabato*, 2006]. Instead of the rapid ventilation that occurs today [*Naveira Garabato et al.*, 2007], deep waters would have needed to travel further equatorward in order to be mixed upwards into lighter density classes and eventually returned to the surface, therefore increasing deep ocean isolation and storage of CO_2 [*Watson and Naveira Garabato*, 2006]. However, reduced glacial sea level, due to freshwater storage on land, could be expected to cause more vigorous tidal flow over the more pronounced topography which may have the opposite effect, although this may have only been the case in the North Atlantic [*Egbert et al.*, 2004; *Oliver and Edwards*, 2008]. Inflow of colder NADW may also increase deep ocean stratification and suppress vertical mixing [*Fučkar and Vallis*, 2007; *Gildor and Tziperman*, 2001; *Gildor et al.*, 2002].

The final proposed way to alter Southern Ocean ventilation is through altered Ekman transport as a consequence of variations of the Southern Ocean westerly wind stress at the unblocked latitude band of Drake Passage. The current paradigm for wind driven upwelling [e.g. *Sigman and Boyle*, 2000; *Toggweiler et al.*, 2006] is that a northward shift in the westerly wind belt may have occurred during glacial periods with weaker or more northerly positioned winds thought to reduce deep water ventilation and therefore increase Southern Ocean stratification [*Toggweiler*, 1999]. A strengthening and/or southward shift to the modern position of the westerlies then occurs around deglaciation. *Toggweiler et al.* [2006]'s contention is that in a model with surface nutrient restoring [e.g. *Najjar and Orr*, 1998] the Southern Ocean "biogeochemical divide" [*Marinov et al.*, 2006] is manipulated so that the abyssal AABW cell that controls CO_2 escape to the atmosphere is suppressed while the upper AAIW cell that controls global productivity is maintained, thus causing accumulation of carbon in the deep ocean and preventing its efficient return to the atmosphere through upwelling of LCDW. An important point is that they do not explicitly shift the Southern Ocean westerlies but merely weaken them *in situ*, which they argue achieves the same ends.

Evidence for such shifts comes from pollen stratigraphy from the Chilean Lake District, showing an increase in plant species commonly found in subantarctic environments and above the Andean treeline today, at 41°S and near sea level around the LGM [*Moreno et al.*, 1999]. This could be explained by a large equatorward shift in the Southern Hemisphere westerly wind belt because of the cool, wet climate under the storm tracks. *McCulloch et al.* [2000] were able to follow the increased precipitation from the storm track as it migrated poleward in both vegetation and glacier extent between 40–55°S to the present position of ~50°S over 2500 years. During the last 3000 years there may be a link between incoming solar radiation and the position of the extratropical Southern Hemisphere westerlies based on paleoclimate records from Chile controlled by precipitation changes [*Varma et al.*, 2010]. However, increased precipitation may come from changes in moisture convergence associated with changes in sea surface temperatures without large changes in wind strength or pattern [*Dong and Valdes*, 1998; *Sime et al.*, 2010].

An increase in atmospheric equator to pole temperature gradient might suggest stronger winds [*Keeling and Visbeck*, 2001], yet wind strength could depend more on regional, not global, temperature differences and so a possible decrease in the gradient across the Antarctic could lead to the reverse [*Sigman and Boyle*, 2001]. In this case, increased

sea ice extent and colder Antarctic sea surface temperatures could be expected to increase atmospheric baroclinicity resulting in stronger winds. Increased dust content from Patagonia in Antarctic ice cores [*Petit et al.*, 1999] is also ambiguous, pointing to either increased wind strength or more arid conditions at the source region (suggesting weaker winds). A variety of proxies from Australia and New Zealand assessed by *Shulmeister et al.* [2004] all point to enhanced westerly winds at the LGM and reduced winds at the start of the Holocene. Modelling efforts of the LGM are inconclusive. Coupled climate model simulations for the Paleoclimate Model Intercomparison Project (PMIP) suggest no significant latitudinal shifts of the Southern Hemisphere westerlies [*Menviel et al.*, 2008] but do not agree on magnitude while general circulation models of the atmosphere and ocean suggest either no real change [*Dong and Valdes*, 1998], northward shift [*Williams and Bryan*, 2006], southward shift [*Kitoh et al.*, 2001], weakening and northward shift [*Kim et al.*, 2003], strengthening and southward shift [*Shin et al.*, 2003] and increasing in strength with no latitudinal shift [*Otto-Bliesner et al.*, 2006]. The problem is complex because of the different treatment of sea surface temperature (prescribed or prognostically computed), atmospheric circulation and processes in the cryosphere (on land and at sea). Paleoceanographic records of δ^{18}O and δ^{13}C examined by *Govin et al.* [2009] suggest a northward migration of the Southern Ocean hydrographic fronts and decreased upwelling of CDW consistent with northward shifted winds during the LGM but on the contrary, a northward migration of fronts increases the deep water outcrop area and leads to increased outgassing of CO_2 in a geostrophic-frictional balance model [*Tschumi et al.*, 2008]. *Matsumoto et al.* [2001] discerned no change in ACC frontal position from their latitudinal δ^{18}O distributions.

Although a large number of mechanisms have been suggested to account for the full 80–100 ppm change in glacial interglacial CO_2 [e.g. *Archer et al.*, 2000; *Fischer et al.*, 2010; *Sigman and Boyle*, 2000], conflicts with paleocenaographic evidence and timing constraints suggest that a combination of several processes, possibly acting in synergy, are necessary to explain such changes. Recent conjecture [*Peacock et al.*, 2006] has suggested that physical processes need only account for the initial change of CO_2 in to or out of an ice age, after which other processes that are slower in action or constrained by sea level or ice-sheet size come into play such as increased whole ocean nutrient/ alkalinity content, biological activity and carbonate compensation. This is consistent with the timing of sea level and dust flux changes during the second half of a transition [e.g. *Broecker and Henderson*, 1998; *Kohfeld et al.*, 2005]. Furthermore, around 20–40 ppm of the full glacial-interglacial CO_2 change is regularly attributed to changes in

ocean circulation [*Bopp et al.*, 2003; *Brovkin et al.*, 2007; *Fischer et al.*, 2010; *Gildor et al.*, 2002; *Köhler and Fischer*, 2006; *Peacock et al.*, 2006; *Toggweiler*, 1999].

1.3 Role of the Southern Ocean in Present and Future Climate Change

Study of past Southern Ocean circulation and biogeochemistry is relevant to understanding and predicting changes in the modern climate, particularly in terms of the distribution of heat and anthropogenic CO_2. *Goodwin et al.* [2009]'s appraisal of radiative forcing and changes in the carbon cycle and ocean chemistry suggested that the sensitivity of radiative forcing due to CO_2 is probably the same for glacial-interglacial climates and the present day. *Sabine et al.* [2004] calculated that over 40% of anthropogenic carbon dioxide emitted between 1800 and 1994 could be found between 50°S and 14°S and that atmospheric CO_2 concentrations would be approximately 55 ppm higher if it was not for oceanic carbon uptake. However, there is little anthropogenic CO_2 associated with AABW due to low buffering capacity, limited residence time in the surface ocean before export to the abyss, sea ice as a physical barrier to air sea exchange and entrainment of low anthropogenic CO_2 subsurface waters [*Poisson and Chen*, 1987; *Sabine et al.*, 2004].

Recent observations [*Thompson and Solomon*, 2002] of the Southern Annular Mode (SAM), the dominant source of high-latitude climate variability in the Southern Hemisphere, have shown a trend towards positive values which translates to stronger westerly circumpolar flow over the Southern Ocean and cooling over the majority of the Antarctic continent, except for the Antarctic Peninsula and Patagonia, which are experiencing a warming trend and reduction in Bellingshausen Sea ice shelf/sea ice coverage. Overall, the monthly average SAM index is strongest when polar temperatures are coldest (i.e. winter) and weakest when polar temperatures are warm (i.e. summer) but the significant positive trend appears to be determined by Antarctic ozone depletion related to the polar "ozone hole" [*Gillet and Thompson*, 2003; *Perlwitz et al.*, 2008], with water vapour and greenhouse gases playing a much smaller part. Coupled model studies that capture these processes have also reproduced the observed strengthening and southward migration of the Southern Hemisphere westerlies [*Fyfe and Saenko*, 2005, 2006]. This relocation of the westerly wind belt drives a southward migration of the ACC in coarse resolution models [*Fyfe and Saenko*, 2006] and an intensification of the Southern Ocean

meridional overturning circulation implying increased Ekman transport, deep water upwelling and flushing of CO_2 to the atmosphere. Variability of transports through Drake Passage derived from Antarctic bottom pressure recorders reflect seasonal SAM variability [*Meredith et al.*, 2004] while *Russell et al.* [2006] also found that a poleward shift in the mean position of the westerlies increased Southern Ocean ventilation.

However, the implication that the positive trend in the SAM index is due to photochemical cooling due to the reduced absorption of ultra violet radiation [*Gillet and Thompson*, 2003] renders the current inference of weaker, northward shifted Southern Hemisphere westerlies during cold conditions and stronger southward shifted winds during warm conditions somewhat invalid. *Perlwitz et al.* [2008] used a chemistry-climate model to simulate the climatic implications of the projected recovery of Antarctic ozone levels with reduced concentrations of halogenated carbon compounds. They found, amongst other things, that increased levels of ozone in the stratosphere during the twenty-first century led to a ~3 K warming of the troposphere and $2\,\mathrm{m\,s^{-1}}$ weaker westerly zonal winds that dominates and opposes small projected greenhouse gas-induced positive tendency of the SAM index. If stronger Southern Hemisphere winds were characteristic of the glacial climate then the moist conditions inferred from the Chilean Lake District may be explained by the same mechanism as Antarctic Peninsula and Patagonian warming today, that is warm maritime air anomalously advected from the region to the west of Drake Passage. Decreasing stratospheric geopotential height with positive SAM, along with general atmopsheric cooling during glacials may then explain the down slope migration of subantarctic and high altitude species.

Nevertheless, the impact of the currently observed pattern of positive trend in the SAM index, likely to continue towards the end of the century is hotly debated [*Law et al.*, 2008; *Le Quéré et al.*, 2007, 2008; *Zickfeld et al.*, 2008]. The emerging consensus is that stronger winds drive increased Ekman divergence that draws a greater volume of carbon rich deep waters to the surface in the Southern Ocean, leading to increased outgassing of natural CO_2 that is partially compensated by increased anthropogenic carbon uptake in regions of AAIW and SAMW formation and subduction [*Le Quéré et al.*, 2007; *Lenton and Matear*, 2007; *Lovenduski et al.*, 2007, 2008; *Wetzel et al.*, 2005] using coarse resolution models. This acts to weaken the Southern Ocean CO_2 sink because the secular trend in the SAM index has reduced the rate of uptake of CO_2 from the atmosphere, which should increase in step with the atmospheric concentration of anthropogenic CO_2 [*Le Quéré et al.*, 2007]. These changes in ocean circulation also fuel changes in phytoplankton abundance with increased upwelling supplying the surface

ocean with nutrients causing increased chlorophyll-*a* concentrations and greater biological productivity [*Lovenduski and Gruber*, 2005], which reduces the evasion of upwelled natural CO_2. The Southern Ocean may also be dependent on other modes of variability such as El Ninõ-Southern Oscillation (ENSO) [*Verdy et al.*, 2007].

Gille [2002] suggested that the mid depth Southern Ocean was warming on average faster than the global ocean by 0.17±0.06 °C between the 1950's and the 1990's possibly due to a southward shift in the ACC, while *Naveira Garabato et al.* [2009] observed a freshening of SAMW and AAIW by ~0.05 in Drake Passage since at least the 1990's. Increased stratification due to warming and freshening of the upper ocean could weaken the uptake of anthropogenic CO_2 in the Southern Ocean by blocking outcropping isopycnals that enable sequestration of carbon dioxide into the ocean interior [*Caldeira and Duffy*, 2000; *Lenton and Matear*, 2007], but this may be countered by reduction in outgassing of naturally upwelled CO_2 from the deep ocean [*Mikaloff Fletcher et al.*, 2007].

Mignone et al. [2006] show that the distribution of anthropogenic carbon dioxide uptake is determined by the strength of the Southern Hemisphere winds, while the magnitude of uptake is dependent on the mesoscale eddy field. A cautious approach is consequently required since the ocean and climate models often used to assess the impact of anthropogenic emissions on the Earth's climate do not have fine enough spatial resolution to capture the response of the mesoscale eddy field to changes in forcing. In a non-eddy resolving model with parameterised sub-grid-scale eddy transfers [e.g. *Gent and McWilliams*, 1990] and forced by projected future extratropical winds and greenhouse gases results in strengthening (12–16 Sv) and poleward migration (0.4–1.5°) of the ACC until the end of the century [*Fyfe and Saenko*, 2005, 2006]. *Saenko et al.* [2005] obtain an even greater increase in transport through Drake Passage of 21 Sv and 12 Sv more intense Southern Ocean meridional overturning circulation under quadruple CO_2 conditions due to the increase in baroclinic potential energy stored in steeply sloping isopycnals. *Fyfe et al.* [2007] attempted to explain increased Southern Hemisphere warming in a coarse resolution Earth system climate model, finding that poleward shifting winds (and ACC) played an important role in setting the subsurface warming structure. However, representing the direct response (i.e. intensification) of the mesoscale eddy field to changes in Southern Hemisphere winds, motivated by results from high resolution eddy-permitting models [*Hallberg and Gnanadesikan*, 2006], greatly enhanced warming south of the ACC and decreased it to the north, consistent with the proposal that the observed warming was caused by increased southward eddy heat transports [*Meredith and Hogg*, 2006].

Employing this scheme resulted in a stronger Southern Ocean CO_2 sink due to reduced wind-driven upwelling and natural CO_2 escape [*Zickfeld et al.*, 2007].

There is a growing body of literature from models [*Hallberg and Gnanadesikan*, 2001, 2006; *Hogg and Blundell*, 2006; *Hogg et al.*, 2008] and observations [e.g. *Meredith and Hogg*, 2006] that highlights the pivotal function of eddies in setting Southern Ocean circulation, with the emerging view that the ACC lies in a saturated regime whereby changes in wind stress magnitude do not drive large changes in zonal and meridional transports, but instead impart energy into the mesoscale eddy field. *Hallberg and Gnanadesikan* [2001] suggest that two regimes exist, namely a buoyancy dominated regime (i.e. large diapycnal water mass transformations occur) under weak wind forcing in which ACC transport is proportional to wind stress while the second is an eddy saturated regime where stronger winds increase mesoscale eddy activity but do not affect current transport. Currently, the ACC may be at the boundary of two regimes where both processes are important, but increase in wind strength will likely be compensated by an increase in mesoscale eddy activity. *Meredith and Hogg* [2006] found increases in wind stress rapidly impart potential energy to the ocean in sloping isopycnals that is released more gradually by baroclinic instability as eddy kinetic energy with a lag of 2–3 years. Thus northward Ekman transports are balanced by southward eddy fluxes, which also carries heat to the region south of the ACC, and there is little variation of zonal ACC transport. *Böning et al.* [2008] demonstrated using the Argo array of profiling floats that despite a 50–80 km southward shift in upper ocean isopycnals, related to the positive trend in the SAM index, there was no associated increase in isopycnal slope. These data suggest that upwelling and ACC transport are insensitive to decadal changes in wind forcing consistent with an eddy saturated regime associated with increased wind-induced eddy fluxes.

1.4 Thesis Aims and Manuscript Structure

It is clear that the Southern Ocean and its unique circulation plays an important, but still poorly constrained role in the global carbon cycle. Reduced communication between the atmosphere and deep ocean in the Southern Ocean is relatively well documented but the ambiguity of the paleoceanographic record defies positive interpretation of the mechanisms that are responsible. This is especially difficult because theoretical, observational and modelling studies show that the ACC and the Southern Ocean overturning circulation are sensitive to a coupled non-linear combination of wind stress, buoyancy

forcing, stratification and mesoscale eddy dynamics that are impossible to recreate in numerical models of the climate system due to the computational expense of the fine grid scales needed to resolve mesoscale eddies or the length of time it would take to run such high resolution models to encompass important processes that act over long timescales such as the meridional overturning circulation itself. This necessitates compromise through lower resolution and parameterisation of sub grid-scale processes such as eddies, simplified physics or more eclectic assumptions like quasigeostrophy in order to run for reasonable timescales. Of course, when compared to observations, these models are found to be considerably different, and therefore careful interpretation is needed of results from climate models for the past as well as the future.

The main aims of this thesis are:

- To simulate ocean circulation and biogeochemical cycling in a coarse resolution primitive equation OGCM.
- To assess the response of ocean circulation to perturbations in external forcing and internal physics, particularly in the Southern Hemisphere.
- To highlight the processes that link ocean circulation, nutrient distributions and biological productivity.
- To determine the extent to which the Southern Ocean governs the partitioning of CO_2 between the atmosphere and ocean.
- To elucidate the implications of these findings for understanding past and future climate changes.

This thesis is arranged in three parts. Part I introduces the Southern Ocean and documents its currently understood participation in past and future climate changes (this chapter), introduces the configuration of global ocean-biogeochemical model and describes the preindustrial control run that will be the foundation to assessing the sensitivity of the global carbon cycle and atmospheric CO_2 to processes in the Southern Ocean (Chapter 2). Part II catalogues a series of perturbation studies to physical and biogeochemical aspects of the Southern Ocean (Chapters 3–6), documenting resultant changes to circulation, nutrient distribution and primary production and identifying the ways in which the Southern Ocean's response changes atmospheric CO_2. Part III draws these individual experiments together to synthesise the role of the Southern Ocean in the global carbon cycle and atmospheric CO_2 change, assess the implications of these

findings for interpretation of past and future climates and identify areas of further work (Chapters 7 and 8).

Chapter 2

Configuration of the Ocean General Circulation Model and Description of the Preindustrial Control Run

The purpose of this chapter is to review the architecture and detail the configuration of the OGCM that will be used forthwith to investigate the Southern Ocean's control of oceanic biogeochemical cycles and atmospheric CO_2 concentrations. In particular, the model domain, boundary conditions and forcings will be described as well as presenting the control model state that will be used as a benchmark against which later experiments are compared. A series of biogeochemical tracers will be formulated to provide supplementary machinery for the diagnosis of changes to the ocean circulation and carbon cycle following idealised perturbations to model forcing or numerics.

The Massachusetts Institute of Technology general circulation model [MITgcm, *Adcroft et al.*, 1997, 2009; *Marshall et al.*, 1997a,b] is a widely portable, efficient, primitive equation circulation model designed for the study of the atmosphere, ocean and climate (also see http://mitgcm.org). A novel feature of MITgcm is its ability to simulate, using one basic algorithm, atmospheric and oceanic flows at both small and large scales by exploiting the isomorphism of the vertical coordinate r to have the units of metres (ocean) or Pascals (atmosphere), depending on the equation of state used. Furthermore, coded "packages" are used in MITgcm to help organise and layer various building blocks that are selected and assembled to perform a specific experiment. The top layer packages are generally specialised to specific simulation types. In this layer there are packages

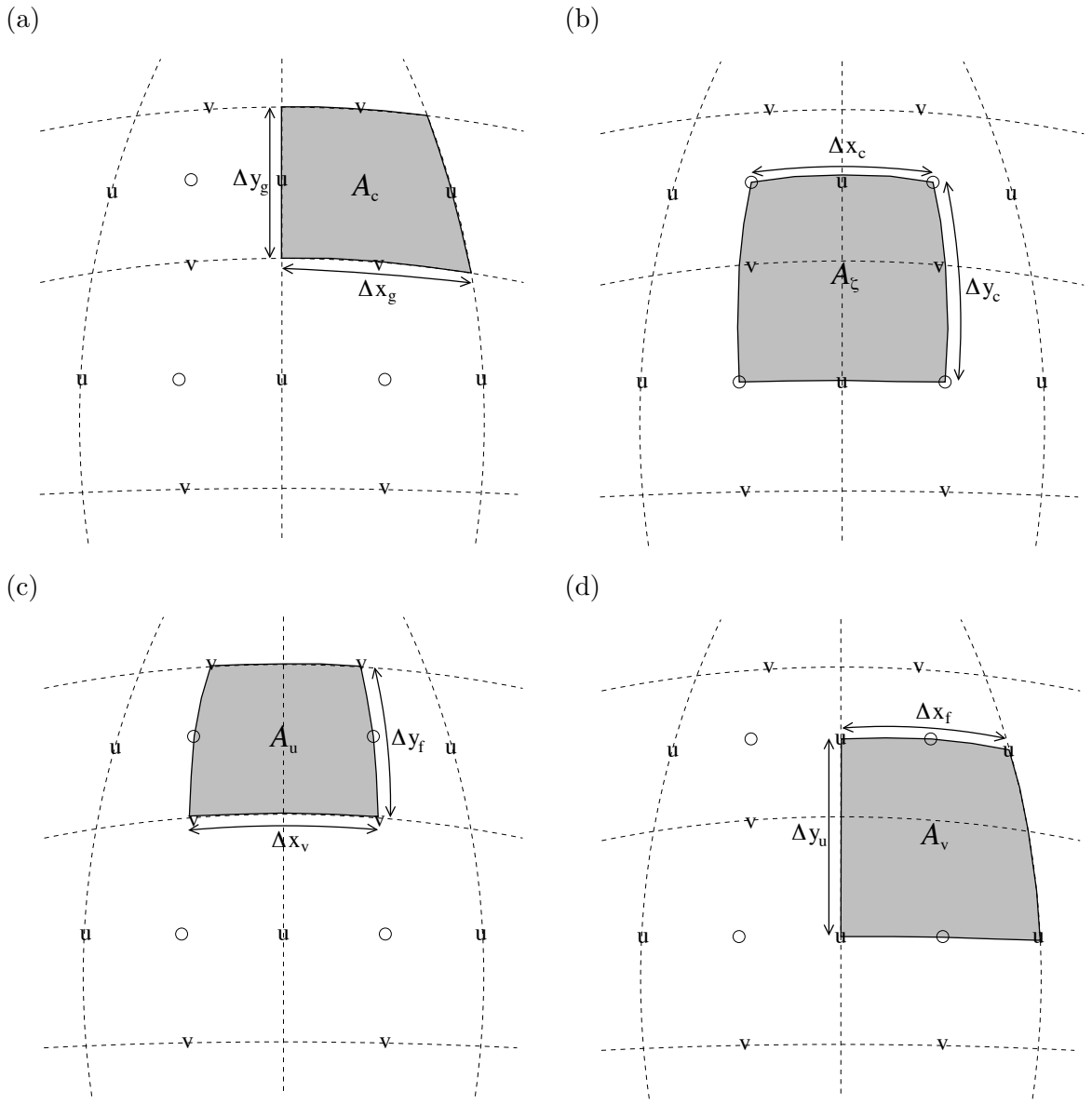

Figure 2.1: Staggering of MITgcm horizontal grid, with the dashed lines indicating the tracer cell boundaries. (a) The area of a tracer cell, A_c, is bordered by the length of the southern edge, Δx_g, and the western edge, Δy_g, with the subscript "g" indicating that the lengths are along the defining grid boundaries and the subscript "c" associating the quantity with the tracer cell centres; (b) The area of the vorticity cell, A_ζ, is bordered by the length of the southern edge, Δx_c and the western edge, Δy_c with the subscript "c" indicating that the lengths are measured between the tracer cell centres and the subscript "ζ" associating the centre point with the vorticity points; (c) The area of the u or "Western" cell, A_u, is defined by the length of the southern edge, Δx_v, and eastern edge, Δy_f with the subscript "v" indicating that the length is measured between the v-points, the subscript "f" indicating that the length is measured between the tracer cell faces and the subscript "u" associating the centre point with the u-points; (d) The area of a v or "Southern" cell, A_v, is bordered by the lengths of the northern edge, Δx_f, and the western edge, Δy_u with the subscript "u" indicating that the length is measured between the u-points, the subscript "f" indicating that the length is measured between the tracer cell faces and the subscript "v" associating the centre point with the v-points. For more details, see *Adcroft et al.* [2009]

that deal with biogeochemical processes, ocean interior and boundary layer processes, atmospheric processes, sea ice, coupled simulations and state estimation. Below this layer are a set of general purpose numerical and computational packages. The numerical packages provide code for numerical alogorithms that apply to many different simulation types. Similarly, the computational packages implement non-numerical alogorithms that provide parallelism, I/O and time-keeping functions.

Spatial discretisation is carried out using the finite volume method, which is similar to grid-point methods but allows boundaries to intersect the regular grid allowing a more accurate representation of ocean bathymetry (so called "lopped" and "shaved" cells, *Adcroft et al.* [1997]). The grid information is quite general and describes cartesian, spherical-polar or curvilinear coordinates systems. Variables are staggered in the horizontal and vertical plane using an Arakawa C-grid [*Arakawa and Lamb*, 1977], with the state of a fluid characterised by velocity components (u, v, w) located at the centre of the cell faces, active tracers of potential temperature (θ) and salinity or moisture (S) averaged over the tracer cell volume (see Figure 2.1 and Figure 2.2), a "geopotential", ϕ, and a density/buoyancy that depends on θ,S and ϕ. The model domain is split into tiles within which is a regular grid that allows for simple parallelisation. At each time step, MITgcm solves a simplified form of the incompressible Navier-Stokes equations, under the Boussinesq and Traditional approximations [*Marshall et al.*, 1997a]. The default time-stepping scheme is the centered quasi-second order Adams-Bashforth method. The model can be used in hydrostatic and nonhydrostatic modes, making it a very flexible tool for studying oceanographic phenomena over the full range of oceanic length and time scales [*Marshall et al.*, 1997a].

2.1 MITgcm Model Configuration

To investigate the sensitivity of the global carbon cycle to Southern Ocean processes, the model is globally configured at a coarse resolution of 2.8° x 2.8° using spherical polar coordinates in the horizontal plane and 15 vertical levels that vary between 50 m at the surface to 690 m at the bottom (Table 2.1). The bathymetry is realistic although fairly coarse and most notably has a closed boundary at 80°N with no representation of the Arctic Ocean to avoid issues with numerical stability and diminutive timesteps resulting from the convergence of meridians at high northern latitudes.

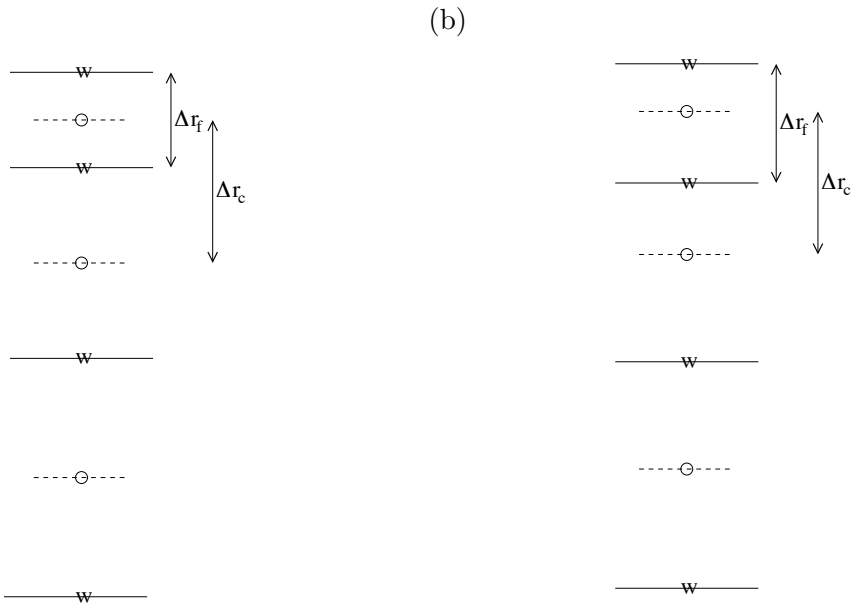

Figure 2.2: Staggering of MITgcm vertical grid. As for the horizontal grid, the subscripts "c" and "f" are used to indicate cell faces and centres. Δr_f is the difference in r (the vertical coordinate) between the tracer cell faces, while Δr_c is the difference in r between tracer cell centres. The units of r are either metres or Pascals depending on the isomorphism (i.e. atmosphere or ocean) being used; (a) is the cell centered approach because the tracer points are at cell centres and the cell centres are equidistant between the cell interfaces; (b) the vertex or interface centred approach is an alternative method. Here, the interior interfaces are positioned equidistant between the tracer nodes, which are no longer the cell centres. This approach is formally more accurate for valuation of hydrostatic pressure and vertical advection but historically the cell centered approach has been used.

The momentum equations solved in this configuration are given in Equations 2.1 and 2.2, with G_{adv} the tendency due to advection (Equation 2.3), and are solved with a timestep of 900 s.

$$\frac{\partial u}{\partial t} + G^u_{adv} + \frac{1}{\rho}\frac{\partial p'}{\partial x} - fv = \nabla^2_h A_h u + A_z \frac{\partial^2 u}{\partial z^2} + G^u_{forcing} \tag{2.1}$$

$$\frac{\partial v}{\partial t} + G^v_{adv} + \frac{1}{\rho}\frac{\partial p'}{\partial y} + fu = \nabla^2_h A_h v + A_z \frac{\partial^2 v}{\partial z^2} + G^v_{forcing} \tag{2.2}$$

$$G_{adv} = u\frac{\partial}{\partial x} + v\frac{\partial}{\partial y} + w\frac{\partial}{\partial z} \tag{2.3}$$

The velocity field is subject to Laplacian horizontal and vertical viscous dissipation parameterised with the horizontal and vertical eddy viscosities A_h and A_z. The value of the horizonatal Laplacian dissipation coefficient was chosen to ensure that the frictional boundary layer (~600 km) is adequately resolved at low latitudes (Δx ~300 km) [*Adcroft*

Table 2.1: Vertical grid (cell centred) used in this configuration of MITgcm.

Level	Thickness (m)	Depth of Interface (m)	Depth of Centre (m)
0	-	0	-
1	50	−50	−25
2	70	−120	−85
3	100	−220	−170
4	140	−360	−290
5	190	−550	−455
6	240	−790	−670
7	290	−1080	−935
8	340	−1420	−1250
9	390	−1810	−1615
10	440	−2250	−2030
11	490	−2740	−2495
12	540	−3280	−3010
13	590	−3870	−3575
14	640	−4510	−4190
15	690	−5200	−4855

et al., 2009]. The vertical velocity is derived from continuity (Equation 2.4).

$$\frac{\partial u}{\partial x} + \frac{\partial v}{\partial y} + \frac{\partial w}{\partial z} = 0 \tag{2.4}$$

To reduce computational load and maximise the efficiency of the model to achieve millennial scale integrations the hydrostatic approximation is made so that the pressure at any level can be computed from the weight of fluid above (Equation 2.5).

$$p' = \int_{-z}^{0} g\rho' dz \tag{2.5}$$

Potential temperature (θ, Equation 2.6) and salinity (S, Equation 2.6) are advected by the velocity field (Equation 2.3) and diffused in the vertical using a uniform eddy diffusivity, κ_z. Note that horizontal/isopycnal diffusion is treated in a separately, a description of which is given below.

$$\frac{\partial \theta}{\partial t} + G^{\theta}_{adv} = \kappa_z \frac{\partial^2 \theta}{\partial z^2} + G^{\theta}_{forcing} \tag{2.6}$$

$$\frac{\partial S}{\partial t} + G^{S}_{adv} = \kappa_z \frac{\partial^2 S}{\partial z^2} + G^{S}_{forcing} \tag{2.7}$$

The $G_{forcing}$ terms represent arbitrary functions of state, time and space that convert input forcing values into time tendencies of velocity ($\mathrm{m\,s^{-2}}$), temperature ($^{\circ}\mathrm{C\,s^{-1}}$) and

salinity (psu/s). Wind stress forcing ($\mathrm{N\,m^{-2}}$) is added to the momentum equations in the zonal and meridional directions (Equations 2.8 and 2.9), where ρ_0 is reference density and Δz_1 is the thickness of the surface layer.

$$G^u_{forcing} = \frac{\tau_x}{\rho_0 \Delta z_1} \tag{2.8}$$

$$G^v_{forcing} = \frac{\tau_y}{\rho_0 \Delta z_1} \tag{2.9}$$

Potential temperature and salinity forcing (Equations 2.10 and 2.11) account for heat (Q, $\mathrm{W\,m^{-2}}$) and freshwater ($E-P-R$, $\mathrm{m\,s^{-1}}$) fluxes, as well as climatological relaxation to Sea Surface Temperature (θ^*) and Salinity (S^*) using a specific heat capacity, C_p, a reference salinity, S_0, and over given timescales, λ_θ and λ_S.

$$G^\theta_{forcing} = -\lambda_\theta(\theta - \theta^*) - \frac{Q}{C_p \rho_0 \Delta z_1} \tag{2.10}$$

$$G^S_{forcing} = -\lambda_S(S - S^*) - \frac{S_0(E - P - R)}{\Delta z_1} \tag{2.11}$$

The heat flux term also contains a contribution from the latent heat of fusion of water in regions where the surface temperature falls below the freezing point and sea ice is formed. A polynomial approximation to the full nonlinear equation of state is employed.

To simulate mixing in the ocean and account for the presence of mesoscale eddies, the *Redi* [1982] parameterisation of along isentropic (neutral density surface) diffusion is coupled with the *Gent and McWilliams* [1990, hereafter GM90] eddy parameterisation [*Griffies et al.*, 1998], as well as using implicitly calculated viscosity and implicit diffusion with a vertical convective mixing scheme that diffuses tracers in unstable regions at a much greater rate. The GM90 parameterization aims to account for the advective effect of geostrophic eddies by means of a "bolus" velocity, $\mathbf{v}^*$, with the divergence of this advective flux added to the advective part of the tracer tendency equations (Equations 2.1 to 2.7). The zonal and meridional bolus velocities are defined as the negative partial vertical derivatives of streamfunctions F_x and F_y specified in terms of isopycnal slopes and the GM thickness diffusivity (Equations 2.12 and 2.13), where $F_x = \kappa_{GM} S_x$ and $F_y = \kappa_{GM} S_y$ with boundary conditions $F_x = F_y = 0$ on their upper and

lower boundaries. The vertical bolus velocity is derived from continuity (Equation 2.14).

$$u^* = -\partial_z F_x \tag{2.12}$$

$$v^* = -\partial_z F_y \tag{2.13}$$

$$w^* = \partial_x F_x + \partial_y F_y \tag{2.14}$$

This is the form of the GM90 parameterisation as applied by *Danabasoglu and McWilliams* [1995]. Since the streamfunctions F_x and F_y are proportional to the slopes of isopycnals, one problem may be encountered in regions of deep convection and in the mixed layer where density is homogenised and stratification is weak. This can lead to very large, even infinite, values for S_x and S_y that would generate abnormal bolus velocities, over zealously re-stratify convective regions or lead to numerical instability. To prevent such spurious circulation, one strategy is to simply restrict the isopycnal slope parameters by an upper limit, S_{max}. However, this can produce an unacceptable amount of diapycal difusion so the strategy commonly employed in MITgcm is the use of a tapering scheme, such as *Gerdes et al.* [1991], where the clipping of slopes is replaced by a tapering of the entire GM/Redi mixing tensor to zero in low-stratification regimes. This means the direction of fluxes is unaffected as the amplitude is reduced when $|S| \geq S_{max}$. The maximum slope, S_{max}, is also set fairly high to allow greater freedom of the eddy bolus circulation to respond to idealised perturbations to model forcing [e.g. *Farneti et al.*, 2010].

To ensure property conservation over long integrations, a "rigid lid" formulation is used, as global conservation is not possible using the free-surface [*Adcroft et al.*, 2009; *Campin et al.*, 2004]. Table 2.2 shows the standard physical model parameters and their values in this study.

At the sea-surface the model is forced by an annual climatological cycle of monthly surface wind stresses [*Trenberth et al.*, 1989], heat and freshwater fluxes [*Jiang et al.*, 1999] with additional relaxation in the upper layer toward climatological sea surface temperature (Figure 2.3), with a timescale of 2 months, and salinity, with a timescale of 3 months [*Levitus and Boyer*, 1994a,b].

The advective and diffusive transports calculated by the physical model are used to redistribute passive tracers carried within an online dissolved inorganic carbon biogeochemistry model [e.g. *Dutkiewicz et al.*, 2005a,b; *Parekh et al.*, 2005] that considers the

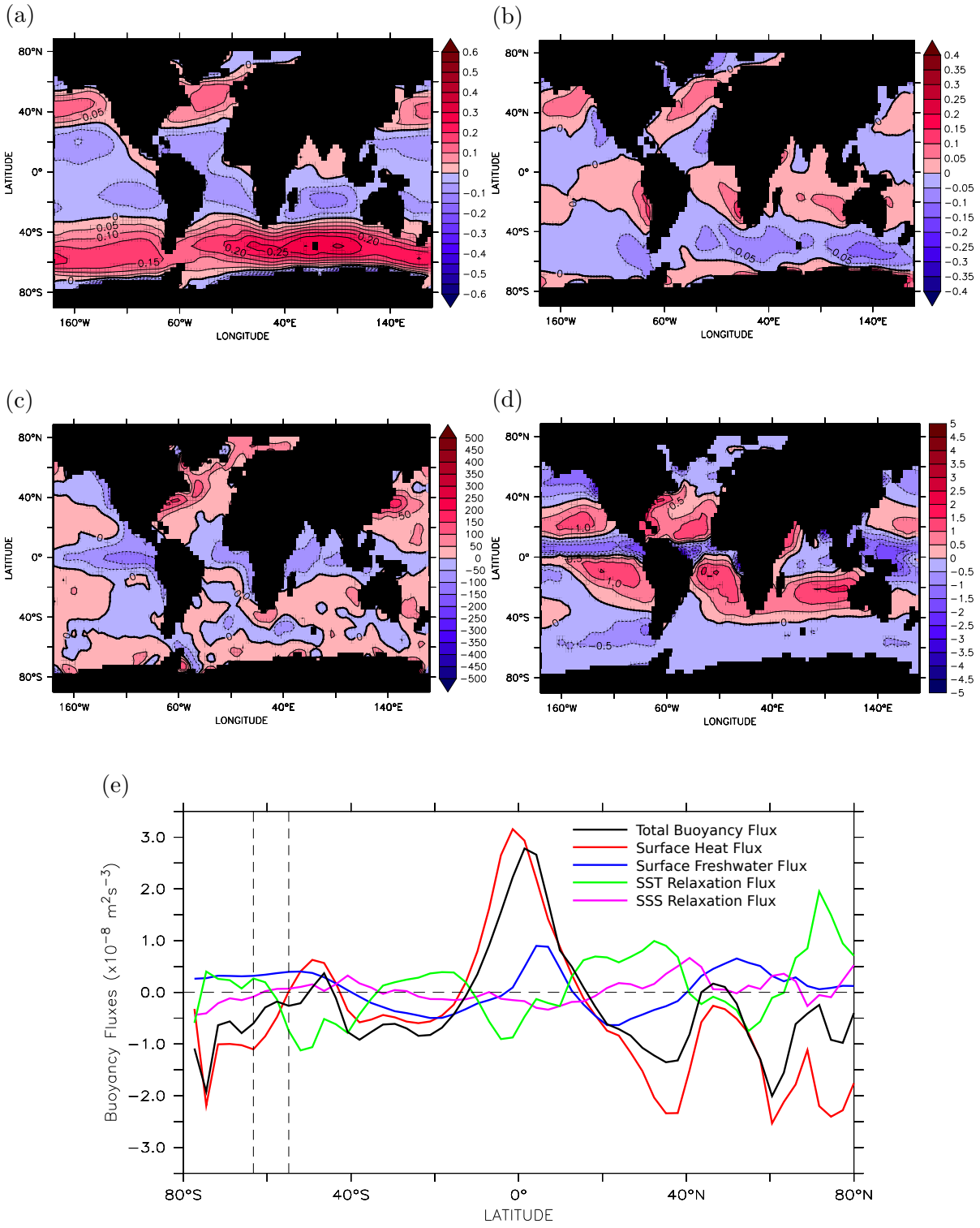

Figure 2.3: MITgcm forcing fields for the physical model (a) and (b) annual average of *Trenberth et al.* [1989] zonal and meridional wind stresses ($\mathrm{N\,m^{-2}}$), (c) and (d) annual averages of the *Jiang et al.* [1999] net heat ($\mathrm{W\,m^{-2}}$) and freshwater fluxes ($\mathrm{m\,yr^{-1}}$) and (e) zonal average surface buoyancy flux ($\mathrm{m^2\,s^{-3}}$) and its components from the net heat and freshwater fluxes above plus surface relaxation (see Section 6.1 and Equation 6.2). Positive values indicate a gain of buoyancy (an increase in heat or freshwater/reduced salinity) while negative values indicate buoyancy loss (reduced heat or freshwater/increased salinity). Dashed vertical lines denote the position of the unblocked latitudes at Drake Passage.

Table 2.2: Parameter values used in the MITgcm physical model

Parameter Name	Symbol	Value
Domain size	N_xxN_yxN_z	$128 \times 64 \times 15$
Acceleration due to gravity ($m\,s^{-2}$)	g	9.81
Momentum timestep (s)	t_m	900
Tracer timestep (s)	t_ε	43 200
Vertical Eddy Viscosity ($m^2\,s^{-1}$)	A_z	1×10^{-3}
Horizontal Eddy Viscosity ($m^2\,s^{-1}$)	A_h	5×10^{5}
Diapycnal Eddy Diffusivity ($m^2\,s^{-1}$)	κ_z	5×10^{-5}
Reference Density ($kg\,m^{-3}$)	ρ_0	1035
Reference Salinity (psu)	S_0	35
Specific Heat Capacity ($J\,°C^{-1}\,kg^{-1}$)	C_p	3994
θ Relaxation Period (s)	$1/\lambda_\theta$	5 184 000
S Relaxation Period (s)	$1/\lambda_S$	7 776 000
Implicit Vertical Diffusivity for Convection ($m^2\,s^{-1}$)	κ_{ivdc}	100
GM90 "Background" Isopycnal Diffusivity ($m^2\,s^{-1}$)	κ_{GM}	1×10^{3}
Max. slope of isopycnals	S_{max}	1×10^{-2}

coupled cycles of carbon, phosphorus (organic/inorganic), oxygen and alkalinity. For any passive tracer, A (Equation 2.15)

$$\frac{\partial A}{\partial t} = -G^A_{adv} + \kappa_z \frac{\partial^2 A}{\partial z^2} + S^A \tag{2.15}$$

Each passive tracer considered has additional sources and sinks (S^A, see Equations 2.19 to 2.26) handled within the biogeochemical package that are akin to $G_{forcing}$ in Equations 2.8 to 2.11. See descriptions below and Table 2.3 for parameter values used.

In a simple parameterisation of primary production, J_{prod}, the biological consumption of phosphorus is limited by the availability of light, I_{PAR}, that declines with depth, and either phosphate or iron, whichever is the scarcest, following Michaelis–Menten kinetics [e.g. *Dutkiewicz et al.*, 2005a; *Parekh et al.*, 2005]. A fraction of this productivity, γ, enters the dissolved organic phosphorus (DOP) pool (Equation 2.16) that has an e-folding timescale for remineralization, λ_{remin}, of 6 months [*Yamanaka and Tajika*, 1997].

$$S_{DOP} = \gamma J_{prod} - \lambda_{remin}[DOP] \tag{2.16}$$

The remaining fraction of this productivity is exported as particulate organic phosphorus (POP) throughout the water column and is remineralised and accumulated as dissolved inorganic phoshate instantaneously, $\partial F_P/\partial z$, which is reasonable given the much shorter timescale for sinking particles compared to basin wide advective timescales [*Najjar and*

Orr, 1998].

$$S_{PO_4} = -\gamma J_{prod} - \frac{\partial F_P}{\partial z} + \lambda_{remin}[DOP] \tag{2.17}$$

The POP flux decreases with depth due to remineralisation following a power law relationship (Equation 2.18) where z_c is the depth of the base of each layer with layer thickness of Δz where production occurs [*Dutkiewicz et al.*, 2005b] and α_{remin} is chosen guided by sediment trap data *Martin et al.* [1987] and modelled phosphate distributions [*Yamanaka and Tajika*, 1997] giving remineralisation length scales of the order of one hundred metres.

$$F_P = (1-\gamma) J_{prod} \Delta z \left(\frac{z}{z_c}\right)^{-\alpha_{remin}} \tag{2.18}$$

The fate of carbon (Equation 2.19) is related to the consumption and recycling of phosphate by a constant Redfield ratio, $R_{[C:P]}$, modified by *Anderson and Sarmiento* [1994].

$$S_{DIC} = R_{[C:P]} S_{PO_4} + J_{CaCO_3} + F_{CO_2} + V_{CO_2} \tag{2.19}$$

Alkalinity is related to phosphorus through the constant ratio, $R_{[N:P]}$, of phosphate to nitrate (Equation 2.20) whose redox reactions that occur as a result of biological activity affect the ocean's charge balance.

$$S_{ALK} = -R_{[N:P]} S_{PO_4} + 2J_{CaCO_3} + V_{ALK} \tag{2.20}$$

The cycling of particulate inorganic carbon, J_{CaCO_3}, which affects alkalinity and DIC in a 2:1 ratio, assumes a fixed production ratio to organic carbon, R_{rain}, and is remineralised exponentially with a scale depth of 3.5 km following Ocean Carbon-Cycle Model Intercomparison Project (OCMIP) guidelines [*Najjar and Orr*, 1998].

Oxygen varies inversely to the cycling of phosphate by constant stoichiometric ratio and is consumed by DOP remineralisation but anoxic respiration is allowed if levels drop below a critical concentration, $O_{2,crit}$.

$$S_{O_2} = \left\{ \begin{array}{ll} -R_{[O:P]} S_{PO_4} & \text{if } [O_2] > O_{2,crit} \\ 0 & \text{if } [O_2] < O_{2,crit} \end{array} \right\} \tag{2.21}$$

The air-sea exchange of carbon dioxide, F_{CO_2}, and oxygen, F_{O_2}, is determined by Equation 2.22, where the bracketed part is the difference in CO_2 concentration, in this instance, between the water-vapour saturated atmosphere and ocean, where k_0 and f the respective CO_2 solubilities, with the oceanic concentration of aqueous CO_2 diagnosed

from the pH and alkalinity of the surface waters, solved explicitly [*Follows et al.*, 2006].

$$F_{CO_2}\,(\mathrm{mol\,m^{-3}\,s^{-1}}) \;=\; K_w \cdot \left(k_0 pCO_2^{sat} - fpCO_2^{surf}\right) \Big/ \Delta\, z_1 \tag{2.22}$$

$$K_w\;(\mathrm{m\,s^{-1}}) \;=\; cu^2 \cdot Sc_{660}(\Theta)^{-\frac{1}{2}} \tag{2.23}$$

K_w represents an exchange coefficient (Equation 2.23), dependent on the square of the supplied climatological local wind speed, u (Figure 2.4b), and the square root of the Schmidt number, Sc, which is the ratio of kinematic viscosity of water, dependent on potential temperature, Θ, and the diffusivity of the gas [*Wanninkhof*, 1992]. The constant, $c = 0.337$, was adjusted to obtain the correct global mean gas transfer velocity deduced from natural and bomb radiocarbon [*Najjar and Orr*, 1998].

In addition to this, the surface concentrations of DIC and ALK are dependent on a "virtual flux" component, V_{CO_2} and V_{ALK} (Equation 2.24–2.25) to maintain global conservation following OCMIP protocols [*Dutkiewicz et al.*, 2005b; *Najjar and Orr*, 1998]. This is required so as the model can maintain a constant volume in the surface grid cells in accordance with the rigid lid. Therefore local freshwater forcing and relaxation to observed salinity results in a surface flux of salt, not a surface flux of fresh water as in the real world. The virtual flux is the explicit representation of the change in surface concentration that would exist if the atmosphere-ocean freshwater exchange were modelled directly using a free-surface, which would dilute or concentrate tracers in the surface grid box by changing volume without intervention. Such changes are of negligible importance for most tracers except in terms of carbon chemistry [*Dutkiewicz et al.*, 2005b], hence this is only taken into account for DIC and alkalinity, but the flux does not affect the concentration of carbon dioxide in the atmospheric box.

$$V_{CO_2} \;=\; \frac{\overline{DIC_{z=0}}}{\overline{S_{z=0}}} \cdot \frac{S_0 F}{\Delta\, z_1} \tag{2.24}$$

$$V_{ALK} \;=\; \frac{\overline{ALK_{z=0}}}{\overline{S_{z=0}}} \cdot \frac{S_0 F}{\Delta\, z_1} \tag{2.25}$$

Virtual fluxes are parameterised as the product of the surface salinity flux (the local freshwater flux, F, scaled by a reference salinity, $S_0 = 35$) and the ratio of the global mean surface DIC/ALK concentrations and global mean surface salinity, with $\Delta\, z_1$ the thickness of the surface layer.

In addition, the oceanic cycle of iron is explicitly represented (Equation 2.26) following

Parekh et al. [2005]. Dissolved iron is consumed and remineralised following phosphate concentration, related by the constant ratio, $R_{[Fe:P]}$. Aeolian dust deposition is prescribed using the modern monthly fields (Figure 2.4a) of *Mahowald et al.* [2006a,b], of which 3.5% by weight is iron, F_{dust}, and 1% is soluble, α_{Fe}.

$$S_{Fe} = R_{[Fe:P]} S_{PO_4} - \lambda_{scav}[Fe_{free}] + \alpha_{Fe} F_{dust} \tag{2.26}$$

This iron undergoes complexation with an organic ligand (of fixed concentration of $1\,\mu mol\,m^{-3}$) that protects it from depletion by scavenging, is bioavailible and reaches a thermodynamic equilibrium between free and complexed forms. Dissolved iron that is not complexed, Fe_{free}, is subjected to a first-order scavenging rate, λ_{scav}, that removes it from solution and above a fixed limit, Fe_{max}, is immediately precipitated.

Atmosphere-ocean exchange of gases and photosynthetically active radiation is reduced or prevented by the prescribed, non-thermodynamically interactive, monthly fractional cover of sea ice (Figure 2.4c). Table 2.3 shows the standard biogeochemical model parameters and their values employed in this study

2.2 The "Preindustrial" Control Run

Starting from a partially spun-up state (t =5900 years, [*Adcroft et al.*, 2009]), the model is run with the above configuration with a fixed, pre-industrial atmospheric pCO_2 of 278 µatm until a new steady state is reached (~4000 years). Next, a simple well mixed atmospheric carbon reservoir [e.g. *Ito and Follows*, 2003; *Parekh et al.*, 2006b] is coupled to the ocean and integrated until equilibrium is achieved (~10000 years). The atmospheric pCO_2 in this configuration is dynamic and regulated by global net air-sea CO_2 fluxes, which allows a balance between atmosphere and ocean concentrations to be established and for perturbations to the model conditions to raise or lower this steady state. The total burden of atmosphere-ocean carbon is conserved and riverine sources and sediment interaction are not represented.

With these assumptions in mind it is worth noting that the intention of the following model studies is to examine the physical and biogeochemical mechanisms that could be responsible for large changes in atmospheric pCO_2 and do not attempt to recreate

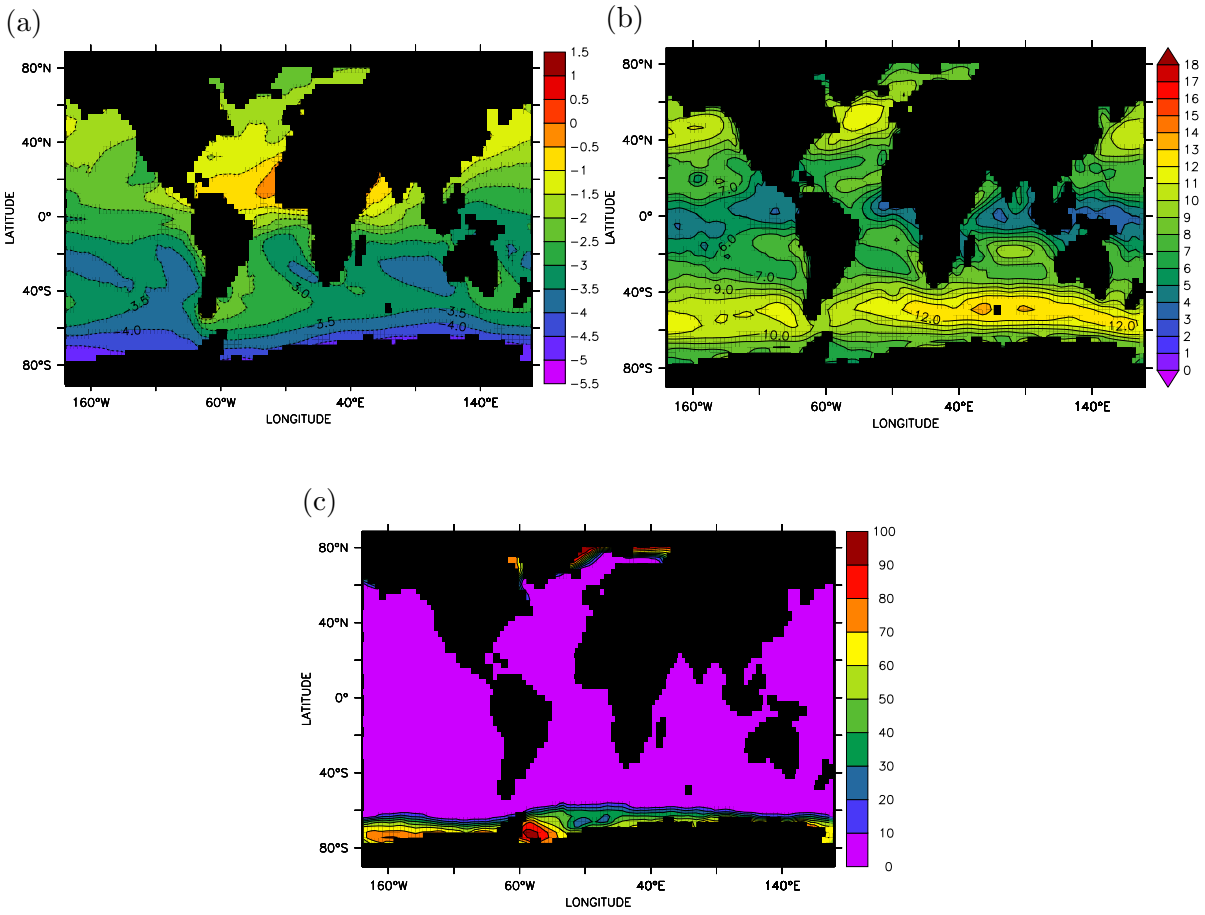

Figure 2.4: MITgcm control run forcing fields for the biogeochemical model (a) annual average of the *Mahowald et al.* [2006a,b] monthly aeolian iron deposition field (log_{10} nmol Fe m^{-2} s^{-1}), (b) annual average of the *Trenberth et al.* [1989] monthly wind speed field m s^{-1} and (c) annual average fractional coverage of sea ice (%).

oceanic conditions as found at the LGM. Indeed, while most of the forcing scenarios presented are more relevant to cold, glacial climates, some are more applicable to warmer climates than today. A substantial volume of data has been generated and it would be impossible to account for the entire three dimensional circulation and water mass structure of the global ocean in completeness in these pages. However presenting zonal-mean meridional-vertical sections for each of the Atlantic, Pacific and Indian oceans as well as global zonal averages allows the largest scale properties of major circulation and water mass patterns in the world ocean to be revealed. In particular, for ease of presentation, all properties herein are averaged onto the grid of the tracer cell, A_c (Figure 2.1a), with pointwise properties interpolated to the cell centre and volumetric quantities averaged over the tracer cell volume.

Table 2.3: Parameter values used in the MITgcm biogeochemistry model. (DOP = Dissolved Organic Phosphorus, PAR = Photosynthetically Active Radiation)

Parameter Name	Symbol	Value
Timescale for Biological Activity (s^{-1})	α	6.43×10^{-11}
New Production going to DOP (%)	γ	67
DOP remineralisation rate (s^{-1})	λ_{remin}	6.43×10^{-8}
Max. Depth of Biological Activity (m)	z_c	-500
Redfield ratio of Elements	$R_{[C:N:P:O]}$	$117:16:1:-170$
Rain ratio of Inorganic/Organic C (%)	R_{rain}	7
Fraction of light that is PAR (%)	I_{PAR}	40
Light Attentuation coefficient (m^{-1})	k_w	0.02
Half Saturation constant for Light ($W\,m^{-2}$)	k_I	30
Half Saturation constant for PO_4 ($mol\,m^{-3}$)	k_{PO_4}	5×10^{-4}
Half Saturation constant for Fe ($mol\,m^{-3}$)	k_{Fe}	1.2×10^{-7}
Critical O_2 concentration ($mol\,m^{-3}$)	$O_{2,crit}$	4×10^{-3}
Power law remineralisation coefficient	α_{remin}	0.9
Solubility of Aeolian Fe (%)	α_{Fe}	1
Iron Scavenging Rate (s^{-1})	λ_{scav}	6.1×10^{-9}
Max. Solubility of Free Fe ($mol\,m^{-3}$)	Fe_{max}	3×10^{-7}
Redfield ratio of Fe:P	$R_{[Fe:P]}$	$4.68 \times 10^{-7}:1$

The "pre-industrial" control state resembles climatological values for sea surface temperature (Figure 2.5a) and salinity (Figure 2.5b) as one would expect from relaxing boundary conditions (Figure 2.5c and d). Buoyancy fluxes (Figure 2.3e) tend to make polar and subtropical waters denser with lightening of equatorial and subpolar regions and are dominated by mean heat fluxes, which are generally anticorrelated to the smaller fluxes generated by temperature relaxation. Similarly, salinity relaxation generally opposes the mean freshwater fluxes but their magnitudes are much more comparable. In the Southern Ocean, freshwater fluxes play a key role in the decrease in density of upwelled waters flowing north in the surface Ekman layer with decreasing heat loss and, eventually, heat gain by the ocean between 40–50°S aiding the formation of intermediate and mode waters. Close to the Antarctic continent, salinity relaxation acts to remove buoyancy from the surface ocean, as does heat loss to the atmosphere (although perhaps too much given the positive SST relaxation), enabling the formation of dense bottom waters.

The barotropic streamfunction (Figure 2.6a) captures the major current systems including the intensified western boundary currents in the northern and southern hemisphere subtropical gyres and the unbounded eastward flowing Antarctic Circumpolar Current

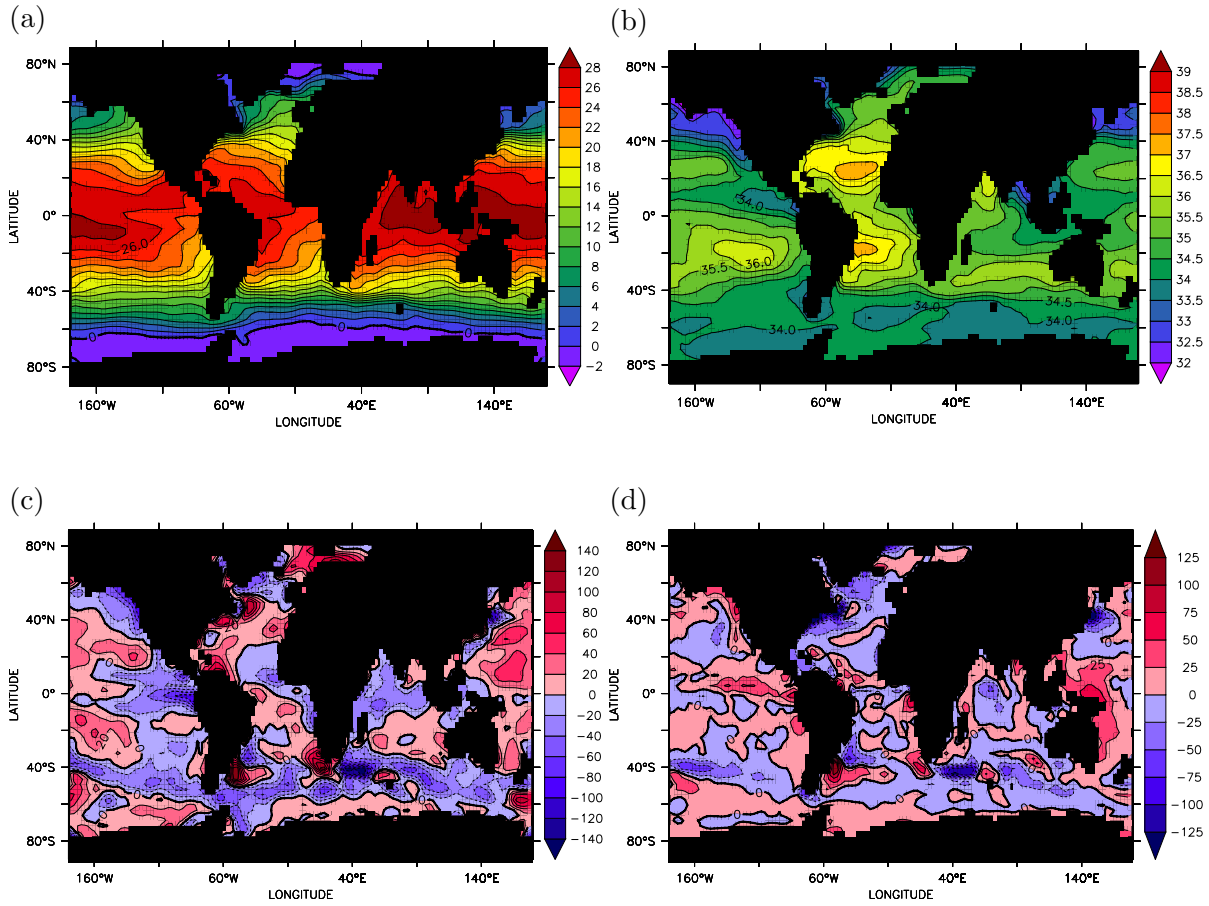

Figure 2.5: MITgcm output for the control configuration at 20000 years after spin up sequence detailed above (a) surface potential temperature (°C), (b) surface salinity, (c) surface temperature relaxation ($\mathrm{W\,m^{-2}\,yr^{-1}}$) and (d) surface salinity relaxation ($\mathrm{kg\,m^{-2}\,yr^{-1}}$).

(ACC) that has a transport through Drake Passage of 139.82 Sv, which compares reasonably well to values of $\mathbf{O}$(130–140 Sv) from observations [e.g. *Cunningham et al.*, 2003; *Nowlin and Klinck*, 1986] and models [e.g. *Ganachaud and Wunsch*, 2000; *Gent et al.*, 2001] and can be partially attributed to the choice of wind stress forcing [*Dutkiewicz et al.*, 2005a; *Parekh et al.*, 2005]. The zonal averaged global meridional overturning stream function (Figure 2.6b), which represents the "residual" circulation after combining the effects of the wind-driven Eulerian-mean and mesoscale eddy-induced circulations [*Karsten and Marshall*, 2002; *Marshall*, 1997], consists of three major cells, the northern Atlantic meridional overturning circulation has a strength of 17.39 Sv associated with the production of North Atlantic Deep Water (NADW), which compares reasonably to the 15±2 Sv estimated by *Ganachaud and Wunsch* [2000]. The Southern Ocean overturning circulation is composed of partially compensating clockwise Eulerian-mean flow (Figure 2.6c), due to northward surface Ekman transport driven by the strong

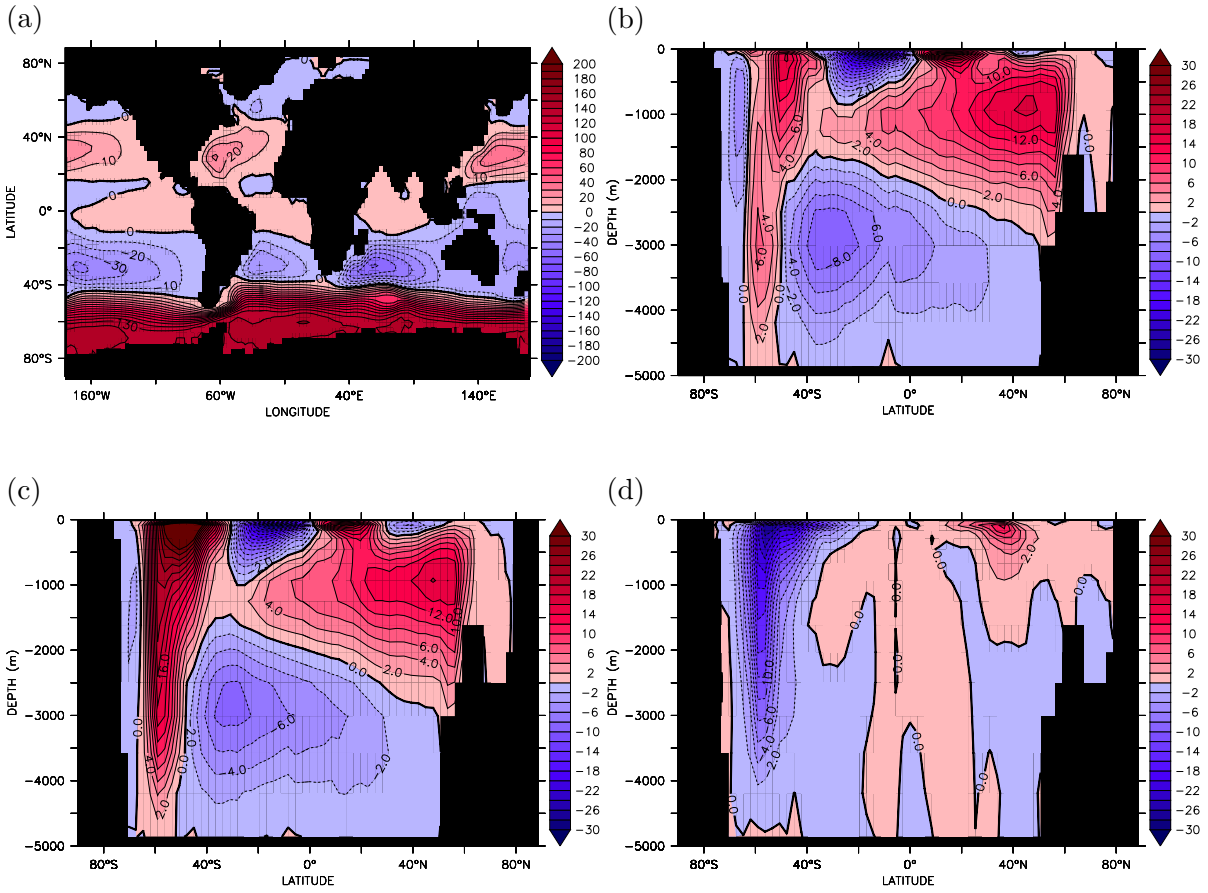

Figure 2.6: MITgcm output for the control configuration at 20000 years after the spin up sequence detailed above (a) Barotropic streamfunction (Sv), (b) residual overturning stream function (Sv), which is the sum of (c) Eulerian-mean and (d) Eddy-driven overturning circulations (Sv)

westerly winds, and a counter-clockwise eddy driven return flow (Figure 2.6d) that produces a residual overturning of 16.3 Sv, which is slightly high when compared to the ~14 Sv estimated from the distribution of transient tracers such as CFC-11, bomb-Δ^{14}C and anthropogenic CO_2 [*Ito et al.*, 2004b]. Finally, the abyssal cell of 9.8 Sv is associated with the circulation of Antarctic Bottom Water (AABW) that is formed in the Southern Ocean from upwelling Circumpolar Deep Water (CDW) and is returned south at deep and intermediate levels. Its magnitude compares well to the average volume of 8±2 Sv from an inverse model of trans-basin hydrographic data [*Ganachaud and Wunsch*, 2000].

Zonally-averaged meridional sections of temperature and salinity (Figure 2.7) are qualitatively similar to observations to a good degree. Potential temperature sections show warm waters at the surface between 40°N to 40°S and cooler waters towards the poles.

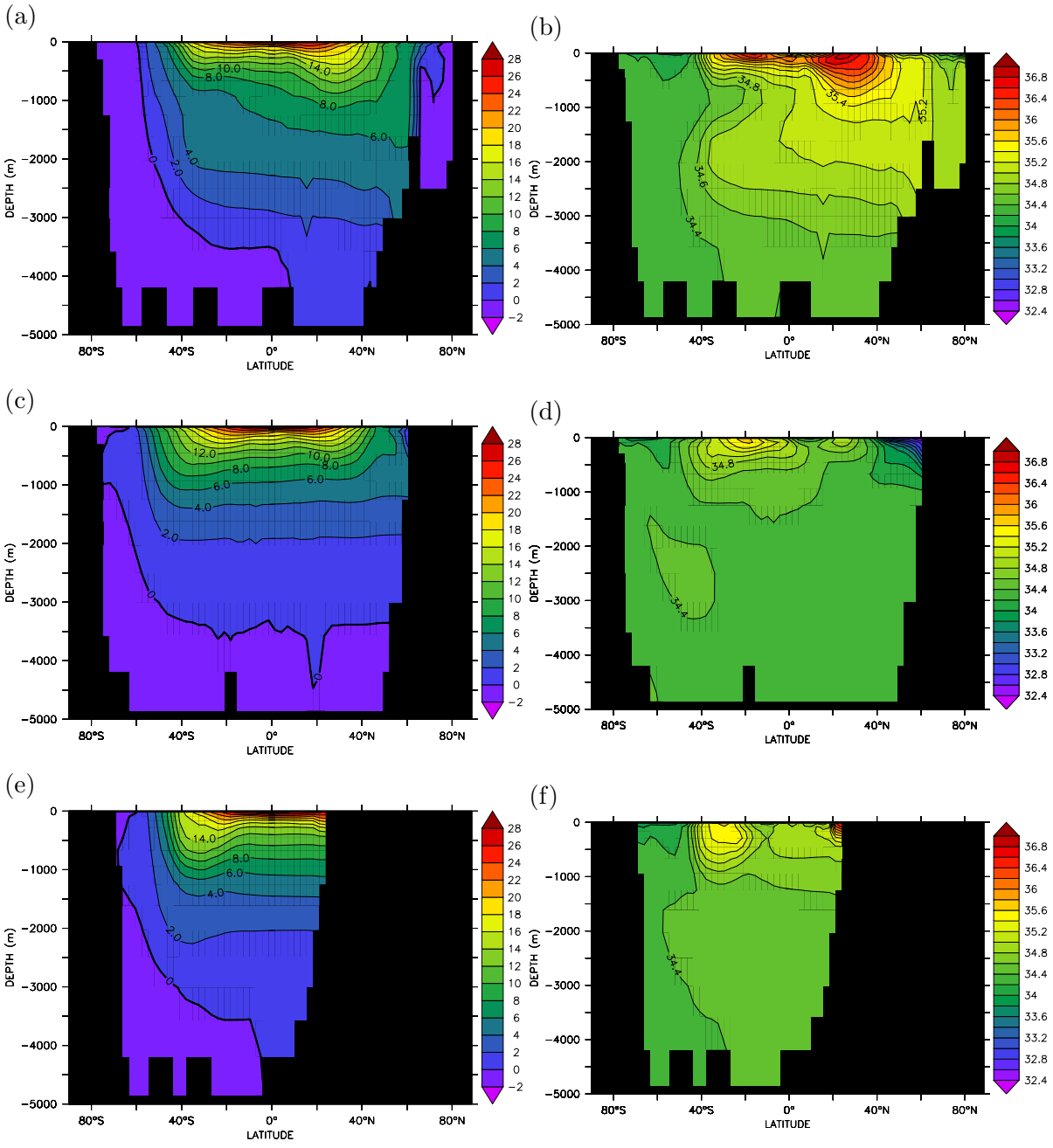

Figure 2.7: Equilibrium MITgcm output for the control configuration at 20000 years. Meridional sections of Potential Temperature (°C, left column) and Salinity (right column). (a) and (b) are in the Atlantic Ocean, (c) and (d) are in the Pacific Ocean, and (e) and (f) are in the Indian Ocean.

In particular, AABW is evident adjacent to the Antarctic continent and in the deep ocean as waters below 0 °C, although elevated production of these waters compared to observations does make the deep ocean temperature slightly low. Similarly, elevated Atlantic overturning results in relatively elevated upper ocean temperatures as an increased volume of thermocline waters are required to supply the conversion of light to dense water [*Gnanadesikan*, 1999; *Gnanadesikan and Hallberg*, 2000] that originates from dense to light conversion and formation of AAIW and SAMW in the Southern Ocean. This causes depression of upper ocean isopycnals and increased temperature when compared to climatology. Salinity reveals a similar pattern with similar discrepancies as the temperature distribution. The Atlantic basin is much saltier than the Indian or Pacific with a saline tongue of NADW spreading south at 2000 m. The deep salinity maximum in the Southern Hemisphere of the Indian Ocean associated with the eastward flow of NADW is also captured [*Cox*, 1989]. Above this, in all basins but particularly noticeable in the Atlantic, is the mid-depth salinity minimum signature of AAIW. However, the deep ocean is slightly too fresh due to relatively higher abundance of AABW while the upper ocean is too saline due to depression of the upper ocean isopycnals in connection with elevated Atlantic overturning.

The biogeochemical model and simple parameterisation of primary production broadly recreates the observed surface distribution of macronutrients (Figure 2.8a) with phosphate/iron dynamics capturing elevated surface PO_4 concentrations in the High Nutrient Low Chlorophyll (HNLC) and upwelling regions of the north and equatorial Pacific and Southern Ocean without use of spatially varying production rates or surface nutrient restoring boundary conditions [*Najjar and Orr*, 1998; *Parekh et al.*, 2005]. However, the upwelling waters tend to come from too deep due to overly simplified circulation, such as poorly resolved equatorial undercurrent dynamics as a result of coarse resolution [*Dutkiewicz et al.*, 2005a; *Parekh et al.*, 2005], or heightened upwelling of CDW to supply greater formation of Antarctic water masses, resulting in greater concentrations of nutrients compared to observations. Despite the paucity of oceanic dissolved iron concentration measurements [*Parekh et al.*, 2005], the model produces plausibly elevated levels (Figure 2.8b) under the main dust plumes in the Atlantic and Indian oceans with reduced concentrations in remote regions of the Southern Ocean and in the oligotrophic subtropical gyres, which may be excessive due to the upwelling of waters from too deep with a greater than observed iron deficit (see below). Furthermore, lack of additional riverine or hydrothermal sources of iron and spatially constant aeolian iron

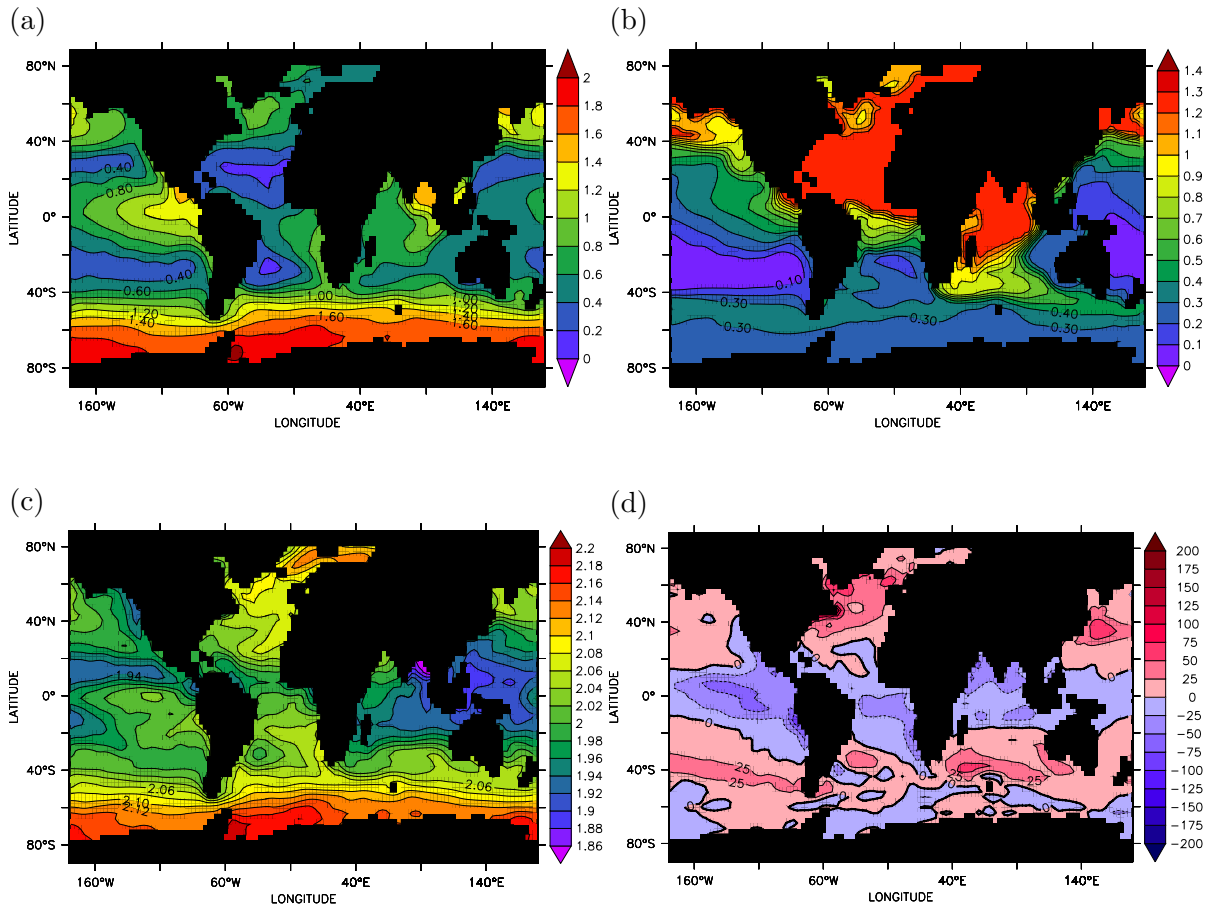

Figure 2.8: MITgcm output for the control configuration at 20000 years after spin up sequence detailed above (a) Surface phosphate concentration mmol P m^{-3}, (b) Surface dissolved iron concentration (µmol Fe m^{-3}), (c) Surface DIC concentration (mol C m^{-3}) and (d) Surface air-sea flux of CO_2 (mmol C m^{-3} yr^{-1}) calculated from Equation 2.22 and expressed as the change in concentration of DIC in the surface cell, that is negative values indicate outgassing while positive values represent oceanic carbon dioxide uptake.

solubility may exacerbate this situation leading to artificially high biological iron limitation. The surface distribution of DIC (Figure 2.8c) is influenced by both solubility, biological production and the upwelling of remineralised organic matter particularly in the Southern Ocean, which is successfully represented in the model. Gas exchange of CO_2 between the atmosphere and ocean (Figure 2.8d) is consistent with preindustrial flux reconstructions [e.g. *Gloor et al.*, 2003], with equatorial outgassing and uptake at temperate and high latitudes because of increased CO_2 solubility in lower temperature waters, particularly influencing regions where warm water is transported poleward and heat loss occurs causing undersaturation with respect to the atmosphere and therefore oceanic uptake. The Southern Ocean is relatively neutral, neither a source nor a sink of

CO_2 especially in the zonal average as a result of atmosphere-ocean steady state. Modern observations [*Takahashi et al.*, 2002] suggest that there is definite oceanic uptake in the Southern Ocean due to the additional absorption of anthropogenic carbon from the atmosphere that is not captured here, but a similar pattern of fluxes elsewhere.

Meridional sections in the Atlantic and Indo-Pacific basins of DIC (Figure 2.9a and b) and phosphate (Figure 2.9c and d) follow the same pattern with low concentrations at the surface in the subtropical gyres and newly formed deep waters in the North Atlantic, increasing concentrations in the Southern Hemisphere and other upwelling regions and high concentrations in the oldest waters of the deep North Pacific. This is the integrated effect of the biological pump [c.f. *Volk and Hoffert*, 1985] exporting nutrients and carbon from the surface ocean to depth where it is respired or remineralised and accumulated. Sections of iron (Figure 2.9e and f) illustrate the additional role of complexation and scavenging. High concentrations of iron occur under regions of aeolian deposition such as the Atlantic and North Indian Oceans and in the thermocline as a result of remineralisation. This signal is carried into the deep ocean by NADW formation in the North Atlantic and as this water mass is advected southward and throughout the deep ocean, scavenging acts to deplete excess iron such that the lowest concentrations are found in the deep Southern Ocean and North Pacific, consistent with observations [*Parekh et al.*, 2005], but the magnitude may be too low due to lack of hydrothermal iron input to the deep ocean. The surface concentration of iron in the Southern Ocean is not fully depleted due to protection from scavenging by complexation with organic ligand and other factors such as underutilisation due to light limitation of primary production.

The interplay between light and available macro- and micronutrients produces a reasonable distribution of biological productivity (Figure 2.10). There is a large standing stock in the equatorial regions, North Pacific and in the Southern Ocean, even though these regions are likely iron limited, but the levels are perhaps too high due to elevated nutrient concentrations for the reasons described above. The model also reproduces the low productivity of the oligotrophic subtropical gyres. Integrated globally the net production fixes $25.80\,\mathrm{Gt\,C\,yr^{-1}}$, which given the simplicity of the parameterisation and lack of distinct groups of phytoplankton, zooplankton or bacteria/detritus, compares reasonably favourably to the $35\text{–}57\,\mathrm{Gt\,C\,yr^{-1}}$ from modelling, observational and remote sensing estimates [*Dutkiewicz et al.*, 2005a, and references therein].

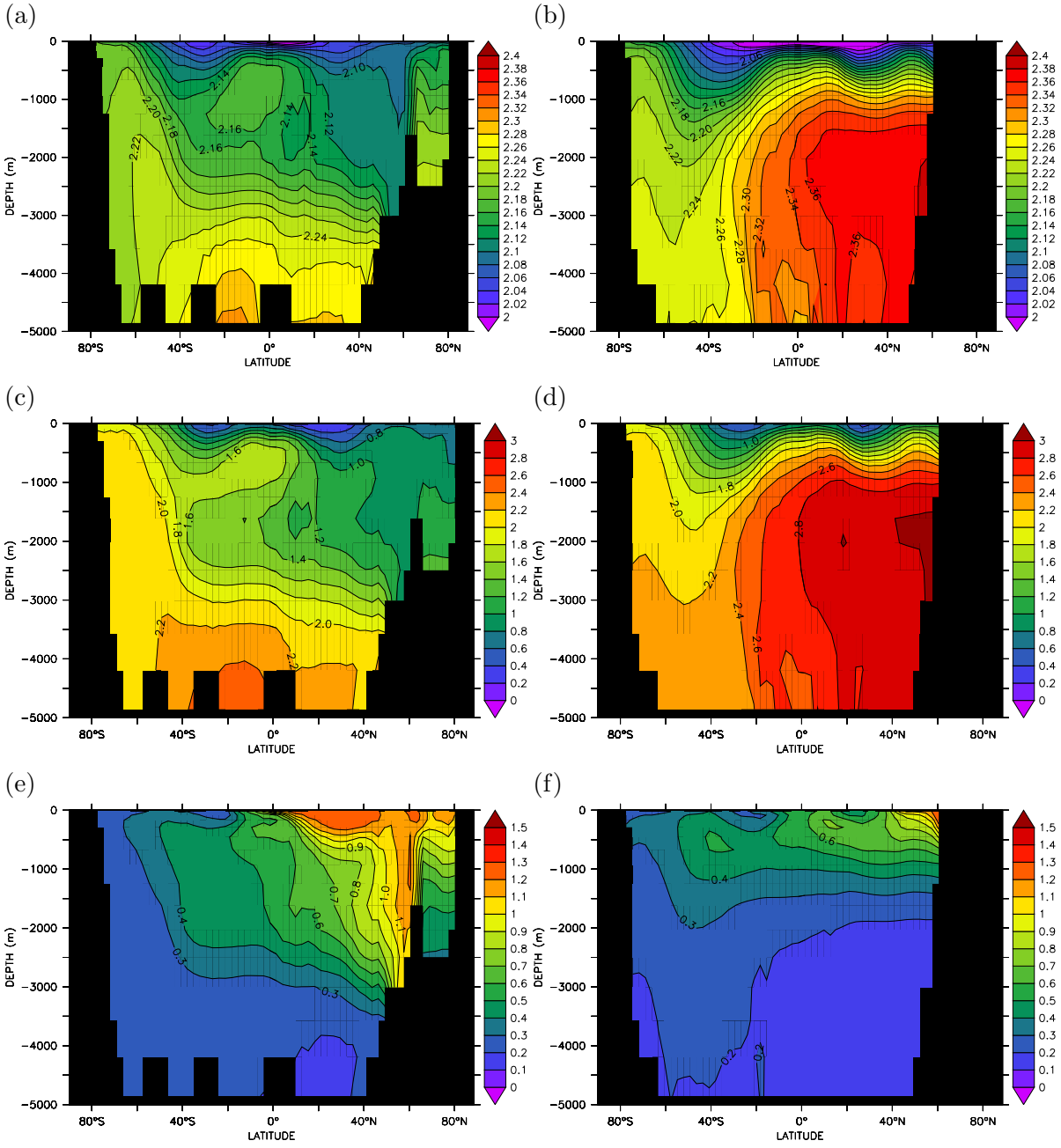

Figure 2.9: Equilibrium MITgcm output for the control configuration at 20000 years. Meridional sections of tracers in the Atlantic Ocean (left column) and in the Indo-Pacific Oceans (right column) for (a) and (b) dissolved inorganic carbon (mol C m^{-3}), (c) and (d) phosphate (mmol P m^{-3}) and (e) and (f) dissolved iron (µmol Fe m^{-3}).

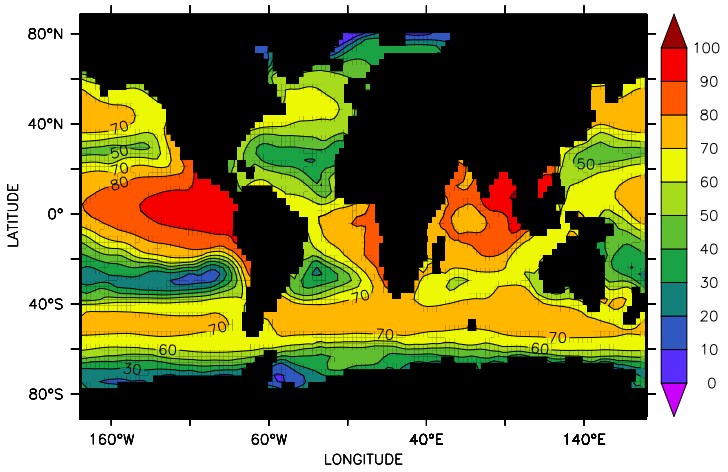

Figure 2.10: Equilibrium MITgcm output for the control configuration at 20000 years. Sea surface biological primary productivity (mmol C m^{-3})

Table 2.4: Comparison of the preindustrial control state with modern climatological data (R^2) and Relative Standard Deviations (RSD) calculated as the ratio of a variable's standard deviation and mean expressed as a percentage. RSD could not be computed for the air-sea flux of carbon dioxide as the mean is very close to zero, producing unrealistically high values.

Variable	R^2	RSD (%)	Data Source
θ	0.94	2.1	*Stephens et al.* [2002]
Salinity	0.76	1.5	*Boyer et al.* [2002]
Preindustrial DIC	0.87	5.1	*Key et al.* [2004]
Alkalinity	0.81	1.9	*Key et al.* [2004]
Phosphate	0.81	34	*Conkright et al.* [2002]
Dissolved Oxygen	0.78	36	*Locarnini et al.* [2002]
CO_2 flux	0.48	-	*Takahashi et al.* [2002]
pCO_2	0.49	10	*Takahashi et al.* [2002]

A more rigorous comparison of model state to observations of the real ocean was also pursued. Climatological data representing the physical model (θ and S) and the biogeochemical model (DIC, Alkalinity, Phosphate, Dissolved Oxygen, pCO_2 and air-sea CO_2 flux) were interpolated onto the model grid and then the model output was linearly regressed onto these regridded climatologies to determine their spatial correlation. The coefficient of determination (R^2) was also calculated to assess the proportion of the variance of the regridded climatological data that is described by the configuration (see Table 2.4 and data references therein). Despite the fairly coarse resolution and the fact that interpolation of often finer scale observations (1° and 33 depth levels) onto the 2.8° grid with only 15 levels does remove a proportion of the sub-gridscale variance, the values in Table 2.4 indicate that this configuration of MITgcm does appear

to capture the main features of the large-scale circulation and distribution of tracers. Of course, performance is influenced by climatological restoring and the imperfect handling of atmosphere-ocean freshwater fluxes, however in some cases where the model performs less well such as pCO_2 and the air-sea CO_2 flux, the carbon climatologies used here [*Takahashi et al.*, 2002] include the effects of anthropogenic carbon emissions with non-zero global average air-sea fluxes, while the model is configured to represent pre-industrial conditions with an atmospheric CO_2 concentration of 278 µatm and has close to zero net surface flux because it is in a steady state with the atmosphere. The CO_2 data are on a coarser grid than the model, but averaging the control fields onto the climatological axes makes only a small difference to the correlation.

2.3 Using Composite Tracers to Investigate Biogeochemical Cycles

Primary production in the surface ocean converts inorganic carbon and nutrients into organic matter, which contains a particular ratio of these elements. By exploiting the constant stoichiometric ratios of elements within the biogeochemistry model (see Table 2.3) it is possible to extract further information from the observed tracer fields to create additional composite conservative tracers, although there is evidence in the real ocean that these ratios do not strictly hold in some circumstances [*Ganeshram et al.*, 2002; *Geider and La Roche*, 2002].

2.3.1 Partitioning phosphate concentration into biologically regenerated phosphate and unutilised preformed phosphate.

Export and remineralisation of biogenic carbon from the surface to the deep ocean, or the soft tissue pump [*Volk and Hoffert*, 1985] as previously described, is dependent on the concentration of nutrients, the presence of which in the surface ocean, particularly at high latitudes, suggests that the soft tissue pump is not operating at full efficiency. When these surface waters are injected into the ocean interior, they carry these unutilised nutrients conservatively while gaining nutrients from the remineralisation of organic matter, thus the observed concentration can be divided into two pools following *Ito and*

Follows [2005] (Equation 2.27):

$$PO_4^{obs} = PO_4^{pref} + PO_4^{reg} \tag{2.27}$$

(1) "preformed" (PO_4^{pref}) nutrients, unused at the surface and subducted into the interior, and (2) "regenerated" (PO_4^{reg}) nutrients, accumulated by the breakdown of organic material. Regenerated phosphate can be estimated using the Apparent Oxygen Utilisation (AOU) method [Equation 2.28 *Ito and Follows*, 2005; *Ito et al.*, 2004a] where the amount of dissolved oxygen consumed by respiration is calculated from the observed oxygen tracer field, O_2^{obs}, and the saturated concentration of oxygen, O_2^{sat}, which is a function of *in situ* temperature and salinity, assuming that the oxygen concentration is close to saturation at the surface.

$$AOU = O_2^{sat}(T,S) - O_2^{obs} \tag{2.28}$$

The regenerated component of phosphate is then related to the AOU by the constant ratio of phosphorus to oxygen (Equation 2.29) while the preformed component is calculated as the difference between the observed and the regenerated concentrations.

$$PO_4^{reg} = R_{PO_4:O_2} \cdot AOU \tag{2.29}$$

Dissolved oxygen concentrations (Figure 2.11a and b) can be used to give an indication of the "age" of a water mass. "Young" water masses where ventilation has recently occurred have elevated oxygen concentrations, such as near the surface and in the deep waters of the North Atlantic and intermediate and deep waters of the Southern Ocean, where surface waters are exported to the interior. "Old" water masses are associated with low concentrations of oxygen through consumption by respiration and remineralisation, such as in the low latitude thermocline and the deep North Pacific. The assumption of surface saturated dissolved oxygen is generally valid because the rate of air-sea exchange of O_2 is relatively rapid compared to the residence time of waters at the surface, however disequilibrium may be introduced especially in high latitude regions by rapid heat loss and subsequent increase in solubility, mixing and entrainment of older, low oxygen intermediate and deep waters and by sea ice cover decreasing the rate of equilibration with the atmosphere [*Ito et al.*, 2004a]. These result in overestimation of AOU, respiration and the regenerated nutrient concentration in the immediate vicinity of the disequilibrium but also in the deep ocean as the high latitude disequilibrium concentration is carried in newly formed deep and bottom waters. *Ito et al.* [2004a]

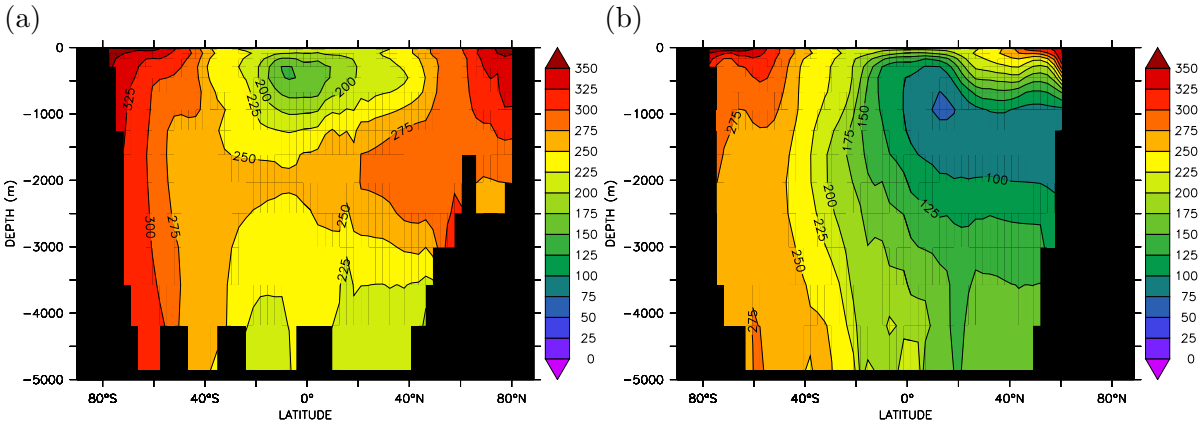

Figure 2.11: Equilibrium MITgcm output for the control configuration at 20000 years. Meridional sections of dissolved oxygen (mmol O m^{-3}) in the (a) Atlantic Ocean and (b) Indo-Pacific Oceans.

found simulated errors of −73 µmol O l^{-1} between apparent oxygen utilisation and true oxygen utilisation (effectively the difference between the preformed oxygen concentration and the saturated concentration of oxygen) in the Weddell Sea and −18 µmol l^{-1} in the Labrador Sea with lesser undersaturation in the swift western boundary currents and slight oversaturation in the surface waters of the tropics and subtropics due to photosynthesis. However, in these results, which are similar to the conditions presented in *Ito and Follows* [2005], the maximum disequilibrium concentration (the difference between the saturation and surface concentrations), also found in the Weddell Sea, was approximately half as large at −36.9 µmol O l^{-1} (equivalent to −36.9 mmol O m^{-3}) while the zonally-averaged disequilibrium in the Northern and Southern Hemisphere high latitudes in the Atlantic and Indo-Pacific was approximately −9 µmol O l^{-1} in both cases.

Regenerated phosphate concentrations (Figure 2.12a and b) calculated from Apparent Oxygen Utilisation using Equation 2.28 and Equation 2.29 are low in the newly ventilated water masses at the surface and at depth, such as NADW. As with the phosphate concentration (Figure 2.9c and d) and inversely with dissolved oxygen (Figure 2.11a and b) the concentration of regenerated phosphate increases as biogenic phosphate is remineralised and accumulated in the thermocline and in the deep waters that are advected around the global ocean, with the highest concentration found in the deep North Pacific. The concentration of preformed phosphate (Figure 2.12c and d), calculated from Equation 2.27, is also low at the surface and in the waters formed in the North Atlantic, while preformed phosphate is elevated in the deep and intermediate waters

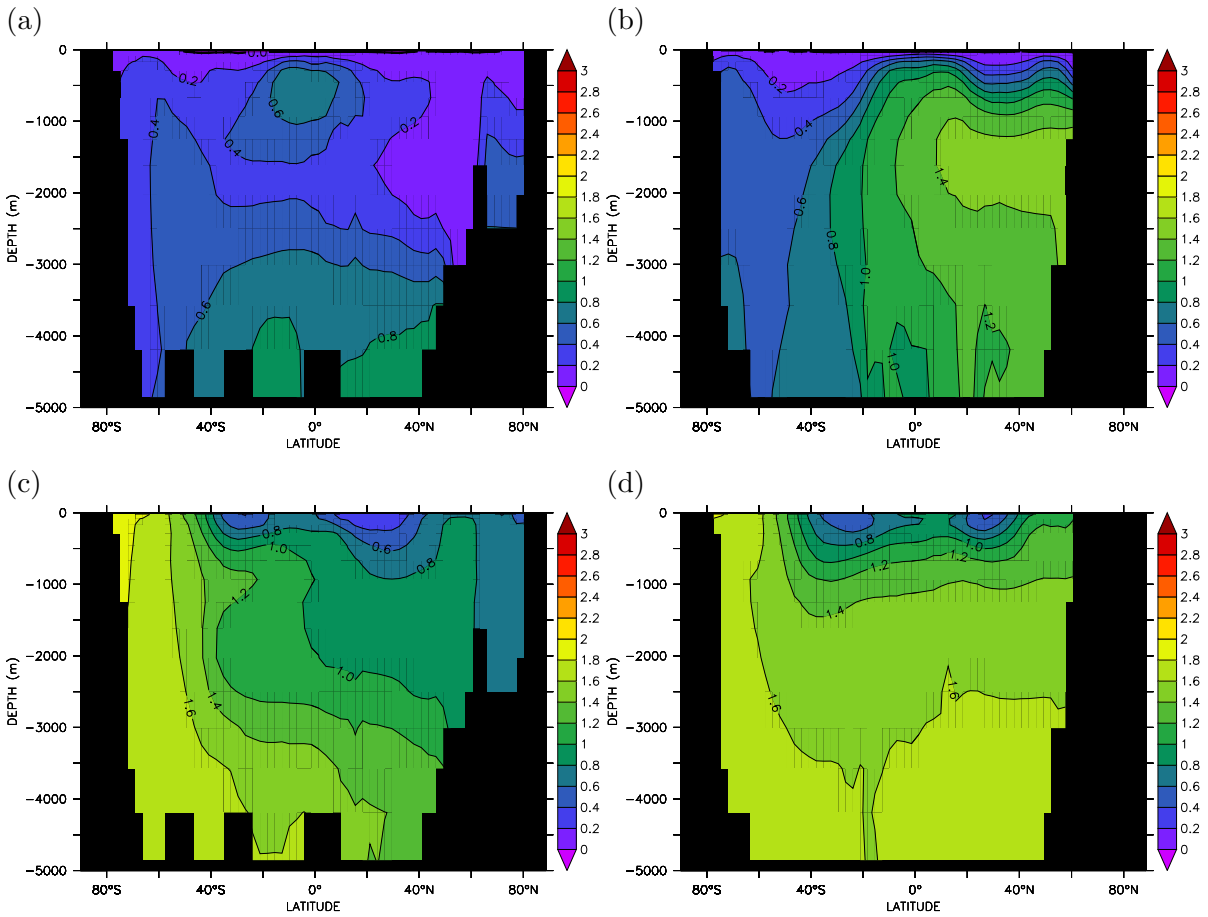

Figure 2.12: Equilibrium MITgcm output for the control configuration at 20000 years. Meridional sections of tracers in the Atlantic Ocean (left column) and in the Indo-Pacific Oceans (right column) for (a and b) regenerated phosphate (mmol P m^{-3}) calculated from AOU using Equations 2.28 2.29, and (c and d) preformed phosphate (mmol P m^{-3}) calculated using the regenerated component and Equation 2.27.

formed in the Southern Ocean reflecting surface nutrient concentrations in the regions of isopycnal outcrop.

The return of nutrients to the ocean interior via the regenerated, biologically mediated pathway or the preformed, physically mediated pathway illustrates the efficiency of the modelled soft tissue pump: were there no primary production then the concentration of PO_4^{pref} would equal PO_4^{obs} and all the surface nutrients would be returned to the ocean interior by subduction and water mass formation. However, if all the surface nutrients were depleted by primary production then PO_4^{reg} would equal PO_4^{obs} and all the surface nutrients would be returned to the ocean interior by the soft tissue pump. If the soft tissue pump operated at such efficiency then simple box models predict that atmospheric CO_2 would be reduced by 163 µatm [*Sarmiento and Toggweiler*, 1984]. A metric for the

efficiency of the soft tissue pump is the ratio of the globally-averaged concentration of regenerated phosphate to that of total phosphate [*Ito and Follows*, 2005]. Applying this measure, the soft tissue pump in the control run is 35.7% efficient, which compares well to the 36% calculated from World Ocean Atlas data [*Ito and Follows*, 2005].

2.3.2 Calculating the oceanic concentration of Dissolved Inorganic Carbon that is out of equilibrium with the atmosphere.

The balance between the atmospheric and surface ocean CO_2 concentrations, which may be relatively supersaturated or undersaturated even in steady state, is not instantaneous and has a time scale that lies between that for oxygen and CFCs (weeks/ months) and radiocarbon (decades) [*Ito et al.*, 2004b]. Furthermore, this is comparable to the residence time of waters in the surface ocean, so it is possible that in many regions equilibration does not occur before the surface waters are exported into the interior. If perturbations to Southern Ocean circulation alter the rate of residual overturning, modulating the volume of carbon rich deep waters brought to the surface then two processes, air-sea exchange driven by solubility and concentration gradients (Equation 2.22) and altered residence time of waters in the surface layer, must compete. If remineralised nutrients are brought to the surface and rapidly converted to preformed nutrients and subducted into the ocean interior before biology and gas exchange are able to influence the water mass composition then little loss of carbon dioxide will occur and the disequilibrium concentration will be large and the ocean will effectively store more CO_2 than the nutrient fields suggest [*Gnanadesikan and Marinov*, 2008]. Also the reverse is possible where biological activity and rapid cooling and export from the surface layer prevent water mass from attaining its equilibrium concentration with the atmosphere and therefore the ocean holds a lower concentration of CO_2 than expected. It is beneficial to determine if equilibrium is actually achieved because it's effects may have significant influence on ocean carbon storage and atmospheric CO_2- an increase in ocean atmosphere disequilibrium concentration is an additional oceanic carbon sink, while a decrease in disequilibrium concentration is an additional source of CO_2 to the atmosphere.

The disequilibrium concentration of DIC that a water mass has when it was last in contact with the atmosphere can be diagnosed by correcting the observed carbon distribution for photosynthesis, respiration and remineralisation of organic carbon (the soft

tissue pump) and the formation and dissolution of calcium carbonate (the carbonate pump, [*Volk and Hoffert*, 1985]) and then calculating its deviation from the equilibrium concentration with respect to the atmosphere, following the "back-calculation" method of *Gruber et al.* [1996]. A conservative tracer C^* is defined (Equation 2.30) where the distribution of DIC is corrected for the effect of the soft tissue pump via proportional changes in the dissolved oxygen concentration using a constant stoichiometric ratio, $R_{C:O_2}$, since oxygen is consumed as the DIC concentration increased by remineralisation. Similarly, changes in the carbonate pump are accounted for by variations in alkalinity with a correction for the redox reactions that occur as a result of biological activity, which is largely the result of changing nitrate concentration determined by the proportional change in dissolved oxygen content and the constant $R_{N:O_2}$. These relationships are the same as calculated within the MITgcm biogeochemistry code.

$$C^* = DIC - R_{C:O_2}O_2 - \frac{1}{2}\Big(ALK + R_{N:O_2}O_2\Big) \tag{2.30}$$

The distribution of C^* from Equation 2.30 reflects the distribution and origin of water masses in the ocean as it has no sources or sinks in the interior and is conservatively mixed. Higher values occur in the Southern Ocean compared to the North Atlantic due to temperature and salinity effects on the solubility of oxygen and differences in the preexisting concentrations of DIC and alkalinity [*Gruber et al.*, 1996]. However this trend can be eliminated by considering deviations of C^* from a similarly formed conservative tracer, $C^{*\ pref}$ (Equation 2.31), that contains the surface geographical variability that is subducted into the ocean interior, or "preformed", using values of saturated oxygen and DIC concentrations and surface alkalinity observations.

$$C^{*\ pref} = DIC^{pref} - R_{C:O_2}O_2^{pref} - \frac{1}{2}\Big(ALK^{pref} + R_{N:O_2}O_2^{pref}\Big) \tag{2.31}$$

The preformed DIC was first estimated from the equilibrium carbon concentration at the current atmospheric CO_2 concentration and *in situ* alkalinity, temperature, salinity, phosphate, boron (parameterised as a function of salinity) and silicate (assumed constant and taken from monthly climatology [*Conkright et al.*, 2002]) concentrations using the method of *Follows et al.* [2006] employed within the biogeochemistry model. The preformed oxygen concentration was estimated from the current saturation concentration (as in Equation 2.28) and the preformed alkalinity was estimated by multiple linear regression (Equation 2.32 and Figure 2.13). For the majority of the surface ocean, alkalinity is dominated by the freshwater budget, which yields a strong correlation with salinity, however in regions such as the Southern Ocean this relationship

breaks down due to the upwelling of high alkalinity deep waters [*Gruber et al.*, 1996]. Therefore, surface alkalinity is regressed against salinity and the conservative water mass tracer PO of *Broecker* [1974] to improve the predictive value of the regression, where $PO = O_2 - R_{P:O_2} PO_4$ is the oxygen distribution with alterations due to respiration and remineralisation of biogenic carbon removed. To calculate preformed alkalinity, this relation (Equation 2.32) is applied throughout the model domain and highlights the effect of dissolution of carbonates in the interior ocean (Figure 2.13).

$$ALK^{pref} = 0.1114 + (0.062426 \times S) + (0.095896 \times PO), \quad R^2 = 0.97223 \tag{2.32}$$

The difference between C^* and $C^{*\ pref}$ produces a new quantity, ΔC^* (Equation 2.33), which reveals the air-sea CO_2 disequilibrium concentration of DIC when interior water masses were last in contact with the atmosphere plus any residual effects due to parameter choices and calculation uncertainties. When the saturated values and the constant elemental ratios (see Table 2.3) are substituted in to Equation 2.33, the soft tissue pump may be represented by the AOU in a similar way to Equation 2.29 and ΔC^* can be thought of as the preformed DIC concentration (akin to preformed phosphate) with a correction for air-sea exchange at the surface..

$$\begin{aligned} \Delta C^* = DIC - DIC^{eq}(S,T,ALK,pCO_2) - R_{C:O_2}\Big(O_2 - O_2^{sat}(T,S)\Big) \\ -\frac{1}{2}\Big[ALK - ALK^{pref} + R_{N:O_2}\Big(O_2 - O_2^{sat}(T,S)\Big)\Big] \end{aligned} \tag{2.33}$$

The disequilibrium concentration of carbon in the interior ocean (Figure 2.14a and b) is generally positive, showing oversaturation with respect to the atmosphere and makes up a significant portion of the total DIC concentration of approximately 25% on average. In particular, Antarctic Intermediate and Bottom Water formed in the Southern Ocean show relatively high air-sea disequilibrium due to the rapid circulation and short residence time in the surface layer compared with the timescale of CO_2 equilibration that prevents excess upwelled deep ocean carbon dioxide from effectively escaping to the atmosphere. Cooling and sinking of surface waters by convection in the North Atlantic also prevents atmosphere-ocean equilibrium and results in slight undersaturation of NADW compared to the atmosphere, with a similar process occurring in the surface layer between 20–40°S. These signals are eroded by conservative mixing with high disequilibrium southern-sourced water masses. The high disequilibrium concentrations in the northern Indo-Pacific Oceans may result from the accumulation of high disequilibrium water masses such as AAIW and general upwelling of high disequilibrium deep

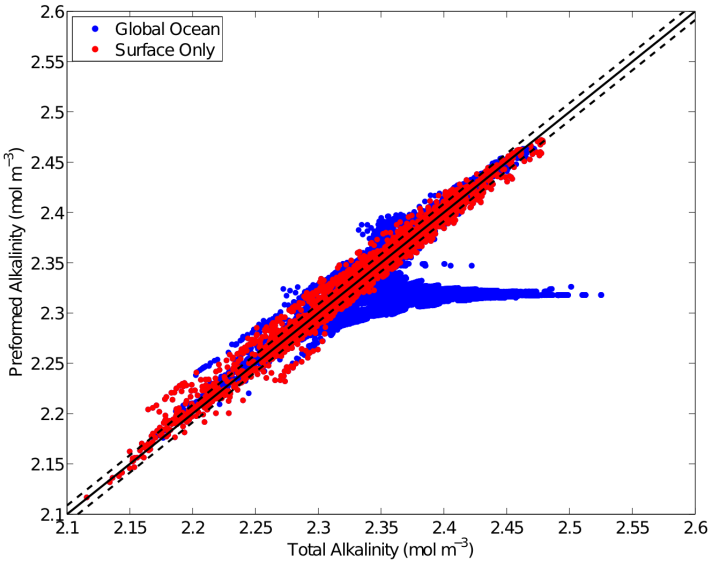

Figure 2.13: Regressed preformed alkalinity (calculated from salinity and PO [*Broecker*, 1974]) against modelled alkalinity for the surface (red) and global (blue) ocean. The dashed lines are the 1-σ concentrations of the alkalinity-preformed alkalinity anomaly which is 8.7 mmol eq m^{-3}. Note the large deviation in total alkalinity in the interior ocean as a result of the carbonate pump.

and bottom waters sourced from the Southern Ocean. However, as with preformed and regenerated phosphate, there is error associated with overestimation of respiration by AOU, particularly for deep and bottom waters sourced at high latitude [*Ito et al.*, 2004a] that would act to increase disequibrium concentration. Indeed, *Gruber et al.* [1996] show that error of ΔC^* increases at high levels of AOU. Also, the North Indian and Pacific basins are associated with high alkalinities of greater than 2.4 mol eq m^{-3} and therefore are subjected to the largest corrections when calculating preformed alkalinity that might also artificially elevate disequilibrium DIC. Since perturbations to atmospheric CO_2 are considered then the magnitude of the disequilibrium becomes increasingly dependent on another assumption that the entire ocean is instantaneously in equilibrium with the atmosphere when estimating the preformed equilibrium carbon concentration. In reality different parts of the interior will be in equilibrium with the atmospheric concentration of CO_2 at the time when it was last at the surface.

This method was originally developed to determine the distribution of anthropogenic CO_2 from biogeochemical observations, by subtracting an estimate of air-sea disequilibrium (Equation 2.34):

$$\Delta C^* = \Delta C_{diseqm} + \Delta C_{ant} \tag{2.34}$$

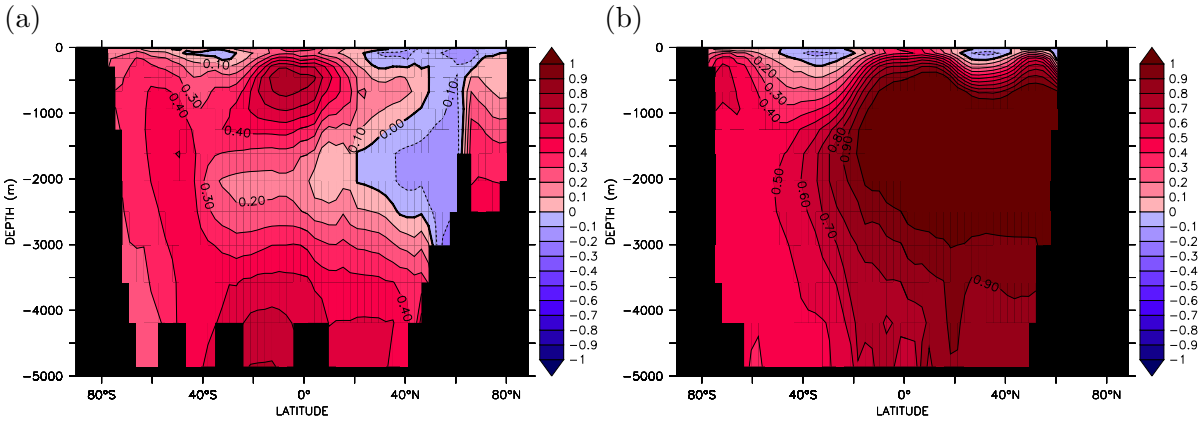

Figure 2.14: Equilibrium MITgcm output for the control configuration at 20000 years. Air-sea disequilibrium concentration of Dissolved Inorganic Carbon (mol C m^{-3}) in (a) the Atlantic and (b) Indo-Pacific Oceans at the time interior water masses were last at the surface, diagnosed as the difference between the DIC concentration in equilibrium with the atmosphere and the observed DIC concentration after "correction" for the effects of organic carbon remineralisation and calcium carbonate dissolution. Positive values indicates oversaturation with respect to the atmosphere while negative values represent undersaturation.

The initial formulation of Equation 2.33 with estimated saturated and equilibrium fields in order to disclose the anomalous increase in carbon due to uptake of anthropogenic CO_2 by the ocean is motivated by availability of data, or more specifically, the unavailability of the preindustrial distributions of DIC, alkalinity and dissolved oxygen concentrations in the 1800's before the anthropogenic perturbation to atmospheric CO_2 levels. In contrast, the model control state provides these initial conditions, which are substituted instead of the estimated fields in Equation 2.31 to give Equation 2.35 and a modified definition of ΔC^* (Equation 2.36):

$$C^{*\ ctrl} = DIC^{ctrl} - R_{C:O_2} O_2^{ctrl} - \frac{1}{2}\left(ALK^{ctrl} + R_{N:O_2} O_2^{ctrl}\right) \tag{2.35}$$

$$\begin{aligned} \Delta C^* &= DIC - DIC^{ctrl} - R_{C:O_2}\left(O_2 - O_2^{ctrl}\right) \\ &- \frac{1}{2}\left[ALK - ALK^{ctrl} + R_{N:O_2}\left(O_2 - O_2^{ctrl}\right)\right] \end{aligned} \tag{2.36}$$

This formulation of ΔC^* allows the increase or decrease in atmosphere-ocean CO_2 disequilibrium concentration due to model perturbations to be directly calculated.

2.3.3 Calculating the internal distribution of the air-sea gas exchange pump

The effect of altered ocean-atmosphere CO_2 fluxes on the content and distribution of carbon in interior water masses can be extracted from the DIC concentration using a similar method as Equation 2.30. The local DIC concentration is corrected for the "potential" soft tissue and "potential" carbonate pumps using nutrient concentration instead of dissolved oxygen concentration in the formulation of C^* (with $R_{C:P}$ and $R_{N:P}$)[*Gloor et al.*, 2003; *Gruber and Sarmiento*, 2002; *Gruber et al.*, 2009; *Mikaloff Fletcher et al.*, 2007]. These are the distributions of DIC associated with biological processes in the absence of air-sea exchange since this process acts to reduce the magnitude of variations that are induced by biological processes. Once removed, changes in concentration of this new tracer, $C_{gas\ exch}$, are governed only by natural air-sea exchange of carbon dioxide at the sea surface and ocean transport and mixing in the interior (Equation 2.37).

$$C_{gas\ exch} = \frac{S_0}{S}\Big[DIC - R_{C:P}PO_4 - \frac{1}{2}\Big(ALK + R_{N:P}PO_4\Big)\Big] - const \tag{2.37}$$

$C_{gas\ exch}$ is normalised to a constant reference salinity, S_0, of 35 to remove surface effects of evaporation and precipitation and the value of the constant is arbitrarily chosen such that the global average surface $C_{gas\ exch}$ in the control is zero, to match the actual air-sea flux of CO_2 since the model is in a steady state. Most noticeable in Figure 2.15(a) and (b) is the small concentration of $C_{gas\ exch}$ in the Atlantic and Indo-Pacific Oceans with a mean value of $65\,\mathrm{mmol\,C\,m^{-3}}$ compared to the global mean DIC concentration of $2235\,\mathrm{mmol\,C\,m^{-3}}$. The interior distribution of $C_{gas\ exch}$ can be traced back to the pattern of surface fluxes: waters with a low concentration must have lost CO_2 last time they were in contact with the atmosphere, while high values represent CO_2 uptake by the ocean at the sea surface. Upwelling waters in the Southern Ocean have $C_{gas\ exch}$ concentrations of more than $60\,\mathrm{mmol\,C\,m^{-3}}$ while the concentrations found in intermediate and mode waters formed there are depleted to around $50\,\mathrm{mmol\,C\,m^{-3}}$ or lower that might suggest net outgassing of CO_2 as the water masses are transported northwards at the surface and subducted into the interior as seen in the estimated preindustrial distributions of the gas exchange pump in *Gruber and Sarmiento* [2002] and *Mikaloff Fletcher et al.* [2007]. However the pattern of air-sea fluxes (Figure 2.8d) indicates net CO_2 uptake from the atmosphere, therefore the lower values found may be contributed by entrainment of subtropical waters originating in the negative patch at the surface in the tropics and about the equator. These negative values at low latitudes suggest strong outgassing of

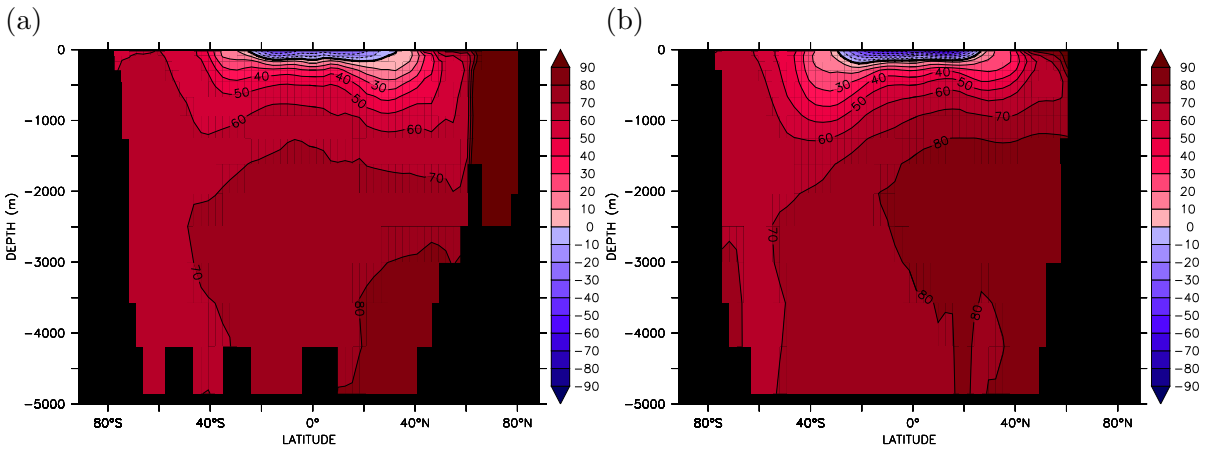

Figure 2.15: Equilibrium MITgcm output for the control configuration at 20000 years. Meridional sections of the quasiconservative tracer $C_{gas\ exch}$ (mmol C m^{-3}) in the (a) Atlantic (b) and Indo-Pacific Oceans calculated from Equation 2.37.

both high $C_{gas\ exch}$ waters upwelled at the equator and waters carried in equatorward surface flows that warm and thus expel CO_2 due to decreased solubility. The deep Indo-Pacific Basins have a more homogenous interior distribution of $C_{gas\ exch}$ compared to the Atlantic because of the imprint of gas exchange carried into the deep ocean by NADW that generally sequesters CO_2 at the surface due to cooling and export [*Gruber and Sarmiento*, 2002].

Anomalies of $C_{gas\ exch}$ compared to this control state will illuminate the water masses that act as sources and sinks of CO_2 to the atmosphere due to model perturbations. However, the fact that both $C_{gas\ exch}$ and ΔC_{diseqm} show elevated concentrations in the North Pacific (Figures 2.14 and 2.15), the same region of elevated regenerated phosphate (Figure 2.12b) strongly suggest that the entire effect of the soft tissue and/or the carbonate pumps have not been properly accounted for. Indeed, both tracers exhibit a widespread positive correlation with regenerated phosphate concentrations calculated from Equation 2.29. Therefore changes in these tracers should be treated with caution, especially if the balance of preformed and regenerated nutrients is altered, reflecting changes in actual biological productivity but not potential productivity.

2.4 Summary

A coarse resolution configuration of the Massachusetts Institute of Technology general circulation model (MITgcm) and coupled biogeochemistry model was spun-up until a

steady state was achieved. This state compares fairly well with modern climatological data but with a coarse resolution and an atmospheric CO_2 of approximately 278 µatm, cause some deviation from observations, particularly those attributed to the invasion of anthropogenic CO_2. This control state represents "preindustrial" conditions to which perturbations of model forcings and physics will be compared. Variants of this configuration have been used extensively elsewhere to explore interactions between physical and biogeochemical processes [*Dutkiewicz et al.*, 2005a,b, 2006; *Ito and Follows*, 2005; *Ito et al.*, 2004b; *Parekh et al.*, 2005, 2006b]. To aid investigation of oceanic adjustments within the carbon cycle to these perturbations, a series of additional tracers were introduced that exploit the constant stoichiometric ratios of elements within the model, providing information on the efficiency of the soft tissue pump, extent of atmosphere-ocean CO_2 equilibrium at the time of water mass subduction and effect of surface CO_2 fluxes on internal gas exchange pump distribution.

Part II

Perturbations to the Preindustrial Model State

Chapter 3

Response of the Global Carbon Cycle to Southern Ocean Wind Stress Magnitude

Evidence for the behaviour of the extratropical Southern Hemisphere westerly winds from paleocenographic proxies and climate model studies is ambiguous. In order to examine the sensitivity of atmospheric pCO_2 to Southern Ocean circulation, the residual mean flow, that is the net transport by the Eulerian mean and eddy advection, was conveniently modulated by changing the zonal wind stress over the ACC [c.f. *McDermott*, 1996; *Toggweiler and Samuels*, 1995; *Toggweiler et al.*, 2006] by ±50% (Figure 3.1) and then integrating the model until a new stable state was reached. The wind stress field was modified in a stepwise fashion to obtain the largest extent of maximum perturbation but avoid introducing large discontinuities at its boundaries while wind speed, which is used only in calculation of the air-sea fluxes of CO_2 in the biogeochemistry routines, was maintained at control levels. See Chapter 6.3 for assessment of this assumption. Despite these relatively large changes in wind stress forcing, only modest changes in Southern Ocean circulation and atmospheric CO_2 concentrations are induced. While the system approaches equilibrium after approximately 5000 years, where the following analysis will concentrate, the majority of the adjustment actually occurs in the first five centuries. With stronger wind stress, atmospheric CO_2 levels rise due to increased outgassing from the Southern Ocean and reduced biological pump efficiency, whilst with weaker wind stress, atmospheric CO_2 levels decline due to increased Southern Ocean

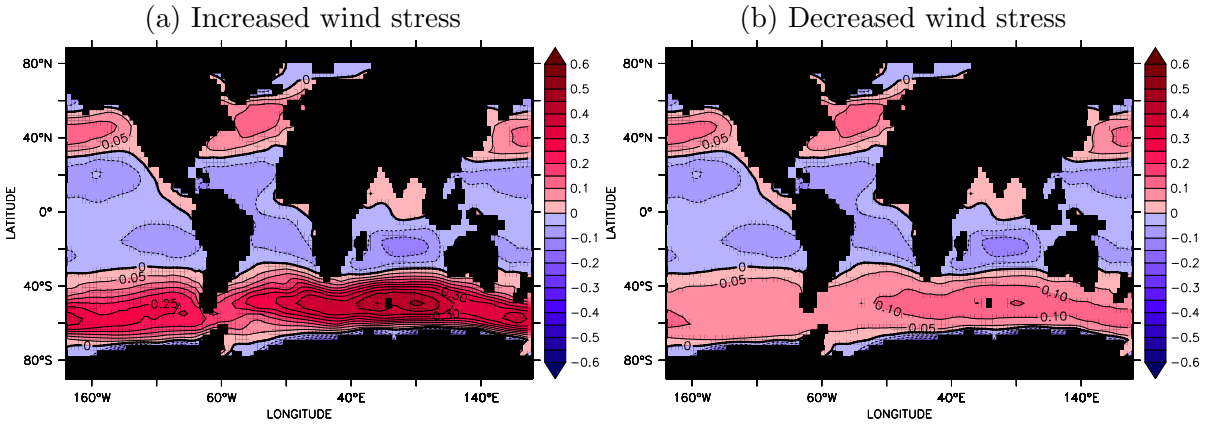

Figure 3.1: Perturbed zonal wind stress inputs ($\mathrm{N\,m^{-2}}$) (a) annual mean zonal wind stress with 50% increase in the Southern Ocean and (b) annual mean zonal wind stress with 50% reduction in the Southern Ocean.

uptake and a more efficient biological pump. The signatures of air-sea exchange in these perturbations are carried into the ocean interior at intermediate, not abyssal depths and are accompanied by significant and opposing anomalies of air-sea CO_2 disequilibrium concentration.

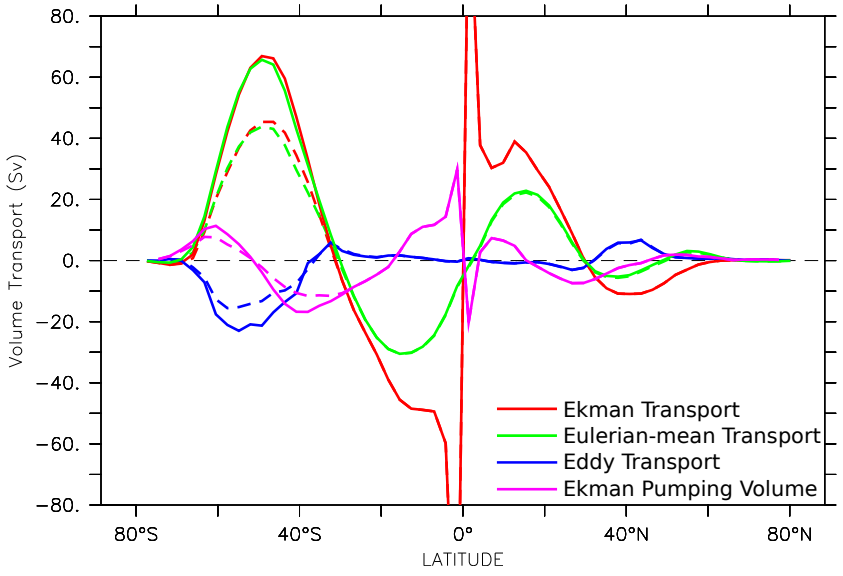

Figure 3.2: Meridional transports for enhanced Southern Ocean winds (solid lines) compared to the control (dashed lines) for Ekman transport (Sv) calculated directly from wind stress (red), Eulerian-mean transport (green), GM eddy transport (blue) and zonally integrated Ekman pumping flux (purple) in the surface Ekman layer (~100 m as observed by *Lenn and Chereskin* [2009]).

3.1 Increased wind stress perturbation

After 5000 years, with increased wind stress (Figure 3.1a) applied to the Southern Ocean, atmospheric CO_2 concentration had increased by 15.6 µatm to 293.6 µatm, so despite a relatively large change in wind stress forcing only modest changes in atmospheric CO_2 are induced.

3.1.1 Response of oceanic circulation and temperature and salinity distributions

Enhanced Southern Ocean wind stress induced an increase of 21.5 Sv global northward transport across 50°S in the Ekman layer (Figure 3.2, calculated using a depth of ~100 m as observed by *Lenn and Chereskin* [2009]), while modification to the curl of the wind stress intensifies Ekman pumping by 3.8 Sv upwelling at 60°S and 6.2 Sv downwelling at 40°S. The global Eulerian-mean flow (Figure 3.2 and 3.3a) is increased in concert with Ekman transport by 21.9 Sv causing an increase in isopycnal tilt and baroclinicity that acts to enhance mesoscale eddy activity in this region as parameterised by a 11.1 Sv increase in global southward GM bolus transports (Figure 3.3b) throughout the water column (not confined to the surface *Keeling and Visbeck* [2001]; *Sigman and Boyle* [2000]. Partial compensation of the two flows occurs because the two maxima are separated in latitude by approximately 5°, resulting in a net strengthening of the global residual Southern Ocean meridional overturning circulation in the region of 14.8 Sv (Figure 3.3c). Also, the eddy flow is distributed throughout the water column with direct compensation in the Ekman layer of only 8.0 Sv returning south (Figure 3.2). Elsewhere in the ocean interior, there is a decrease of 1–2 Sv in the anticlockwise deep ocean circulation cell (a positive anomaly) at 3000 m with a 200–300 m deepening of the interface between the upper-ocean and abyssal cells. Furthermore, in the Pacific at 1500 m there is a reduction of around 1–2 Sv in Southern Hemisphere upwelling which is substituted for a ~1 Sv increase in the Northern Pacific Intermediate Water circulation cell at 40°N that pushes further south at this level. Also, there is a decline in the anticlockwise abyssal circulation at ~3000 m depth from −7.2 Sv to −6.3 Sv.

Residual velocity anomaly averaged over the top 100 m (Figure 3.4a) shows that away from the ~1–3 $cm\,s^{-1}$ increase in the ACC, there is a consistent increase in northward velocity in the western boundary current in the Atlantic, which contributes the majority of

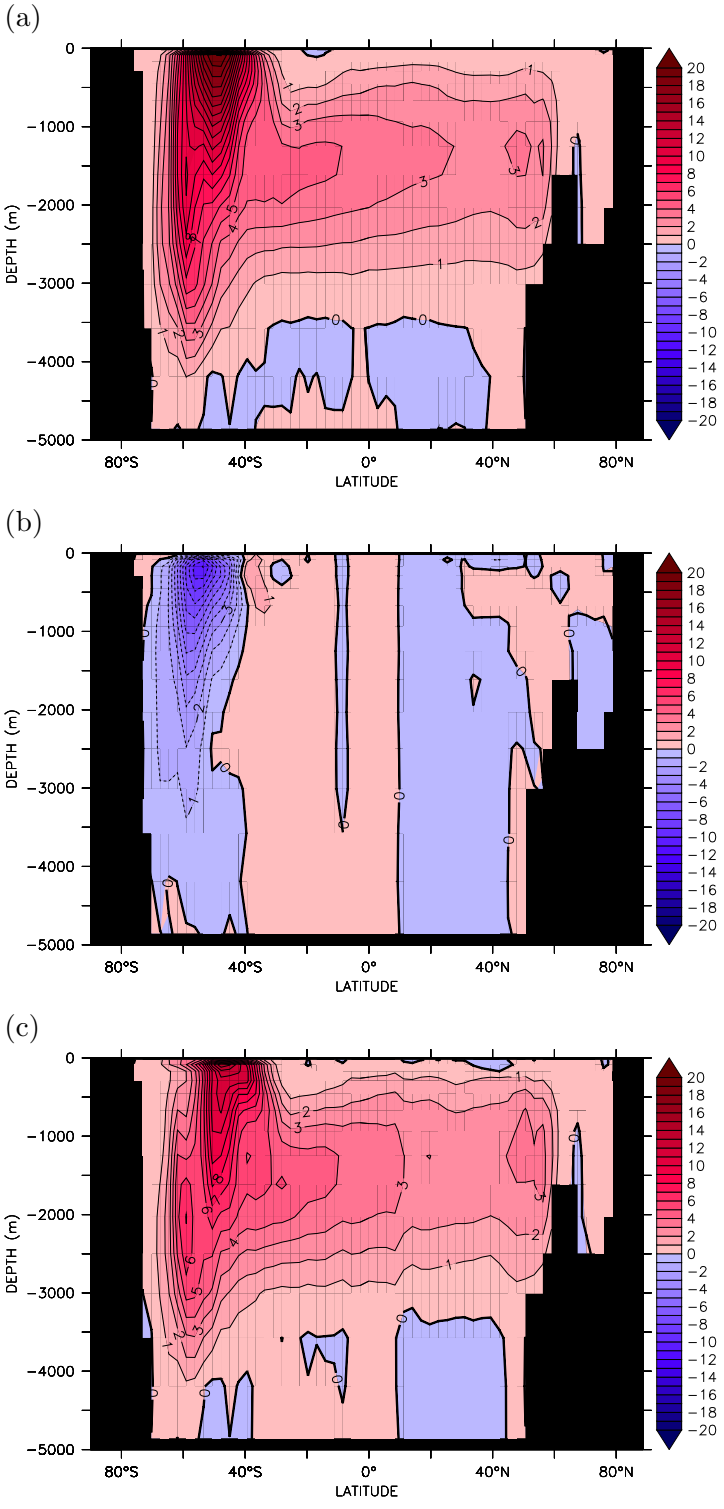

Figure 3.3: Equilibrium MITgcm output for the increased Southern Ocean wind stress perturbation (a) Zonal average Global meridional Eulerian-mean overturning stream function anomaly (Sv), (b) Zonal average meridional eddy overturning stream function anomaly (Sv) and (c) Zonal average Global meridional residual overturning stream function anomaly (Sv).

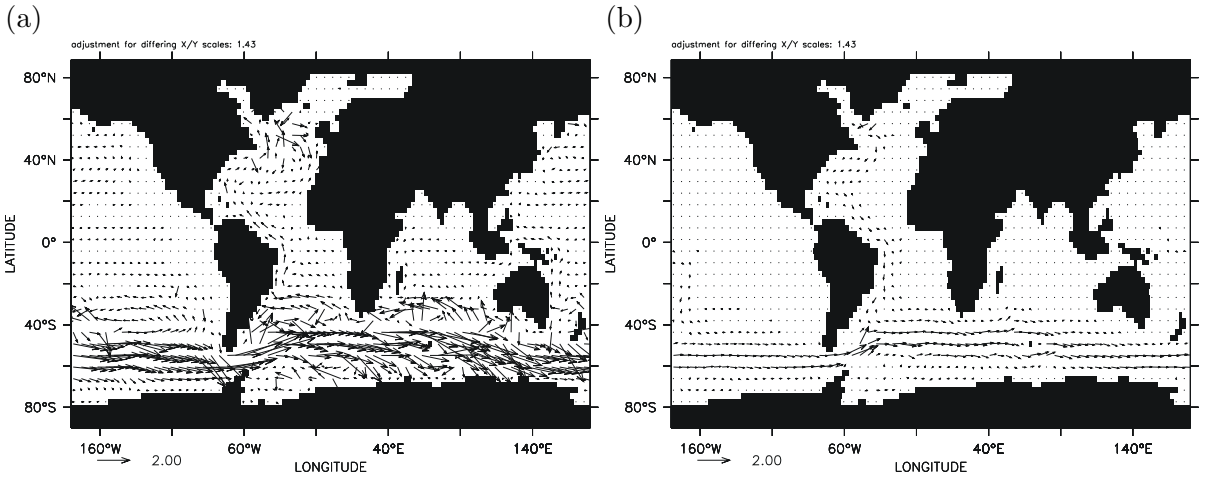

Figure 3.4: Equilibrium MITgcm output for the increased Southern Ocean wind stress perturbation. Residual velocity anomalies ($\mathrm{cm\,s^{-1}}$) (a) averaged over the surface 100 m and (b) at 2500 m depth.

the 0.6 Sv Eulerian-mean transport anomaly at 40°N in Figure 3.2, that then circulates anti-cyclonically in the region of 40–60°N, before sinking and flowing in an enhanced southward deep western boundary current at around 2500 m (Figure 3.4b). Figure 3.3a and Figure 3.3c also display a response in the Atlantic Meridional Overturning Circulation of 3.4 Sv exported south across 30°S. The velocity anomaly (Figure 3.4a) in the surface western boundary current in the southern Pacific slightly intensifies the North Pacific gyre accounting for the remainder of the northward Eulerian flow anomaly in Figure 3.2 with the signal recirculating anti-cyclonically but with little change in deep north Pacific currents. Changes to the barotropic streamfunction are dominated by an increase of 56.1 Sv transport through Drake Passage and 5–15 Sv enhancement of the adjacent subtropical gyres. *McDermott* [1996] describes the initialisation and establishment of this circulation pattern in his transient, spin up, simulations of a Southern Hemisphere wind stress perturbation as the excitement of Kelvin-like baroclinic waves by enhanced barotropic streamfuction after 40 days to 400 days that propagate northwards along the western boundary and are deflected east at the Equator. At the eastern boundary, energy is both directed northward as boundary Kelvin modes and westward as Rossby modes, which become trapped at the western boundary and act to enhance the surface western boundary current. Depression of isopycnals as the waves advance is halted in the North Atlantic where homogenisation of the water column by deep convection offers a "path of least resistance" between the upper and deep ocean, which is maintained by surface buoyancy forcing, enhancing pre-existing sinking in this region. Figure 3.4 shows near equilibrium velocity anomaly where the flow is concentrated at

the western boundary, although signs of surface westerly motion remain at the equator.

Global mean potential temperature increases by 0.37 °C due to more rapid exchange between the surface and deep ocean via the deeper Southern Ocean (~60 m) and North Atlantic (~40 m) mixed layers. In the Atlantic Ocean, temperature increases between 500–3000 m depth by 0.25–0.5 °C (Figure 3.5a) and 0.25–0.75 °C in the Indian and Pacific (Figure 3.5c and e), with the largest anomaly at a latitude of 40°S and 1000 m depth. It is interesting to note that this is in the same region as the kink in Figure 3.3c at 500–1000 m crossing 40°S associated with enhanced eddy activity, which brings warmer waters further south in this region (Figure 3.3b). This feature was also observed by *McDermott* [1996] and *Toggweiler and Samuels* [1995, 1998] that they called the "ageostrophic leakage" caused by increased friction as the ACC flows through Drake Passage. It accounts for 6–7 Sv of the Southern Ocean residual overturning circulation southward flow anomaly and as such plays a significant role in compensating the northward Ekman transport anomalies driven by the increased wind stress. South of 60°S is a slight cooling of around −0.25 °C.

Sea Surface Temperature (SST) anomalies (Figure 3.6a) mirror near-surface anomalies in the meridional sections. Generally there is divergence of surface heat transport south of 40°S due to enhanced northward Ekman transport with convergence at 40°S, particularly in the Indian and Pacific Oceans, leading to the banded effect observed. In the northern North Atlantic there is a large region of SST increase of 0.25 °C in the Labrador and Irminger Seas that is the signature of 45 TW increased poleward heat transport by the western boundary current, also suggested by the surface velocity anomaly (Figure 3.4a). In the northwest Pacific there is a small cooling and in the northeast Pacific there is a small warming that may also be associated with anomalous heat transport due to acceleration of the surface gyre. The sea surface temperature gradient across the ACC remains similar to the control due to more vigorous relaxation, which enables the colder water to cross mean isopycnals and travel northward in the Ekman layer, however, this relaxation also damps the SST response to the wind stress perturbation, such that the surface mean temperature anomaly is −0.5 m°C. The anomalies of surface heat forcing (Figure 3.6c) are dominated by anomalies in SST relaxation. Regions in the Southern Ocean that are warming are subject to a negative heat flux of 5–10 W m^{-2}, while the regions that are cooler are forced with a reduced heat loss (a positive anomaly) since the majority of the Southern Hemisphere is losing heat to the atmosphere. In the North Atlantic, in the region south of Greenland there is a cooling signal of approximately

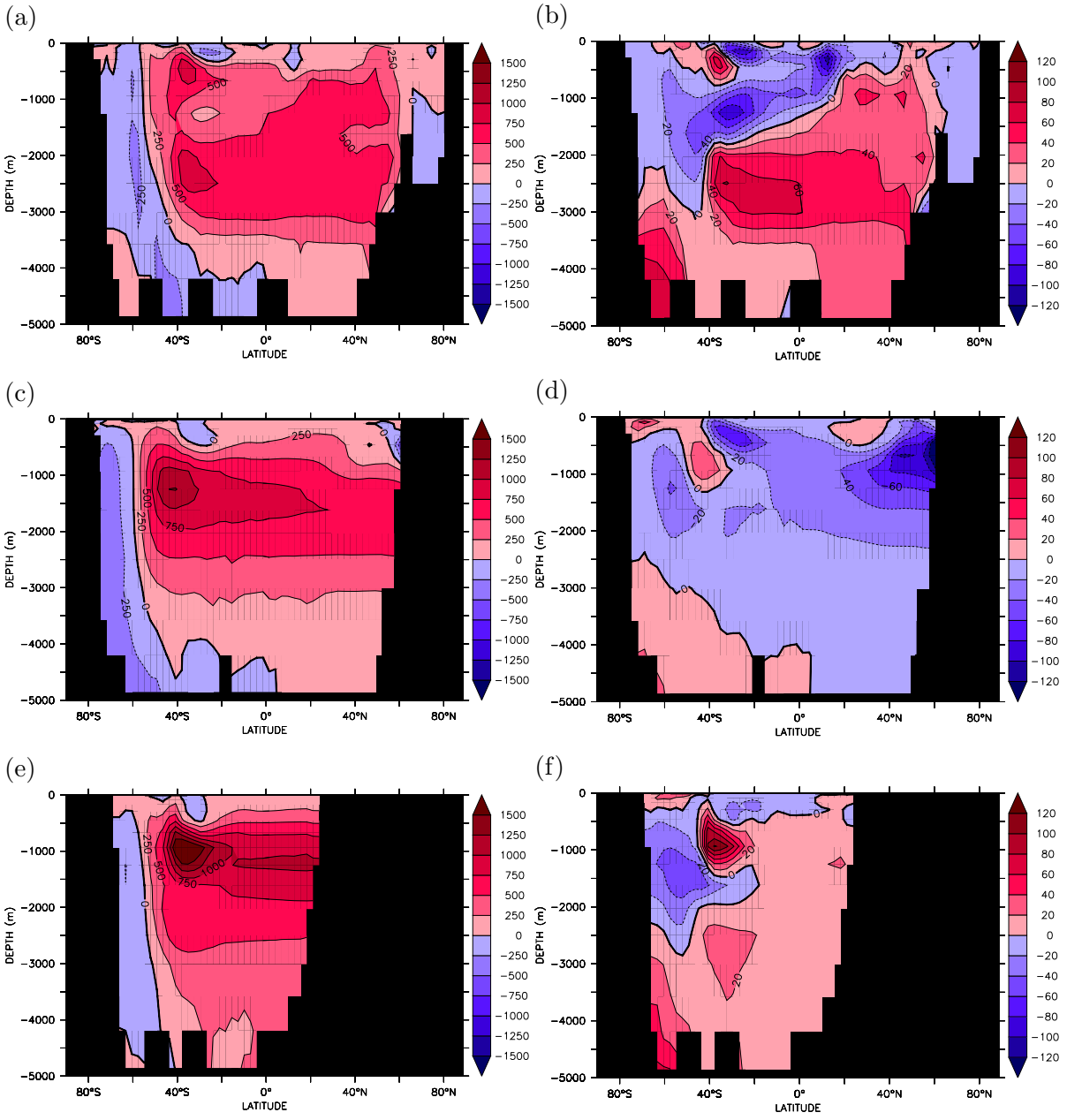

Figure 3.5: Equilibrium MITgcm output for the increased Southern Ocean wind stress perturbation. Zonal averages of Potential Temperature (m°C, left column) and Salinity ($\times 1 \times 10^{-3}$, right column) anomalies. (a) and (b) are in the Atlantic Ocean, (c) and (d) are in the Pacific Ocean, and (e) and (f) are in the Indian Ocean.

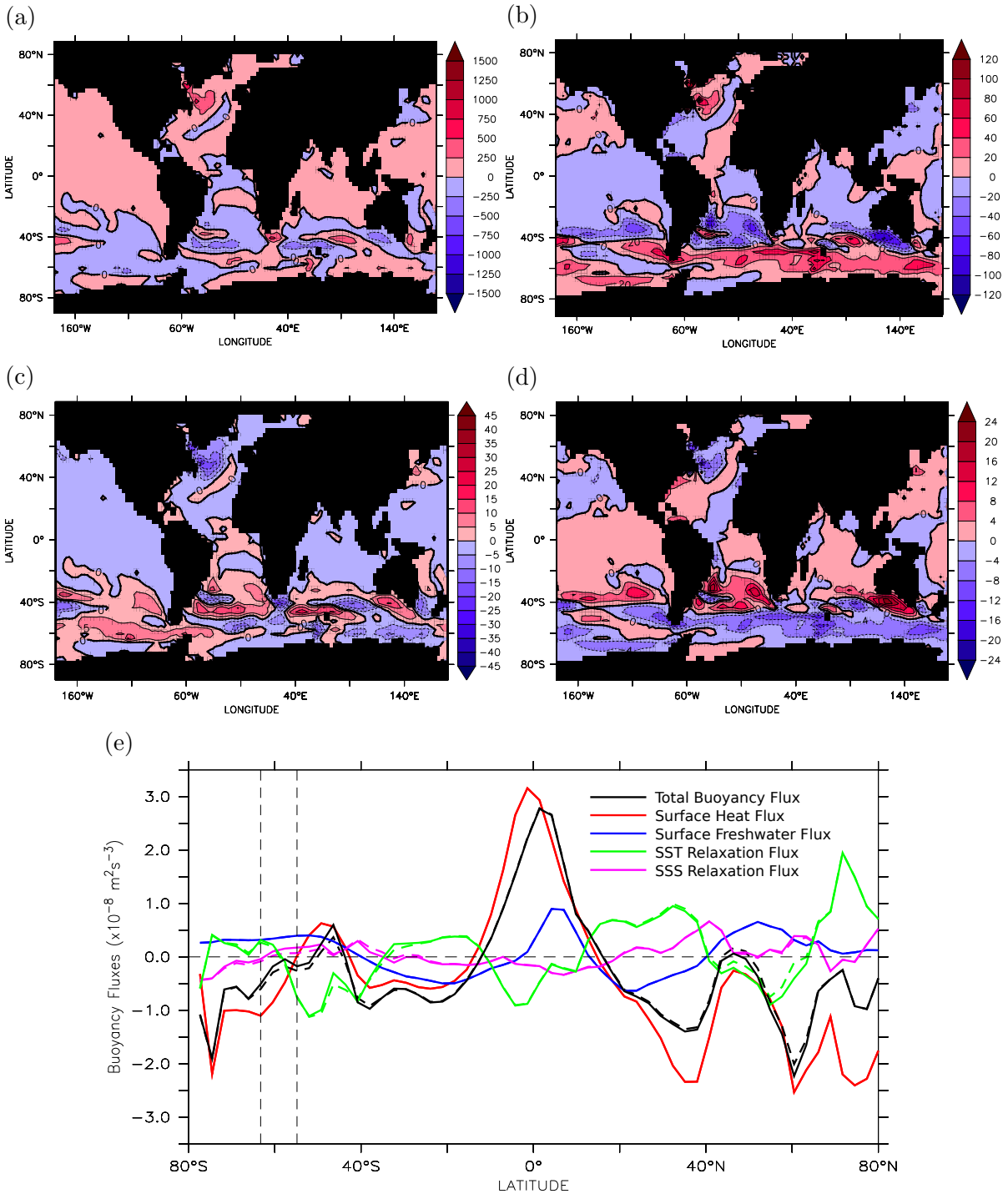

Figure 3.6: Equilibrium MITgcm output for the increased Southern Ocean wind stress perturbation. (a) Sea Surface Temperature anomaly (m°C) and (b) Sea Surface Salinity anomaly (mpsu), (c) Surface Heat Forcing anomaly ($\mathrm{W\,m^{-2}}$, positive values represent oceanic heat input), (d) Surface Salinity Forcing anomaly ($\mathrm{kg\,m^{-2}\,yr^{-1}}$, positive values represent oceanic salinity input or freshwater loss) and (e) zonal average surface buoyancy flux ($\mathrm{m^2\,s^{-3}}$) and its components (see Section 6.1 and Equation 6.2) for the perturbed (solid) and control (dashed) states. Positive values indicate a gain of buoyancy (an increase in heat or freshwater/reduced salinity) while negative values indicate buoyancy loss (reduced heat or freshwater/increased salinity). Dashed vertical lines denote the position of the unblocked latitudes at Drake Passage.

$10\,\mathrm{W\,m^{-2}}$, which again points to increased northward heat transport there. Similarly, positive relaxation in the northwest Pacific suggests that this area is experiencing increased export of heat by advection in a slightly stronger gyre circulation.

Global mean Salinity decreases by 0.0037 and shows a complex spatial pattern with a decrease of ~0.02–0.04 around 40°S from the surface to 2500 m separated from a deep increase of 0.02–0.04 in the Atlantic and Indian Oceans by a sloping interface rising towards the surface at, or just north of, the Equator (Figure 3.5b and f). This is punctuated at 40°S, 1000 m depth by an increase of 0.02 which may be connected with surface salinification and northerly ageostropic currents, as with potential temperature. In the Pacific Ocean (Figure 3.5d) almost the entire Northern Hemisphere experiences a freshening, particularly concentrated at 1000 m depth north of 40°N. Again, this freshening is punctuated by salinification of the upper 500 m between 20°N and 40°N. The deep Southern Ocean also becomes more saline by 0.02–0.08 in all basins.

Sea Surface Salinity (SSS) anomalies (Figure 3.6b) reflect this distribution. In the South Atlantic, enhanced advection carries the relatively fresher southern waters north across the 34.25–34.50 isohalines, which are located at 40°S. Increased strength of the North Atlantic western boundary current carries a slightly increased volume of freshwater further north. As with SST, there is a SSS increase in the northern North Atlantic of 0.02, a small decrease of 0.01 in the northwest Pacific, and an increase of 0.01 in the northeast Pacific. Also, surface salinity relaxation damps the SSS response to the wind stress perturbation, such that the surface mean salinity anomaly is 2×10^{-6}. Sea surface salinity forcing (Figure 3.6d) is dominated by salinity relaxation which opposes the perturbations to the SSS field. There is an increase of freshwater input to the Southern Ocean (or rather a greater loss of salt) south of 40°S and an increase in freshwater output (or gain of salt) to the north of 40°S. This is also true of the North Atlantic to the south of Greenland and in the western boundary current.

Zonally-averaged surface buoyancy fluxes (Figure 3.6e) become increasingly positive in the Southern Ocean south of 40°S, mainly as a result of surface salinity relaxation, that supports greater northward advection of surface waters in the Ekman layer. However, in the Northern Hemisphere, slightly reduced buoyancy fluxes that are mainly due to negative surface temperature relaxation in the North Atlantic (Figure 3.6c) support enhanced Atlantic meridional overturning circulation by damping the signal of increased northward heat transport that would otherwise have a stabilising effect [*Rahmstorf and England*, 1997].

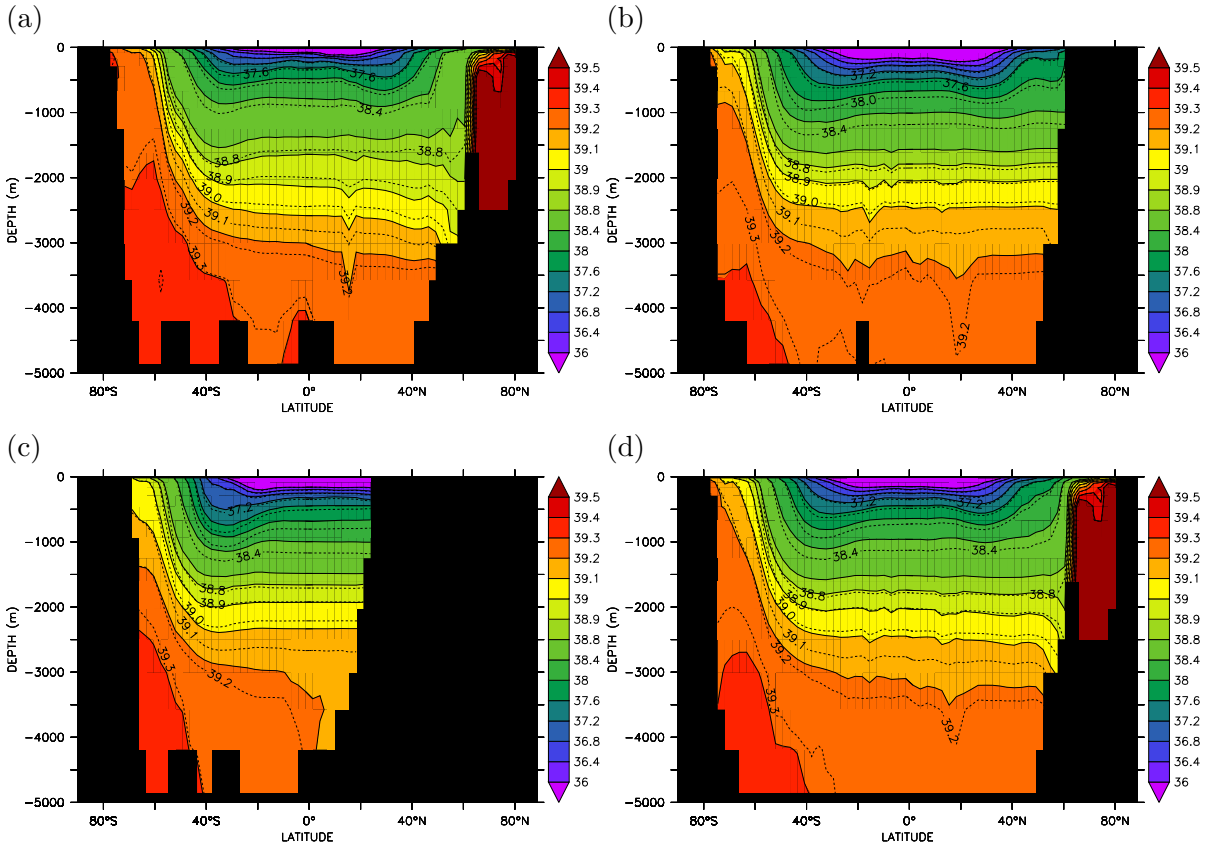

Figure 3.7: Equilibrium MITgcm output for the increased Southern Ocean wind stress perturbation. Coloured fill and solid contours are Control Run zonally averaged density ($\sigma_{2.5}$, $\mathrm{kg\,m^{-3}}$) with enhanced wind stress perturbation density overlay in dashed contours in the (a) Atlantic, (b) Pacific and (c) Indian Oceans, and (d) the Global average.

3.1.2 Adjustment of the oceanic density field

Subsequent changes in the density field are shown in Figure 3.7. The general pattern of shoaling isopycnals south of 60°S, depressed isopycnals further north and increased isopycnal gradient between is consistent with enhancement of the Southern Ocean overturning and eddy circulations. Indeed the greatest change in density occurs centred at 40°S between 500 m and 2000 m depth at the boundary between the ACC and Southern Hemisphere subtropical gyre where the isopycnals have descended between 200–300 m. The mid-depth decrease in density is driven primarily by an increase in heat content while salinity drives the increase in density in the deep Southern Ocean and modulates upper-ocean variation, particularly in the South Atlantic where an increase in salinity at around 2000–2500 m offsets an increase in temperature, while higher in the water

column, lower salinity acts to enhance the density decrease by 50%. When potential temperature and salinity are simply, linearly scaled by typical coefficients of thermal expansion ($\alpha = 2 \times 10^{-4}\,\mathrm{K}^{-1}$) and saline contraction ($\beta = 7.4 \times 10^{-4}$), respectively, it becomes clear that the dominating effect is due to change in global heat content ($\overline{\alpha\Theta}' = 7.4 \times 10^{-5}$) rather than salt content ($\overline{\beta S}' = -2.8 \times 10^{-6}$) by almost two orders of magnitude although salinity plays a more important role in the Atlantic Ocean. As a result of these changes to density structure within the ocean, stratification ($\partial\rho/\partial z$) decreases in the upper ~1000–1500 m and increases slightly in the deep ocean below ~1000–1500 m (Figure 3.8).

These perturbations to the physical environment can be interpreted in the framework of a simple theory of the oceanic pycnocline after *Gnanadesikan* [1999]. A change in water mass transformation rate induced by changes in wind stress via Ekman transport, particularly the formation of Antarctic Intermediate Water (AAIW) and Subantarctic Mode Waters (SAMW) from upwelled Circumpolar Deep Water (CDW), alters the depth of the low-latitude pycnocline (*Gnanadesikan and Hallberg* [2000] defines this as the $\sigma_0 = 27.4\,\mathrm{kg\,m^{-3}}$ isopycnal, which is roughtly equivalent to the $\sigma_{2.5} = 38.8\,\mathrm{kg\,m^{-3}}$ isopycnal in Figure 3.7) from a mean position of −1428 m in the control to −1656 m. This perturbs the north-south density gradient, necessitating the Northern Hemisphere overturning rate to respond by converting an equivalent volume of thermocline water to dense water [*Gnanadesikan and Hallberg*, 2000]. This is especially the case for scenarios with low vertical diffusivity, which inhibits the direct upwelling of dense waters into the tropical thermocline [*Gnanadesikan*, 1999] but also because low latitude upwelling is inversely proportional to pycnocline depth [*Levermann and Fürst*, 2010]. Furthermore, the increased volume of North Atlantic Deep Water (NADW) occurs at the expense of Antarctic Bottom Water (AABW) [*McDermott*, 1996] causing the two-level temperature anomaly in the Atlantic Ocean (Figure 3.5a). The response of Southern Ocean eddy transport can also be related to the pycnocline perturbation, with increasingly negative overturning with greater pycnocline depth due to the increase in potential energy of the more steeply sloping isopycnals [*Levermann and Fürst*, 2010]. Changes in ACC transport can also be linked to the depression of isopycnals because deep ocean temperatures to the north of the ACC warm, whereas deep temperatures to the south remain relatively unchanged, which alters the meridional density gradient and ACC transport is enhanced due to the increased deep thermal wind shear [*Gnanadesikan and Hallberg*, 2000].

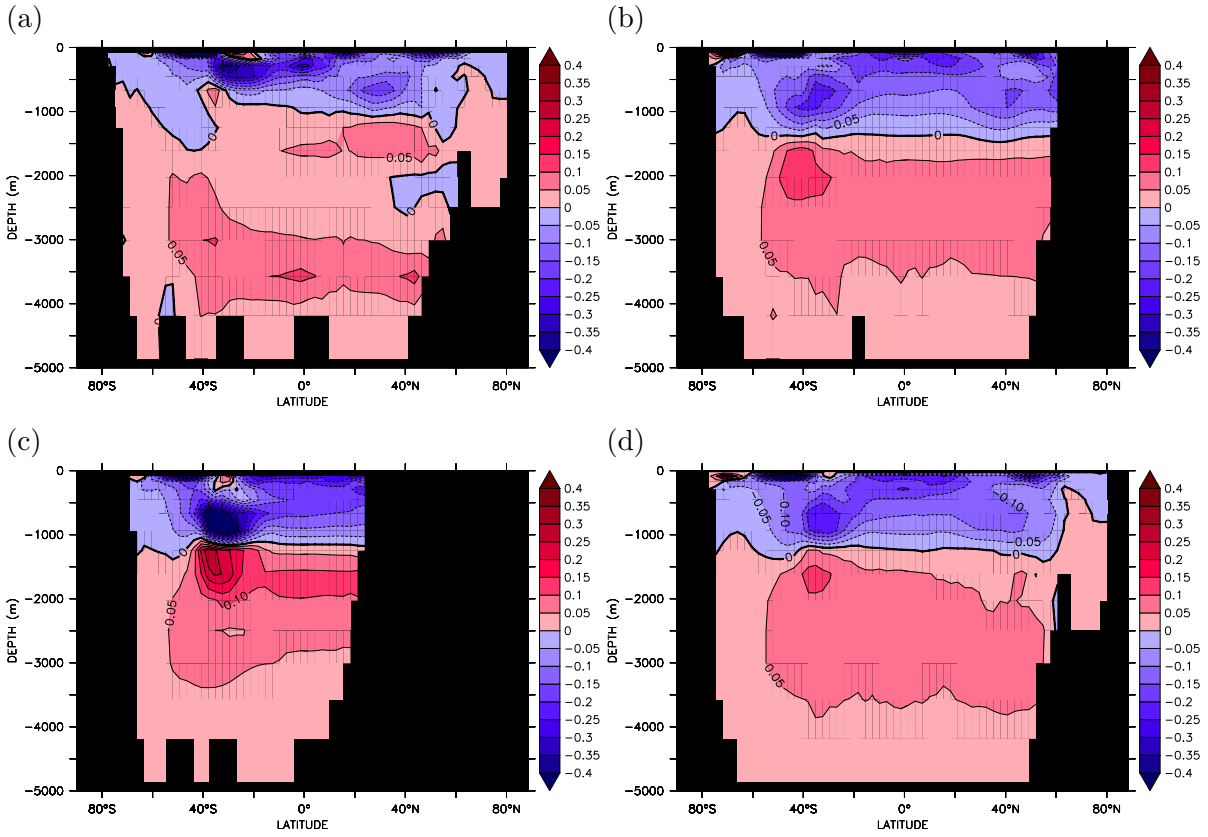

Figure 3.8: Equilibrium MITgcm output for the increased Southern Ocean wind stress perturbation. Zonally averaged stratification anomalies ($\partial\rho/\partial z$, $\mathrm{g\,m^{-4}}$) for the (a) Atlantic, (b) Pacific, (c) Indian and (d) Global Oceans.

It is enlightening to consider the anomalies created by this perturbation taken after first converting the data from depth coordinates to density coordinates in order to remove the obscuring effect of the change in depth, or heave, of isopycnals (Figure 3.9). For comparison with previous sections, these anomalies have been recast onto a depth axis by processing the pressure field in the same way to obtain the average depth of each isopycnal at a particular latitude and then using this information to regrid the anomaly calculated on isopycnal surfaces back to depth coordinates. It is possible for this averaging to alter the details of the maximum and minimum depth of the water column and further changes may result from density anomalies of the deepest/shallowest waters causing unpaired values between the perturbed and control fields and these values flagged as missing. Furthermore, potential temperature and salinity have been simply, linearly scaled by typical coefficients of thermal expansion and saline contraction, ($\alpha = 2 \times 10^{-4}\,\mathrm{K^{-1}}$ and $\beta = 7.4 \times 10^{-4}\,\mathrm{psu^{-1}}$), in order to aid comparison of the two fields. The remaining (dimensionless) anomalies in potential temperature and salinity are the result

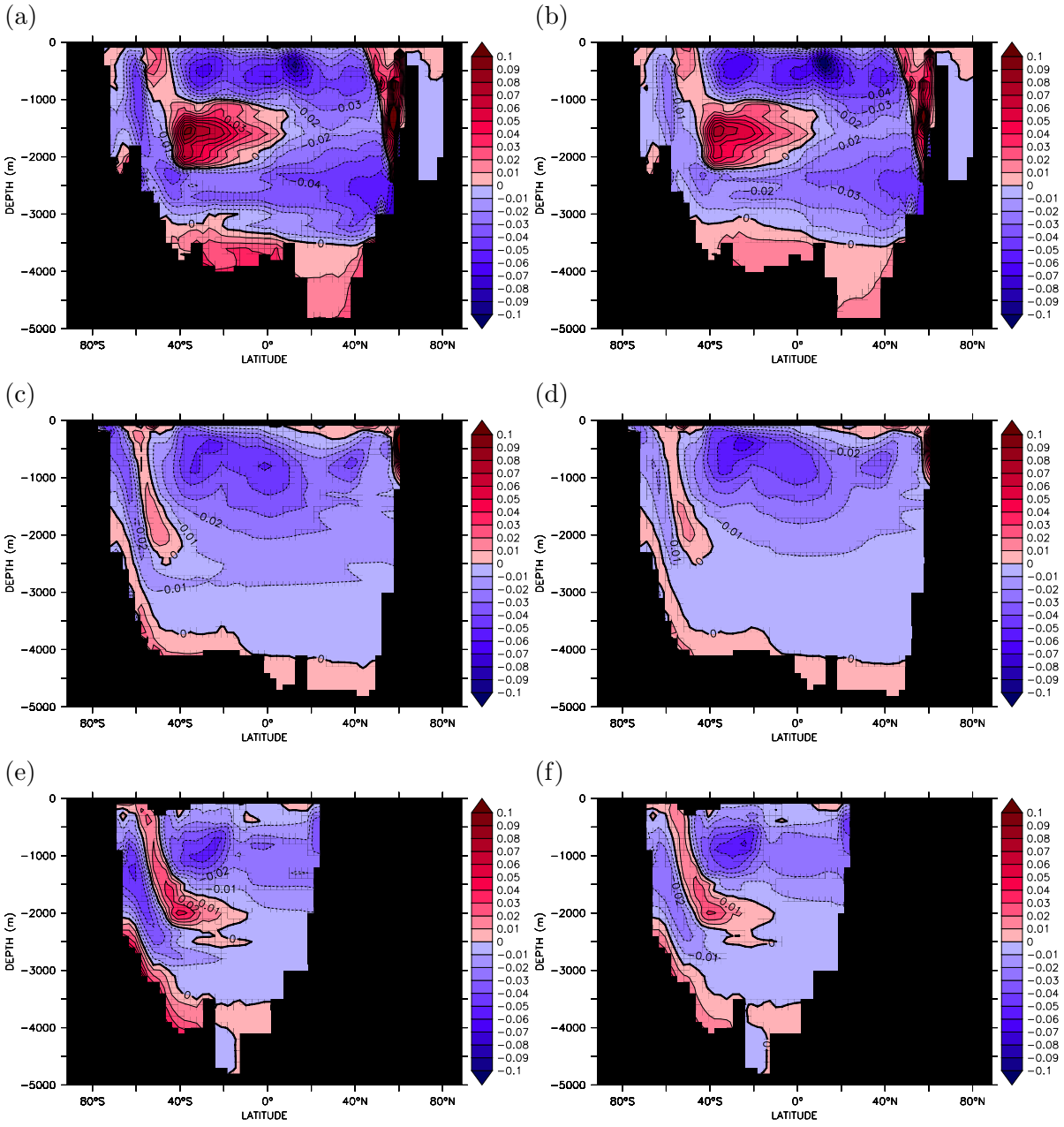

Figure 3.9: Equilibrium MITgcm output for the increased Southern Ocean wind stress perturbation. Zonal averages of Potential Temperature (left column) and Salinity (right column) taken after first converting to density coordinates, then regridding back into depth coordinates and linearly scaling by their typical expansion/contraction coefficients ($\alpha = 2 \times 10^{-4}\,\mathrm{K}^{-1}$ and $\beta = 7.4 \times 10^{-4}$) multiplied by 1000. (a) and (b) are in the Atlantic Ocean, (c) and (d) are in the Pacific Ocean, and (e) and (f) are in the Indian Ocean.

(a)

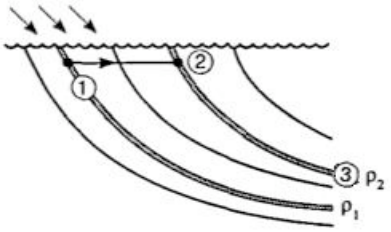

(b)

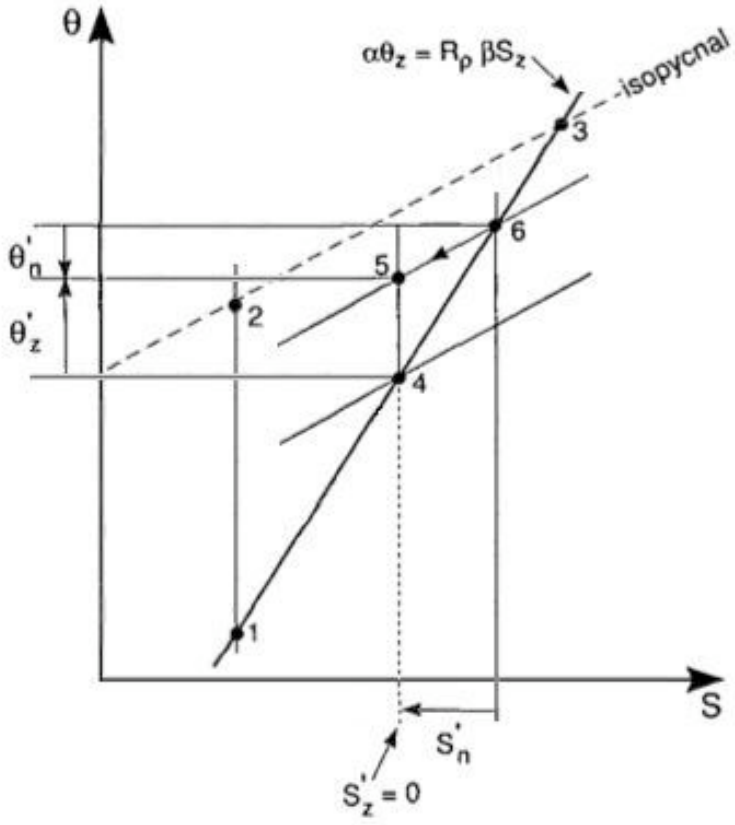

Figure 3.10: (a) An increase in surface heat flux (at constant salinity) reduces the density of surface water (parcel 1) such that it is now subducted along a lower density surface than in the control ($\rho_2 < \rho_1$). These warmer waters (parcel 2) enter the interior ocean at the same density as parcel 3. (b) The volume averaged properties before and after the anomalous heating lie at points 4 and 5 on a Θ-S diagram; the salinity remains constant, however the heat content has increased. Furthermore, the original density class is reduced in volume, while the lower density class increases in volume, therefore the density surfaces within the range, ρ_1–ρ_2, are shifted downwards while those outside the range are unaffected. Compared on depth surfaces (parcels 4 and 5) there is no change in salinity ($S'_z = 0$) and an increase in potential temperature ($\Theta'_z > 0$), whereas on constant density surfaces (parcels 5 and 6) the modified water mass appears *cooler* ($\Theta'_n < 0$) and *fresher* ($S'_n < 0$) than previously. This holds for values of the Stability ratio, R_ρ, greater than one [adapted from *Bindoff and McDougall*, 1994].

of the anomalies in SST and SSS being injected into the ocean interior by water mass formation or transformation. Both variables in Figure 3.9 are mostly compensating, although the anomalies of $\alpha\Theta$ are perhaps slightly larger than those of βS but this is likely a consequence of the zonal averaging process and the linear scaling of Potential Temperature and Salinity in this way since the actual equation of state in the model is non-linear.

Care is needed in the interpretation of Θ-S anomalies on isopycnal surfaces as the conclusions can be somewhat counterintuitive. Under a "pure warming" scenario in surface forcing with no change in salinity (see Figure 3.10), it is possible to generate *cool* and *fresh* anomalies along isopycnal surfaces [*Bindoff and Church*, 1992; *Bindoff and McDougall*, 1994; *Church et al.*, 1991]: (1) An increase in surface heat flux (at constant salinity) reduces the density of surface water (parcel 1, Figure 3.10a) such that it is now subducted along a lower density surface (parcel 2) than in the control. (2) These warmer waters enter the interior ocean at the same density as parcel 3. (3) The volume averaged properties between ρ_1 and ρ_2 before and after the anomalous heating lie at points 4 and 5 on a Θ-S diagram (Figure 3.10b) — salinity remains constant, however the heat content has increased. (4) Also, the original density class is reduced in volume, while the new, lower density class increases in volume, therefore the density surfaces within the density range, ρ_1 to ρ_2, are shifted downwards while those outside the range are unaffected. (5) Compared on constant depth surfaces (parcels 4 and 5 on Figure 3.10b) there is no change in salinity ($S'_z = 0$) and an increase in potential temperature ($\Theta'_z > 0$) of the modified water mass, as expected from the surface forcing. (6) Compared along isopycnal surfaces (parcels 5 and 6) the modified (warmer) water mass appears *cooler* ($\Theta'_n < 0$) and *fresher* ($S'_n < 0$) than previously. The same is true for a "pure freshening" scenario whereby, following similar reasoning as above, it is possible to observe *cool* and fresh anomalies along isopycnal surfaces. A caveat of this is that the stability ratio, R_ρ, that is the ratio of the vertical gradients of potential temperature and salinity multiplied by their expansion/contration coefficients (see Figure 3.10b), must be larger than one, however, for other values the same process applies but the sense of the change is altered [*Bindoff and McDougall*, 1994].

In the deep North Atlantic where the stability ratio is greater than unity and the density of the surface waters off the southern tip of Greenland decreases (by 20–30 $\mathrm{g\,m^{-3}}$ on average, Figure 3.11) as a result of the competing effects of increased SST and SSS in that region (Figure 3.6a and b), cooler and fresher anomalies than in the control when compared on density surfaces (Figure 3.9a and b) are consistent with "pure warming"

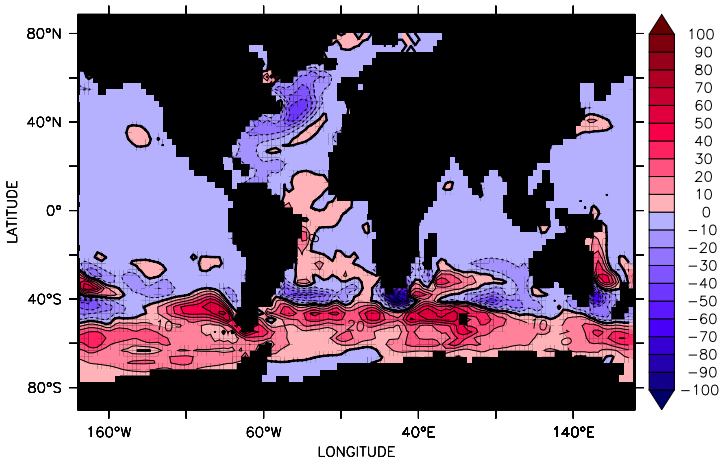

Figure 3.11: Equilibrium MITgcm output for the increased Southern Ocean wind stress perturbation. Sea surface density anomaly (g/m^3).

of the surface waters by the excess, uncompensated, anomalous SST leading to a slight decrease in density of the NADW formed in this region. These warmer waters may also be seen upwelling at roughly 60°S in all three basins as colder, fresher CDW. Another coherent feature in all three basins is the freshening and cooling in the upper 1000 to 1500 m. R_ρ is greater than one in this region and surface density to the north of 40°S generally shows a decrease (Figure 3.11) as the result of partial compensation between sea surface cooling (Figure 3.6a) and freshening (Figure 3.6b). This may be therefore be attributed to "pure freshening" of SAMW and the lower thermocline waters, as the subduction of fresher SAMW along lighter isopycnal surfaces leads to a cool and fresh anomaly when compared to the control along isopycnals [*Bindoff and McDougall*, 1994].

The warm saline anomaly in the Southern Hemisphere that is particularly obvious in the Atlantic sections, centred at ~1500 m (Figure 3.9a and b) may be attributed to a change in AAIW properties. Here, in the mid-depth salinity minimum, R_ρ is less than zero so the anomalies along isopycnals are related to the surface forcing anomalies in a different manner [*Bindoff and McDougall*, 1994]. Warm and saline anomalies in density coordinates are consistent with "pure salinification", which is possible given the coincidence of incompletely compensating warm SST and salty SSS anomalies in a region in the Atlantic Sector at about 50°S causing sea surface density to increase (Figure 3.11). Similar regions of increased SST and SSS also occur in the Pacific and Indian Sectors between 40°S and 60°S, although their longitudinal extent is not as significant and they are partially compensated in the zonal mean by regions of Southern Ocean density decrease (Figure 3.11). However, a similar feature is present in the Pacific and Indian Ocean sections (Figure 3.9c to f) at the same depth as in the Atlantic sections. Finally,

there is a warm, salty anomaly in the densest waters in the Southern Ocean around 2500–3000 m depth between 40–60°S. Surface density is largely unchanged in the Weddell Sea (Figure 3.11) but density increases in the Amundsen and Ross Sea's as a result of incomplete compensation between increased SST and SSS. Since the stability ratio in the deep ocean is positive, the leading explanation for these anomalies is "pure salinification" of AABW, the increase of AABW salinity due to surface forcing and increased freshwater divergence leading to warmer, saltier anomalies on isopycnal surfaces.

3.1.3 Distribution of biogeochemical tracers and primary productivity

Alteration of the physical circulation drives the redistribution of passive tracers leading to adjustment of the partitioning between oceanic and atmospheric carbon sinks through changes in the air-sea flux of carbon and biological productivity. Nutrient supply to the surface layer is particularly influenced by vertical velocity at the base of the mixed layer [*Ito et al.*, 2005]. The wind-dominated Eulerian-mean vertical velocity (Figure 3.12a) shows a largely consistent zonal structure with upwelling primarily south of 45°S and downwelling to the north that is intensified by enhanced Southern Ocean wind stress (Figure 3.12b) as shown previously (Figure 3.3a). Mesoscale eddy vertical velocity (Figure 3.12c) shows a similar pattern with downwelling generally south of 45°S and upwelling to the north, which also intensifies (Figure 3.12d) with increased wind stress (Figure 3.3b).

However, despite the smooth appearance of the residual overturning streamfunction (Figure 3.3c), the superposition of the eddy and Eulerian-mean components creates a complex system of upwelling and downwelling residual vertical velocity (Figure 3.12e) with significant zonal variation that is intimately coupled to air-sea buoyancy fluxes [*Karsten and Marshall*, 2002; *Marshall*, 1997]. Indeed, there are regions where, instead of opposing each other as suggested in Figure 3.3, the eddy and wind-driven circulations act in the same direction, such as in the Atlantic Sector between 45–60°S. Furthermore, the maximum positive anomaly (increased upwelling, Figure 3.12f) in the residual vertical velocity occurs in a band near 45°S in the Indian Ocean and is driven by eddy bolus velocity in a region where the Eulerian-mean velocity suggests there should be downwelling, while south of 45°S enhanced upwelling is generally directly associated with greater Eulerian-mean vertical velocity. As hinted at in Figure 3.3b the eddy upwelling

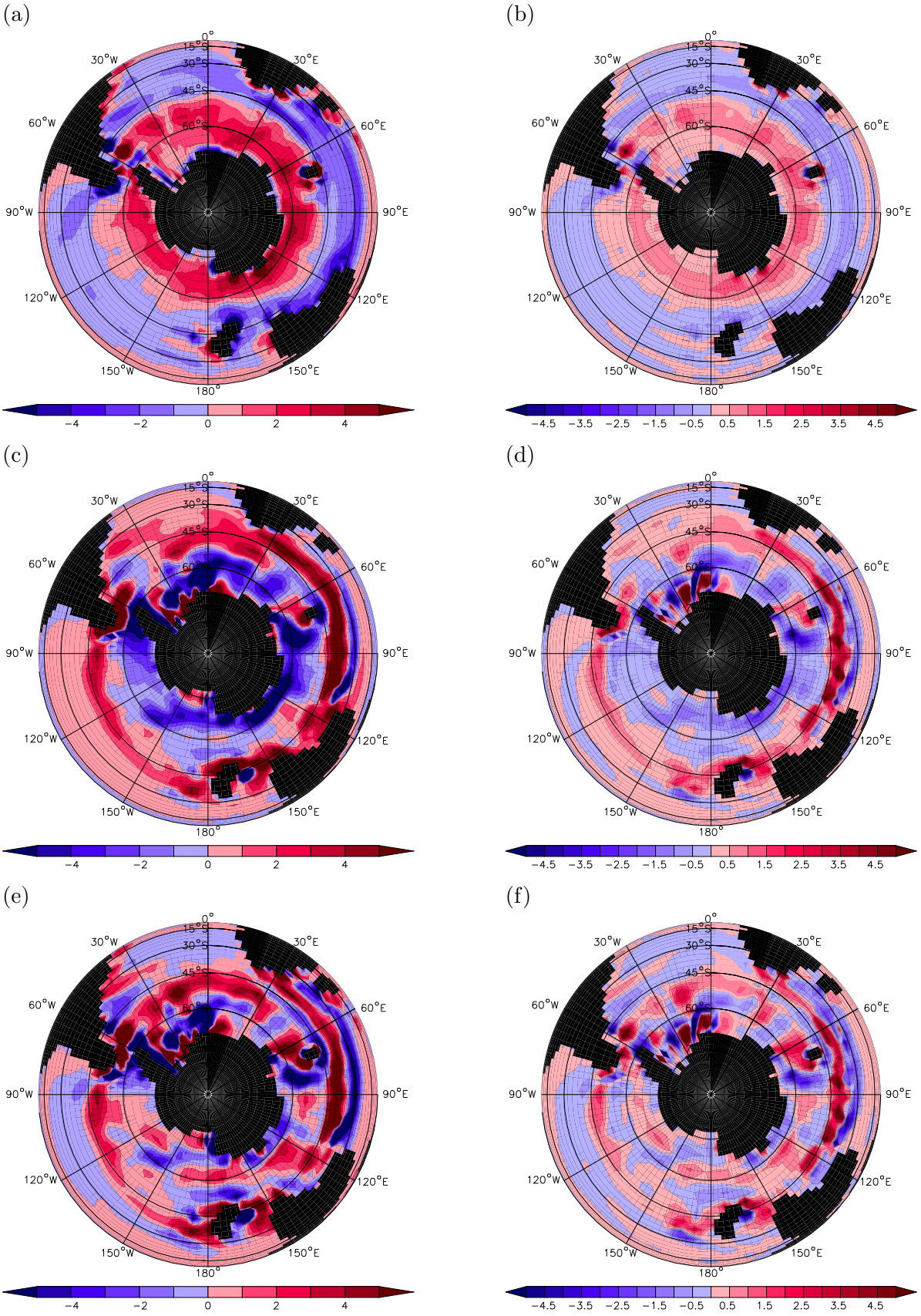

Figure 3.12: Equilibrium MITgcm output for the increased Southern Ocean wind stress perturbation. (a) Vertical Eulerian-mean, (c) eddy and (e) residual velocities $1 \times 10^{-6}\,\mathrm{m\,s^{-1}}$ and their anomalies (b, d and f, respectively) at the base of the mixed layer (~290 m).

north of 45°S comes from a much shallower level (~1000 m) than that of the Eulerian-mean upwelling and therefore is likely to have a much lower effect on the quantity of carbon upwelled to the surface from the deep ocean.

Nevertheless, the resultant pattern of increased net upwelling in the Southern Ocean, with some regions of enhanced downwelling, tends to carry carbon and nutrients to the sea surface causing positive DIC and phosphate anomalies (Figure 3.13). Transient anomalies at an early stage in the perturbation (Figure 3.13a, c and e) reflect the broad pattern of vertical velocity and further illustrate that it is the Southern Ocean that is the geographical source of the equilibrium anomaly in carbon and nutrients (instead of elsewhere on the globe) which then influences biogeochemical processes throughout the global ocean. Also noticeable in Figure 3.13b and Figure 3.13d is the difference in the surface concentrations of macronutrients in the Southern and Atlantic Oceans and the Indian and Pacific Oceans.

Increased wind-driven northward Ekman transport in the Southern Ocean supplies the adjacent gyres in the Atlantic and Pacific Oceans with nutrients and carbon. Furthermore, the Atlantic basin's nutrient supply is controlled by the volume of northward residual flow [*Dutkiewicz et al.*, 2005a; *Williams and Follows*, 1998] and by nutrient supply from regions of intermediate and mode water formation [*Sarmiento et al.*, 2004], which both increase, in order to replace nutrients exported from the basin by enhanced NADW flow (Figure 3.3a). Therefore, more intense overturning enhances nutrient and carbon delivery into the Atlantic that is either distributed along the length of the basin in the enhanced western boundary current system at the surface (Figure 3.4a) or upwelled into the subtropical gyres from within the thermocline. The Indian and Pacific basins on the other hand are supplied with nutrients by the inflow and upwelling of deep/bottom waters [*Parekh et al.*, 2006b], which under enhanced residual overturning is diverted to supply the enhanced upwelling demand in the Southern Ocean driven by the increased wind stress [*McDermott*, 1996], therefore leading to reduced supply of nutrients. This can also be viewed from a conservation perspective: Since phosphate has no external sources or sinks in this model, the enhanced concentration of nutrients to the Atlantic must be countered by a reduction in concentration elsewhere, that is in the Indo-Pacific basins.

The general small decrease of the surface iron (Fe) concentration with increased upwelling in the Southern Ocean compared to the control ($-6.5\,\mathrm{nmol\,Fe\,m^{-3}}$ at 20010 years to $-3.5\,\mathrm{nmol\,Fe\,m^{-3}}$ at 25000 years south of 40°S) is somewhat surprising given

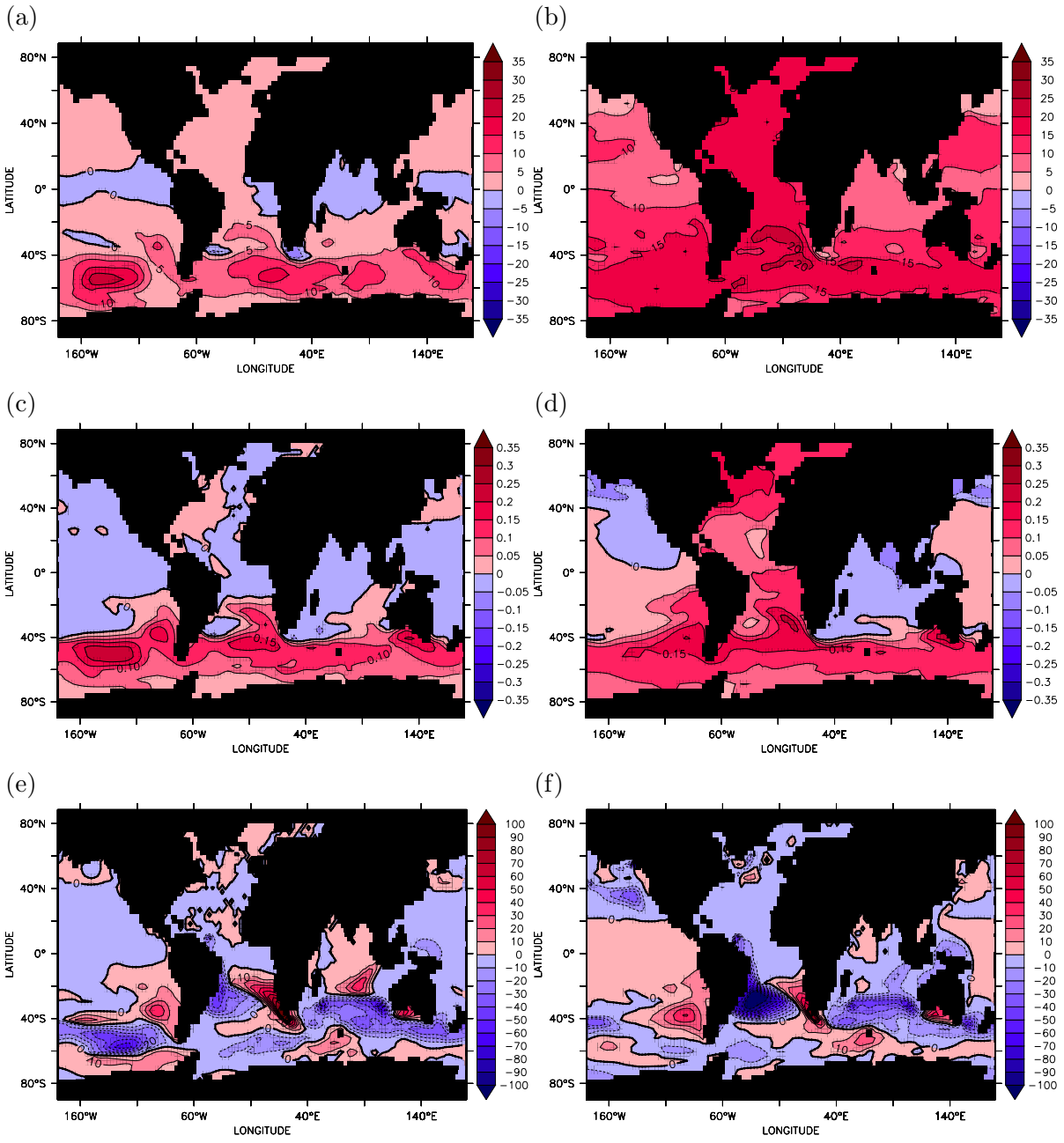

Figure 3.13: Equilibrium MITgcm output for the increased Southern Ocean wind stress perturbation. Sea surface tracer anomalies near the begining of the perturbation run after 10 years (left column) and near equilibrium after 5000 years (right column) for (a) and (b) dissolved inorganic carbon (mmol C m^{-3}), (c) and (d) phosphate (mmol P m^{-3}) and (e) and (f) dissolved iron (nmol Fe m^{-3}).

current conjecture from data [*Meskhidze et al.*, 2007] and models [*Bopp et al.*, 2003; *Dutkiewicz et al.*, 2005a; *Parekh et al.*, 2005, 2006b] that emphasises the importance of Fe contained in upwelling waters compared to aeolian inputs in the global and Southern Oceans [40–70% and 83% respectively, *Parekh et al.*, 2005]. The decoupling of macro- and micronutrients in the ocean interior was discussed in Chapter 2.2 and by *Parekh et al.* [2005]. With aeolian deposition and the rate of scavenging constant, as is the case with these perturbations, enhanced upwelling of "micronutrient depleted, macronutrient enriched" waters should inevitably lead to a reduction in supply of iron to the surface, a decrease in surface concentrations of dissolved iron and exacerbation of Fe limitation in this region.

Vertical sections of carbon and nutrient anomalies, both in the Atlantic and Indo-Pacific Oceans, provide further evidence for the interpretation of differing behaviour between macro- and micronutrients and between basins, representing alternative nutrient budgets (Figure 3.14). Carbon and phosphate concentrations are elevated in the Southern Ocean, particularly south of 60°S, due to increased upwelling and are supplied to the surface where they are advected north along the entire length of the Atlantic basin (Figure 3.14a and c) and returned to the deep ocean by NADW formation. In the Indo-Pacific (Figure 3.14b and d), on the other hand, these tracers are advected into the subtropical Southern Hemisphere by the gyre circulation but, apart from DIC that is also affected by increasing atmospheric carbon content, do not cross the equator to produce large anomalies in the Northern Hemisphere. At mid-depths, the concentration of DIC and phosphate both decrease possibly explaining why nutrient supply to the surface is slightly reduced when these waters are upwelled. Interestingly, deep North Pacific concentrations actually increase slightly, which suggests that reduction of the AABW circulation cell reduces the ventilation rate of these waters, leaving them more isolated and able to store a greater volume of carbon and nutrients. Also, the increased volume occupied by intermediate and mode waters in the upper/mid-depth ocean displaces the nutrient concentration maximum at ~1500–2000 m downwards and exaggerates the magnitude of the anomaly. Dissolved iron (Figure 3.14e and e), in contrast, is reduced in the majority of the Southern Ocean and at the surface of most of the Southern Hemisphere due to enhanced upwelling of scavenged, Fe depleted, waters with low surface aeolian iron inputs, consistent with the surface concentrations in Figure 3.13e and f. In the North Atlantic, where dust deposition is naturally higher, the enhanced overturning circulation carries this signal further into the ocean interior before it is eroded by scavenging. Expansion of the NADW circulation cell, however, also acts to depress this

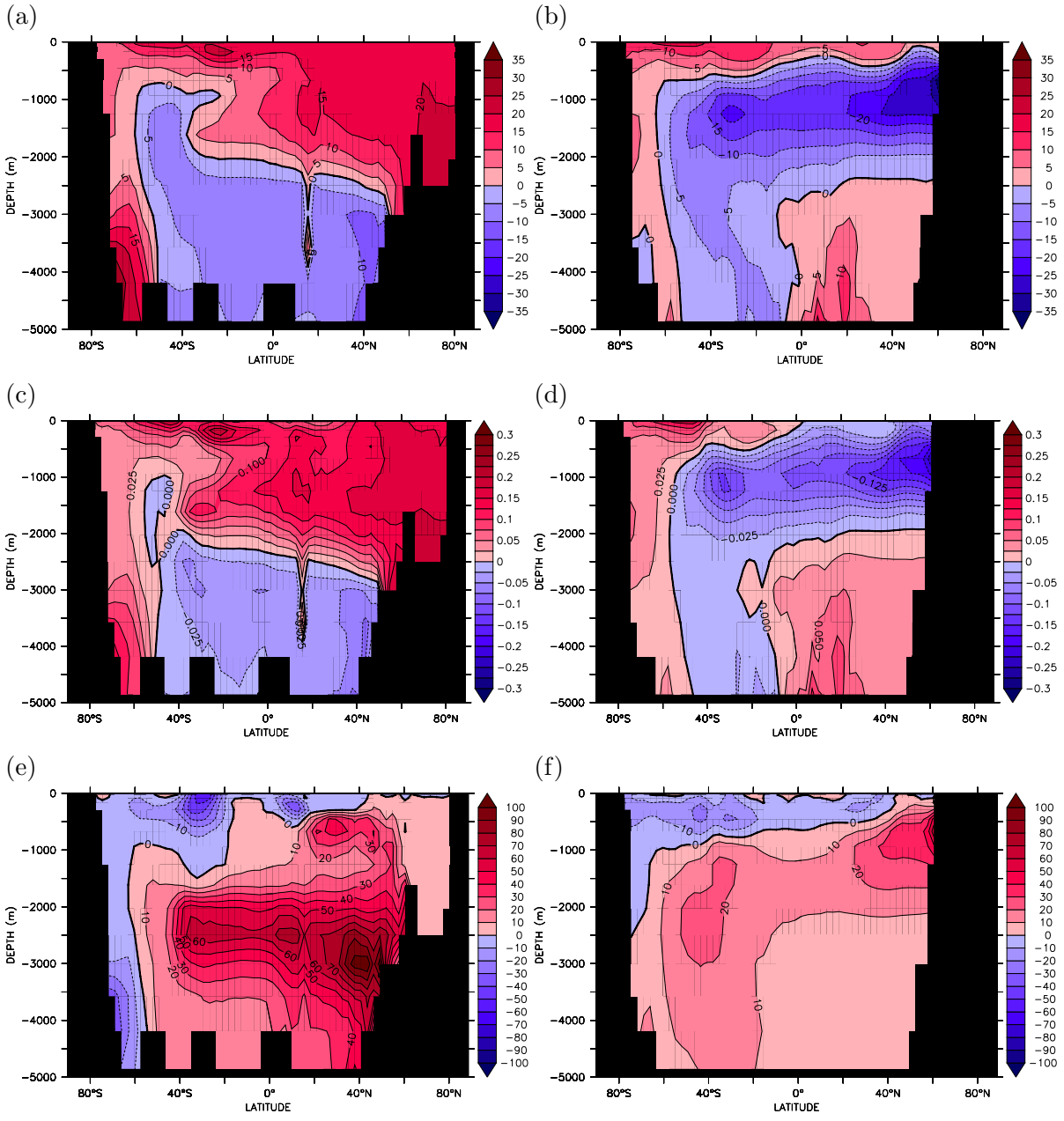

Figure 3.14: Equilibrium MITgcm output for the increased Southern Ocean wind stress perturbation. Meridional anomaly sections of tracers in the Atlantic Ocean (left column) and in the Indo-Pacific Oceans (right column) for (a) and (b) dissolved inorganic carbon (mmol C m^{-3}), (c) and (d) phosphate (mmol P m^{-3}) and (e) and (f) dissolved iron (nmol Fe m^{-3}).

relatively iron-replete water mass into the relatively iron-poor bottom waters. This can also be observed in the North Pacific (and North Indian) where iron deposition is fairly high and is injected into the upper-ocean in northern-source intermediate waters whose circulations have also increased resulting in deeper invasion of the relatively iron-poor waters below. However, interpretation of these anomalies is once again obscured by the change in depth of isopycnals that has particular impact in the upper 2000 m of the water column and at 40°S, and can be accounted for by calculating anomalies in density coordinates as in Figure 3.9.

Concentrations of DIC, phosphate and iron averaged zonally on isopycnals (not shown) closely resemble those concentrations where the zonal-avererage was calculated on depth levels, but are smoother since they take into account the zonal gradients in density, particularly over large distances such as for the Indo-Pacific. As before, the combined effects of overturning circulation and biological pump results in low concentrations of carbon and macronutrients in the surface waters and newly formed deep waters in the Atlantic with increased concentrations in the deep South Atlantic, Southern Ocean and highest concentrations in the deep North Pacific. Dissolved iron, on the other hand, shows the transport of iron-rich surface waters from under the North Atlantic aeolian input maximum to the deep ocean in NADW and subsequent depletion by scavenging as this water mass is advected into the South Atlantic. The Indo-Pacific has a similar pattern of surface iron export to the interior although the enriched waters are far shallower, being advected south at around 1000 m depth as North Pacific and Indian Intermediate Waters. The oldest, most isolated waters in the deep North Pacific, with high macronutrients, have had the greatest length of time for scavenging to deplete the concentration of iron, thus have the lowest concentrations in the model.

In contrast, the anomalies of DIC, phosphate and iron calculated on isopycnals (Figure 3.15) in the Atlantic and Indo-Pacific Oceans are somewhat different from those calculated on depth levels (Figure 3.14) due to the removal of the anomaly signal created by isopycnal heave, particularly at 40°S. While these anomalies are affected by "pure warming" type scenarios [*Bindoff and Church*, 1992; *Bindoff and McDougall*, 1994; *Church et al.*, 1991] where water masses may be subducted along lighter or denser isopycnal surfaces than previously, unlike potential temperature and salinity their interpretation reflects the actual changing concentrations of tracers on those isopycnal surfaces, illustrating the changing sources and sinks in the ocean. This pattern is overlaid on the actual changes in concentration of the individual water masses. In the Atlantic there is clear indication of the increased supply of DIC and phosphate at the

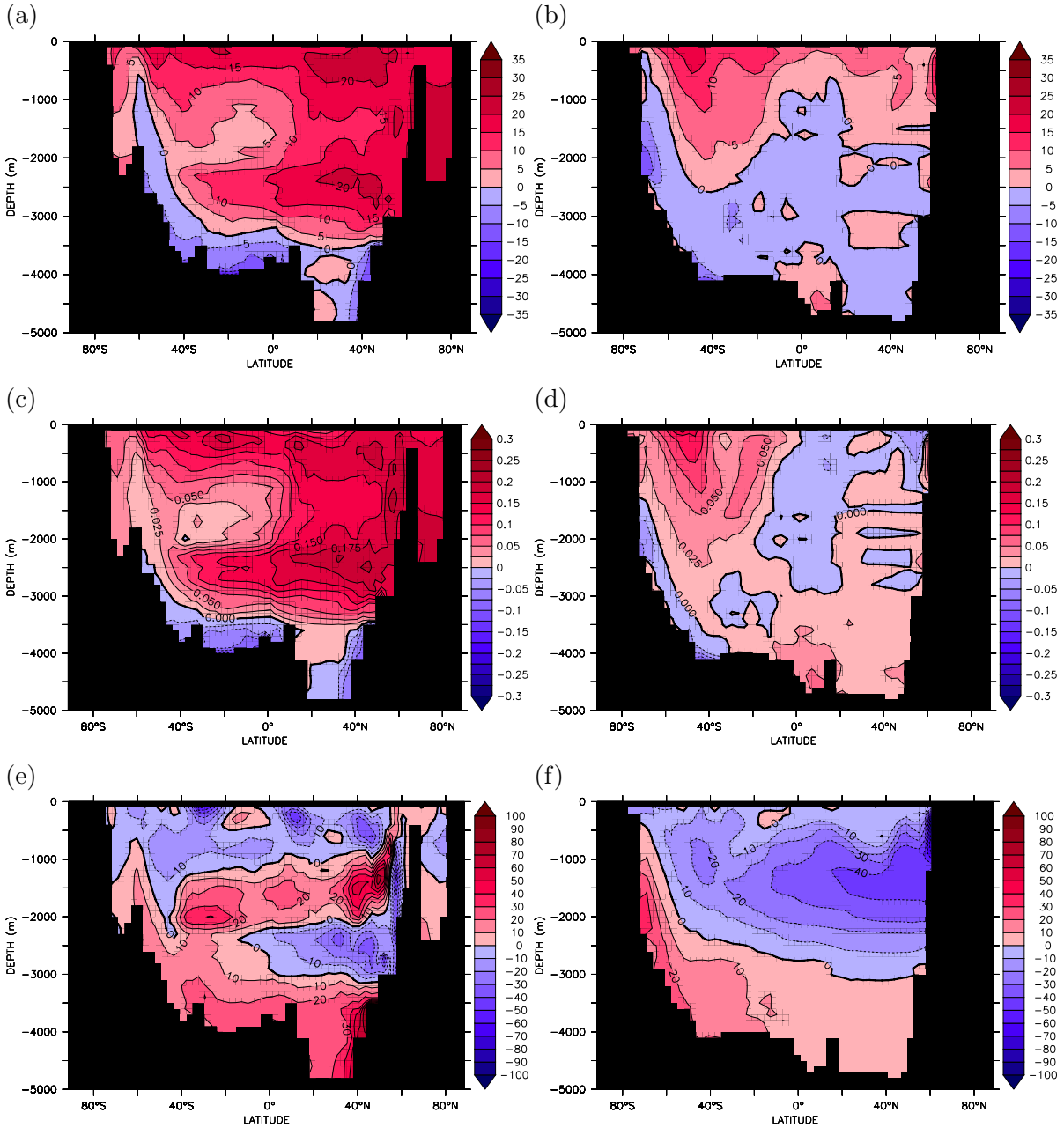

Figure 3.15: Equilibrium MITgcm output for the increased Southern Ocean wind stress perturbation. Meridional sections of tracer anomaly in the Atlantic Ocean (left column) and in the Indo-Pacific Oceans (right column) calculated and zonally-averaged in density coordinates and regridded back into depth coordinates for (a) and (b) dissolved inorganic carbon (mmol C m^{-3}), (c) and (d) phosphate (mmol P m^{-3}) and (e) and (f) dissolved iron (nmol Fe m^{-3}).

surface and in Subantarctic Mode Waters, and its eventual export to the deep ocean in the newly formed deep waters produced in the North Atlantic (Figure 3.15a and c), with the value of the anomaly changing little between approaches (10–15 mmol C m^{-3} and 0.075–0.125 mmol P m^{-3}). The mid-depth tongue of decreased concentration in Figure 3.14a and Figure 3.14c is therefore due to the expansion of the lower concentration NADW circulation cell into the higher concentration abyssal ocean. The pattern of anomalies on isopycnals is augmented by slightly less dense SAMW and NADW, which in both cases results in higher concentration waters entering lighter isopycnals. Indeed, the denser mid-depth AAIW tongue produces an increase in DIC and phosphate concentrations where anomalies in depth coordinates suggest a decrease, while similarly, the very deepest waters in the basin, AABW, show a decline in DIC and phosphate content, also as a result of slightly denser waters bringing slightly lower concentration waters into heavier isopycnals.

In the Indo-Pacific (Figure 3.15b and d), the general pattern of DIC and phosphate anomalies are consistent, but the magnitude of the change is greatly reduced when the differences are calculated on isopycnals. The surface and much of the Southern Hemisphere increases in both carbon and macronutrient concentration compared to only the Southern Ocean, south of approximately 50°S, in Figure 3.14b and Figure 3.14d, by a similar degree (5–10 mmol C m^{-3} and 0.025–0.05 mmol P m^{-3}). In particular, this anomaly appears to be linked to the subduction of SAMW and AAIW in all three basins due to increase in concentration, suggested in depth coordinates, and injection of these waters along different isopycnals. The deep North Pacific retains a slight increase in carbon and macronutrients of around 5 mmol C m^{-3} and 0.025 mmol P m^{-3} respectively as a result of decreased AABW ventilation, which is partially masked by advection of denser AABW with a slightly lower concentration along deeper isopycnals. Also notable is the retreat in latitudinal extent (from 50–60°S to the equator) and decline in magnitude (from ~−20 mmol C m^{-3} to less that −5 mmol C m^{-3} and ~−0.1 mmol P m^{-3} to less than −0.025 mmol P m^{-3}) of the intermediate depth anomalies in the North Pacific and North Indian Oceans. This results from removed isopycnal heave and the injection of SAMW which is less dense and has a slightly elevated concentration of tracers into shallower isopycnals that causes an increase in North Pacific DIC and a reduced decrease in North Pacific phosphate concentrations. Dissolved iron anomalies (Figure 3.15e and f) also display significant alterations in distribution and magnitude in the North Atlantic and throughout the Indo-Pacific basins but due to the added effects of scavenging and complexation, a complex pattern of anomalies is produced. The region between

1000–2000 m depth in the Indo-Pacific switches from a 10 nmol Fe m^{-3} increase to a 10–20 nmol Fe m^{-3} decrease as a result of removing vertical isopycnal movement, due to the northward export of anomalously low-Fe (and slightly altered density) intermediate and mode waters from the Southern Ocean. But some similarities are retained such as the 10 nmol Fe m^{-3} decrease in concentration in the upper-ocean, again due to reduced SAMW source-water concentration and slightly reduced water mass density, and the band of 10–20 nmol Fe m^{-3} increase along the length of the Atlantic owing to reduced Fe scavenging as a result of faster NADW advection and reduced NADW density causing higher concentration waters to flow into originally lower concentration isopycnals between 1000–2000 m depth. The decrease in the concentration of iron of 10 nmol Fe m^{-3} at 2500 m in the northern part of the Atlantic also originates from the less dense NADW. The densest varieties of this water mass lie at the boundary of the higher-Fe mid-depth waters and the lower-Fe, scavenged bottom waters so the reduction in density injects these depleted waters into the previously higher concentration isopycnals. The reverse process also accounts for the increase in iron concentration of the abyssal waters in the Atlantic and Indo-Pacific because the denser AABW injects relatively iron-rich waters into previously iron-poor isopycnals.

The interplay between light and the anomalies of iron and phosphate combine to produce variations in biological production (Figure 3.16). The decreased primary production in the North Pacific and Indian Oceans is caused by the reduced phosphate supply from below (as seen in both Figure 3.14d and Figure 3.15d). On the other hand, the increase in phosphate concentration in the Southern Ocean does not stimulate biological production there, implying that another factor is limiting in this region as is well documented in models [*Dutkiewicz et al.*, 2005a, 2006; *Parekh et al.*, 2005, 2006b] and the real ocean [*de Baar et al.*, 2005]. Indeed, reduction in the concentration of micronutrients in the Southern Ocean leads to no change in activity either, while production also remains similar to the control run in the region to the south of Kerguelen, where iron concentration increases. This implies that light limitation, due to deep mixed layer depth and prescribed prolonged sea-ice cover, plays an important role in limiting primary production in the Southern Ocean [*Dutkiewicz et al.*, 2006; *Mitchell et al.*, 1991; *van Oijen et al.*, 2004] as phosphate is not limiting in this "High Nutrient-Low Chlorophyll" region and further north in the South Australian Bight, where phosphate and iron both increase and light is not limiting, primary production increases. Macronutrient limited regions such as the Atlantic subtropical gyres respond to increased phosphate concentration with increased primary production drawing down much of the anomalous phosphate to

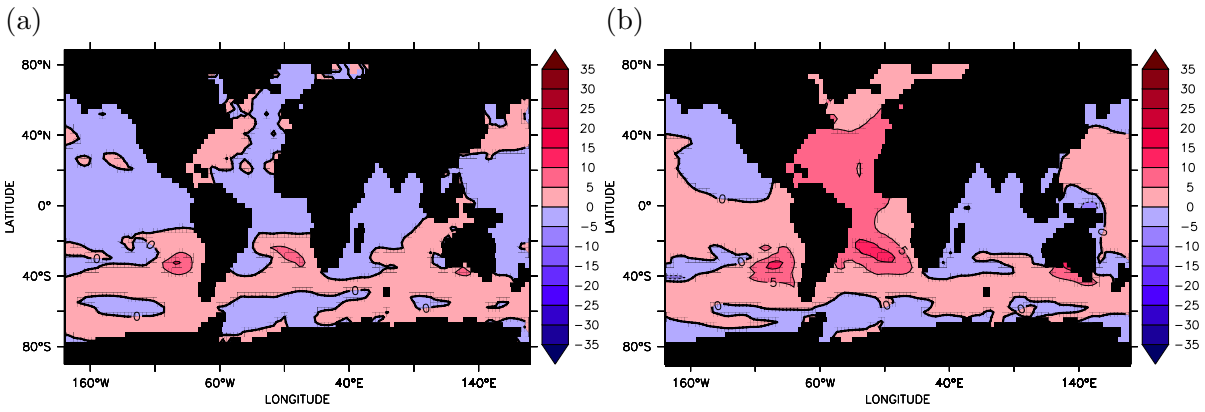

Figure 3.16: MITgcm output for the increased Southern Ocean wind stress perturbation. Sea surface anomaly of primary production (mmol C m^{-3} yr^{-1}) (a) near the begining of the perturbation run after 10 years and (b) near equilibrium after 5000 years.

control levels. In fact while the North Atlantic is iron replete benefitting from excess dust deposition from the Sahara, the South Atlantic gyre has a much lower surface concentration. The increase in phosphate concentration here stimulates primary production that outpaces iron deposition leading to almost complete Fe depletion, along with the reduced concentration of Fe advected from the neighbouring Southern Ocean. The South Pacific appears to benefit from increases in both macro- and micronutrients, due to advection of Chilean aeolian-sourced iron and upwelled phosphate by an enhanced gyre circulation into a region with sufficient light levels, leading to an increase of primary production. In this region and other parts of the Atlantic where light limitation is not an issue [*Dutkiewicz et al.*, 2006], the excess nutrients transported to the surface remain somewhat underutilised because the maximum rate of nutrient uptake has been reached and further production is limited by the Michaelis-Menton formulation. Nevertheless, the net effect of these changes is a global increase in productivity of 0.58 Gt C yr^{-1}.

Anomalies of dissolved oxygen in the Atlantic and Indo-Pacific basins (Figure 3.17a to d) both in depth coordinates and density coordinates attest to the increased ventilation of the upper-ocean by the increased supply of intermediate and mode waters from Southern Ocean circulation, with a lesser increase in the ventilation of the North Atlantic due to a smaller change in the overturning anomaly. Alteration of water mass densities particularly influences the bottom waters in the Atlantic and Indo-Pacific Oceans because with the reduced abyssal circulation seen in Figure 3.3, oxygen concentration should be observed to decrease, especially because these waters are increasingly saline, which reduces the oxygen saturation concentration. However, denser AABW may result

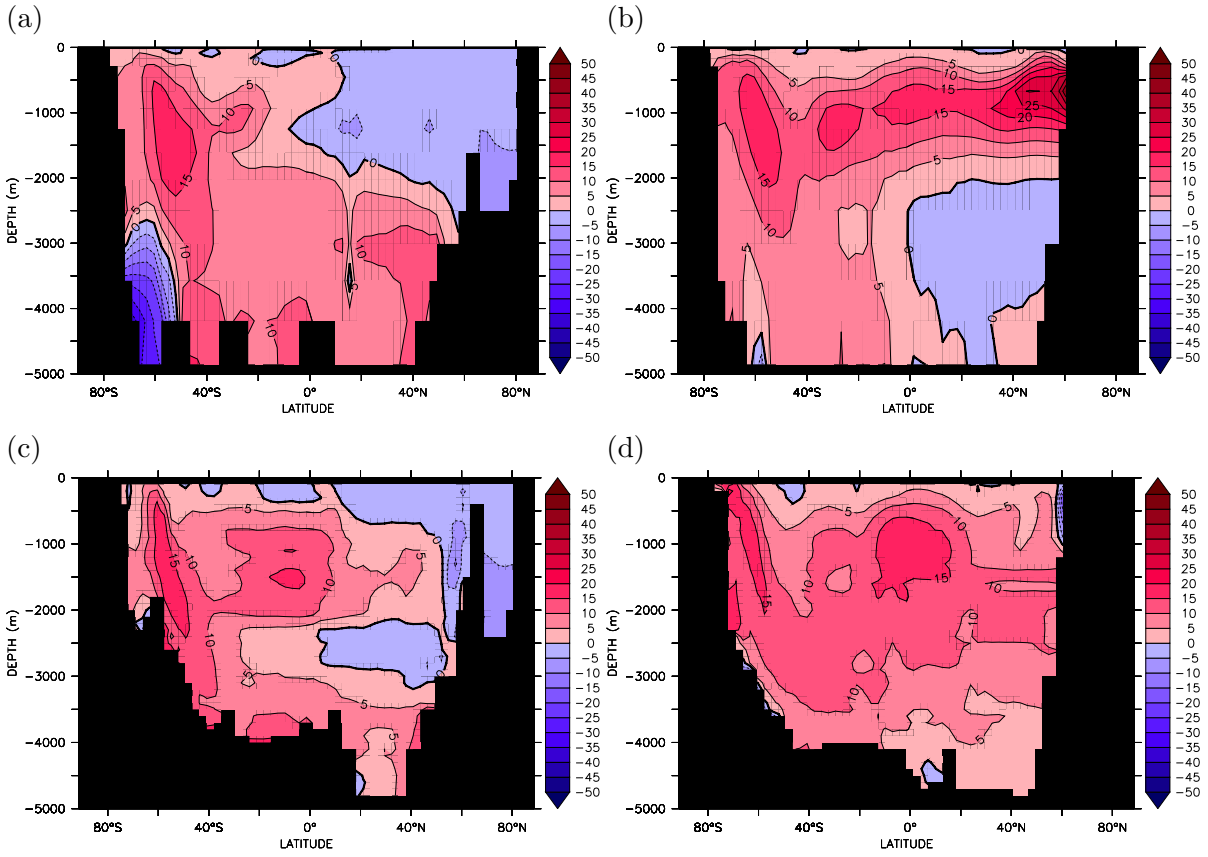

Figure 3.17: Equilibrium MITgcm output for the increased Southern Ocean wind stress perturbation. Meridional sections of dissolved oxygen anomaly (mmol O m^{-3}) in the Atlantic Ocean (left column) and in the Indo-Pacific Oceans (right column) calculated in (a) and (b) depth coordinates (mmol O m^{-3}), and (c) and (d) calculated and zonally-averaged in density coordinates and regridded back into depth coordinates (mmol O m^{-3}).

in waters with a relatively higher oxygen content being injected into deeper isopycnal layers with relatively lower oxygen concentrations, thus causing a positive anomaly on isopycnal surfaces.

The maximum oxygen disequilibrium concentration anomaly, the difference in oxygen disequilibrium between the perturbed and control experiments, is an order or magnitude smaller than the original disequilibrium seen in the control run (Chapter 2.3.1). These uncertainties lead to errors in subsequently calculated regenerated (and thus preformed) phosphate of 0.22 µmol P l^{-1} for the absolute fields (0.05 µmol P l^{-1} for zonally-averaged fields) and 0.006 µmol P l^{-1} for the anomalies. Therefore, although there is some error associated with calculating regenerated phosphate using Apparent Oxygen Utilisation and some overestimation of the regenerated nutrient component, the change in circulation induced by enhanced Southern Ocean wind stress changes is insufficient to drive

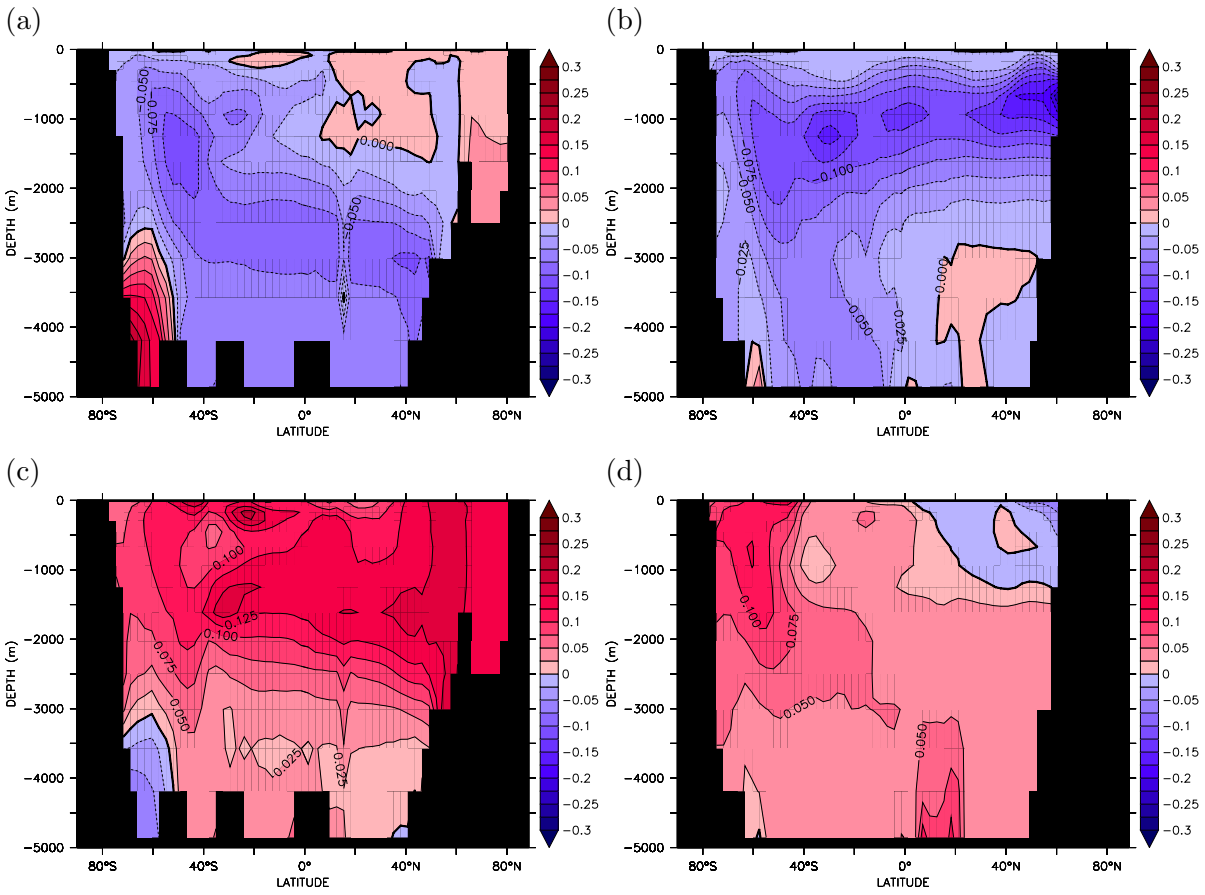

Figure 3.18: MITgcm output for the increased Southern Ocean wind stress perturbation. Meridional sections of tracer anomaly in the Atlantic Ocean (left column) and in the Indo-Pacific Oceans (right column) for (a and b) regenerated phosphate anomaly (mmol P m^{-3}) calculated from Apparent Oxygen Utilisation using Equation 2.28 and Equation 2.29, and (c and d) preformed phosphate anomaly (mmol P m^{-3}) calculated using the regenerated component and Equation 2.27.

a large change in dissolved oxygen disequilibrium due to rapid air-sea gas exchange so that comparison between the control and perturbation experiments is acceptable and the anomalies are representative of perturbations to physical and biogeochemical processes.

The anomalies of regenerated and preformed phosphate in the Atlantic (Figure 3.18a and c) and Indo-Pacific Oceans (Figure 3.18b and d) show a reduction in the concentration of surface nutrients returning to the ocean interior by remineralisation. Concurrently the concentration of nutrients returned by subduction and water mass formation increases in the Southern Ocean and throughout the entire Atlantic Basin and in the Southern Ocean in Indo-Pacific Basins. However, as with the anomaly of total phosphate (Figure 3.14c and d), the effect of the change in isopycnal depth causes a negative anomaly in the Atlantic due to the expansion of the NADW cell, while in the Indo-Pacific the

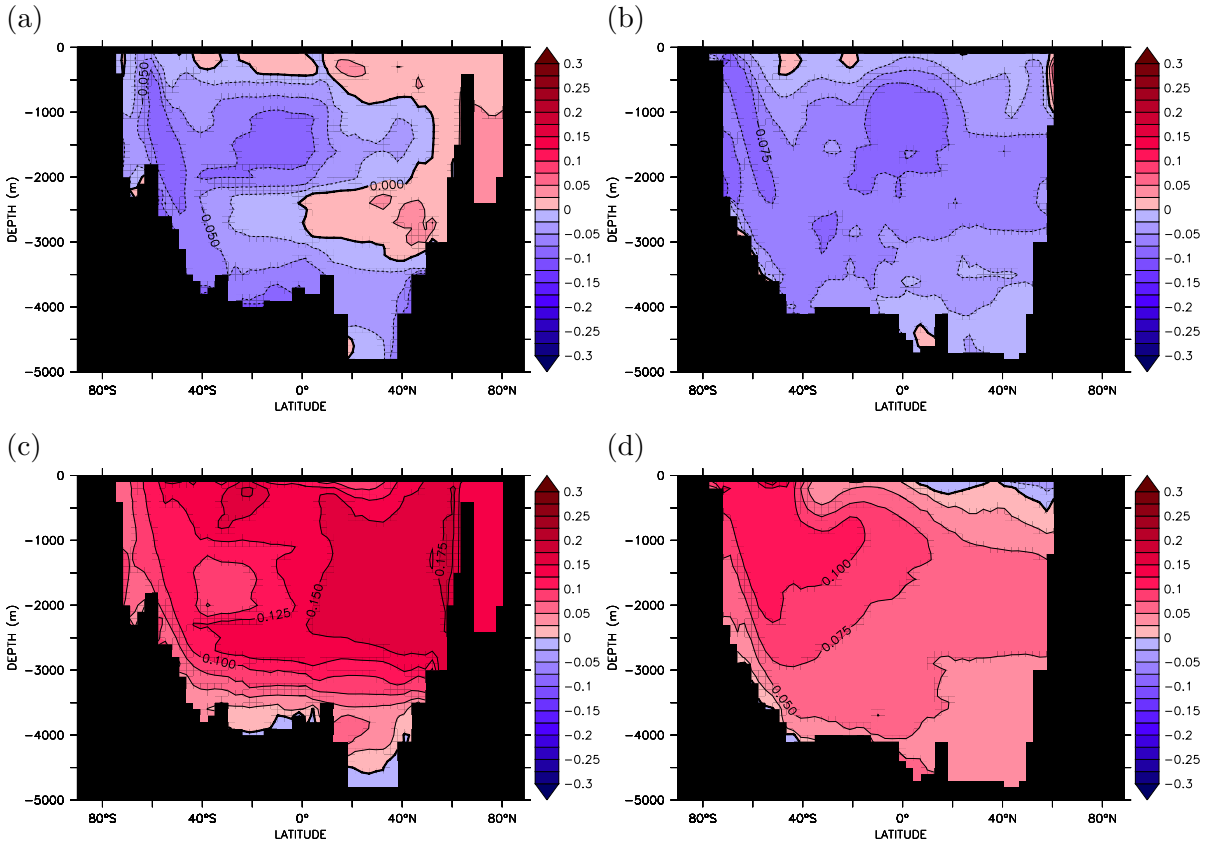

Figure 3.19: MITgcm output for the increased Southern Ocean wind stress perturbation. Meridional anomaly sections of tracers in the Atlantic Ocean (left column) and in the Indo-Pacific Oceans (right column) calculated and zonally-averaged in density coordinates and regridded back into depth coordinates for (a and b) regenerated phosphate anomaly ($\mathrm{mmol\,P\,m^{-3}}$) calculated from Apparent Oxygen Utilisation using Equation 2.28 and Equation 2.29, and (c and d) preformed phosphate anomaly ($\mathrm{mmol\,P\,m^{-3}}$) calculated using the regenerated component and Equation 2.27.

injection of intermediate and mode waters into the thermocline displaces the nutrient concentration maximum at ~1500–2000 m downwards and exaggerates the magnitude of the anomaly. Recalculating these anomalies in density coordinates (Figure 3.19) shows that they are actually quite consistent with the anomalies in depth coordinates (and the anomalies of oxygen in Figure 3.17c and d), revealing that there is a true decrease in regenerated phosphate in the upper 2000 m of the global ocean with a slight bias towards the Southern Hemisphere, although there is also an increase in remineralised phosphate in the North Atlantic at the surface and carried to depth in the deep waters associated with increased production in the whole basin that was not present before. The preformed phosphate anomalies in density coordinates are also fairly consistent with the anomalies in depth coordinates and highlight the increase in unutilised nutrients returned to the interior from the increased Southern Ocean overturning circulation

and by the enhanced Atlantic meridional overturning circulation due to the incomplete drawdown of nutrients supplied to the South Atlantic by enhanced northward Ekman transport. Applying the metric of efficiency of the soft tissue pump calculated from the ratio of the globally-average concentrations of regenerated phosphate to total phosphate [*Ito and Follows*, 2005] displays a decrease from the control value of 35.7 % to 33.1 % for increased wind stress despite increased primary production (Figure 3.16). The lower efficiency suggests a smaller fraction of macronutrients are returned from surface to deep ocean via the biological pathway because of the increased influence of Southern Ocean-sourced intermediate and mode water masses ventilating a greater volume of the interior ocean. Their increased circulation and elevated nutrient concentration, enriched with upwelled nutrients from further south, return a larger proportion of macronutrients into the ocean interior via the physical pathway.

3.1.4 Appraisal of the air-sea flux of carbon dioxide

Opposing the export and isolation of carbon by the biological pump is the outgassing of upwelled carbon from the deep ocean into the atmosphere, although the calculated flux actually includes the contribution due to biological uptake. There are widespread negative values in the total tendency of the surface DIC concentration in the Southern Hemisphere, south of 40°S (Figure 3.20a and b), in the same region as the upwelling of carbon rich deep waters (Figure 3.13a and b). This change is composed of a strengthening of outgassing due to air-sea exchange (Figure 3.20c and d) south of 55°S and reduced uptake between 55°S and 30°S, both as a result of the increased oceanic carbon concentration. Virtual fluxes resulting from changes in surface salinity relaxation (Figure 3.20e and f) reinforce the decreasing tendency of DIC concentration south of 50°S because negative surface salinity relaxation (Figure 3.6d) implies a gain of freshwater by the ocean that should reduce the concentration of salt and passive tracers at the surface, which explicitly results in a virtual evasion of carbon from the ocean. However, the positive salinity relaxation to the north actually opposes the air-sea flux trend leading to a small net increase in DIC concentration between 40°S and 20°S (Figure 3.20a and b). The North Atlantic shows net decrease in surface concentration due to both the solubility-driven ocean to atmosphere flux resulting from increased northward heat transport and increased virtual dilution of the DIC concentration. On average, K_w is of the order of $1 \times 10^{-5}\,\mathrm{m\,s^{-1}}$ and does not change significantly (it actually increases by $4 \times 10^{-7}\,\mathrm{m\,s^{-1}}$, or ~1% between 40°S and 60°S) showing that the dominant term is the

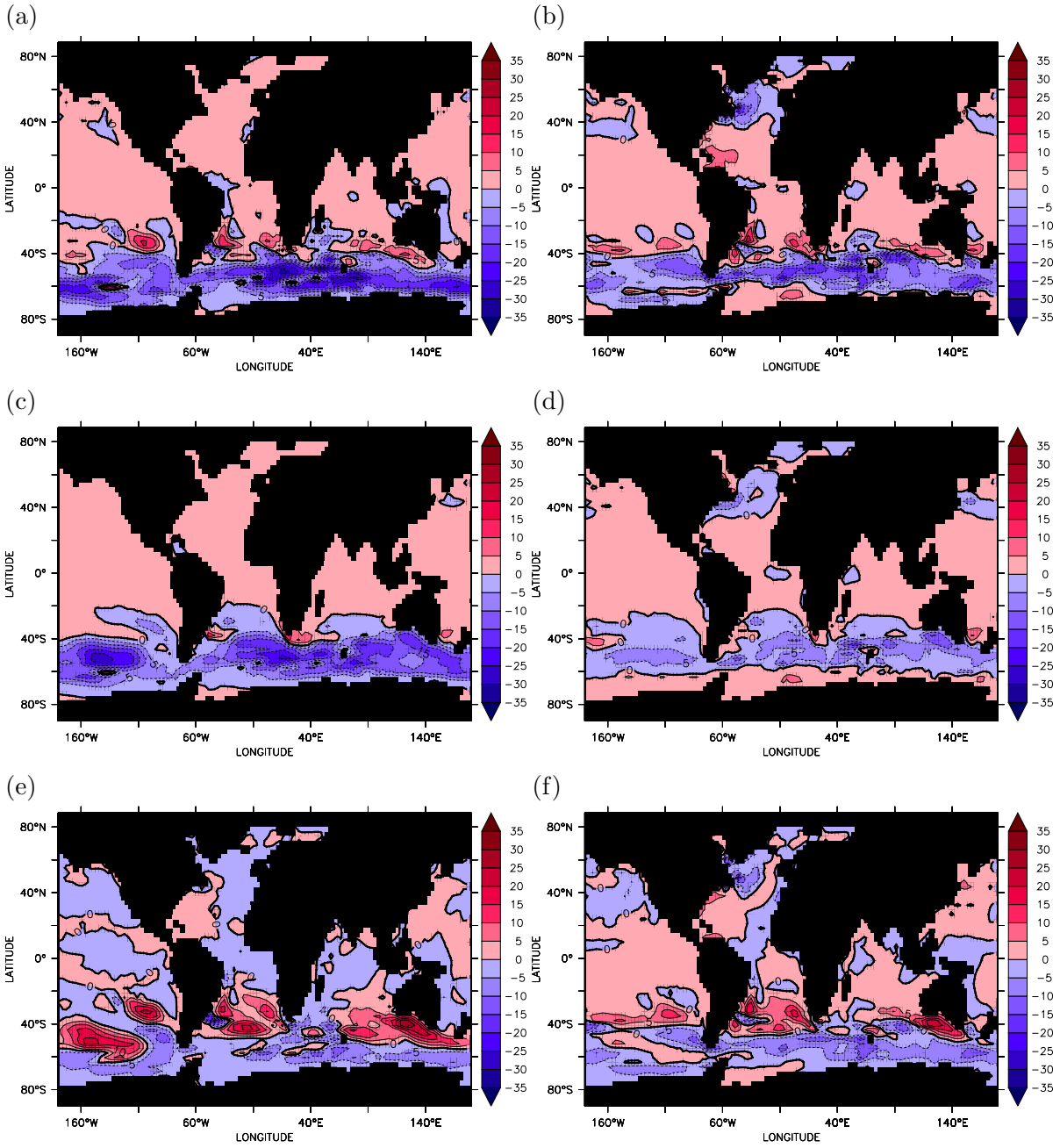

Figure 3.20: Equilibrium MITgcm output for the increased Southern Ocean wind stress perturbation. Anomalies of the surface tendency of carbon concentration due to surface fluxes near the begining of the perturbation run after 10 years (left column) and near equilibrium after 5000 years (right column) for (a) and (b) the total surface tendency of carbon due to surface fluxes (mmol C m^{-3} yr^{-1}), which is the sum of (c) and (d), the tendency of carbon due to air-sea exchange (mmol C m^{-3} yr^{-1}, where negative values indicate oceanic outgassing, causing a decrease in surface concentration, while positive values indicate oceanic uptake) and, (e) and (f), the "virtual flux" of carbon to account for concentration/dilution of tracers by surface salinity restoration (mmol C m^{-3} yr^{-1}, where negative values indicate dilution of DIC, causing a decrease in surface concentration, while positive values indicate concentration of DIC). Note that the atmosphere is influenced only by the air-sea exchange term.

wind speed but small variations in K_w may be noticed due to the Schmidt number's dependence on sea surface temperature, which changes relatively little due to surface temperature relaxation. The integrated readjustment of the air-sea flux of carbon is to release 33.13 Gt C to the atmosphere over 5000 years, before the atmosphere and ocean return to a stable-state of zero global net fluxes.

These trends are represented in the zonal average fluxes in the Southern Hemisphere (Figure 3.21a) at 10 years (thin lines) and 5000 years (thick lines) after the perturbation, compared to the control (dashed lines). The total tendency for surface DIC concentration (green) shows decreasing concentrations everywhere south of 40°S (Figure 3.21b) peaking between 50–60°S and after 10 years of perturbation with the degree of change decaying during the integration period. The overall magnitude of the change in concentration in Figure 3.21a is driven by the virtual fluxes (blue) while the concentration anomaly in the early stages of the perturbation is controlled by the air-sea fluxes (red) and then roughly equal contributions at the end of the perturbation.

The virtual flux is generally enhanced after 5000 years due to freshwater divergence in the Southern Ocean, particularly south of 50°S. During model adjustment to the change in wind stress however, the virtual flux anomaly between 55–40°S actually reverses, promoting carbon concentration increase, but this is countered by concurrent outgassing driven by the strong atmosphere-ocean concentration gradient leading to net DIC decrease. To the north of 40°S, DIC concentrations are increasing slightly as a balance between the virtual fluxes that promote slight increase in carbon concentration due to gain of freshwater after 10 and 5000 years while the air-sea fluxes of CO_2 are at or slightly below control levels suggesting reduced uptake from the atmosphere. At model equilibrium in the control run, the Southern Ocean is approximately neutral, neither a source nor a sink of CO_2, south of 55°S in terms of the air-sea flux. This balance is disturbed by the upwelling of carbon-rich deep waters that promotes oceanic outgassing, which over the course of the integration period reduces the concentration gradient and hence the flux. After 5000 years the balance between ocean and atmosphere is nearly restored south of 60°S, however net outgassing remains between 50–60°S while reduced uptake remains between 40–50°S suggesting that the Southern Ocean still carries excess DIC.

The timescale for the balance between the atmospheric CO_2 content and the surface ocean CO_2 concentration (Figure 3.20), which may be relatively supersaturated or undersaturated even in steady state, is not instantaneous and has a time scale that lies

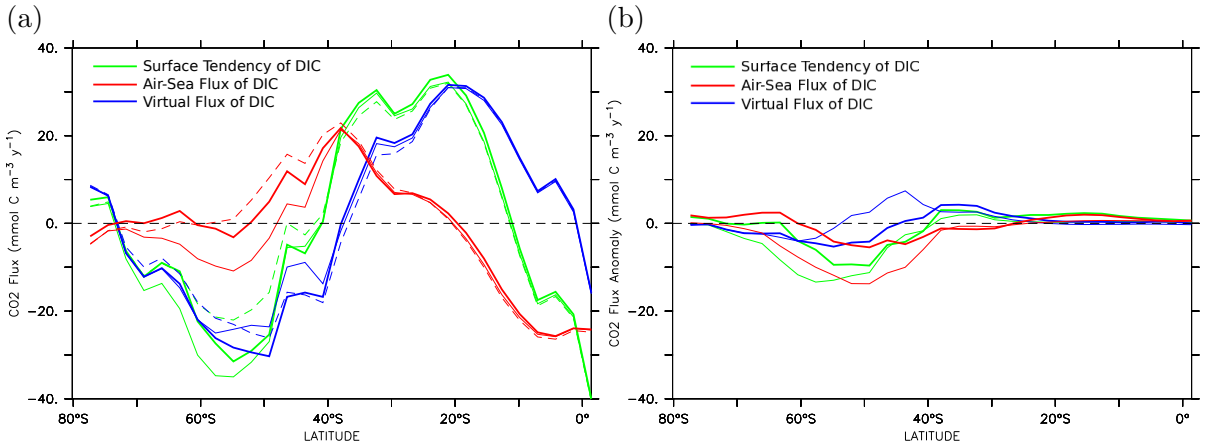

Figure 3.21: MITgcm output for the increased Southern Ocean wind stress perturbation. (a) Zonally averaged components of DIC concentration tendencies in the surface cell ($\mathrm{mmol\,C\,m^{-3}\,yr^{-1}}$) and (b) their anomalies. Total surface tendency (green), which is the sum of the air-sea flux (red) and the virtual flux (blue), is plotted for the control run (dashed, part (a) only), during model adjustment after 10 years (thin) and near equilibrium after 5000 years (thick). Negative values indicate oceanic outgassing (air-sea flux) or parameterised freshwater gain (virtual flux), causing a decrease in surface concentration, while positive values indicate oceanic uptake (air-sea flux) or parameterised freshwater loss (virtual flux) causing an increase in surface concentration. Note that the atmosphere is influenced only by the air-sea exchange term.

between oxygen and CFCs (weeks/months) and radiocarbon (decades) [*Ito et al.*, 2004b]. Furthermore, this time scale is comparable to the residence time of waters in the surface Southern Ocean [around two years calculated from zonally averaged vertical velocity at 100 m, *Ito and Follows*, 2003]. Therefore increasing the residual mean flow and bringing carbon rich deep waters to the surface should result in increased outgassing, but because these carbon rich waters have a shorter residence time at the surface before being subducted, is equilibrium actually achieved?

Evaluating the absolute disequilibrium concentration using the tracer ΔC^*_{pref} (Equation 2.33, [*Gruber et al.*, 1996]) produces results similar to those in Figure 2.14a and b. However, the directly calculated disequilibrium anomalies using Equation 2.36 in depth coordinates (Figure 3.22a and b) show that indeed, with enhanced Southern Ocean overturning, air-sea disequilibrium increases near the surface and in the regions of deep water formation in the Southern Hemisphere and North Atlantic by ~5–10 $\mathrm{mmol\,m^{-3}}$, accounting for the majority of the increase in DIC in the Southern Ocean and half of the increased concentration in the North Atlantic (Figure 3.14a and b), while in the Indo-Pacific Southern Ocean, the disequilibrium anomalies are slightly greater than the

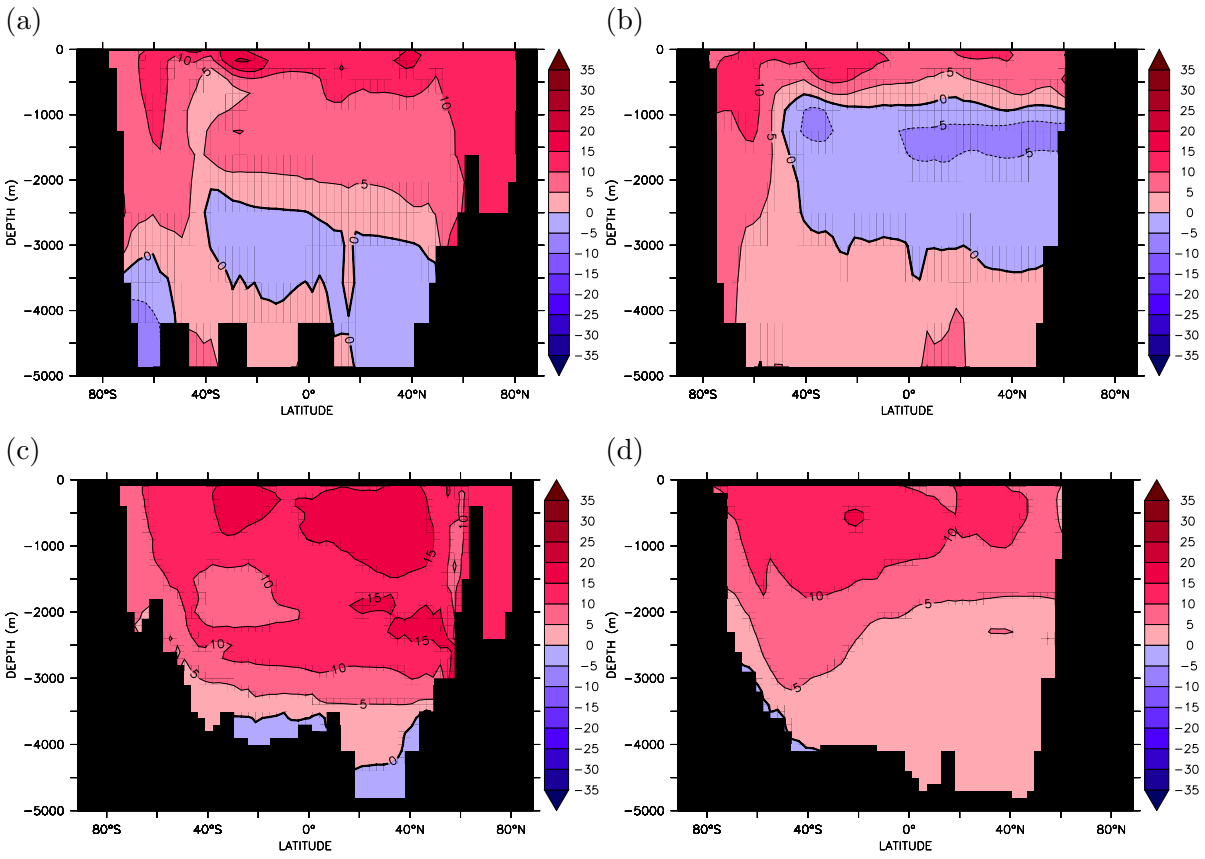

Figure 3.22: Equilibrium MITgcm output for the increased Southern Ocean wind stress perturbation. Anomalies of the Air-Sea disequilibrium concentration of Dissolved Inorganic Carbon (mmol C m^{-3} yr^{-1}) in the Atlantic (left column) and Indo-Pacific Oceans (right column) at the time interior water masses were last at the surface, diagnosed using control "preindustrial" concentrations and the observed DIC concentration after "correction" for the effects of organic carbon remineralisation and calcium carbonate dissolution calculated in (a and b) depth coordinates and (c and d) calculated and zonally-averaged in density coordinates and regridded back into depth coordinates. Positive values indicates oversaturation with respect to the atmosphere while negative values represent undersaturation.

total DIC anomalies at depth. These differences must therefore be partially offset by the change in biogenic carbon regeneration suggested in Figure 3.18. The decreased disequilibruim concentrations below 2000 m in the Atlantic and 500 m in the Indo-Pacific also occur in the same locations as seen elsewhere for carbon and nutrients (Figure 3.14) and are probably influenced by changes in isopycnal depths. When calculated in density coordinates (Figure 3.22c and d), the majority of the decrease is removed and the magnitude of the disequilibrium is increased to 10 mmol m^{-3} in the Atlantic and 5–10 mmol m^{-3} in the Indo-Pacific now accounting for a large fraction of the DIC anomalies in all basins (Figure 3.15a and b). The distribution of the air-sea disequilibrium is reminiscent of the anomaly in preformed phosphate (Figure 3.19c and d) further supporting the link

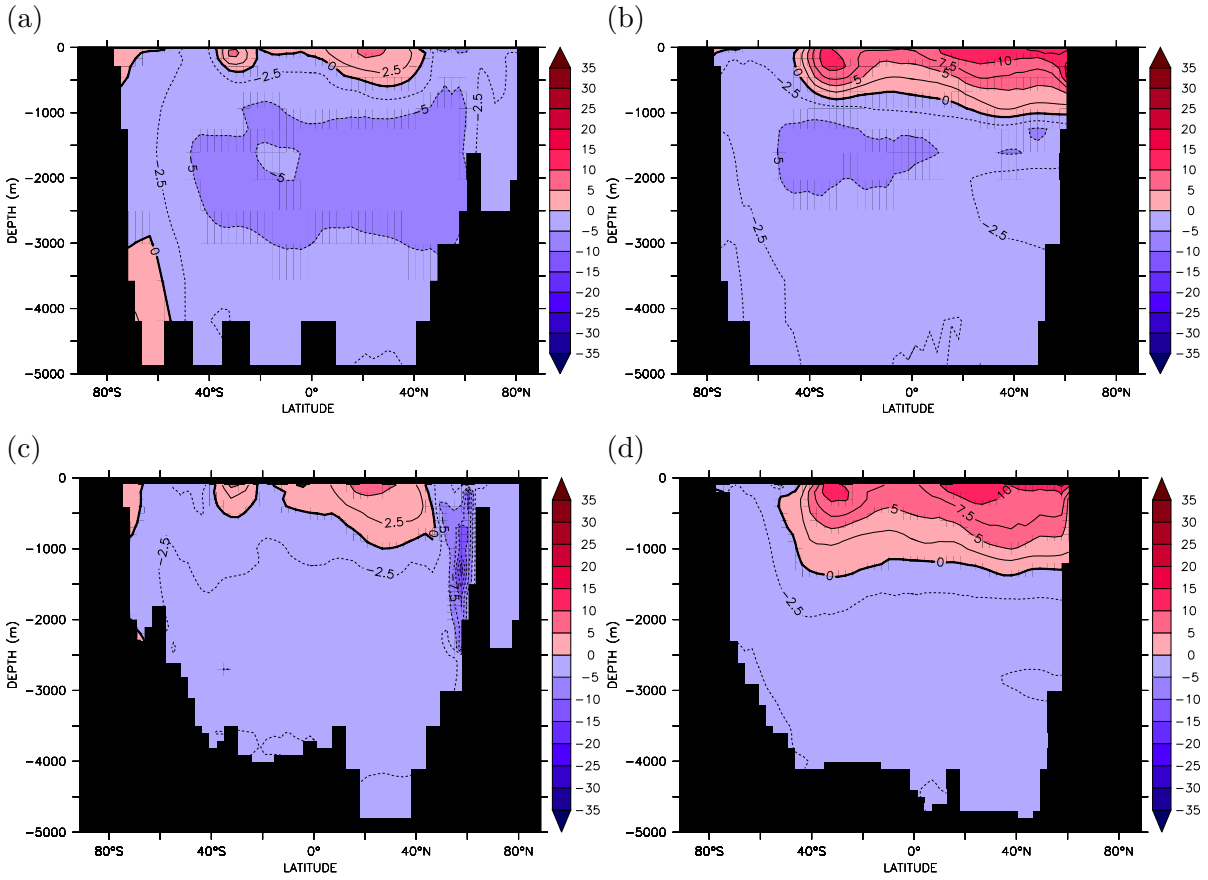

Figure 3.23: Equilibrium MITgcm output for the increased Southern Ocean wind stress perturbation. Meridional sections of the quasiconservative tracer $C_{gas\ exch}$ anomalies (mmol C m^{-3}) in the Atlantic (left column) and Indo-Pacific (right column) Oceans calculated from Equation 2.37 compared to the control (a and b) calculated and zonally-averaged in depth coordinates and (c and d) calculated and zonally-averaged in density coordinates and regridded back into depth coordinates.

between increased circulation and increased air-sea disequilibrium of CO_2. Interestingly, the integrated change in oceanic carbon concentration due to the change in disequilibrium (33.40 Gt C) is roughly equal to the total carbon gained by the atmosphere at the end of the integration and opposes the rising atmospheric concentration of CO_2 by trapping and injecting an elevated concentration of carbon into the ocean interior. Therefore, not accounting for changes in atmosphere-ocean CO_2 equilibrium would have resulted in twice as much outgassing, and therefore twice the sensitivity of atmospheric CO_2 to perturbations in Southern Ocean wind stress.

Finally, removing the soft tissue and carbonate pumps from the internal distribution of DIC allows the source of extra atmospheric CO_2 to be identified. The anomalies of $C_{gas\ exch}$ calculated in depth coordinates Figure 3.23(a) and (b) show a decrease over

most of the Atlantic indicating enhanced ocean to atmosphere CO_2 transfer, particularly between 1000–2000 m between 40°S and 60°N reaching a minimum of $-5\,\mathrm{mmol\,C\,m^{-3}}$ associated with NADW in the Atlantic and AAIW in the Atlantic and Indo-Pacific at ~1500 m. Increased concentrations at the surface in the North Indian and North Pacific Oceans balance the enhanced outgassing in the Southern Hemisphere and North Atlantic. In density coordinates Figure 3.23(c) and (d) however, the minimum concentration decreases to $-2.5\,\mathrm{mmol\,C\,m^{-3}}$ associated with NADW and water masses of Southern Ocean origin, but still indicates increased net outgassing when these water masses were last at the surface. The globally integrated anomaly of $C_{gas\ exch}$ after 5000 years indicates a total of 34.50 Gt C released from the ocean into the atmosphere under enhanced Southern Ocean wind stress, which as an independent method, compares very well with the value of integrated air-sea CO_2 flux during the perturbation.

3.2 Decreased wind stress perturbation

After 5000 years, with decreased wind stress (Figure 3.1b) applied to the Southern Ocean, atmospheric CO_2 concentration had decreased by 16.3 µatm to 261.7 µatm. Again, the system approaches equilibrium after approximately 5000 years, with the majority of the adjustment occurring in the first five centuries. Decreased wind stress invokes the opposite responses of increased wind stress compared to the control in terms of physical circulation and biogeochemical changes as expected from previous work [*McDermott*, 1996; *Parekh et al.*, 2006b; *Toggweiler and Samuels*, 1995]. Instead of an exhaustive description of the model state, a more concise synopsis of the adjustments is presented, in particular, highlighting where the two perturbations are not so simply linearly related.

3.2.1 Response of oceanic circulation and density structure

Reduced Southern Ocean wind stress causes a decrease in the global northward transport across 50°S in the Ekman layer of 21.54 Sv, while Ekman pumping is weakened by 6.2 Sv at 40°S causing reduced downwelling and 3.8 Sv at 60°S causing reduced upwelling. This is further expressed by a 19.95 Sv more sluggish global Southern Hemisphere Eulerian-mean flow (Figure 3.24a) that results in a flattening of Southern Ocean isopycnals and reduced baroclinity that acts to suppress mesoscale eddy transfer as parameterised by a 9.42 Sv decrease in Southern Hemisphere GM bolus transports (Figure 3.24b), that

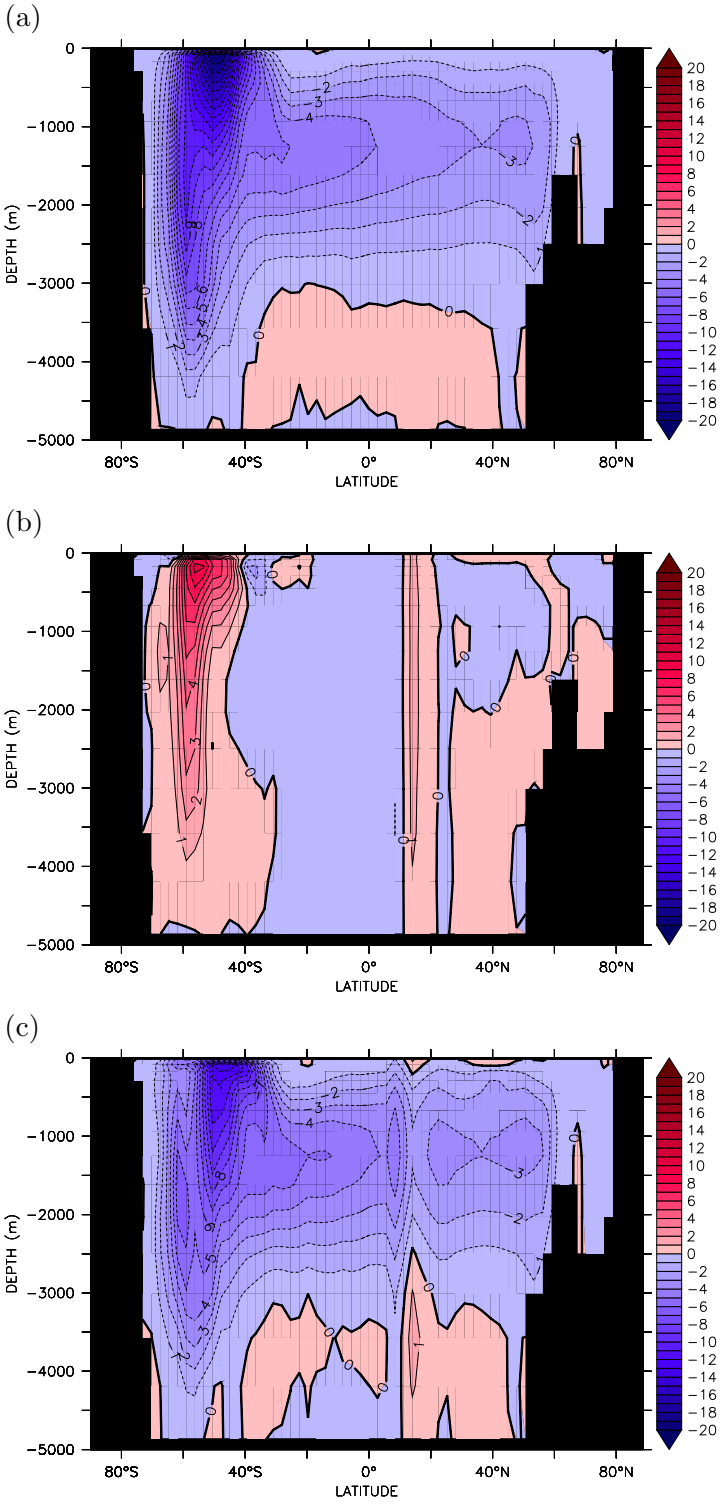

Figure 3.24: Equilibrium MITgcm output for the decreased Southern Ocean wind stress perturbation (a) Zonal average Global meridional Eulerian-mean overturning stream function anomaly (Sv), (b) Zonal average meridional eddy overturning stream function anomaly (Sv) and (c) Zonal average Global meridional residual overturning stream function anomaly (Sv).

is, a more positive circulation compared to the control. Despite the slower eddy and Eulerian-mean flows, partial compensation still occurs and there is a net weakening of the global residual Southern Ocean meridional overturning circulation in the region of 13.81 Sv (Figure 3.24c) that brings the Southern Ocean overturning almost to a standstill. There is also a 1–2 Sv intensification and slight upwards shift in the anticlockwise deep ocean circulation cell at 3000 m with a 200–300 m shoaling of the interface between the abyssal and upper-ocean cells. In the Atlantic, there is a reduction in the Atlantic Meridional Overturning Circulation of 5.72 Sv, while in the Pacific at 1500 m there is a ~3 Sv increase in Southern Hemisphere upwelling which somewhat suppresses the Northern Pacific Intermediate Water circulation cell at 40°N and a 1.11 Sv increase in the abyssal circulation cell centred at ~2500 m. Furthermore, a 52.3 Sv decrease in the ACC transport through Drake Passage is the main feature of the barotropic streamfunction anomaly, followed by a 5–10 Sv reduction of the adjacent subpolar gyres.

Global mean potential temperature decreases by 0.50 °C due to more sluggish exchange between the surface and deep ocean via the shallower Southern Ocean (~45 m) and North Atlantic (~25 m) mixed layers, while global mean Salinity is also lowered by 0.015. Furthermore, zonally averaged buoyancy fluxes (Figure 3.25) show that reduced buoyancy gain and weaker positive buoyancy gradient in the Southern Ocean is due to negative surface salinity relaxation, accompanied by more negative temperature relaxation, that is associated with a reduced northward flow of upwelled waters and less vigorous Southern Ocean meridional overturning circulation. The signal of increased buoyancy gain in the North Atlantic due to surface temperature relaxation again damps the cooling of the deep water formation region that would otherwise intensify the production of NADW, thus supporting the reduced Atlantic meridional overturning circulation. The structure of these changes follows the inverse pattern of those found under increased Southern Ocean wind stress so that the oceanic density field (Figure 3.26) adjusts in such a way that isopycnals south of 60°S become deeper, isopycnals further north shoal and there is a reduced isopycnal gradient between that is consistent with slackening of the Southern Ocean overturning and eddy circulations (Figure 3.24). The greatest change in density occurs centred at 40°S between 500 m and 2000 m depth, in the same region as in the enhanced wind stress perturbation, at the boundary between the ACC and Southern Hemisphere subtropical gyre where the isopycnals have ascended between 200–300 m.

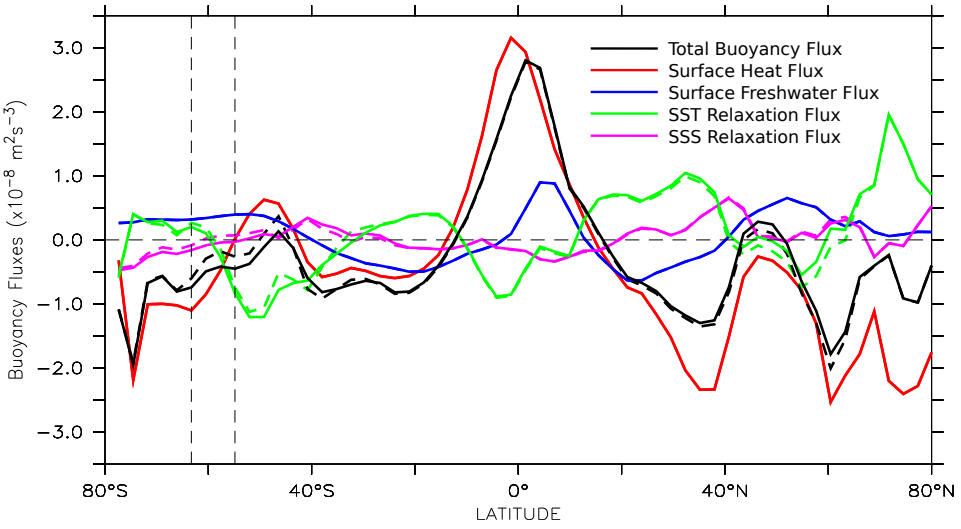

Figure 3.25: Equilibrium MITgcm output for the reduced Southern Ocean wind stress perturbation. Zonal average surface buoyancy flux ($m^2\,s^{-3}$) and its components (see Section 6.1 and Equation 6.2) for the perturbed (solid) and control (dashed) states. Positive values indicate a gain of buoyancy (an increase in heat or freshwater/reduced salinity) while negative values indicate buoyancy loss (reduced heat or freshwater/increased salinity). Dashed vertical lines denote the position of the unblocked latitudes at Drake Passage.

As a result of these changes to density structure, oceanic stratification ($\partial\rho/\partial z$) increases in the upper ~1000–1500 m with a slight decrease in the deep ocean below ~1000–1500 m (Figure 3.27).

Under *Gnanadesikan* [1999]'s simple theory of the oceanic pycnocline, a reduction in water mass transformation rate induced by a decrease in wind stress via Ekman transport, particularly the formation of AAIW and SAMW from upwelled waters in the Southern Ocean, causes the depth of the low latitude pycnocline ($\sim \sigma_{2.5} = 38.8\,kg\,m^{-3}$ isopycnal in Figure 3.26) to shoal from a mean depth of −1428 m in the control to −1180 m. This perturbs the north-south density gradient, retarding the Northern Hemisphere overturning since a smaller volume of thermocline water is supplied for conversion to dense waters. Furthermore, a reduced volume of deep water upwelling in the Southern Ocean [*McDermott*, 1996] and the inversely proportional relationship between low latitude upwelling and pycnocline depth [*Levermann and Fürst*, 2010], allows for an increased diapycnal flux into the thermocline causing the cool temperature anomaly in the upper-ocean. Furthermore, reduction in eddy-induced overturning, linked to less steeply sloping isopycnals and thus reduced available potential energy is explained by reduction in pycnocline depth [*Levermann and Fürst*, 2010]. Changes in ACC transport can also be linked to the shoaling of isopycnals because deep ocean temperatures to the north of the ACC cool, whereas deep temperatures to the south remain relatively

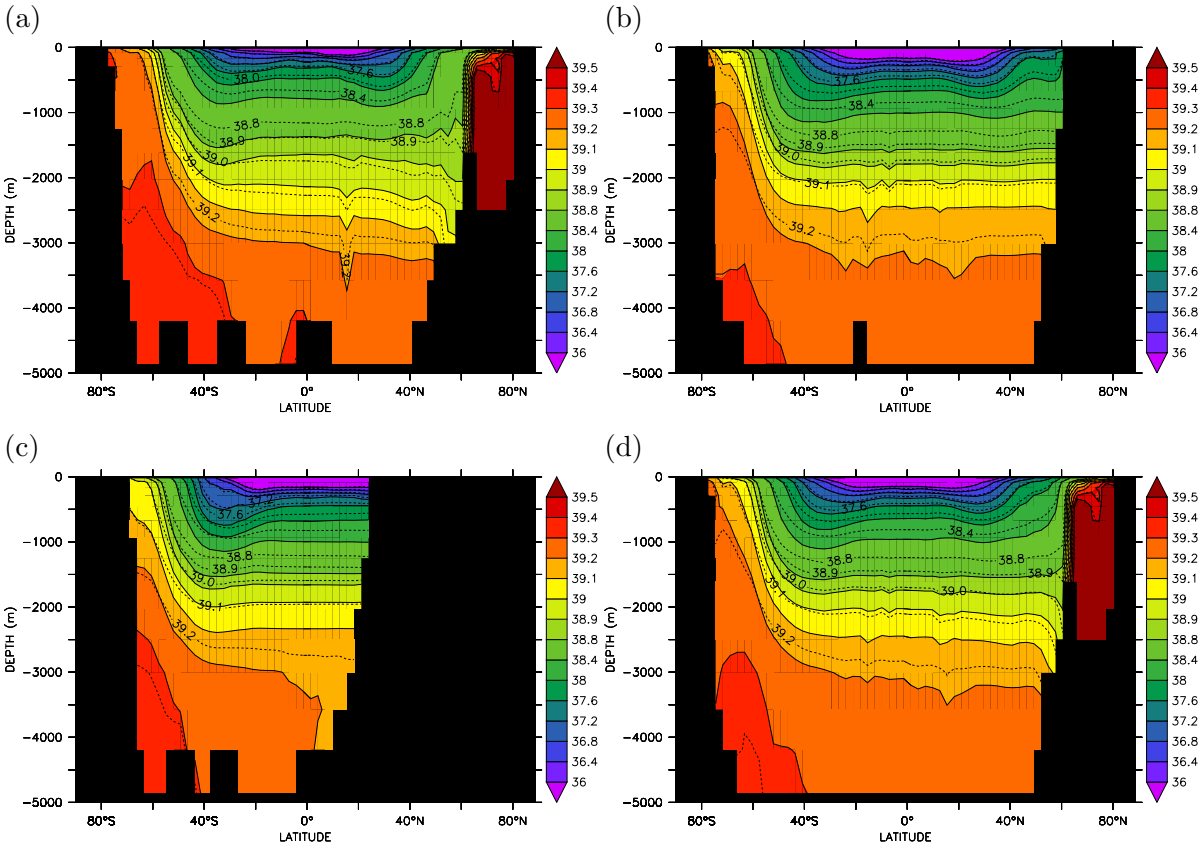

Figure 3.26: Equilibrium MITgcm output for the decreased Southern Ocean wind stress perturbation. Coloured fill and solid contours are Control Run zonally averaged density ($\sigma_{2.5}$, $\mathrm{kg\,m^{-3}}$) with decreased wind stress perturbation density overlay in dashed contours in the (a) Atlantic, (b) Pacific and (c) Indian Oceans, and (d) the Global average.

unchanged, which reduces the meridional density gradient and, due to the smaller deep thermal wind shear, ACC transport decreases [*Gnanadesikan and Hallberg*, 2000].

When the obscuring effect of the heave of isopycnals is removed by considering temperature and salinity anomalies calculated in density coordinates, the converse anomalies occur compared to the increased wind stress perturbation with apparent "pure cooling" of NADW, "pure salinification" of SAMW and the lower thermocline waters, "pure freshening" of AAIW, particularly in the Atlantic Ocean, and finally "pure freshening" of AABW.

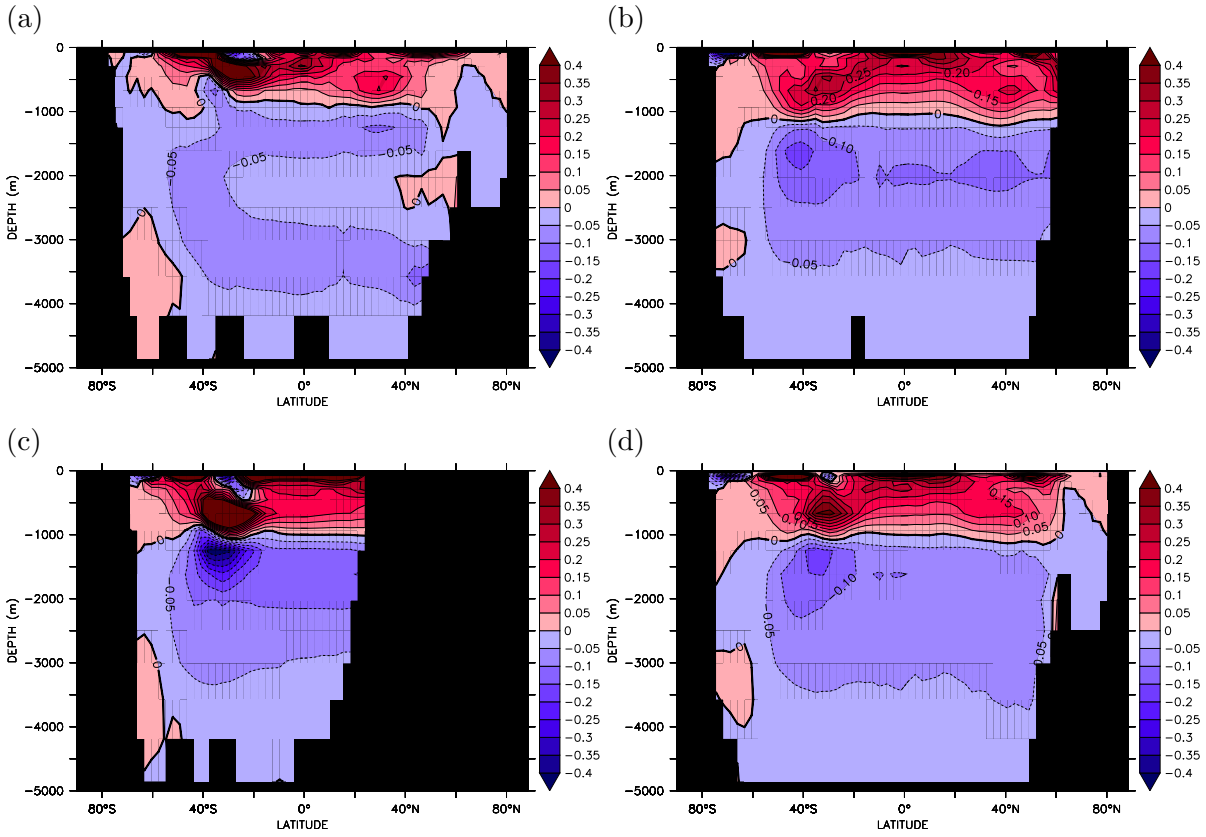

Figure 3.27: MITgcm output for the decreased Southern Ocean wind stress perturbation. Zonally averaged stratification anomalies ($\partial\rho/\partial z$, $\mathrm{g\,m^{-4}}$) for the (a) Atlantic, (b) Pacific, (c) Indian and (d) Global Oceans.

3.2.2 Distribution of biogeochemical tracers and primary productivity

The dwindling oceanic overturning circulation and increased surface stratification produces weaker vertical velocities at the base of the mixed layer (Figure 3.28) that greatly influences the redistribution of passive tracers and adjustment of oceanic and atmospheric carbon reservoirs. The superposition of sluggish eddy and Eulerian-mean components and air-sea buoyancy fluxes [*Karsten and Marshall*, 2002; *Marshall*, 1997] creates a region of more diffuse downwelling south of ~60°S (Figure 3.28a) where regions of weak upwelling have undergone a reversal in direction of flow. The circumpolar pattern of upwelling residual vertical velocities between 45–60°S remains similar to the control but their magnitude is reduced, particularly in the Atlantic and Pacific Oceans and around the Kerguelen Plateau in the Indian Ocean. As before, there are regions where, instead of opposing each other as suggested in Figure 3.24, the eddy and wind-driven

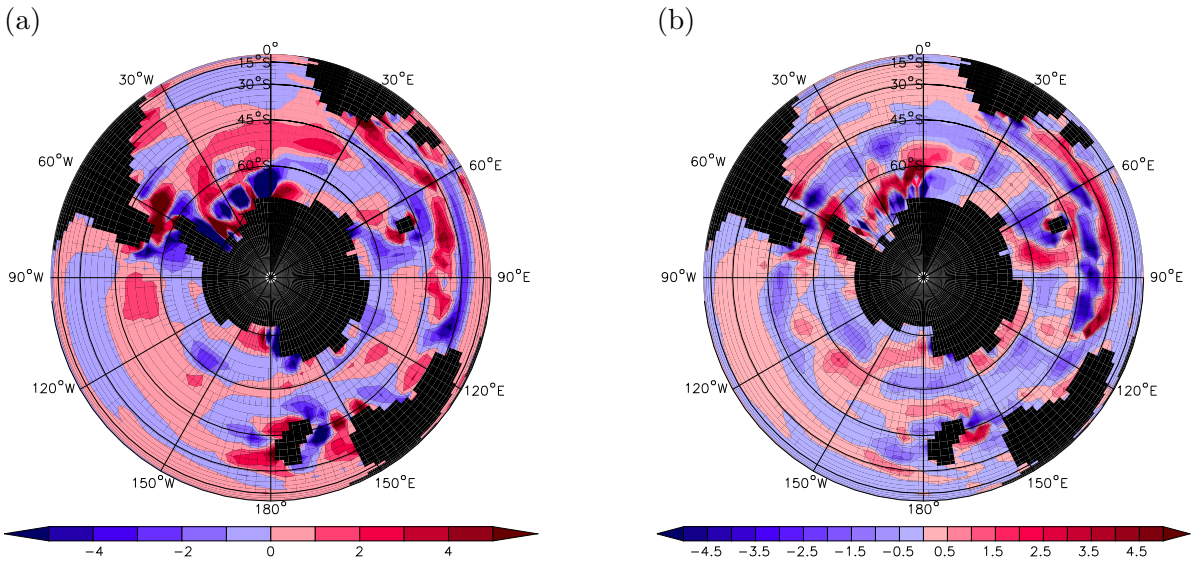

Figure 3.28: Equilibrium MITgcm output for the decreased Southern Ocean wind stress perturbation. (a) residual vertical velocity $\times 1 \times 10^{-6}\,\mathrm{m\,s^{-1}}$ and (b) its anomaly at the base of the mixed layer (~290 m).

circulations act in the same direction, such as in the Atlantic Sector between 45–60°S. The region of largest anomalies (Figure 3.28b) remains in the Indian Ocean, largely attributable to the eddy circulation between 30–45°S.

Generally, the resultant pattern of reduced upwelling south of 45°S and reduced downwelling further north tends to prevent carbon and nutrients from reaching the surface ocean causing negative DIC and phosphate anomalies (Figure 3.29). There is also a reversal of the pattern in surface concentrations in the Southern and Atlantic Oceans and the Indian and Pacific Oceans seen previously (Figure 3.13b and Figure 3.13d) particularly for phosphate concentration. Decreased wind-driven northward Ekman transport in the Southern Ocean deprives the adjacent gyres in the Atlantic, Indian and Pacific Oceans with nutrients and carbon. Since the volume of the northward residual flow [*Dutkiewicz et al.*, 2005a] and flow from regions of intermediate and mode water formation [*Sarmiento et al.*, 2004] control the Atlantic nutrient budget, the reduction of both these supplies coupled with the reduced export of nutrients from the basin contained in NADW (Figure 3.24a) decreases the nutrient and carbon delivery from the Southern Ocean (Figure 3.29b and d). The Indian and Pacific Basins on the other hand receive an enhanced supply of carbon and nutrients from the increased upwelling of deep/bottom waters. From a conservation perspective, since phosphate has no external sources or sinks in this model, the lower concentration of nutrients to the Atlantic must

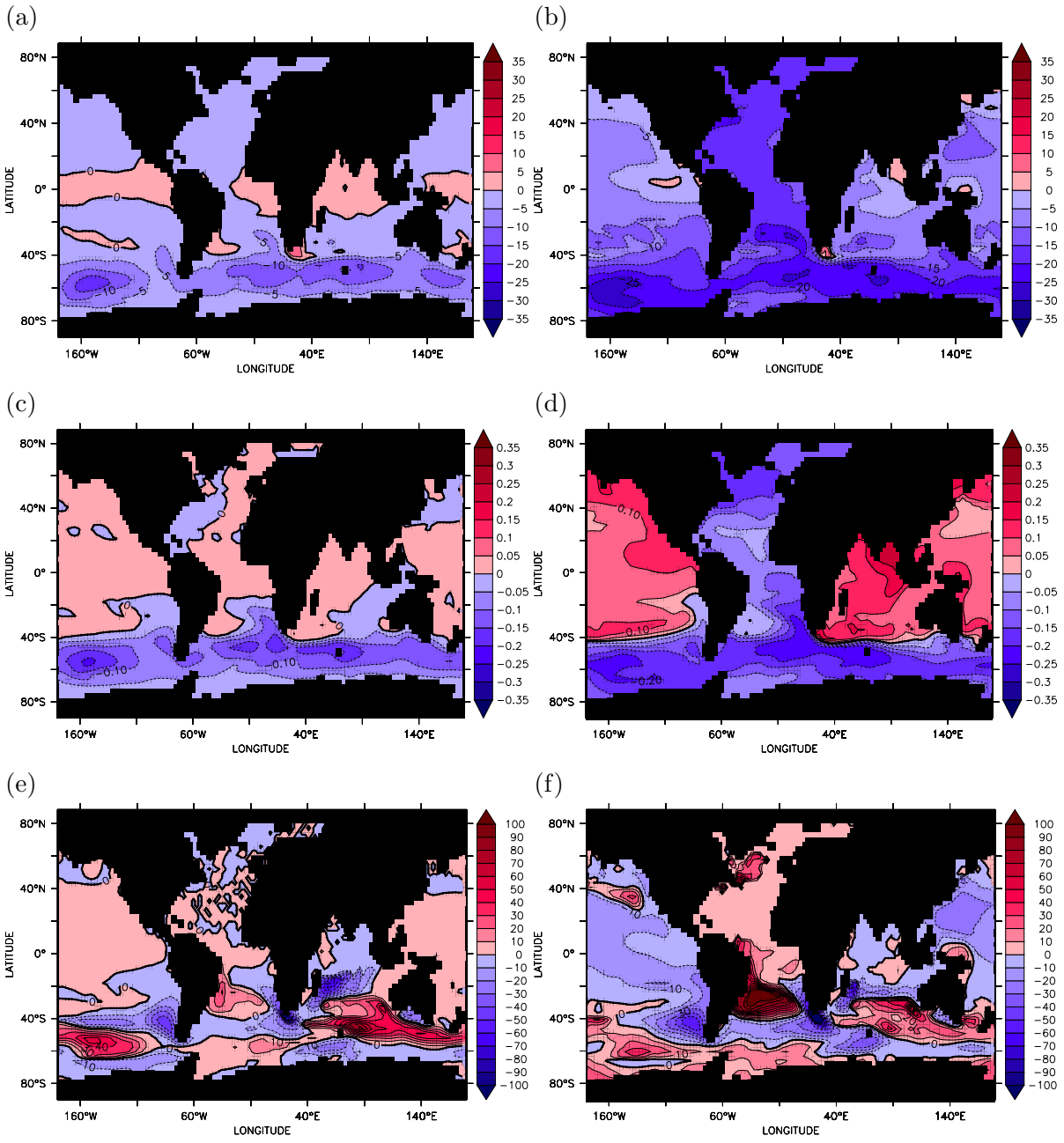

Figure 3.29: Equilibrium MITgcm output for the decreased Southern Ocean wind stress perturbation. Sea surface tracer anomalies near the begining of the perturbation run after 10 years (left column) and near equilibrium after 5000 years (right column) for (a) and (b) dissolved inorganic carbon (mmol C m^{-3}), (c) and (d) phosphate (mmol P m^{-3}) and (e) and (f) dissolved iron (nmol Fe m^{-3}).

be countered by a increase in concentration in the Indo-Pacific basins. Dissolved Iron supply to the Southern Ocean (Figure 3.29e and f) initially increases slightly on average south of 40°S (4.5 nmol Fe m^{-3} at 20010 years) due to increased stratification, reduced upwelling of Fe-deficient deep waters and continued aeolian input, but as adjustment to the wind stress perturbation continues, Southern Ocean iron supply becomes slightly depleted on average (−0.7 nmol Fe m^{-3} at 25000 years). Indeed, increased upwelling in the Pacific Ocean has a similar effect on dissolved Fe concentrations as upwelling in the Southern Ocean under increased wind stress—upwelling of old "micronutrient depleted, macronutrient enriched" waters acts to reduce available iron in the surface waters.

Meridional sections in the Atlantic and Indo-Pacific basins of DIC and phosphate (not shown) are qualitatively similar to those from the control and the increased wind stress perturbation and follow the same pattern with low concentrations at the surface in the subtropical gyres and newly formed deep waters in the North Atlantic, increasing concentrations in the Southern Hemisphere and other upwelling regions and high concentrations in the oldest waters of the deep North Pacific. Furthermore, the sections of iron illustrate the additional role of complexation and scavenging with high concentrations of iron under regions of aeolian deposition such as the Atlantic and North Indian Oceans and in the thermocline as a result of remineralisation. However there are noticeable differences such as (1) decreased tracer concentration (particularly Fe) at 2000 m in the North Atlantic associated with weakened Atlantic meridional overturning circulation, (2) reduced tracer concentrations in the Southern Ocean (particularly DIC and PO_4) and in AAIW (particularly noticeable in the Atlantic) due to decreased upwelling of macronutrient and carbon rich deep waters, (3) increased intrusion of low carbon and nutrient waters between 3000–4000 m, particularly in the Indo-Pacific Oceans, and (4) slight increase in Indo-Pacific carbon and nutrient storage above 1500 m north of 40°N.

Vertical sections of carbon and nutrient anomalies (Figure 3.30) show that carbon and phosphate concentrations are reduced in the Southern Ocean, particularly south of 60°S, due to decreased upwelling (Figure 3.30a and c). These anomalies are gradually advected northward in the Atlantic and returned to the deep ocean by NADW formation. Near the surface in the Indo-Pacific (Figure 3.30b and d), these tracer anomalies are mostly constrained to stay in the Southern Hemisphere by the subtropical gyres, although the negative DIC anomaly does reach further north in the Pacific, while at mid-depths, the concentration of DIC and phosphate both increase possibly explaining why nutrient supply to the surface is slightly reduced when these waters are upwelled. Interestingly,

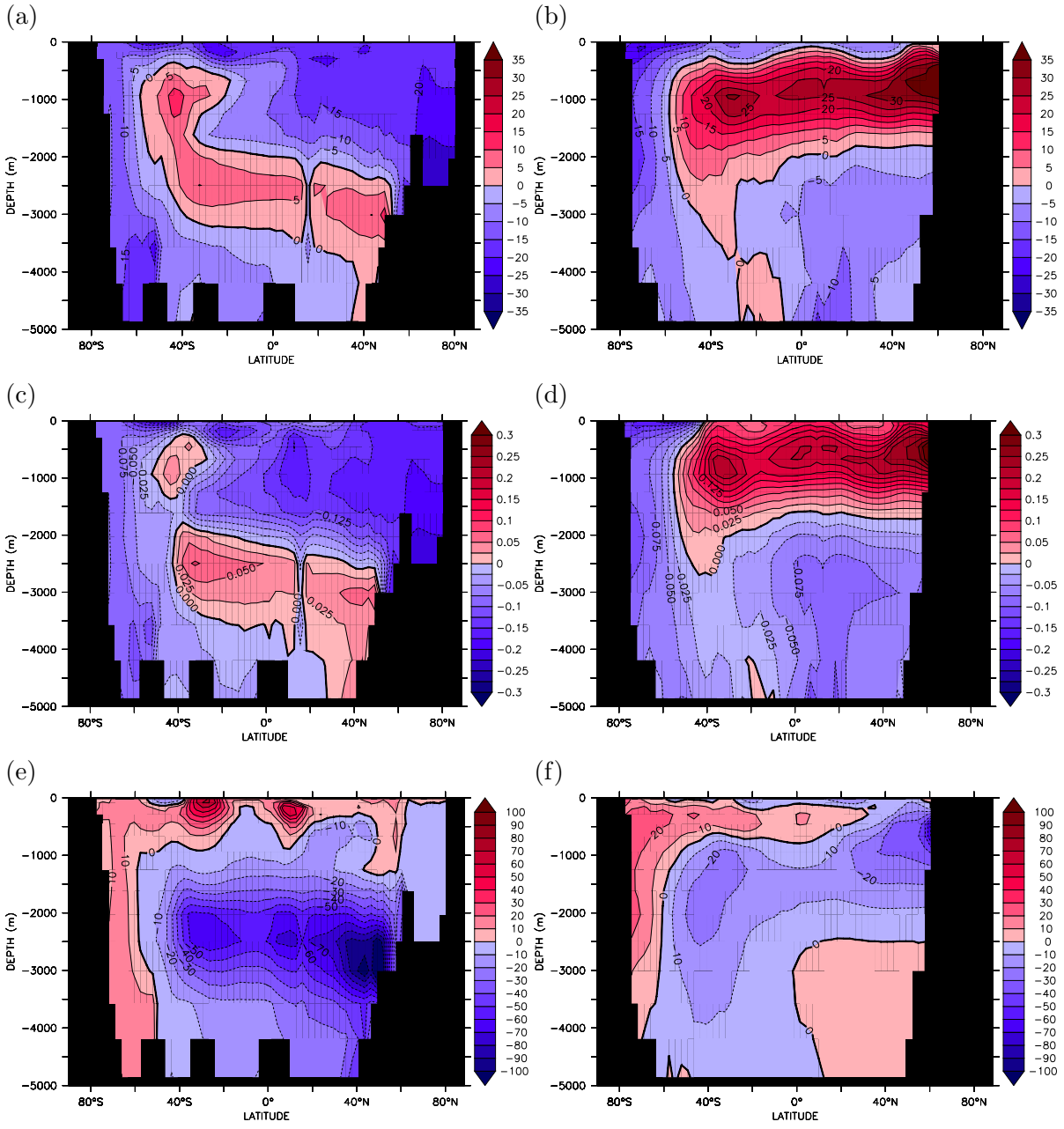

Figure 3.30: Equilibrium MITgcm output for the decreased Southern Ocean wind stress perturbation. Meridional anomaly sections of tracers in the Atlantic Ocean (left column) and in the Indo-Pacific Oceans (right column) for (a) and (b) dissolved inorganic carbon (mmol C m^{-3}), (c) and (d) phosphate (mmol P m^{-3}) and (e) and (f) dissolved iron (nmol Fe m^{-3}).

deep North Pacific concentrations noticeably decrease, which could be a sign of increased ventilation of this region by enhanced AABW circulation, or that these anomalies may be the result of changing isopycnal depths bringing higher concentration mid-depth waters shallower in the water column and decreasing the depth of the Indo-Pacific macronutrient maxima at around 2500 m. Dissolved iron (Figure 3.30e and f), shows a full depth increase in the Southern Ocean and in a tongue in the upper 500–1000 m from reduced export of micronutrient-poor Southern Ocean waters into the upper-ocean. In contrast, in the North Atlantic, the consequences of a reduced overturning circulation can be seen as a decrease in iron concentration due to the extended residence time of NADW flowing south and increased scavenging. There is a similar reduction at ~1500 m in the Indo-Pacific, however, interpretation of these anomalies is once again obscured by the shoaling of isopycnals that has particular impact in the upper 2000 m of the water column and at 40°S, and can be accounted for by calculating anomalies in density coordinates (Figure 3.31), although actual changes in concentration of the individual water masses is complemented by anomalies produced by altered water mass densities.

Accounting for heave, the surface and much of the Southern Hemisphere experience a decrease in both carbon and macronutrient concentration and in the Atlantic there is the clear signal of the decreased supply of DIC and phosphate at the surface and in Subantarctic Mode Waters (-10 to $-15\,\mathrm{mmol\,C\,m^{-3}}$ and -0.075 to $-0.125\,\mathrm{mmol\,P\,m^{-3}}$), and the eventual export to the deep ocean of this negative anomaly in the reduced volume of NADW exported from the North Atlantic (Figure 3.31a and c). Furthermore, the reduced subduction of AAIW compared to the control, down to ~1500 m in all three basins, creates a 5–10 $\mathrm{mmol\,C\,m^{-3}}$ and 0.025–0.05 $\mathrm{mmol\,P\,m^{-3}}$ negative anomaly. As with the increased wind stress perturbation, the DIC and phosphate anomalies in the Atlantic have roughly the same sign, leaving the increases observed in depth coordinates (Figure 3.30a and c) due to the upwards movement of high concentration deep waters. However, these anomalies on isopycnals are supplemented by denser SAMW and NADW, which in both cases results in lower concentration waters entering deeper isopycnals. Indeed, the changing density of AAIW produces a decrease in DIC and phosphate concentrations where anomalies in depth coordinates suggest an increase. Similarly, the very deepest waters in the basin, AABW, show a gain in DIC and phosphate against the inference of increased deep ventilation, also as a result of reduced density waters bringing slightly higher concentration waters into shallower isopycnals. In the Indo-Pacific (Figure 3.31b and d), while the pattern of DIC and phosphate anomalies are broadly consistent to those calculated in depth coordinates, there is a pronounced

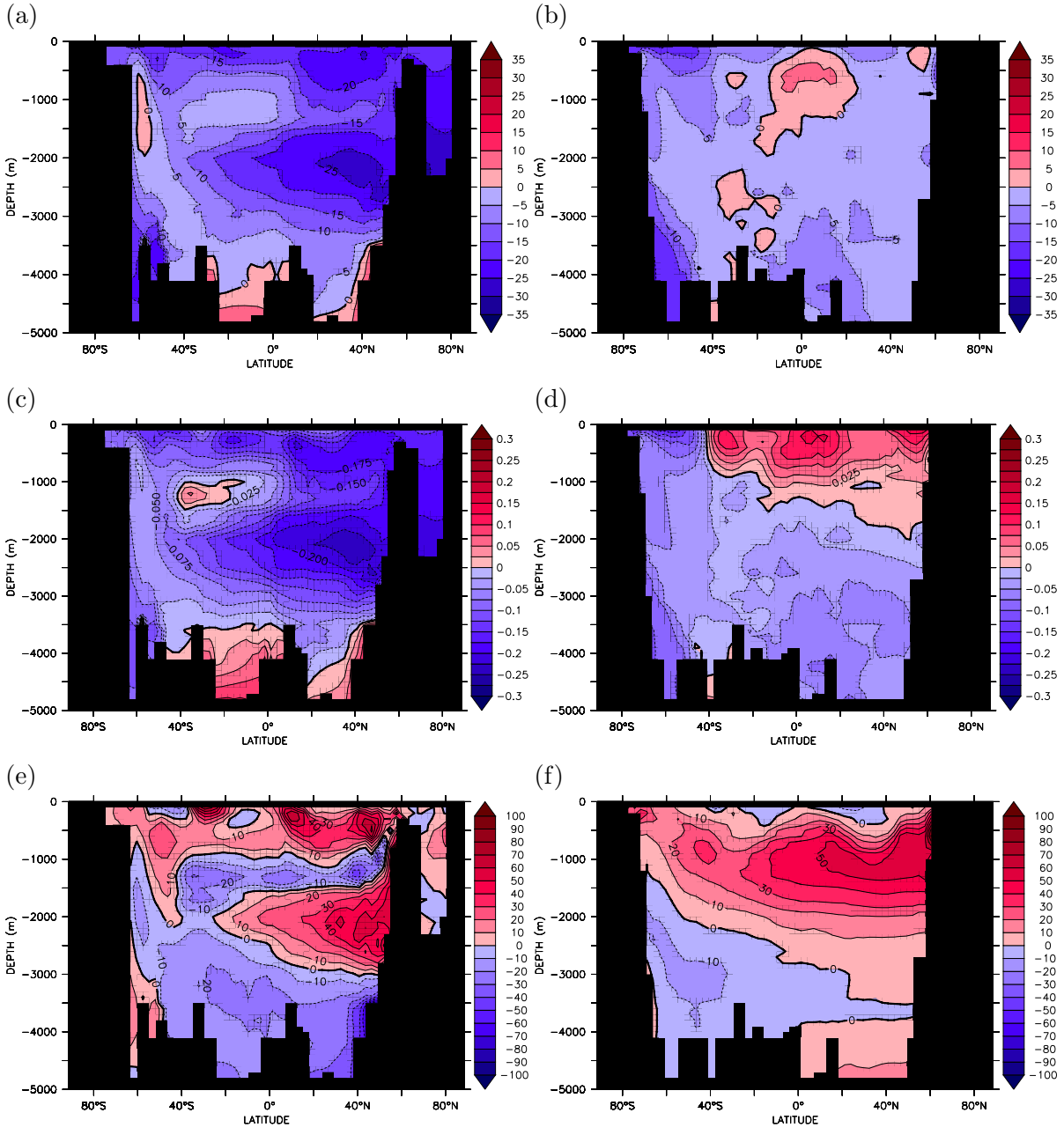

Figure 3.31: Equilibrium MITgcm output for the decreased Southern Ocean wind stress perturbation. Meridional sections of tracer anomaly in the Atlantic Ocean (left column) and in the Indo-Pacific Oceans (right column) calculated and zonally-averaged in density coordinates and regridded back into depth coordinates for (a) and (b) dissolved inorganic carbon (mmol C m^{-3}), (c) and (d) phosphate (mmol P m^{-3}) and (e) and (f) dissolved iron (nmol Fe m^{-3}).

reduction in the upper water column increase in DIC to the north due to shallower mid-depth isopycnals and reduced density AAIW that supplies lighter isopycnals with increased tracer concentrations, thus partially masking the positive anomaly. Elevated carbon and phosphate concentrations at low latitudes due to enhanced upwelling on the other hand appear to be a robust feature since this is a diapycnal process independent of the concentration of tracers being injected isopycnally. Again, more vigorous deep/bottom water circulation promotes a reduction in carbon and macronutrient storage of $-5\,\mathrm{mmol\,C\,m^{-3}}$ and $-0.025\,\mathrm{mmol\,P\,m^{-3}}$ below ~2000–2500 m although in this case since the maximum carbon and macronutrient concentrations are elevated away from the ocean bottom, slightly decreased AABW density causes these lighter isopycnals that are usually enriched with DIC and phosphate to become slightly depleted.

Dissolved iron anomalies (Figure 3.31e and f) retain a modest sub-surface/upper-ocean Southern Ocean increase in concentration of $\sim 10\,\mathrm{nmol\,Fe\,m^{-3}}$ with the upper North Pacific revealing a substantial increase in Fe concentration of 20–30 $\mathrm{nmol\,Fe\,m^{-3}}$ due to reduced dilution of these waters with the low iron concentrations from waters originating in the Southern Hemisphere. This effect is further amplified by increased SAMW density feeding relatively Fe-enriched waters into denser, Fe-depleted isopycnals. Slower NADW circulation in the North Atlantic allows more time for dissolved iron to become scavenged, resulting in the decreased concentration observed at around 1500 m. On the other hand, denser NADW causes the increased concentration in the northern part of the basin because waters rich in aeolian sourced iron are fed into deeper, relatively iron poorer waters. Again, the reverse process also accounts for the decrease in iron concentration of the abyssal waters in the Atlantic and southern Indo-Pacific because the lighter AABW injects relatively iron-poor deep waters into previously shallower, higher iron isopycnals occupied by CDW.

Initially, the interaction between nutrient distributions and the physical circulation produces a decrease in the global rate of primary production of $0.15\,\mathrm{Gt\,C\,yr^{-1}}$ after 10 years (Figure 3.32a) mainly as a reaction to nutrient deprivation in the Southern Ocean and neighbouring subtropical gyres however this is replaced by an increase in productivity for roughly 1000 years, peaking at $0.12\,\mathrm{Gt\,C\,yr^{-1}}$, or roughly 5% higher, 500 years after the start of the reduced wind stress (Figure 3.32a). The majority of this increase occurs in the Indo-Pacific, which benefits from a greater supply of nutrients via upwelling through the thermocline. As the ocean approaches a new steady-state after 5000 years (Figure 3.32c) the rate of net global productivity is in decline and finishes reduced by $0.1\,\mathrm{Gt\,C\,yr^{-1}}$ compared to the control (see also Figure 3.32d). Comparison of the latter

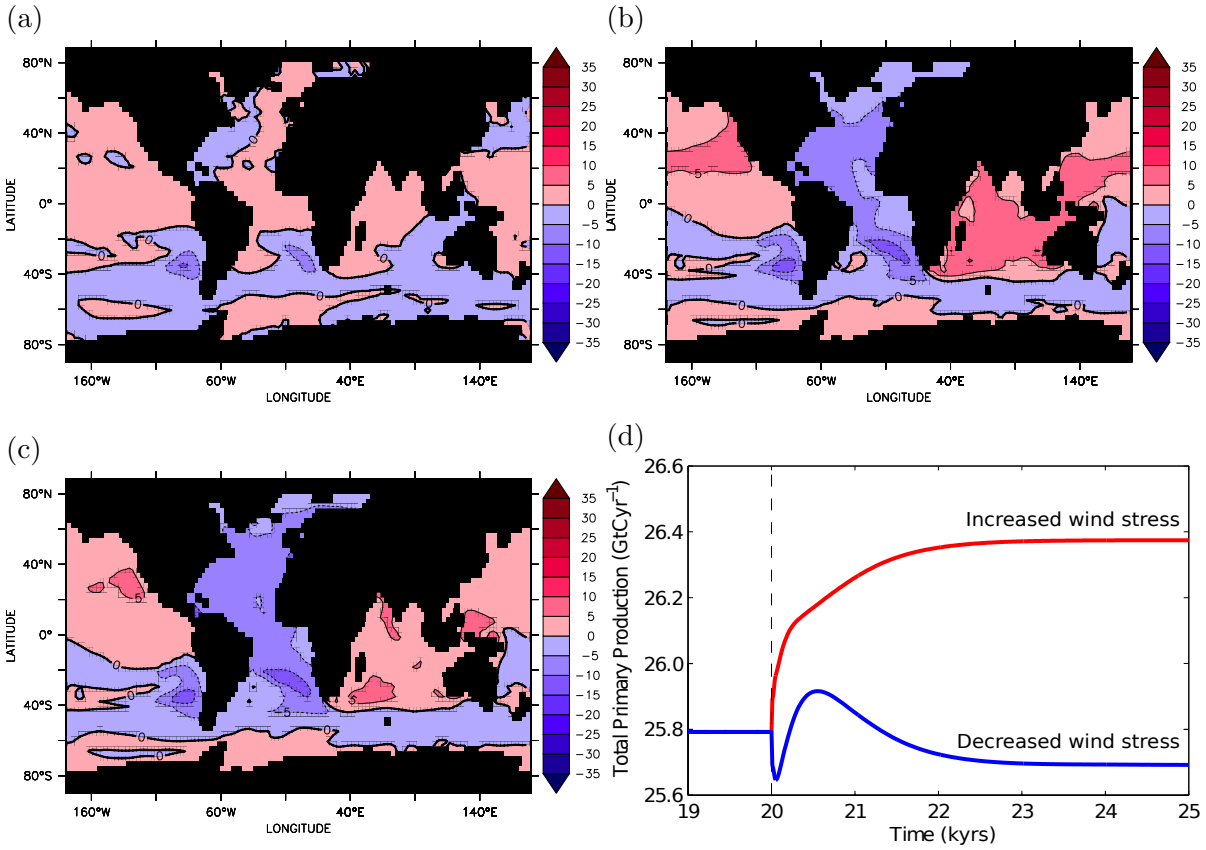

Figure 3.32: MITgcm output for the decreased Southern Ocean wind stress perturbation. Sea surface anomaly of primary production (mmol C m^{-3} yr^{-1}) (a) near the begining of the perturbation run after 10 years, (b) at maximum level after 500 years and (c) near equilibrium after 5000 years; (d) is a timeseries of globally integrated primary production (Gt C yr^{-1}), starting from the control state when t=20 kyrs and applying increased wind stress (red) and decreased wind stress (blue).

stages of adjustment in primary production to the perturbation in wind stress shows that production in the Indo-Pacific, although still enhanced, has decreased slightly due to slight overall reduction in upwelling while the Atlantic has become increasingly less productive due to increased nutrient stress that is compounded by marginally increased productivity south of 60°S. In other words, the integrated productivity anomaly reflects the balance between the more productive Indo-Pacific that dominates the first thousand years after the initial decrease in the Southern Ocean and the less productive Atlantic, which dominates the final part of the adjustment due to gradual decline in meridional overturning circulation and reduced basin nutrient content (Figure 3.32d).

As before, the constant stoichiometric ratios of elements within the biogeochemistry model can be exploited to elucidate changes in circulation and biogeochemical processes by creating additional composite conservative tracers such as regenerated phosphate

(Equation 2.29), estimated using the Apparent Oxygen Utilisation method [*Ito and Follows*, 2005; *Ito et al.*, 2004a], and preformed phosphate (Equation 2.27). Dissolved oxygen concentration anomalies (Figure 3.33a and b) reveal that the decreased Southern Ocean overturning circulation that exports a smaller volume of intermediate and mode waters northwards reduces the ventilation of a large proportion of the upper-ocean while the slightly increased abyssal circulation enhances oxygen concentrations in the deep ocean. Slower Atlantic meridional overturning circulation decreases surface disequilibrium in the North Atlantic caused by convection leading to an increase in dissolved oxygen concentration in the region of 40°N. Anomalies on isopycnals (Figure 3.33c and d) show a similar pattern of decreasing global mid-depth oxygen concentrations and increase in NADW concentration, however the change in density of global bottom waters causes opposing anomalies in the Atlantic and Indo-Pacific. Given the marginally more vigorous abyssal circulation seen in Figure 3.24, oxygen concentration should be observed to increase, especially because these waters are fresher than in the control, which elevates the oxygen saturation concentration. Lighter AABW in the North Atlantic indeed supplies elevated oxygen concentrations into slightly oxygen depleted isopycnals, although because of the ventilating effect of NADW, the change is small. Nevertheless, the oxygen concentration in the deep Southern Ocean in both the Atlantic and Indo-Pacific does increases in concentration.

The assumption of surface saturated dissolved oxygen remains valid because the maximum oxygen disequilibrium concentration anomaly for reduced Southern Ocean wind stress is an order or magnitude smaller than the surface disequilibrium concentration in the control experiment so although the regenerated (and thus preformed) phosphate concentrations retain errors of $0.22\,\mu mol\,l^{-1}$ for the absolute fields ($0.05\,\mu mol\,l^{-1}$ for zonally-averaged fields) and $0.006\,\mu mol\,l^{-1}$ for the anomalies, the change in air-sea gas disequilibrium of oxygen driven by perturbed ocean circulation is comparatively small rendering comparison between the control and perturbation experiments acceptable.

Regenerated phosphate concentrations calculated from Apparent Oxygen Utilisation using Equation 2.28 and Equation 2.29 appear qualitatively similar to those for the control run and the increased wind stress perturbation and are low in the newly ventilated water masses at the surface and at depth, such as NADW, increasing as biogenic phosphate is remineralised and accumulated in the thermocline and in the deep waters that are advected around the global ocean, with the highest concentration found in the deep North

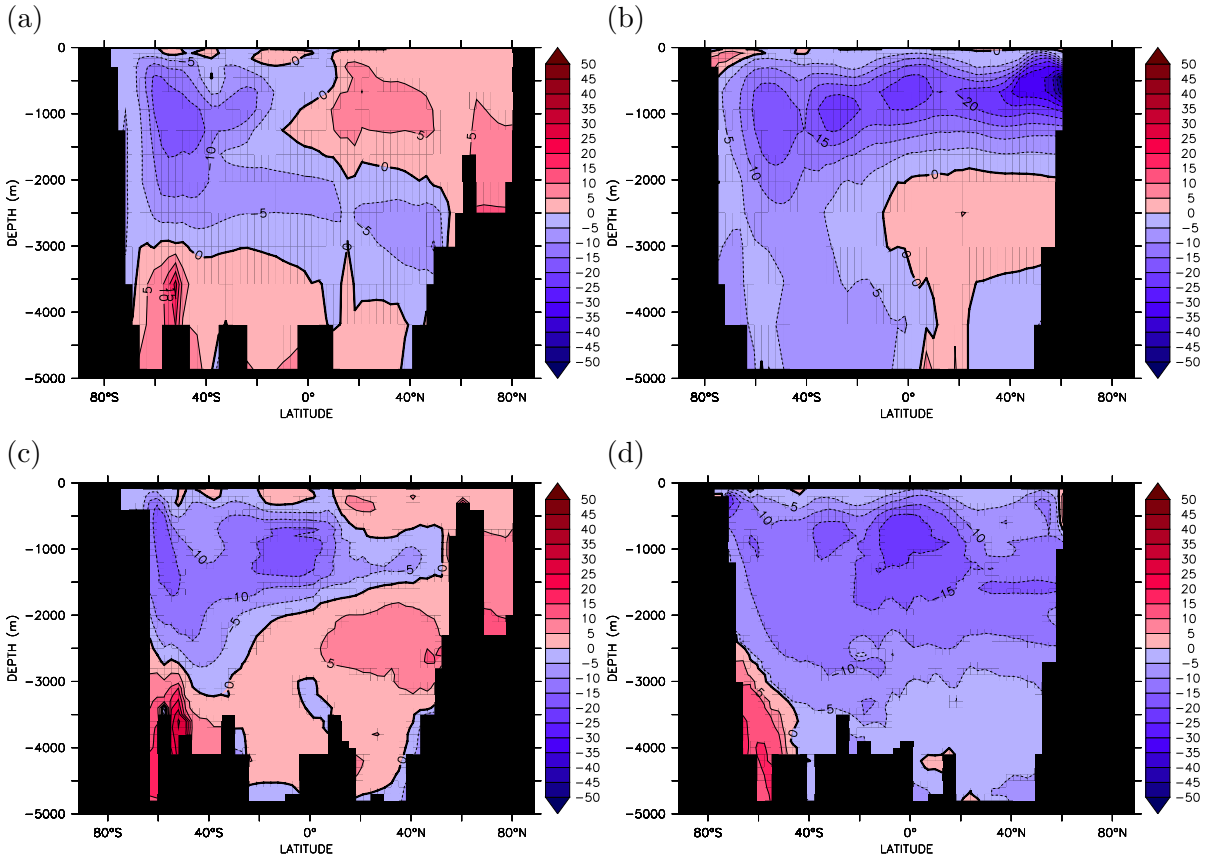

Figure 3.33: Equilibrium MITgcm output for the decreased Southern Ocean wind stress perturbation. Meridional sections of dissolved oxygen anomaly (mmol O m^{-3}) in the Atlantic Ocean (left column) and in the Indo-Pacific Oceans (right column) calculated in (a) and (b) depth coordinates, and (c) and (d) calculated and zonally-averaged in density coordinates and regridded back into depth coordinates.

Pacific. The concentration of preformed phosphate, calculated from Equation 2.27, is also low at the surface and in the waters formed in the North Atlantic and elevated in the deep and intermediate waters formed in the Southern Ocean.

However, the anomalies of regenerated and preformed phosphate in the Atlantic (Figure 3.34a and c) and Indo-Pacific Oceans (Figure 3.34b and d) show a greater proportion of surface nutrients returning to the ocean interior by remineralisation. Concurrently the concentration of nutrients returned by subduction and water mass formation is reduced in the deep ocean, with only a slight increase at the surface in the North Indian and Pacific Oceans, which is probably accounted for by increased upwelling of nutrients there. Recalculating these anomalies in density coordinates (Figure 3.35) highlights that there is a true increase in regenerated phosphate in the upper 2000 m of the global ocean with the reduced primary production in the Atlantic evident in the decreased

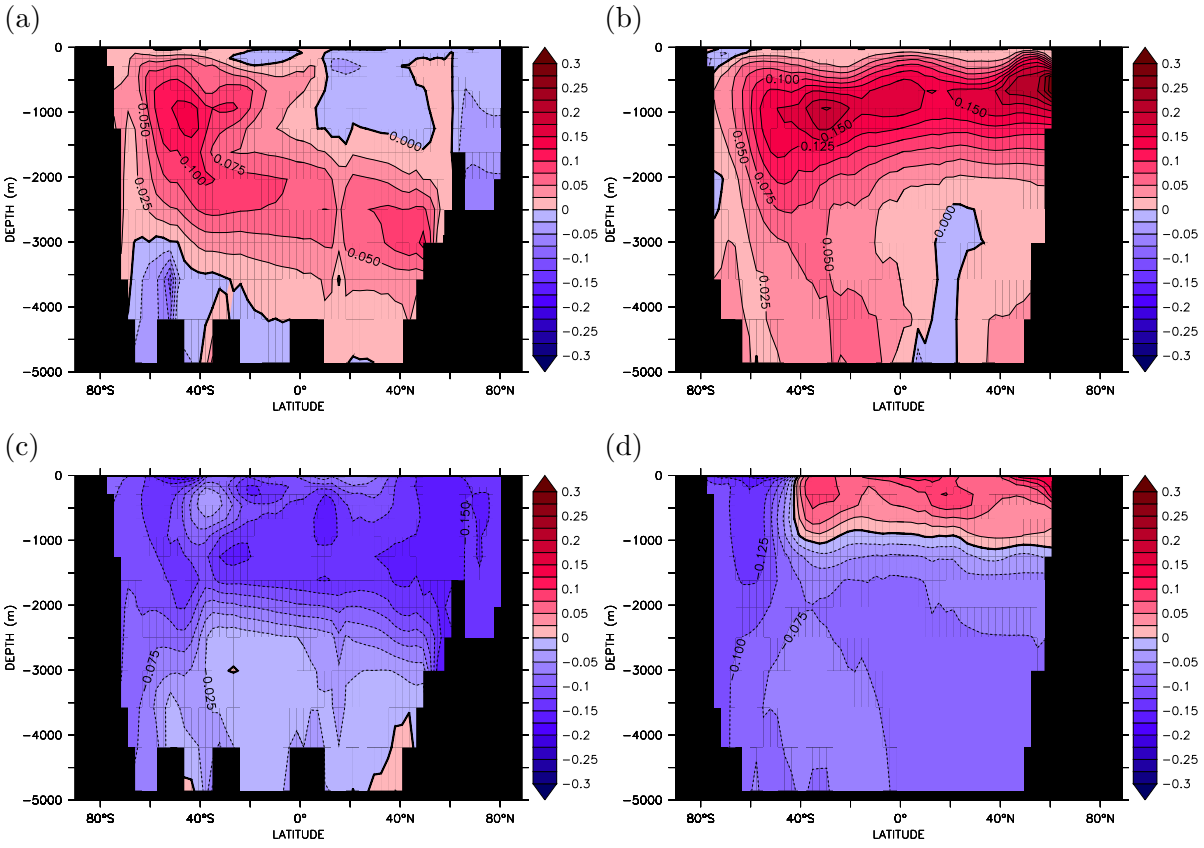

Figure 3.34: MITgcm output for the decreased Southern Ocean wind stress perturbation. Meridional sections of tracer anomaly in the Atlantic Ocean (left column) and in the Indo-Pacific Oceans (right column) for (a and b) regenerated phosphate anomaly (mmol P m^{-3}) calculated from Apparent Oxygen Utilisation using Equation 2.28 and Equation 2.29, and (c and d) preformed phosphate anomaly (mmol P m^{-3}) calculated using the regenerated component and Equation 2.27.

concentration of regenerated nutrients carried in NADW. Reduced Atlantic overturning causes a concurrent decline in preformed phosphate in the Atlantic, while sluggish Southern Ocean residual circulation causes a negative anomaly in the intermediate and mode waters of the Atlantic and Indo-Pacific basins. Employing the ratio of globally-averaged concentration of regenerated phosphate to total phosphate [*Ito and Follows*, 2005], the efficiency of the soft tissue pump in this perturbation is 38.5%, an increase of 2.8%, despite decreased decreased global productivity, primarily attributed to the lessened volume of the interior ocean ventilated by Southern Ocean intermediate and mode waters that are enriched with preformed nutrients.

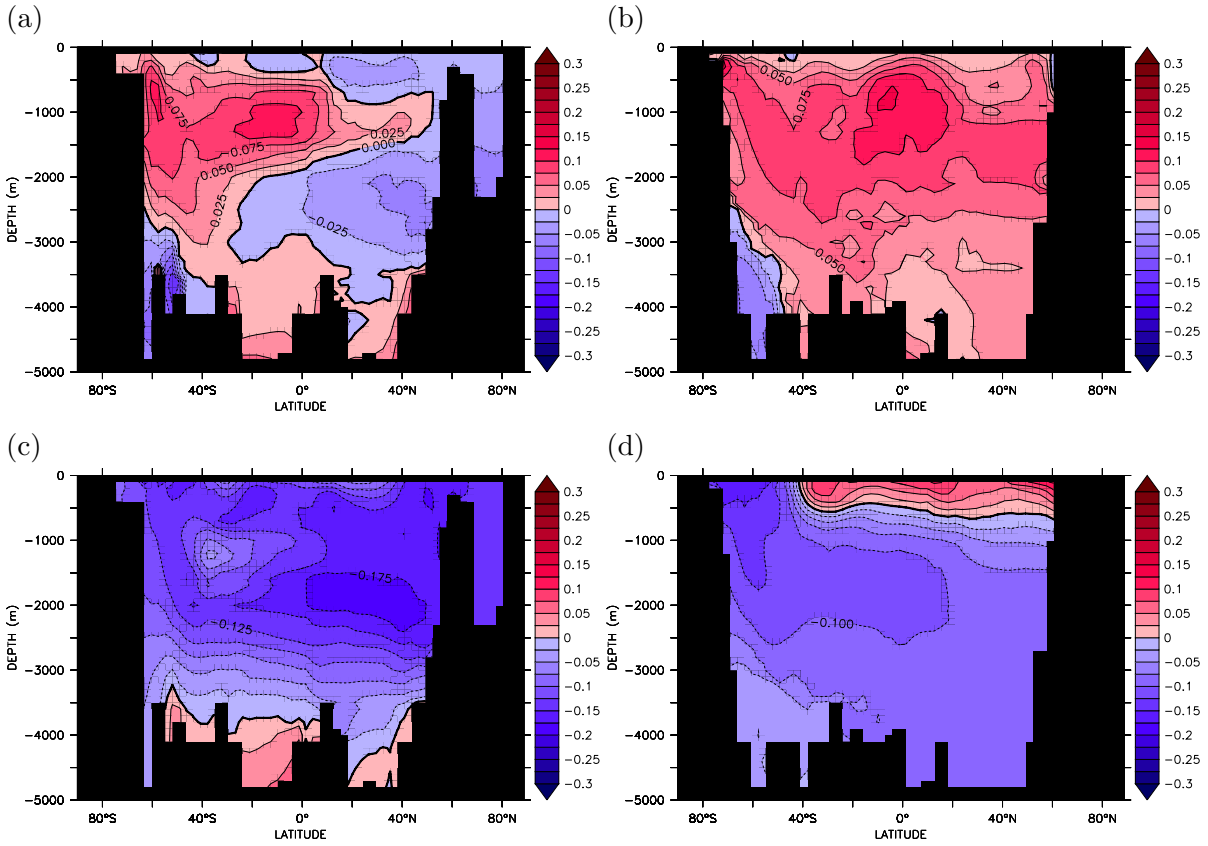

Figure 3.35: MITgcm output for the decreased Southern Ocean wind stress perturbation. Meridional anomaly sections of tracers in the Atlantic Ocean (left column) and in the Indo-Pacific Oceans (right column) calculated and zonally-averaged in density coordinates and regridded back into depth coordinates for (a and b) regenerated phosphate anomaly ($\mathrm{mmol\,P\,m^{-3}}$) calculated from Apparent Oxygen Utilisation using Equation 2.28 and Equation 2.29, and (c and d) preformed phosphate anomaly ($\mathrm{mmol\,P\,m^{-3}}$) calculated using the regenerated component and Equation 2.27.

3.2.3 Appraisal of the air-sea flux of carbon dioxide

The response of the air-sea flux of carbon dioxide to altered circulation and primary production follows a similar, but inverse, pattern of changes as previously described for the increased wind stress perturbation. In particular the positive values of the tendency of DIC due to air-sea exchange anomaly in the Southern Ocean (Figure 3.36a and b) dominate the total tendency of surface concentration anomaly with modulation by virtual flux anomalies due to surface relaxation of salinity. Of course, this region of increased invasion of atmospheric CO_2 is co-located with the reduced Southern Ocean overturning and reduced upwelling of carbon rich deep waters. The North Atlantic also shows an increase in oceanic carbon uptake that can be linked to both the solubility-driven ocean to atmosphere flux resulting from reduced northward heat transport. The integrated

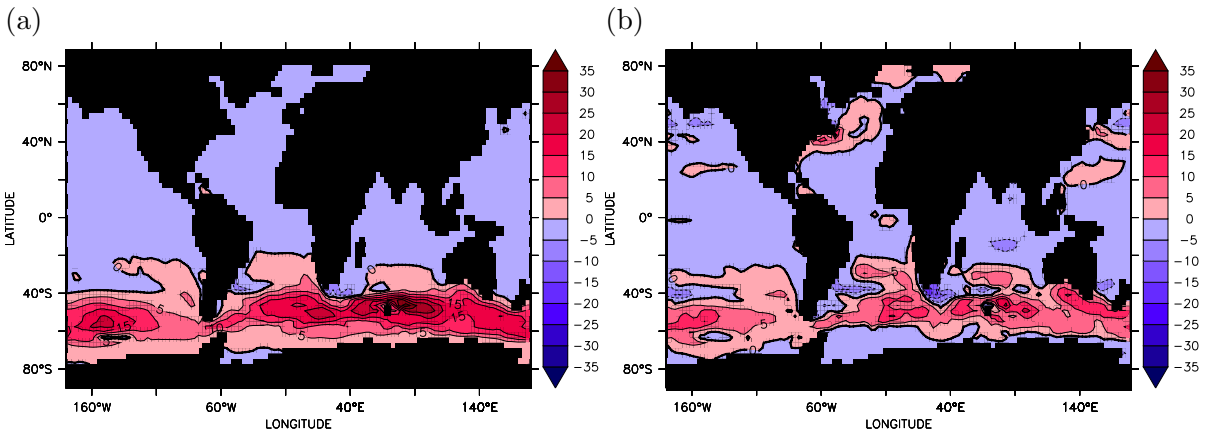

Figure 3.36: Equilibrium MITgcm output for the decreased Southern Ocean wind stress perturbation. Anomalies of the surface tendency of carbon concentration due to air-sea exchange (a) near the begining of the perturbation run after 10 years and (b) near equilibrium after 5000 years, where negative values indicate oceanic outgassing, causing a decrease in surface concentration, while positive values indicate oceanic uptake.

readjustment of the air-sea flux of carbon removes 34.67 Gt C from the atmosphere over 5000 years, before the atmosphere and ocean return to a stable-state of zero global net fluxes.

The reduced circulation not only exerts a control of the atmosphere-ocean CO_2 concentration gradient by redistributing DIC at the sea surface, but also affects the degree of equilibriation of the oceanic carbon and atmospheric carbon reservoirs. Evaluating the absolute disequilibrium concentration using the tracer ΔC^*_{pref} (Equation 2.33, [*Gruber et al.*, 1996]) produces results similar to those in Figure 2.14a and b. However the anomalies (Figure 3.37) calculated using the ΔC^*_{preind} formulation (Equation 2.36) brings to light the widespread decrease of CO_2 disequilibrium between the atmosphere and ocean due to decreasing overturning circulation in the Southern Ocean and North Atlantic along pressure surfaces (note the positive anomalies due to heave) and isopycnals, with the more sluggish circulation allowing more complete gas transfer to occur. As with the increased wind stress perturbation, the change in disequilibrium actually opposes the trend in atmospheric CO_2 so that the globally integrated change in carbon due to disequilibrium is a decrease of 33.94 Gt C, which is roughly equal to the amount of carbon gained by the ocean due to air-sea exchange at the end of the integration.

To observe where the additional carbon from the atmosphere is stored in the ocean, the potential soft tissue and potential carbonate pumps are again subtracted from the DIC concentration to evaluate the tracer $C_{gas\ exch}$ (Equation 2.37, [*Gruber and Sarmiento*,

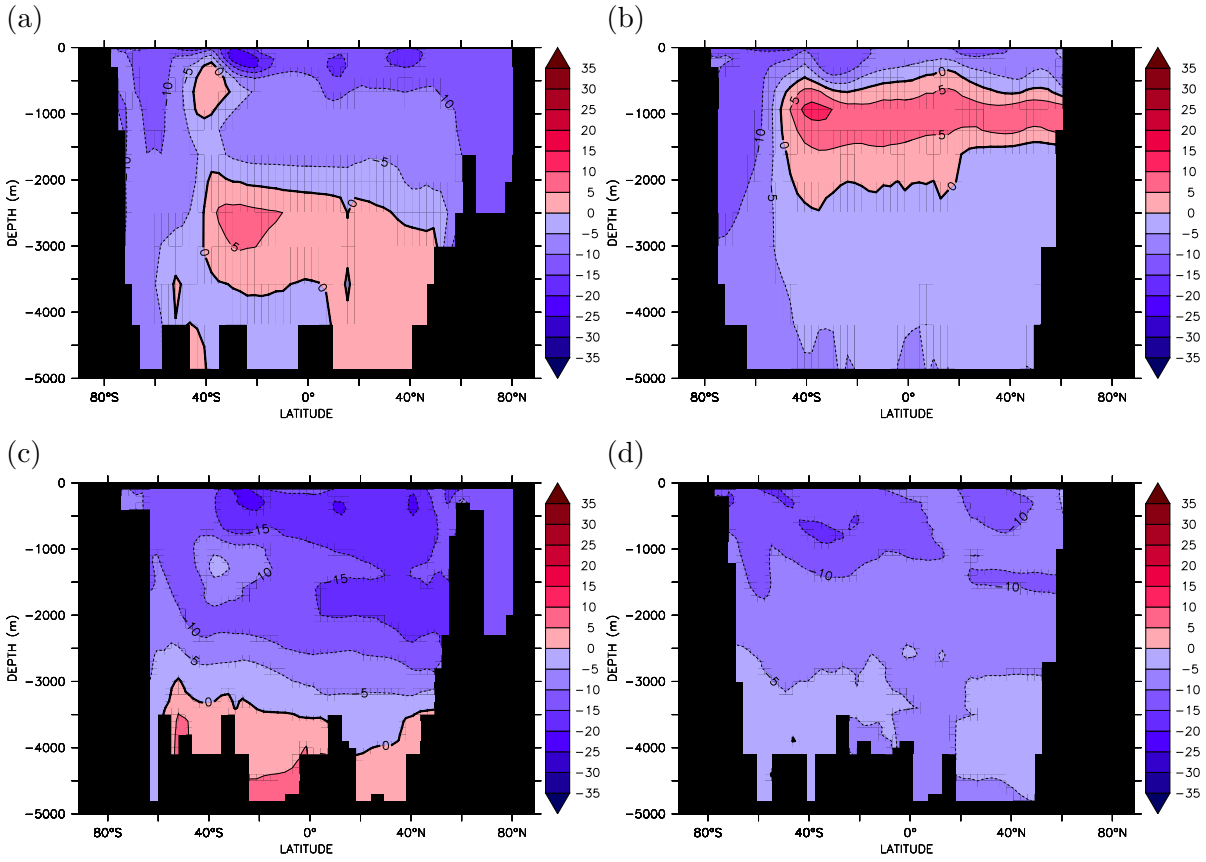

Figure 3.37: Equilibrium MITgcm output for the decreased Southern Ocean wind stress perturbation. Air-Sea disequilibrium concentration of Dissolved Inorganic Carbon anomalies in the Atlantic (left column) and Indo-Pacific Oceans (right column) at the time interior water masses were last at the surface, diagnosed as the difference between the DIC concentration in equilibrium with the atmosphere and the observed DIC concentration after "correction" for the effects of organic carbon remineralisation and calcium carbonate dissolution. These anomalies ($\mathrm{mmol\,C\,m^{-3}\,yr^{-1}}$) were calculated using control "preindustrial" concentrations in (a and b) depth coordinates and (c and d) calculated and zonally-averaged in density coordinates and regridded back into depth coordinates.

2002; *Gruber et al.*, 2009; *Mikaloff Fletcher et al.*, 2007]). The distribution of $C_{gas\ exch}$ is similar to that calculated for the increased wind stress perturbation, except for enhanced concentrations between 1000–3000 m (Figure 3.38). Although the magnitude of the increase in DIC due to gas exchange with the atmosphere is slightly reduced from 5–7.5 $\mathrm{mmol\,C\,m^{-3}}$ to 2.5–5 $\mathrm{mmol\,C\,m^{-3}}$ when the anomaly is calculated on isopycnal surfaces rather that pressure surfaces, the signal of increased oceanic uptake of CO_2 accumulates particularly in mid-depth AAIW and NADW water masses and, interestingly, centred at approximately 10°S in the Indian Ocean in both cases. The globally integrated anomaly of $C_{gas\ exch}$ after 5000 years indicates a total of 34.47 Gt C is accumulated in the ocean, which also compares very well with the value of integrated air-sea

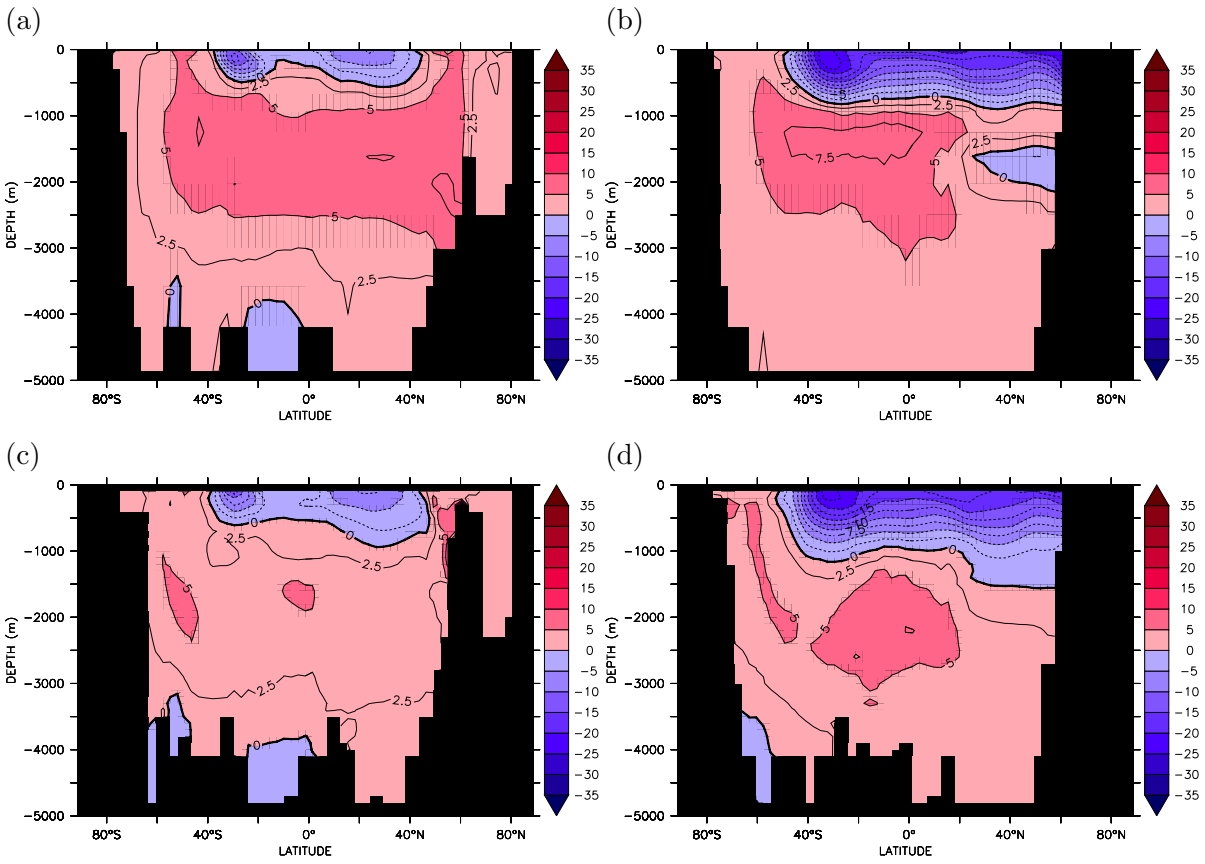

Figure 3.38: Equilibrium MITgcm output for the decreased Southern Ocean wind stress perturbation. Meridional sections of the quasiconservative tracer $C_{gas\ exch}$ anomaly ($\mathrm{mmol\,C\,m^{-3}}$) in the Atlantic (left column) and Indo-Pacific (right column) Oceans calculated from Equation 2.37 and (a and b) calculated and zonally-averaged in depth coordinates and (c and d) calculated and zonally-averaged in density coordinates and regridded back into depth coordinates.

CO_2 flux during the perturbation.

3.3 Summary

After 5000 years, with increased wind stress applied to the Southern Ocean, atmospheric CO_2 concentration had increased by 15.6 µatm to 293.6 µatm. Enhanced wind stress resulted in more vigorous, but opposing Eulerian-mean and eddy-driven overturning circulations in the Southern Hemisphere but incomplete compensation led to doubling of the residual overturning circulation. AABW formation is also slightly decreased producing reduced abyssal ocean ventilation. Depression of the low-latitude pycnocline due to greater water mass export from the Southern Ocean decreases upper-ocean stratification

and slightly enhances the formation and export of dense waters from the North Atlantic, returning the greater volumes of AAIW and SAMW to the deep ocean. Upwelling to the south of the ACC, although spatially complex, brings carbon and macronutrient rich, but slightly iron deficient, waters to the surface. Lack of light and existing iron stress conspire to limit Southern Ocean primary production, however, these unutilised nutrients supply enhanced production in the Atlantic basin through surface Ekman and SAMW flow. Indo-Pacific primary production is largely reduced because of a reduction in upwelling of deep waters through the pycnocline, which is the primary source of nutrients there. Despite net increased global primary production, dominated by the Atlantic basin, the increased volume of the ocean interior ventilated by Southern Ocean water masses with a high concentration of unutilised macronutrients causes a decrease in the efficiency of the soft tissue pump that promotes ocean to atmosphere transfer of CO_2. This enhanced flux occurs south of 40°S where deep waters with a high carbon content regain contact with the atmosphere and exhale CO_2 because primary production is incapable of sequestering the additional carbon back into the deep ocean. However this is offset by roughly 50% by enhanced disequilibrium because the faster overturning prevents complete outgassing from the ocean from occurring, thus locking carbon in the ocean interior due to water mass formation and limiting the extent of atmospheric carbon dioxide increase. Interestingly, although atmospheric CO_2 increases, changes to the abyssal circulation result in an increase in carbon and macronutrient concentrations in the deep Northern Indo-Pacific Oceans, partially as the result of heave but also due a real change in concentration through decreased ventilation by AABW.

With reduced Southern Ocean wind stress, atmospheric CO_2 concentration decreased by 16.3 µatm to 261.7 µatm. More sluggish Eulerian-mean and eddy circulations although slower, compensate more completely leading to a much reduced residual overturning circulation, although abyssal circulation increases marginally. Reduced AAIW and SAMW formation from the Southern Ocean results in shoaling of the low latitude pycnocline, a subsequent increase in upper-ocean stratification and slowing of NADW formation and the Atlantic overturning circulation. Reduced upwelling of carbon and macronutrient rich waters in the Southern Hemisphere affects Southern Ocean productivity, with a marginal increase south of 60°S and a decrease around 40°S. However, reduced supply of nutrients to the Atlantic through decreased preformed nutrient concentrations in the surface Ekman and SAMW flow into the basin, which accounts for reduced upwelling and increased nutrient utilisation results in a dramatic decrease in productivity, while increased low latitude upwelling in the Indo-Pacific leads to enhanced primary production there. The combination of these anomalies results in a slightly lower level of global

primary productivity, however the efficiency of the soft tissue pump is increased somewhat through a decrease in ventilation of the interior ocean by Southern-sourced water masses with lower preformed nutrient concentrations thus promoting oceanic uptake of atmospheric CO_2. Nevertheless, reduced residual overturning increases the completion of CO_2 exchange with the atmosphere, effectively a flux from the ocean to the atmosphere, which compensates 50% of the net invasion of carbon dioxide south of 40°S. Interestingly, much of the atmospheric carbon is stored around 1500–2000 m depth, associated with intermediate waters, and is largely concentrated in the North Indian Ocean while the abyssal concentration of DIC and phosphate actually decreases despite decreased atmospheric CO_2 thanks to stronger ventilation by AABW.

Chapter 4

Response of the Global Carbon Cycle to Southern Ocean Wind Stress Position

Previously, Chapter 3 increased and decreased the zonal wind stress *in situ* as the simplest method to perturb the residual circulation of the Southern Ocean. While there is some evidence for the extratropical Southern Hemisphere westerlies changing in such a way [*Menviel et al.*, 2008; *Otto-Bliesner et al.*, 2006], recent effort has focussed on the effect of latitudinal migration of the winds in response to warming or cooling climate [*Anderson et al.*, 2009; *Sigman and Boyle*, 2000; *Toggweiler et al.*, 2006], despite equivocal direct paleoceanographic records of wind location. In this set of perturbations the residual mean flow was modulated by changing the meridional position of the wind stress maximum in the Southern Ocean by a nominal ±10° shift (Figure 4.1) and then integrating the model until a new stable state was reached. The entire Southern Hemisphere control wind stress was shifted by three grid-points north or south and then the edges were relaxed back to the control values just north of the equator. Unlike the wind stress magnitude perturturbations, the wind speed field was also modified in the same way to ensure enhanced gas exchange in the associated latitude bands. Again, despite these relatively large changes in wind stress position, only modest changes in Southern Ocean circulation and atmospheric CO_2 concentrations are induced. While the system approaches equilibrium after approximately 5000 years, where the following analysis will concentrate, the majority of the adjustment actually occurs in the first five centuries. After 5000 years, with northward-shifted wind stress (Figure 4.1a) applied

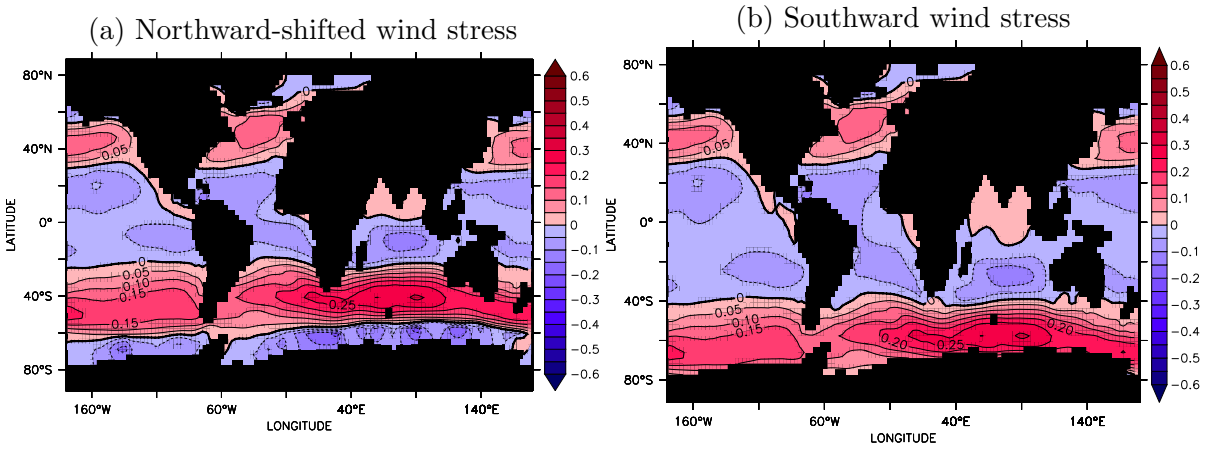

Figure 4.1: Perturbed zonal wind stress inputs ($\mathrm{N\,m^{-2}}$) (a) annual mean zonal wind stress with 10° northward shift in the Southern Ocean with the polar easterlies linearly interpolated to provide complete coverage adjacent to Antarctica and (b) annual mean zonal wind stress with 10° southward shift in the Southern Ocean, again with interpolation of the subtropical easterlies over the Southern Hemisphere gyres.

to the Southern Ocean, atmospheric CO_2 concentration had increased by 8.0 µatm to 286.1 µatm, whilst with southward-shifted Southern Ocean wind stress (Figure 4.1b) atmospheric CO_2 concentration decreased by 9.6 µatm to 268.4 µatm.

4.1 Northward-shifted Southern Hemisphere westerlies

4.1.1 Response of oceanic circulation and density structure

Northward-shifted wind stress with the same peak magnitude in the Southern Hemisphere causes an 8.4°, or approximately a 3 grid-point, northward shift and 14 Sv enhancement of the maximum northward Ekman transport, due to reduced Coriolis parameter (Figure 4.2a), with a similar shift in the compensating eddy return flow and both shift and enhancement of Ekman pumping. The ACC also migrates northwards (Figure 4.2b) particularly in the South Atlantic and Indian Oceans. The shift also acts to accelerate the subtropical gyres in the Southern Hemisphere, with significantly enhanced westward flow in the North Indian Ocean, and leads to a small increase in velocity of the surface western boundary current in the North Atlantic.

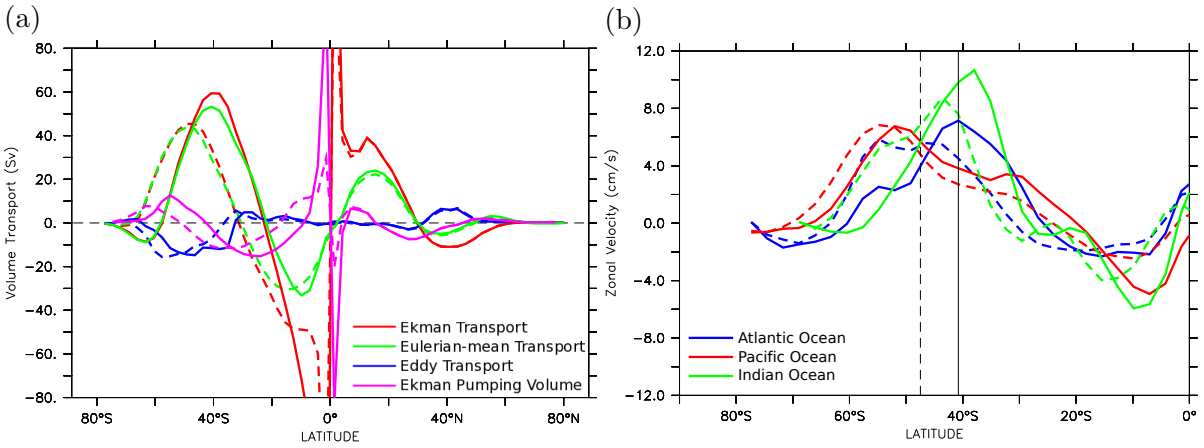

Figure 4.2: Meridional transports and surface zonal velocity for northward-shifted Southern Ocean winds. (a) Perturbed (solid) and Control (dashed) meridional Ekman transports calculate directly from wind stress (red), Eulerian-mean (green) and GM eddy transports (blue) and zonally integrated Ekman pumping (purple) for northward-shifted Southern Ocean Winds (Sv) in the surface Ekman layer and (b) zonally-averaged zonal residual velocity ($\mathrm{cm\,s^{-1}}$) averaged over the surface 100 m from the control run (dashed) and at steady state after 5000 years (solid) of northward-shifted winds in the Atlantic (blue), Pacific (red) and Indian (green) Oceans. Vertical black lines indicate the control (dashed) and perturbed (solid) Global meridional position of the Southern Hemisphere maximum in zonal velocity, used as a surrogate for the position of the ACC.

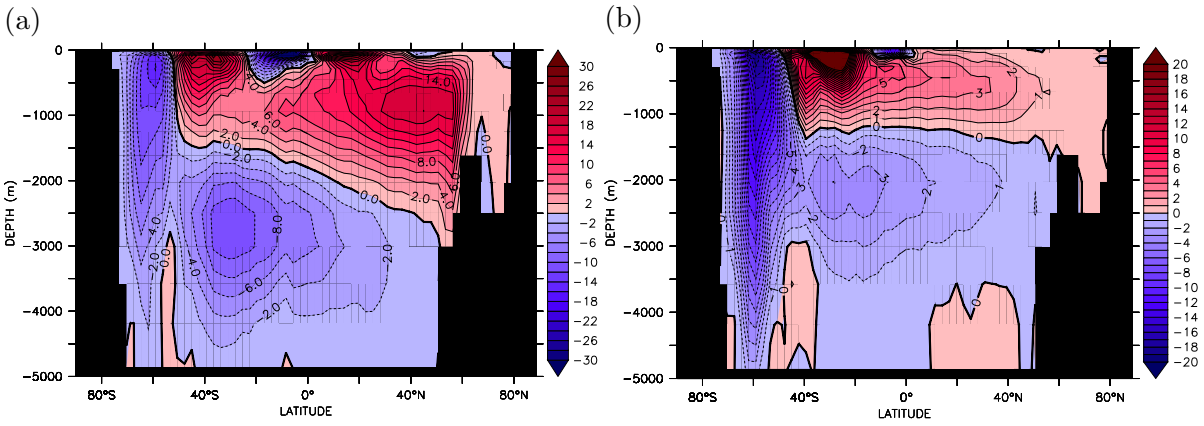

Figure 4.3: Equilibrium MITgcm output for the northward-shifted Southern Ocean wind stress perturbation (a) Zonal average residual meridional overturning stream function (Sv) and (b) Zonal average residual meridional overturning stream function anomaly (Sv).

These surface transports are translated into a northward-shifted and more intense (~11 Sv) Southern Ocean overturning cell (Figure 4.3a) that is significantly shallower than in the control by ~50%, extending no deeper than 1500 m. This pattern of circulation is reminiscent of the changes that occur in coarse resolution numerical simulations when Drake Passage is blocked [*Cox*, 1989; *Gill and Bryan*, 1971; *McDermott*,

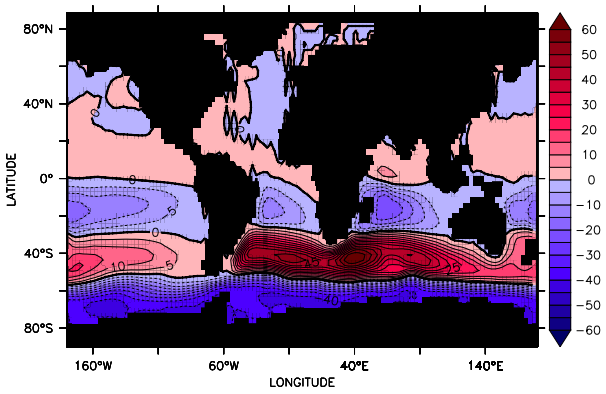

Figure 4.4: Barotropic streamfunction anomaly (Sv) for the northward-shifted Southern Ocean wind stress perturbation.

1996], which allows an east-west pressure gradient to be established and geostrophically balanced southward flow to occur immediately below the surface Ekman transport [*McDermott*, 1996]. Instead, the maximum wind stress becomes situated between the coasts of South America and Oceania (Figure 4.1a) forcing a northward migration of the Southern Hemisphere subtropical gyres and allowing intensification of the preexisting shallow zonal pressure gradient, therefore allowing direct geostrophic compensation of the northward Ekman transport to occur. These sequence of events establishes a Southern Hemisphere subpolar "supergyre" [c.f. *Ridgway and Dunn*, 2007; *Speich et al.*, 2007], mainly in the South Atlantic and Indian oceans with a branch reaching into the South Pacific (Figure 4.4). Since horizontal velocities are also intensified as the ACC flows through Drake Passage and is diverted far to the north, the "ageostrophic leakage" found at 40°S may also intensify [*McDermott*, 1996; *Toggweiler and Samuels*, 1995, 1998]. In place of the usual positive (clockwise) residual Southern Ocean overturning at 60°S is an expanded and intensified negative (counterclockwise), deep-reaching 16 Sv circulation cell with net southward flow across the unbounded latitudes of Drake Passage, due to the greater northward spread of the polar easterlies and is linked with a slightly enhanced (~2 Sv) abyssal circulation. Whereas previously the southern edge of Drake Passage acted as the southern boundary for the control cell, the cell found here has its northern boundary at the northern flank of Drake Passage with a compensating eddy circulation with southerly flow across Drake Passage. Nevertheless, this "Southern" circulation ensures upwelling of deep waters in the Southern Ocean continues at a rate that is similar to the control, with supplementary upwelling from the more northern cell from intermediate depths bringing relatively DIC enriched waters to the surface.

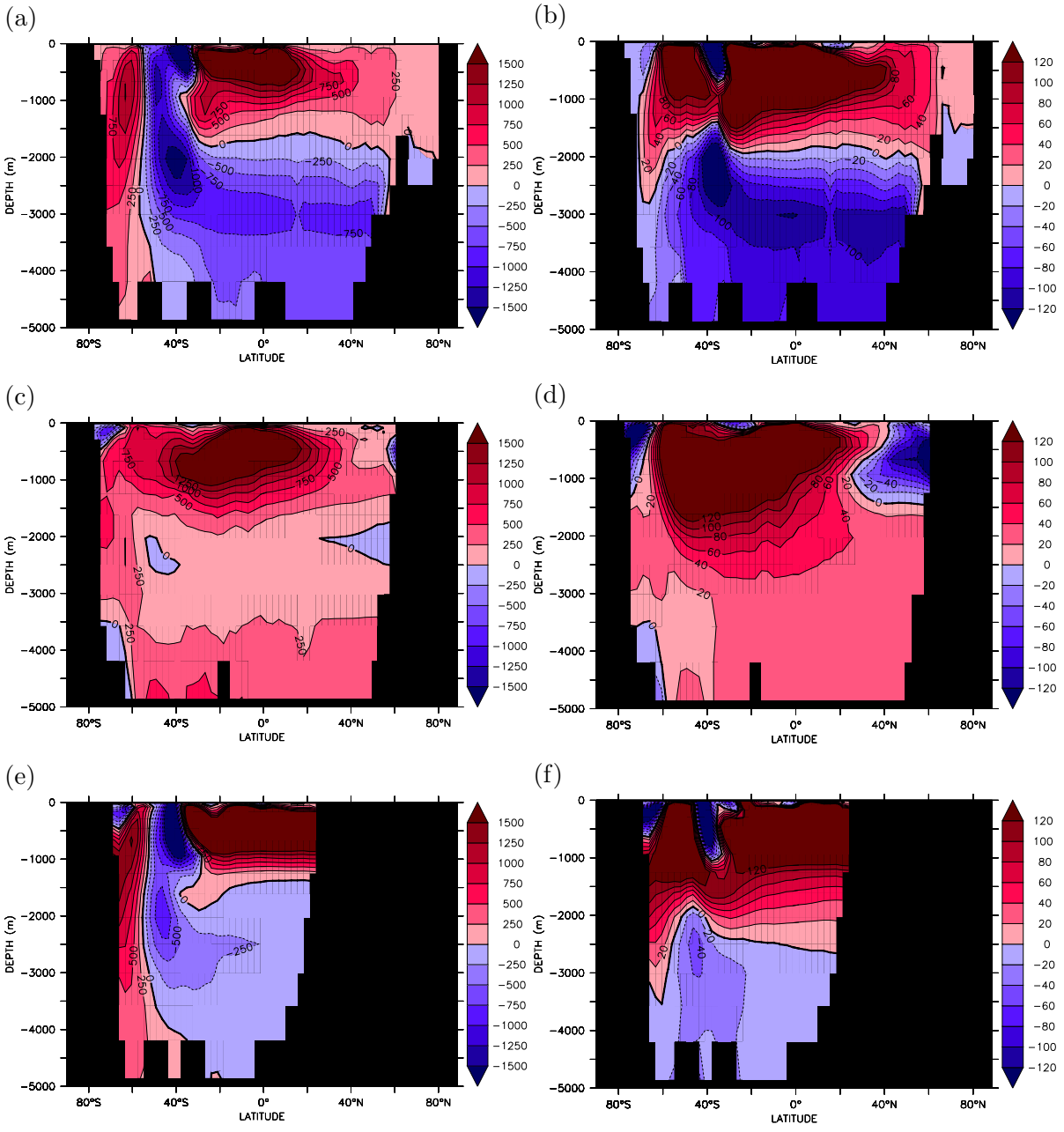

Figure 4.5: Equilibrium MITgcm output for the northward-shifted Southern Ocean wind stress perturbation. Zonal averages of Potential Temperature (m°C, left column) and Salinity (mpsu, right column) anomalies. (a) and (b) are in the Atlantic Ocean, (c) and (d) are in the Pacific Ocean, and (e) and (f) are in the Indian Ocean.

Formation of NADW also increases marginally by 1.3 Sv (Figure 4.3b) due to slightly increased formation of thermocline waters in the Southern Hemisphere.

Global mean potential temperature is increased by 0.30 °C with decreases in Indian and Atlantic Oceans (Figure 4.5a and e) at 40°S and 2000 m, which resembles anomalies produced in experiments where Southern Ocean geometry is altered by "closing the gap" in Drake Passage [*Cox*, 1989; *Gill and Bryan*, 1971; *McDermott*, 1996]. The Pacific Ocean (Figure 4.5c) is not so affected by this because the shift in the core of the ACC is not as great as in the other basins (Figure 4.2b). However, globally, potential temperature increases 0.75–1.0 °C in the upper-ocean waters north of 40°S due to more vigorous upper-ocean overturning (Figure 4.3) and 0.25–0.5 °C south of 60°S due to reduced heat transport and divergence. Reduction in meridional density gradient in this way is partially responsible for the 40 Sv reduction in transport through Drake Passage due to the decreased deep thermal wind shear, however a more sluggish ACC may also result from a reduction of momentum inparted by the northward-shifted winds with the remainder used to drive the subpolar gyre [c.f. *Allison*, 2009; *Allison et al.*, 2010].

Salinity anomaly shows a similar pattern, with an average increase of 0.054. Northward migration of the Southern Hemisphere winds reduces northwards freshwater flux carried from the Southern Ocean towards the subtropics and causes (1) decreased salinity in the Atlantic and Indian Oceans at 40°S and 2000 m with no decrease in the same region in the Pacific Ocean, (2) increased salt content in the upper-ocean north of 40°S because more saline intermediate and mode waters are formed further north due to the shift of the ACC fronts and (3) increased salinity in the Southern Ocean south of 60°S.

Surface buoyancy fluxes (Figure 4.6) in the Southern Ocean show a more pronounced buoyancy gradient with greater buoyancy loss south of approximately 55°S and enhanced buoyancy gain between 55–40°S, which is consistent with the pattern of residual overturning circulation (Figure 4.3a) necessitating loss of heat and freshwater to support southward surface flow across Drake Passage and (in particular) heat and freshwater gain to support northward surface flow about 40°S.

Overall, this leads to a similar pattern of density and stratification reorganisation as in the increased wind stress perturbation, with a depressed midlatitude pycnocline (Figure 4.7) due to enhanced upper-ocean overturning leading to decreased surface stratification. Yet pycnocline depression is not as great as in the increased magnitude pertur-

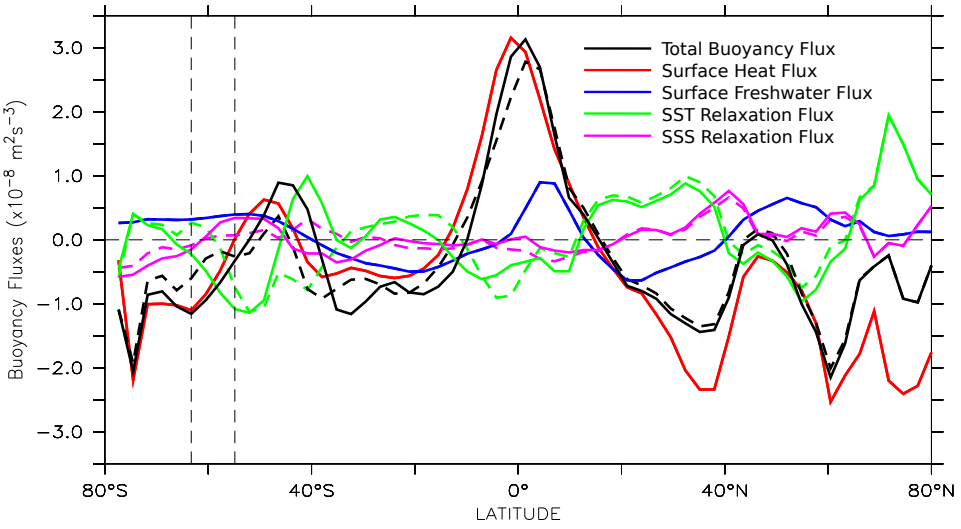

Figure 4.6: Equilibrium MITgcm output for northward-shifted Southern Ocean wind stress perturbation. Zonal average surface buoyancy flux ($m^2\,s^{-3}$) and its components (see Section 6.1 and Equation 6.2) for the perturbed (solid) and control (dashed) states. Positive values indicate a gain of buoyancy (an increase in heat or freshwater/reduced salinity) while negative values indicate buoyancy loss (reduced heat or freshwater/increased salinity). Dashed vertical lines denote the position of the unblocked latitudes at Drake Passage.

bation because a reduced fraction of the more northerly wind stress is driving Ekman transport across circumpolar contours that acts to deepen the mid latitude pycnocline, while a greater fraction of the wind drives redistribution in the upper ocean that does not affect pycnocline depth [e.g. *Allison*, 2009; *Allison et al.*, 2010]. Increased stratification in the intermediate and deep ocean results from stronger abyssal overturning circulation in the Southern Hemisphere. Furthermore a northward-shift in the latitude of Ekman transport (with the winds) coupled with the decrease in vertical penetration of the Southern Ocean Deacon cell allows these deeper isopycnals to shoal since they are no longer being depressed by associated Ekman convergence. Similarly, the northward migration of the region of Ekman divergence deepens the depth of outcropping isopycnals. Despite the outcrop location of surface isopycnals being largely determined by the relaxing boundary conditions, there is some indication of a northward shift, increasing outcrop area. However a northward shift is particularly evident in meridional sections above 2000 m depth in the Atlantic and Indian Oceans (Figure 4.7a and c) where the steepest region of isopycnal slope attempts to align with the westerly wind stress maximum causing decreased stratification and increased density anomaly centred around 40°S.

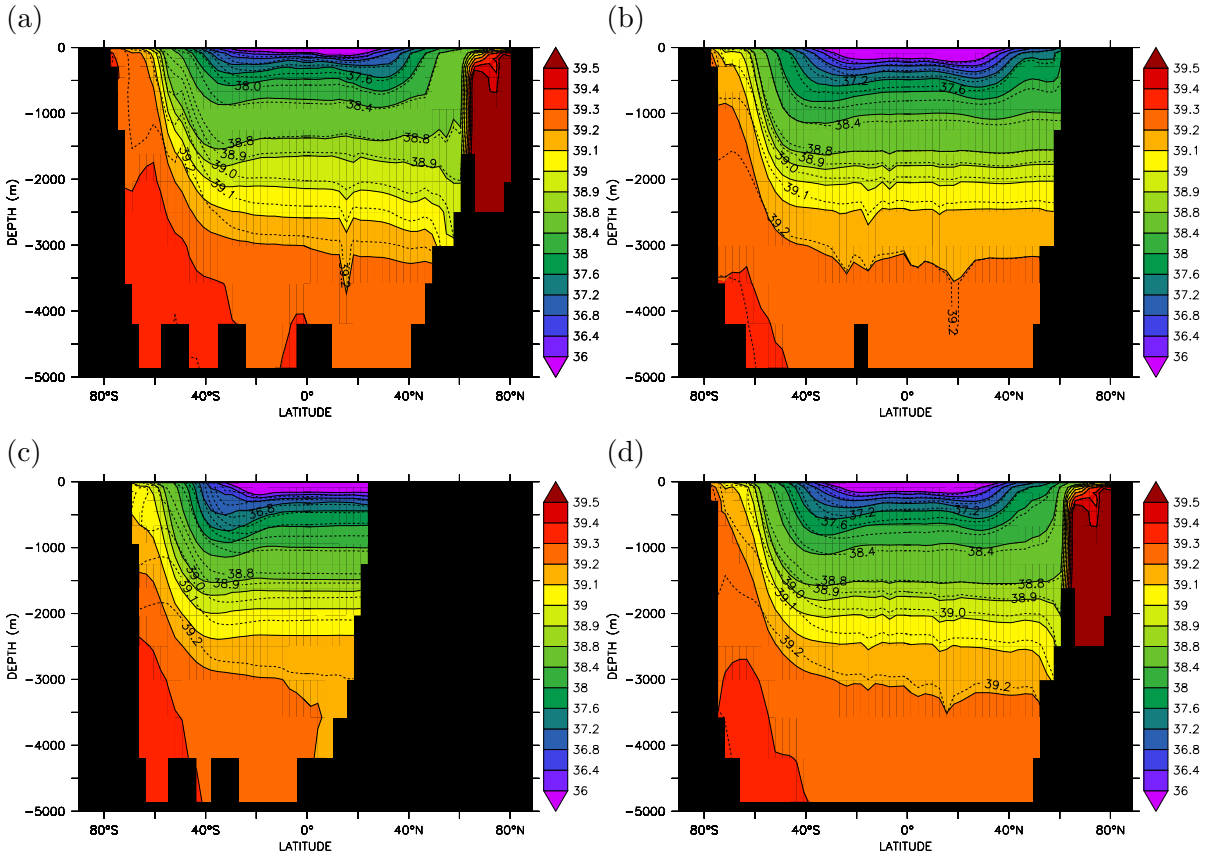

Figure 4.7: Equilibrium MITgcm output for northward-shifted Southern Ocean winds perturbation. Coloured fill and solid contours are Control Run zonally averaged density ($\sigma_{2.5}$, $\mathrm{kg\,m^{-3}}$) with northward-shifted wind stress perturbation density overlay in dashed contours in the (a) Atlantic, (b) Pacific and (c) Indian Oceans, and (d) the Global average.

4.1.2 Distribution of biogeochemical tracers, primary productivity and air-sea exchange of carbon dioxide

Comparing the vertical velocity at the base of the mixed layer between the control run and this perturbation (Figure 4.8) also reveals the northward shift in the region of residual upwelling indicated in the zonally-averaged meridional overturning (Figure 4.3). Again, it is particularly noticeable in the Atlantic and Indian Ocean. Despite the lack of a significant shift in the Pacific sector of the Southern Ocean, the region of upwelling at 45°S intensifies and expands, as does the region of downwelling south of 60°S in all basins to compensate for the intensified Southern Ocean cell. This adjustment of residual upwelling and downwelling produces similar patterns of DIC, phosphate and iron anomalies (Figure 4.9) as seen under increased wind stress (Figure 3.13) because of

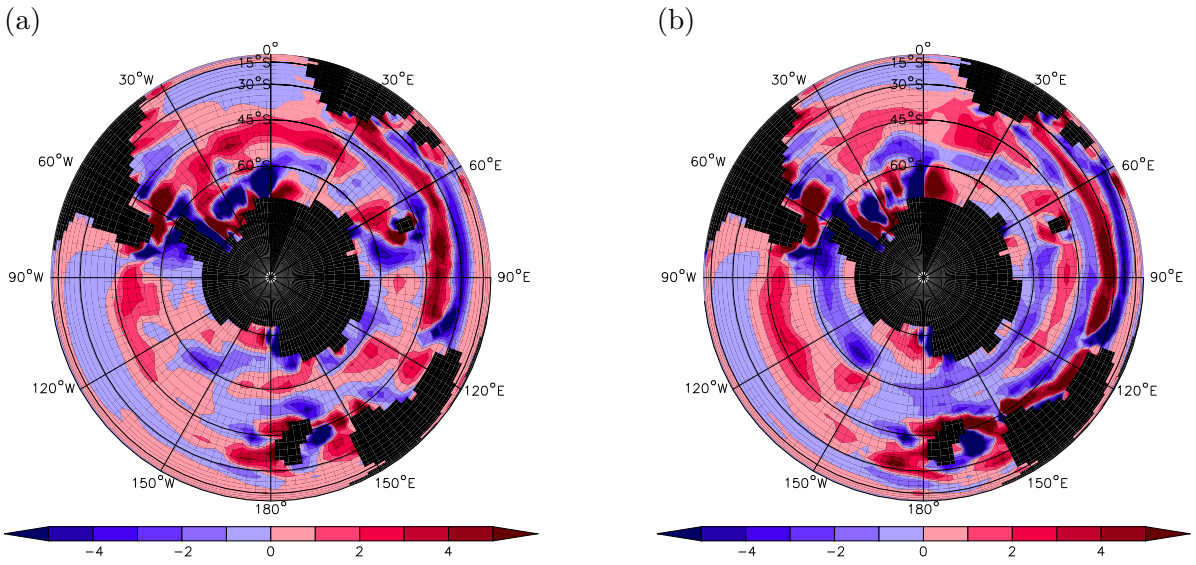

Figure 4.8: Vertical residual velocity ($1 \times 10^{-6}\,\mathrm{m\,s^{-1}}$) at the base of the mixed layer (~290 m) for (a) the control run at 20000 years and (b) northward-shifted Southern Ocean winds.

increased Ekman transport, with elevated concentrations of carbon and macronutrients in a band centred at 40°S, slightly further north than previously due to the location of the convergence of southern and northern Southern Ocean circulations, and along the entire length of the Atlantic Ocean fed by increased Ekman transport and thermocline water subduction in the Southern Ocean [*Dutkiewicz et al.*, 2005a; *Sarmiento et al.*, 2004]. Negative anomalies in the Southern Ocean south of 60°S results from greater downwelling while reduced concentrations in the North Pacific and North Indian Oceans result from the stronger upper-ocean circulation causing downwelling in these regions (or reduced thermocline upwelling [*Tschumi et al.*, 2008]), the inverse relationship between deep water upwelling into low-latitude surface waters and pycnocline depth [*Levermann and Fürst*, 2010] and conservation. Micronutrient concentration also responds in a similar way, with upwelling of deep waters that are depleted in dissolved iron due to scavenging causing surface concentration decreases, while regions where this upwelling is inhibited show increased concentrations. However since the region of increased upwelling between 20–40°S in the Pacific, that originates from higher in the water column than the control, draws micronutrients from the dissolved iron subsurface maximum between 500–1000 m depth, surface iron concentrations actually increase.

Meridional sections of DIC, phosphate and iron anomalies in depth (Figure 4.10) and density vertical coordinates (not shown) show a similar pattern, with minor changes in magnitude associated with heave of isopycnals. All three quantities increase in the

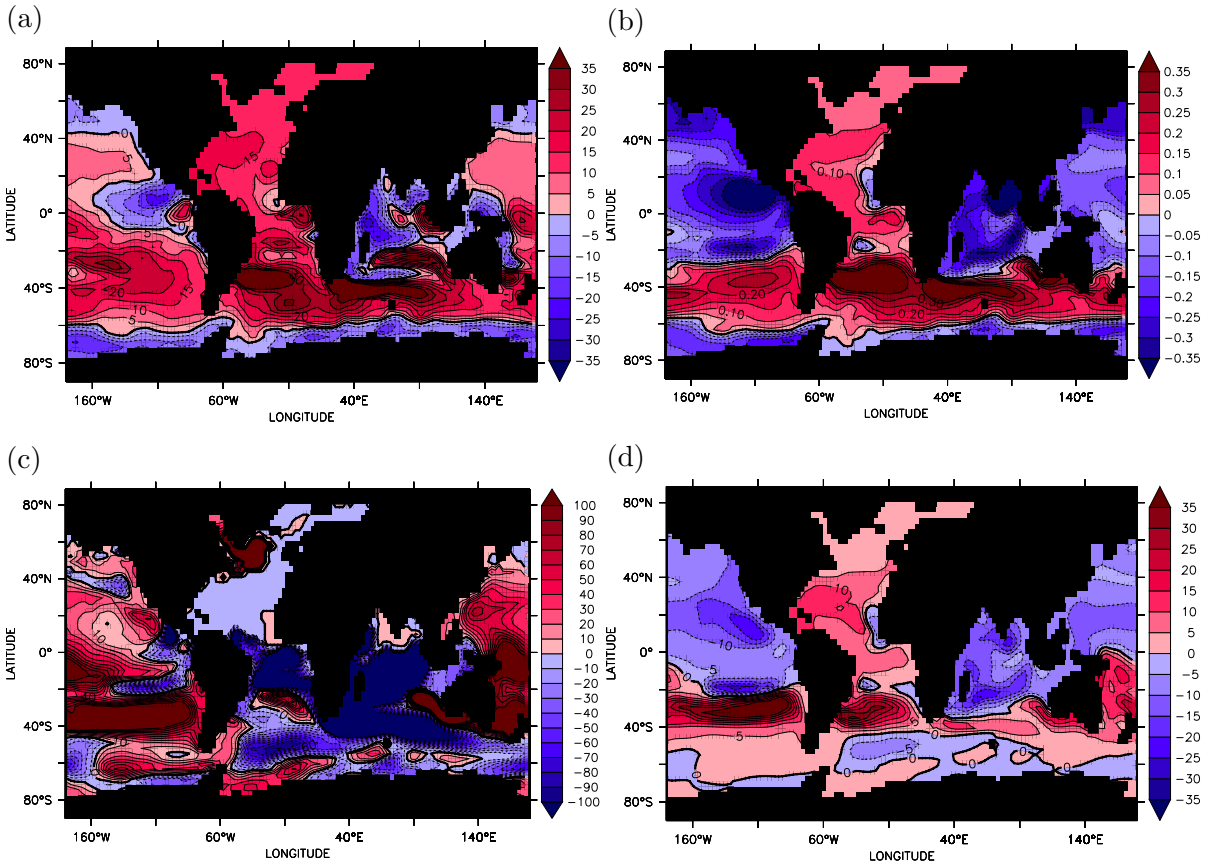

Figure 4.9: Equilibrium MITgcm output for the northward-shifted wind stress perturbation. Sea surface tracer anomalies for (a) dissolved inorganic carbon (mmol C m^{-3}), (b) phosphate (mmol P m^{-3}), (c) dissolved iron (nmol Fe m^{-3}) and (d) primary production (mmol C m^{-3} yr^{-1}).

Atlantic Basin due to enhanced Southern Ocean upwelling from at or below the nutricline between 30°S and 60°S, advection through the Atlantic and injection into the ocean interior within NADW. Increase in the volume occupied by AABW and shoaling of isopycnals at 2500–3000 m causes the enhanced anomalies of DIC and PO_4 and reduced Fe compared on depth levels. The decrease in concentrations of carbon and macronutrients south of 60°S and below 3000 m on the other hand are robust features associated with increased ventilation of the abyssal ocean. Despite the different responses of the Indian and Pacific Ocean circulations, an Indo-Pacific zonal average remains a fair representation of the changes in biogeochemical distributions. As in the Atlantic, the upwelling limbs of the northern and southern cells of the Southern Ocean overturning circulation between 30°S and 60°S enhance concentrations of carbon and macronutrients from the deep and relatively enriched intermediate ocean, but decrease dissolved iron content due to depletion by scavenging. However north of 25–30°S there is a general decrease in all three quantities, particularly in the upper 1000 m due to enhanced downwelling, which

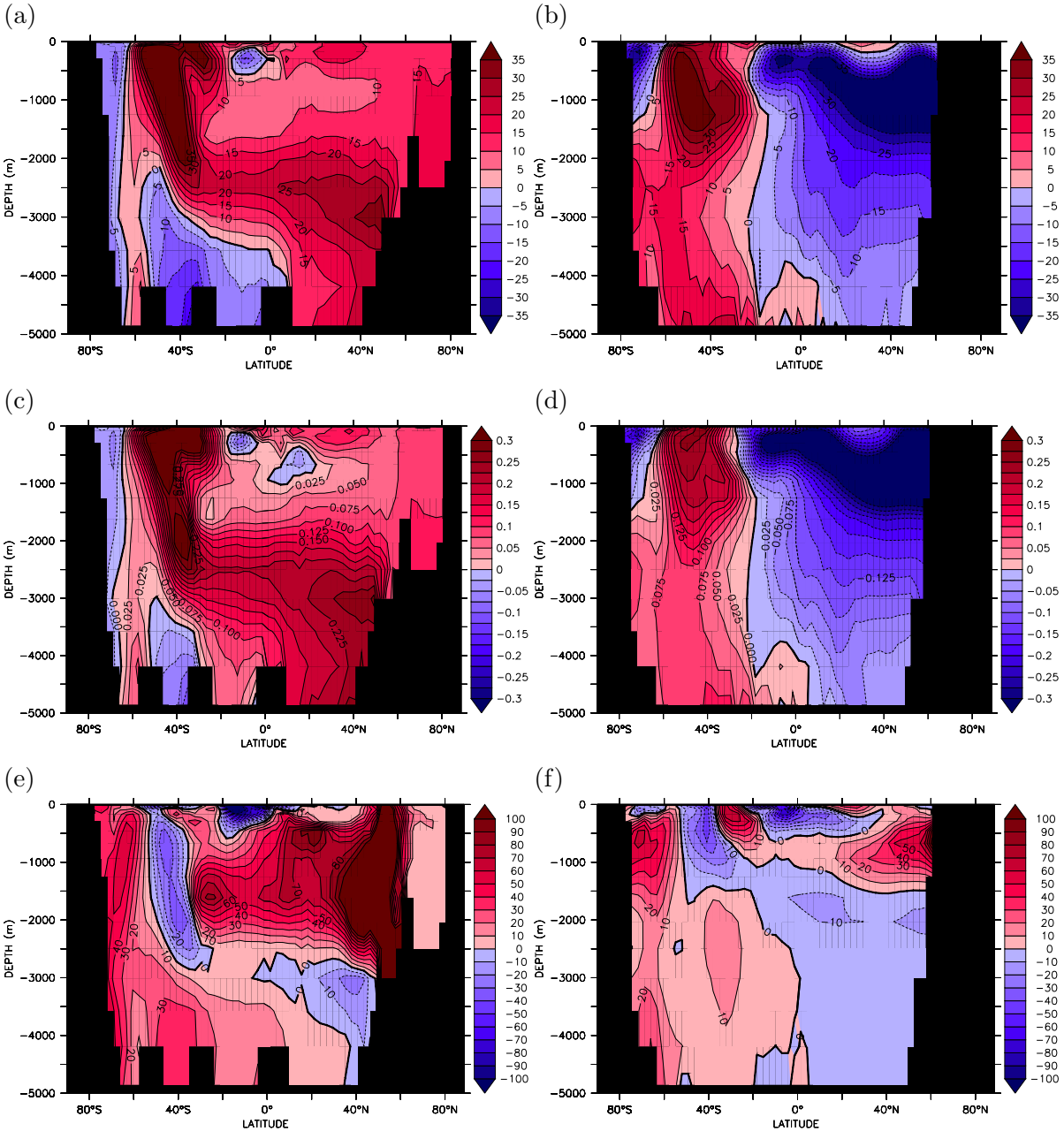

Figure 4.10: Equilibrium MITgcm output for the northward-shifted Southern Ocean wind stress perturbation. Meridional anomaly sections of tracers in the Atlantic Ocean (left column) and in the Indo-Pacific Oceans (right column) for (a) and (b) dissolved inorganic carbon (mmol C m^{-3}), (c) and (d) phosphate (mmol P m^{-3}) and (e) and (f) dissolved iron (nmol Fe m^{-3}).

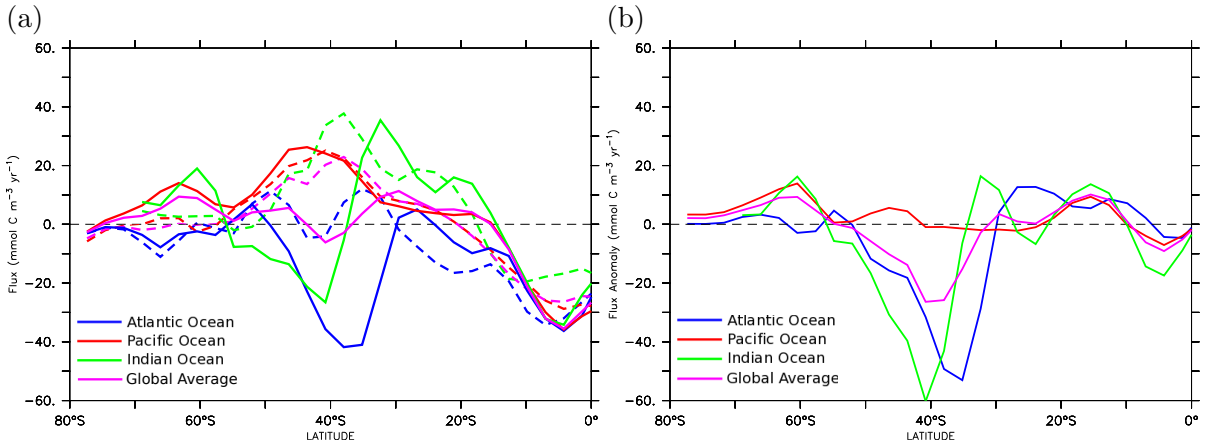

Figure 4.11: MITgcm output for the northward-shifted Southern Ocean wind stress perturbation. (a) Zonally averaged DIC concentration tendency due to air-sea exchange in the surface cell (mmol C m^{-3} yr^{-1}) and (b) their anomalies in the Atlantic (blue), Pacific (red) and Indian (green) sectors and the global zonal average (purple) for the control run (dashed, part (a) only) and near equilibrium after 5000 years (thick). Negative values indicate oceanic outgassing.

also transports aeolian-sourced iron from the surface to depth in the North Pacific, increasing the concentration there.

The balance of macro- and micronutrient supply to the surface results in an increase in primary production (Figure 4.9d) between 20°S and 40°S, particularly in the Pacific Ocean due to increase in supply of both elements. However, as seen previously, the increased upper-ocean circulation favours nutrient supply and productivity in the Atlantic Ocean. This occurs at the expense of the Indian and Pacific Oceans with the decrease here and in the Southern Ocean, mainly due to enhanced iron limitation in the Atlantic sector, dominating the globally integrated rate of primary production, which falls by 0.26 Gt C yr^{-1}.This fall in productivity is accompanied by a small decline in the efficiency of the soft tissue pump of just less than a fifth of a percent from 35.70% in the control run to 35.53%, with increases in preformed, unutilised phosphate associated with the spin up of the Southern Ocean circulation around 40°S and the Atlantic meridional overturning circulation while regenerated phosphate concentration anomalies are similar to those of total phosphate.

The total flux of carbon dioxide from the ocean to the atmosphere was 17.07 Gt C during the 5000 years before net flux equilibrium was restored. The majority of this CO_2 was expelled through the Atlantic and Indian sectors of the Southern Ocean (Figure 4.11) around 40°S associated with increased upwelling of carbon rich waters. Increased downwelling around 60°S, particularly in the Indian and Pacific sectors, in conjunction with

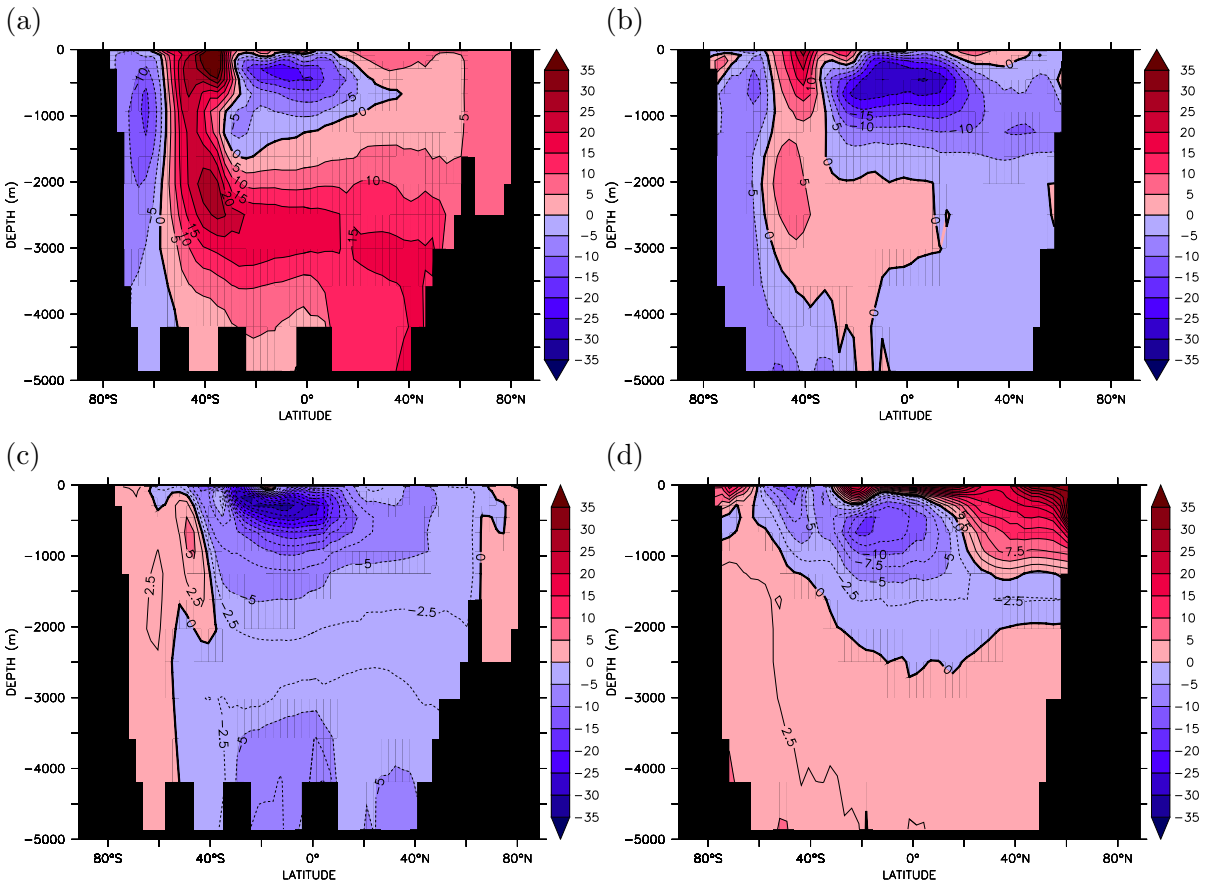

Figure 4.12: Equilibrium MITgcm output for the northward-shifted wind stress perturbation. Meridional sections in the Atlantic (left column) and Indo-Pacific Oceans (right column) of (a and b) air-sea disequilibrium concentration of Dissolved Inorganic Carbon anomaly at the time interior water masses were last at the surface, diagnosed using control "preindustrial" concentrations after "correction" for the effects of organic carbon remineralisation and calcium carbonate dissolution (Equation 2.36) and (c and d) anomalies of the quasiconservative tracer $C_{gas\ exch}$ ($\mathrm{mmol\,C\,m^{-3}}$) calculated using Equation 2.37.

the expanded Antarctic Easterlies converts this region from fairly neutral to a sink of atmospheric CO_2, which combines with a general small Northern Hemisphere increase in uptake to partially offset Southern Ocean outgassing.

More specifically, the source of much of the CO_2 emitted to the atmosphere comes from a 12.67 Gt C reduction in the globally integrated disequilibrium concentration of DIC at the time when an interior water mass was last at the surface (Figure 4.12a and b). Upwelled water masses in the northern cell of the Southern Ocean overturning have a lower initial concentration of CO_2 than those upwelled by the Deacon cell in the control experiment. Therefore these waters require a shorter time to equilibrate with the atmosphere and when subducted are therefore closer to equilibrium than in control, despite increased vigour of the circulation itself.

Increases in atmospheric disequilibrium at 40°S may result from a net northward shift of isopycnals, particularly in the Atlantic Ocean, and as such the anomaly is not correctly represented in latitude coordinates. This pattern is repeated in anomalies of the quasiconservative tracer of air-sea exchange, $C_{gas\ exch}$ (Figure 4.12c and d), with large negative values representing outgassing north of 40°S in the top 1000 m in the Atlantic and Indo-Pacific. Positive values that represent atmospheric carbon uptake occur predominantly in the Southern Ocean near 60°S. The global adjustment of the atmospheric carbon reservoir to northward-shifted winds compares well with the globally integrated decrease in $C_{gas\ exch}$ concentration of −17.25 Gt C.

4.2 Southward-shifted Southern Hemisphere westerlies

4.2.1 Response of oceanic circulation and density structure

After 5000 years with 8.4° southward-shifted wind stress applied to the Southern Ocean (Figure 4.1b) atmospheric CO_2 concentration decreased by 9.6 µatm to 268.4 µatm. Although the size of the CO_2 change is similar to the previous perturbation, the response of the oceanic circulation and biogeochemical processes are quite different.

Southward-shifted winds produce a clear southward shift and reduction of the maximum Ekman transport and a reduction in the magnitude of associated Ekman pumping (Figure 4.13a) due to increased Coriolis parameter. The mean position of the ACC also migrates southward, as indicated by the position of the maximum zonally averaged zonal velocity (Figure 4.13b). Yet the latitude of maximum southward surface eddy return flow remains in a similar position because there is no significant shift in the location of Southern Hemisphere sloping isopycnals (Figure 4.15), and has a comparable volume transport to the control run, leading to increased compensation and reduced residual overturning circulation to 11.83 Sv (Figure 4.14).

Furthermore, from the zonally-averaged perspective, the positive residual circulation in the Southern Ocean is confined within the bounds of Drake Passage with little northward transport of waters further north than ~55°S, although it appears to reach just as deep

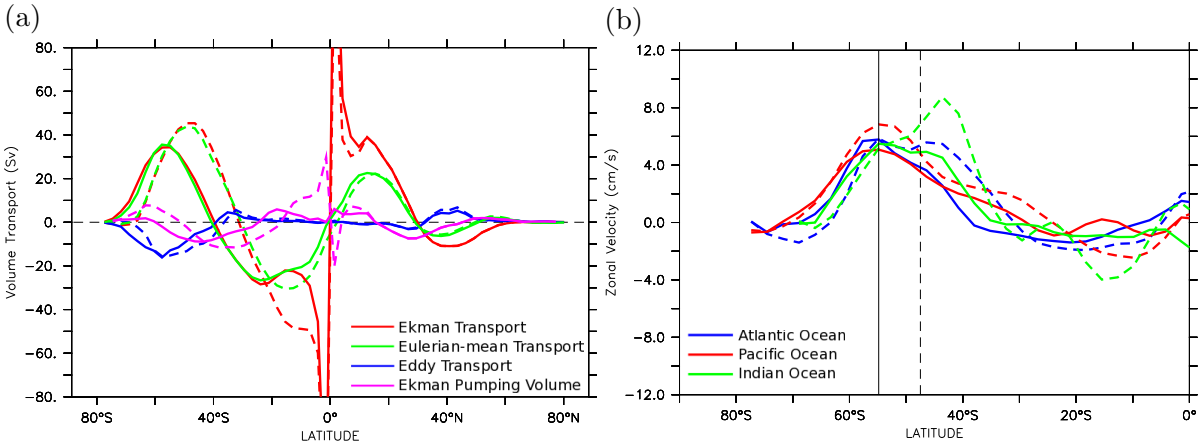

Figure 4.13: Meridional transports and surface zonal velocity for southward-shifted Southern Ocean winds. (a) Perturbed (solid) and Control (dashed) meridional Ekman transport s calculated directly from wind stress (red), Eulerian-mean (green) and GM eddy transports (blue) and zonally integrated Ekman pumping (purple) for northward-shifted Southern Ocean Winds (Sv) in the surface Ekman layer and (b) zonally-averaged zonal residual velocity ($\mathrm{cm\,s^{-1}}$) averaged over the surface 100 m from the control run (dashed) and at steady state after 5000 years (solid) of northward-shifted winds in the Atlantic (blue), Pacific (red) and Indian (green) Oceans. Vertical black lines indicate the control (dashed) and perturbed (solid) Global meridional position of the Southern Hemisphere maximum in zonal velocity, used as a surrogate for the position of the ACC.

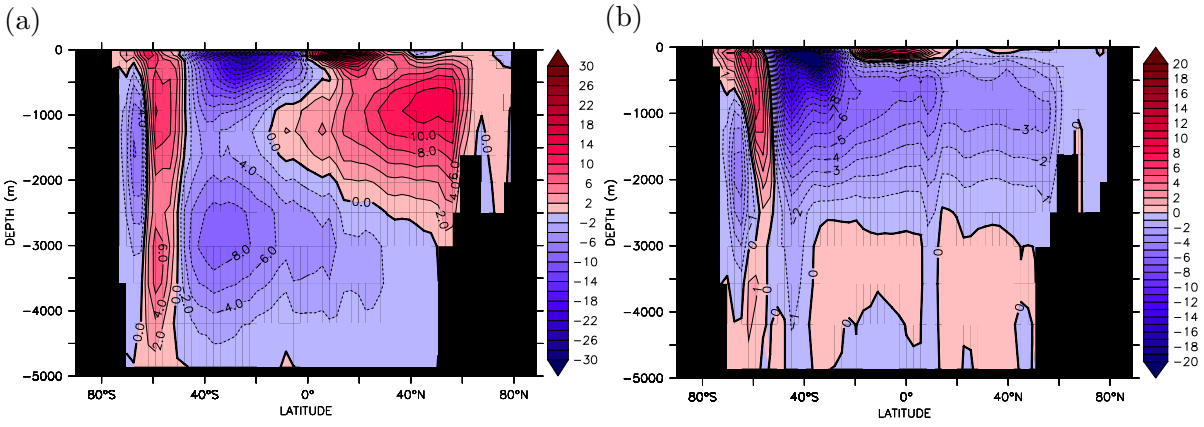

Figure 4.14: Equilibrium MITgcm output for the southward-shifted Southern Ocean wind stress perturbation (a) Zonal average residual meridional overturning stream function (Sv) and (b) Zonal average residual meridional overturning stream function anomaly (Sv).

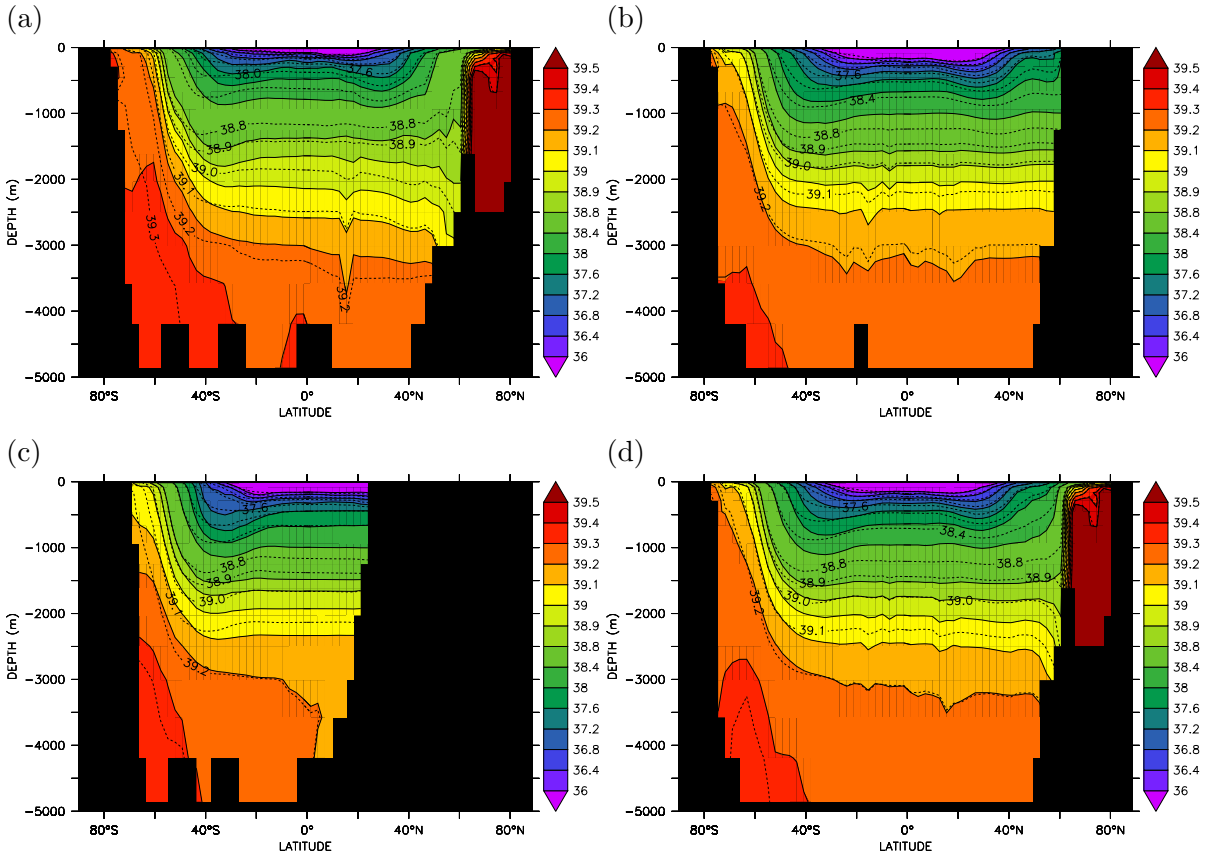

Figure 4.15: Equilibrium MITgcm output for southward-shifted Southern Ocean winds perturbation. Coloured fill and solid contours are Control Run zonally averaged density ($\sigma_{2.5}$, $\mathrm{kg\,m^{-3}}$) with southward-shifted wind stress perturbation density overlay in dashed contours in the (a) Atlantic, (b) Pacific and (c) Indian Oceans, and (d) the Global average.

as the circulation in the control. Furthermore, northward deflection of the ACC after it passes through Drake Passage is almost totally suppressed and coupled with the reduced ACC transports removes the near surface circulation associated with *Toggweiler and Samuels* [1995, 1998]'s "ageostrophic leakage". The Atlantic meridional overturning circulation decreases with ~3 Sv less NADW exported south of 30°S and by a similar rate at its formation region in the North Atlantic while the abyssal circulation of AABW is maintained at −9.85 Sv. The dominating feature, however is the strengthened negative Southern Hemisphere low-latitude, upper-ocean overturning circulation driven by the expanded tropical easterlies that induces upwelling of intermediate waters through the thermocline primarily in the Indo-Pacific Oceans but to a lesser extent in the Atlantic Ocean too.

Temperature and salinity are reduced in all basins by global mean values of −0.96 °C and −0.11, respectively, particularly in the top 2000 m to the north of 40°S as a result

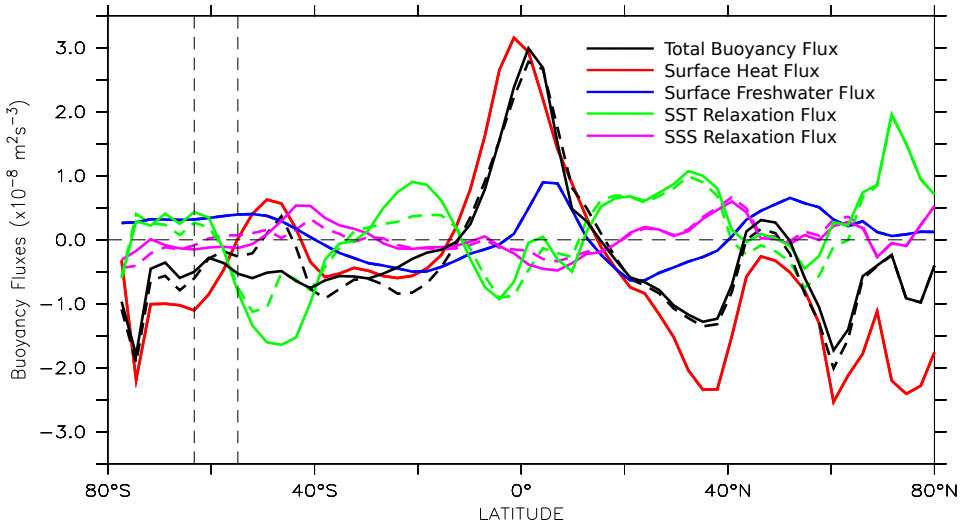

Figure 4.16: Equilibrium MITgcm output for the southward-shifted Southern Ocean wind stress perturbation. Zonal average surface buoyancy flux ($m^2\,s^{-3}$) and its components (see Section 6.1 and Equation 6.2) for the perturbed (solid) and control (dashed) states. Positive values indicate a gain of buoyancy (an increase in heat or freshwater/reduced salinity) while negative values indicate buoyancy loss (reduced heat or freshwater/increased salinity). Dashed vertical lines denote the position of the unblocked latitudes at Drake Passage.

of reduced volume of Southern Hemisphere thermocline waters, which causes noticeable shoaling of upper-ocean isopycnals (Figure 4.15) typified by the dispacement of the low-latitude pycnocline ($\sim \sigma_{2.5} = 38.8\,kg\,m^{-3}$ isopycnal in Figure 4.15) to shoal from a mean depth of −1428 m in the control to −1168 m, a larger rise than achieved by perturbing wind stress magnitude alone. Shifting wind stress south reduces the volume of northward Ekman transport that crosses circumpolar streamlines and therefore reduces the supply of water masses that fill the global pycnocline [*Allison*, 2009; *Allison et al.*, 2010]. A small depression of the deepest isopycnals, particularly in the Southern Ocean and in the Atlantic may be the result of a southward shift of the latitude of Ekman convergence.

Surface buoyancy fluxes (Figure 4.16) in the Southern Ocean are considerably reduced between 40–60°S due to strong heat loss associated with surface temperature relaxation that is of the same order as the prescribed net heat fluxes. This leads to a slight negative buoyancy gradient that prohibits northward transport of upwelled waters in the Southern Ocean and establishment of a significant meridional overturning circulation.

Greater cooling to the north of the ACC than to the south and subsequent reduction in meridional density gradient may be responsible for a 29 Sv reduction in transport through Drake Passage due to the decreased thermal wind shear. However shifting the winds so far south across the southern boundary of the ACC may also reduce the

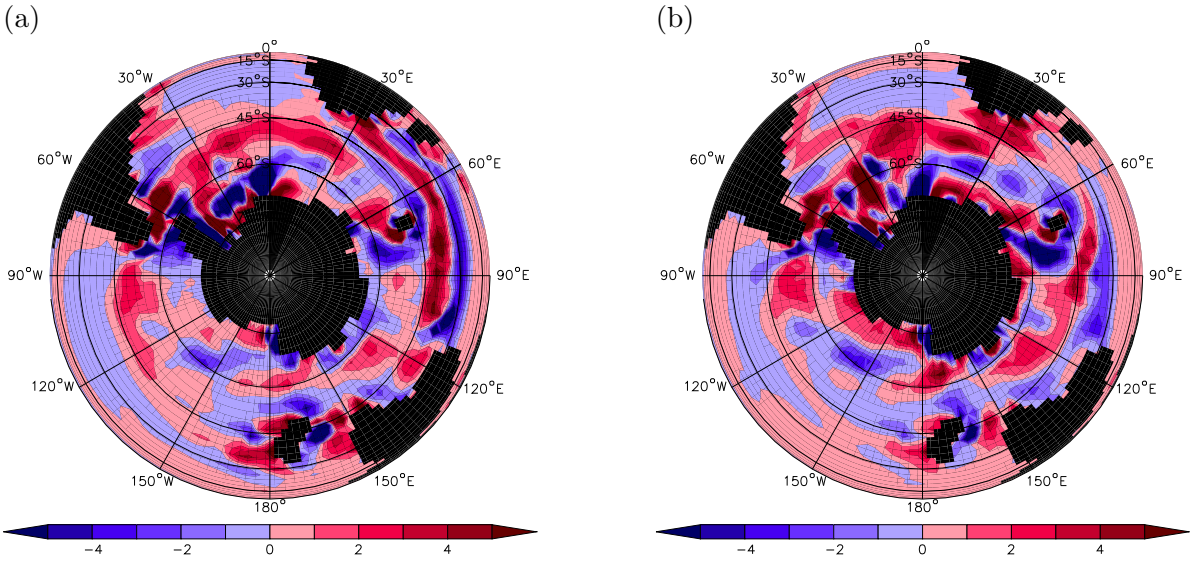

Figure 4.17: Vertical residual velocity ($1 \times 10^{-6}\,\mathrm{m\,s^{-1}}$) at the base of the mixed layer (~290 m) for (a) the control run at 20000 years and (b) southward-shifted Southern Ocean winds.

momentum input into driving the circumpolar current with a fraction diverted into the Ross and Weddell gyres [c.f. *Allison*, 2009; *Allison et al.*, 2010] whilst the reduced surface area of the ocean on which the wind stress acts is also lower and therefore total momentum input is also reduced. Adjustment of the oceanic density structure leads to increased stratification in the surface 500–1000 m with decreased stratification below. Again, despite the surface outcrop location of isopycnals being largely determined by the surface relaxing boundary conditions preventing a larger reduction in Southern Ocean isopycnal outcrop area [e.g. *Tschumi et al.*, 2008], there is a clear southward sub-surface migration in the Southern Hemisphere in the Atlantic Ocean to align with the peak wind stress, although this is not repeated in the other basins.

4.2.2 Distribution of biogeochemical tracers, primary productivity and air-sea exchange of carbon dioxide

These alterations to the circulation and density structure under southward-shifted winds actually enhance upwelling at the base of the mixed layer in the Southern Ocean between 45°S and 60°S (Figure 4.17) as a consequence of the southward migration of the positive Southern Hemisphere overturning cell while the expansion and intensification of the cyclonic surface Southern Hemisphere gyre circulation promotes downwelling around

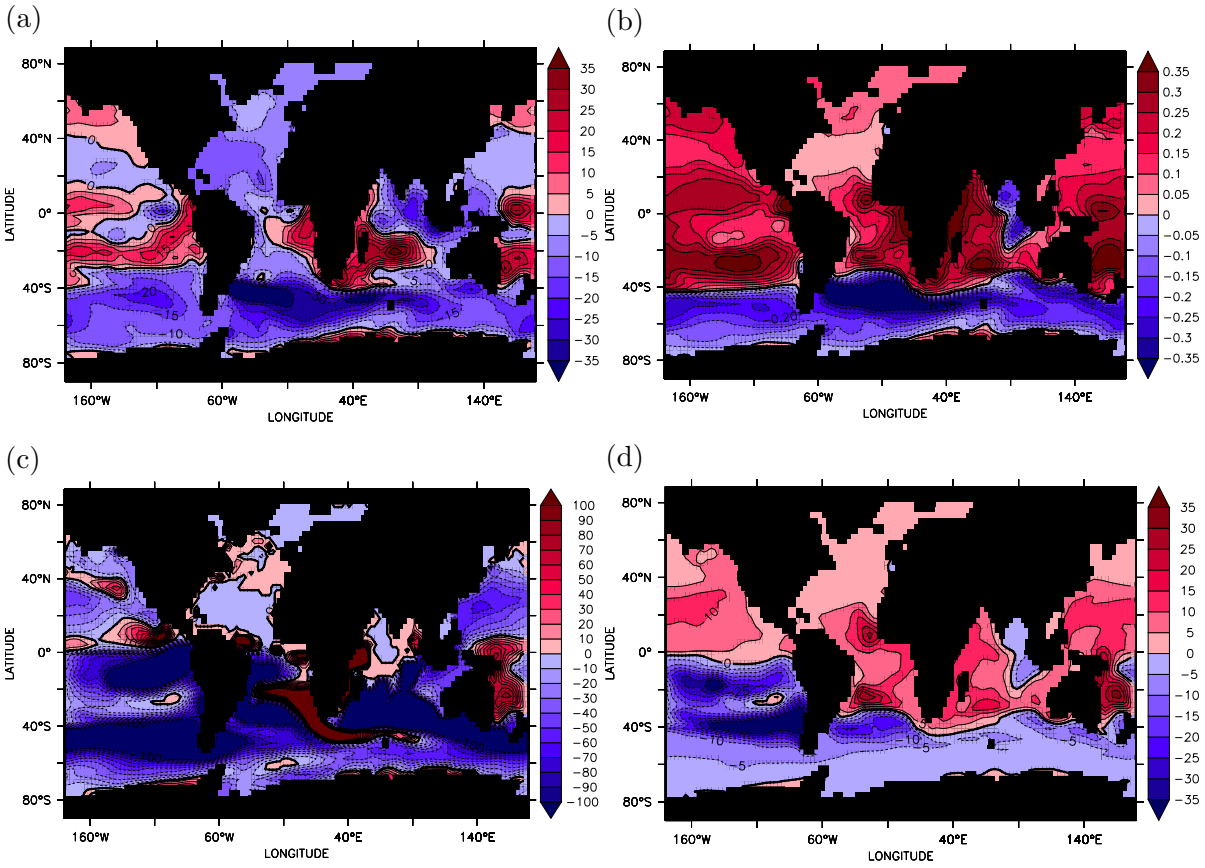

Figure 4.18: Equilibrium MITgcm output for the southward-shifted wind stress perturbation. Sea surface tracer anomalies for(a) dissolved inorganic carbon (mmol C m^{-3}), (b) phosphate (mmol P m^{-3}), (c) dissolved iron (nmol Fe m^{-3}) and (d) primary production (mmol C m^{-3} yr^{-1}).

40°S. Upwelling just north of 45°S in the Atlantic sector at about 30°W and 30°E is also enhanced.

This leads to an unusual departure from the Atlantic/Indo-Pacific seesaw due to their different nutrient supply mechanisms seen previously. For increased wind stress magnitude, increased deep Southern Ocean upwelling and northward residual flow leads to an increase in Atlantic nutrient supply and productivity at the expense of the Indo-Pacific, which is supplied by nutrients upwelled from the deep ocean across the low-latitude pycnocline and vice versa. With southward-shifted winds (Figure 4.18), coupled with the increase in Indo-Pacific nutrient supply by elevated rates of low-latitude upwelling, there is also an increase in Atlantic Ocean nutrients supplied by the enhanced Southern Hemisphere gyre circulation that upwells nutrients directly into the subtropical gyre to be advected north in the surface currents. Thus despite reduced volumes of thermocline waters entering the South Atlantic that would otherwise lead to reduced Atlantic

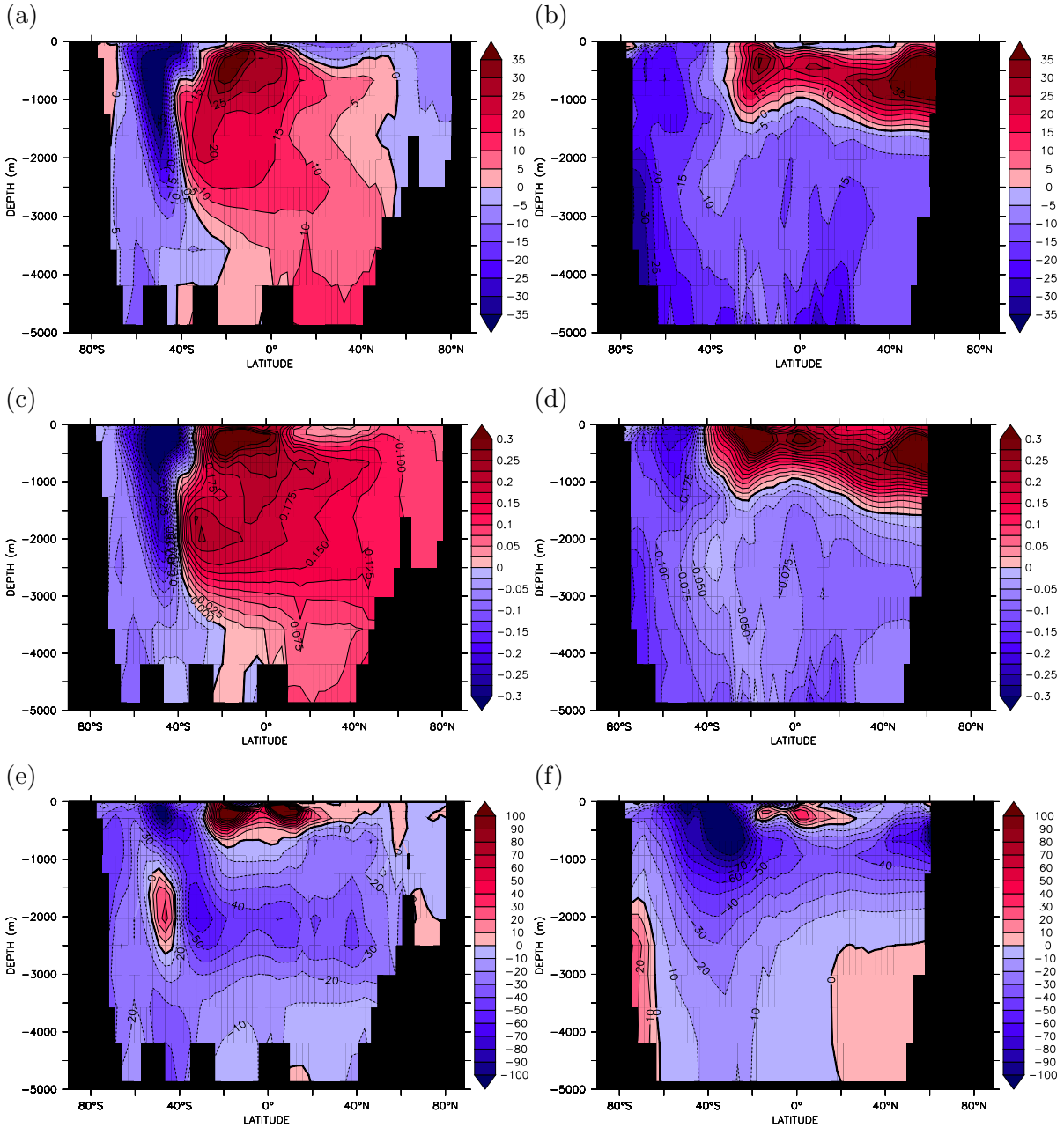

Figure 4.19: Equilibrium MITgcm output for the southward-shifted Southern Ocean wind stress perturbation. Meridional anomaly sections of tracers in the Atlantic Ocean (left column) and in the Indo-Pacific Oceans (right column) for (a) and (b) dissolved inorganic carbon (mmol C m^{-3}), (c) and (d) phosphate (mmol P m^{-3}) and (e) and (f) dissolved iron (nmol Fe m^{-3}).

primary production, with southward-shifted winds much of the surface ocean north of ~40°S sees an increase in productivity. Nevertheless, south of 40°S reduced upwelling of carbon and nutrient rich deep waters decreases biological production, particularly in the South Pacific where decreased surface concentration of iron appears to cause enhanced micronutrient limitation. In total, the rate of global primary production increases by $0.16\,\mathrm{Gt\,C\,yr^{-1}}$.

Meridional sections of carbon and nutrient anomalies in the Atlantic and Indo-Pacific Oceans (Figure 4.19) show a general decrease in concentrations south of 40°S, with a general decrease in the deep Indo-Pacific Oceans further north. In the majority of the Atlantic, the increased concentration of carbon and phosphate results from increased direct nutrient supply by upwelling and rapid subduction at 40°S instead of enhanced advective supply from the Southern Ocean and injection into the deep ocean within NADW, causing a similar pattern seen with increased and northward-shifted wind stress. When heave of isopycnals due to reduced upper-ocean water mass volume is taken into account (Figure 4.20), the distribution of anomalies remains fairly consistent, but with reduction in concentrations of DIC and phosphate at 2000 m in the Atlantic at the depth of southward NADW flow and at the surface in the North Pacific and Indian Oceans, coupled with increases in dissolved iron in the deep North Atlantic and intermediate depths in the North Indian and North Pacific with increased concentrations in the bottom waters of the global ocean. Furthermore, dissolved oxygen (Figure 4.21a and b) follows a similar pattern to DIC and phosphate with the opposite sign.

Sections of regenerated and preformed phosphate (Figure 4.21c to f) follow a pattern consistent with the surface distribution of primary production anomaly with increased upper-ocean primary production reflected in increased regenerated phosphate, primarily in the Atlantic Basin, centered on 20°S, increased concentration in the upper 1000 m of the northern Indo-Pacific Basins and a decrease in concentrations in the Southern Ocean south of 40°S. Preformed phosphate decreases in the Southern Ocean as a result of reduced intermediate water subduction but increases in the northern Indo-Pacific due to more rapid upper-ocean circulation. Again, when isopycnal heave is considered, there is increased concentrations of preformed phosphate anomaly in the Atlantic and Indo-Pacific below 3000 m depth. While regenerated phosphate anomaly in the Indo-Pacific calculated on isopycnal surfaces closely resembles the anomaly on depth levels, in the Atlantic a second maximum of regenerated phosphate increase is revealed in the

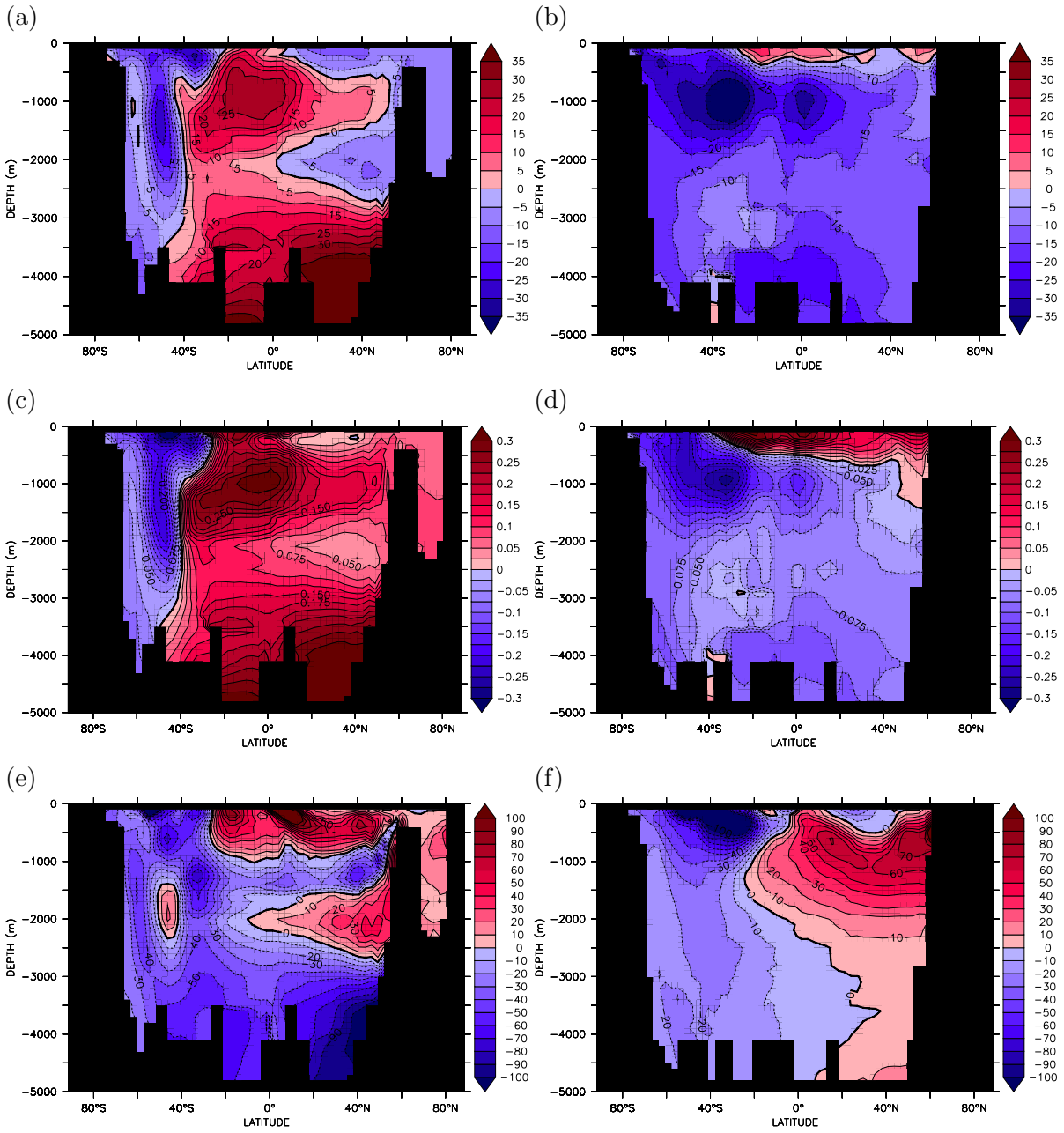

Figure 4.20: Equilibrium MITgcm output for the southward-shifted Southern Ocean wind stress perturbation. Meridional sections of tracer anomaly in the Atlantic Ocean (left column) and in the Indo-Pacific Oceans (right column) calculated and zonally-averaged in density coordinates and regridded back into depth coordinates for (a) and (b) dissolved inorganic carbon (mmol C m^{-3}), (c) and (d) phosphate (mmol P m^{-3}) and (e) and (f) dissolved iron (nmol Fe m^{-3}).

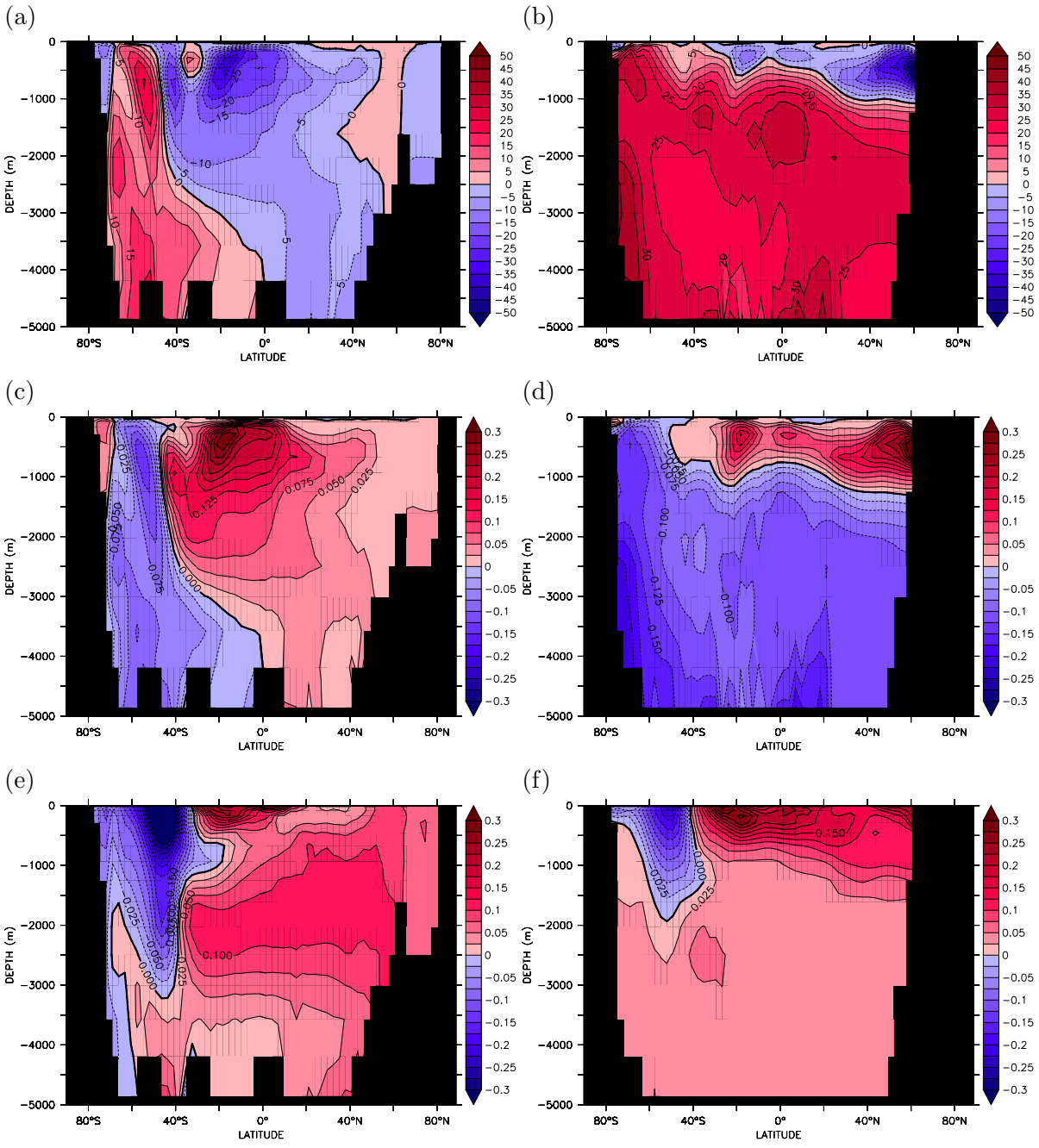

Figure 4.21: MITgcm output for the southward-shifted Southern Ocean wind stress perturbation. Meridional sections of tracer anomaly in the Atlantic Ocean (left column) and in the Indo-Pacific Oceans (right column) for (a) and (b) dissolved oxygen anomaly (mmol O m^{-3})(c and d) regenerated phosphate anomaly (mmol P m^{-3}) calculated from Apparent Oxygen Utilisation using Equation 2.28 and Equation 2.29, and (e and f) preformed phosphate anomaly (mmol P m^{-3}) calculated using the regenerated component and Equation 2.27.

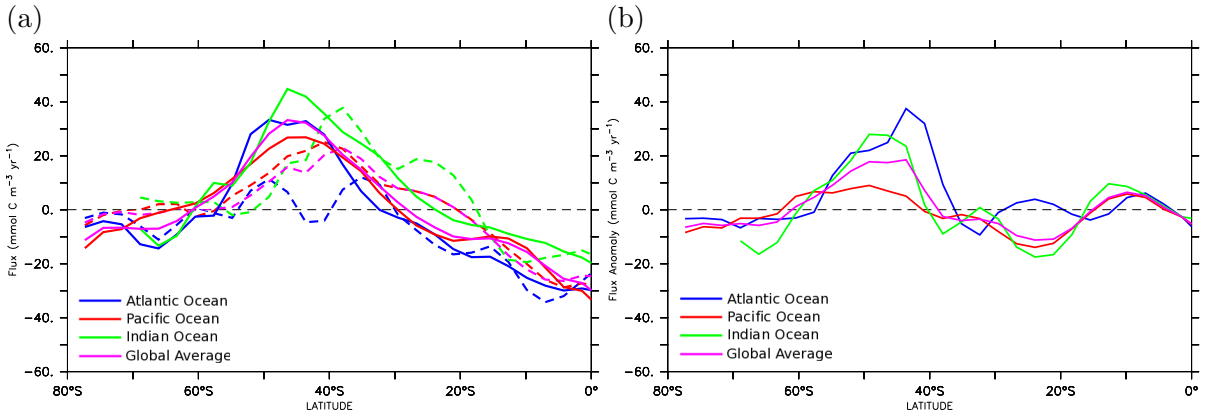

Figure 4.22: MITgcm output for the southward-shifted Southern Ocean wind stress perturbation. (a) Zonally averaged of DIC concentration tendency due to air-sea exchange in the surface cell (mmol C m^{-3} yr^{-1}) and (b) their anomalies in the Atlantic (blue), Pacific (red) and Indian (green) sectors and the global zonal average (purple) for the control run (dashed, part (a) only) and near equilibrium after 5000 years (thick). Negative values indicate oceanic outgassing.

deep ocean between the equator and 40°N that is hinted at in the Atlantic section of DIC anomaly (Figure 4.19a). Estimating the efficiency of the soft tissue pump from these distributions of preformed and regenerated nutrients provides the curious result that although biological productivity increased and atmospheric concentration of CO_2 decreased, the efficiency of the soft tissue pump declined slightly from 35.70% to 33.73%.

Ultimately the ocean absorbs 20.43 Gt C from the atmosphere before the global net air-sea CO_2 flux returns to a steady state. This extra CO_2 mostly invades the Southern Ocean south of 40°S (Figure 4.22) due to a larger atmosphere-ocean concentration gradient, although there is additional uptake in the subtropics probably associated with the increased primary productivity while increased low-latitude upwelling in the Pacific and Indian Oceans, and generally in the Northern Hemisphere, causes net uptake to be slightly offset by increased outgassing. These patterns are essentially captured by the distribution of the air-sea flux tracer $C_{gas\ exch}$ (Figure 4.23a and b, calculated using Equation 2.37) with a parallel increase of integrated carbon storage of 19.68 Gt C mainly stored at 1000 m, but also with a loss of CO_2 to the atmosphere in the North Atlantic carried into the interior by southward deep water flow unlike in the North Pacific where the signal remains near the surface. However, the change in circulation has a profound effect on the extent of equilibration between the ocean and atmosphere (Figure 4.23c and d), with a supplementary 138.3 Gt C prevented from expulsion to the atmosphere

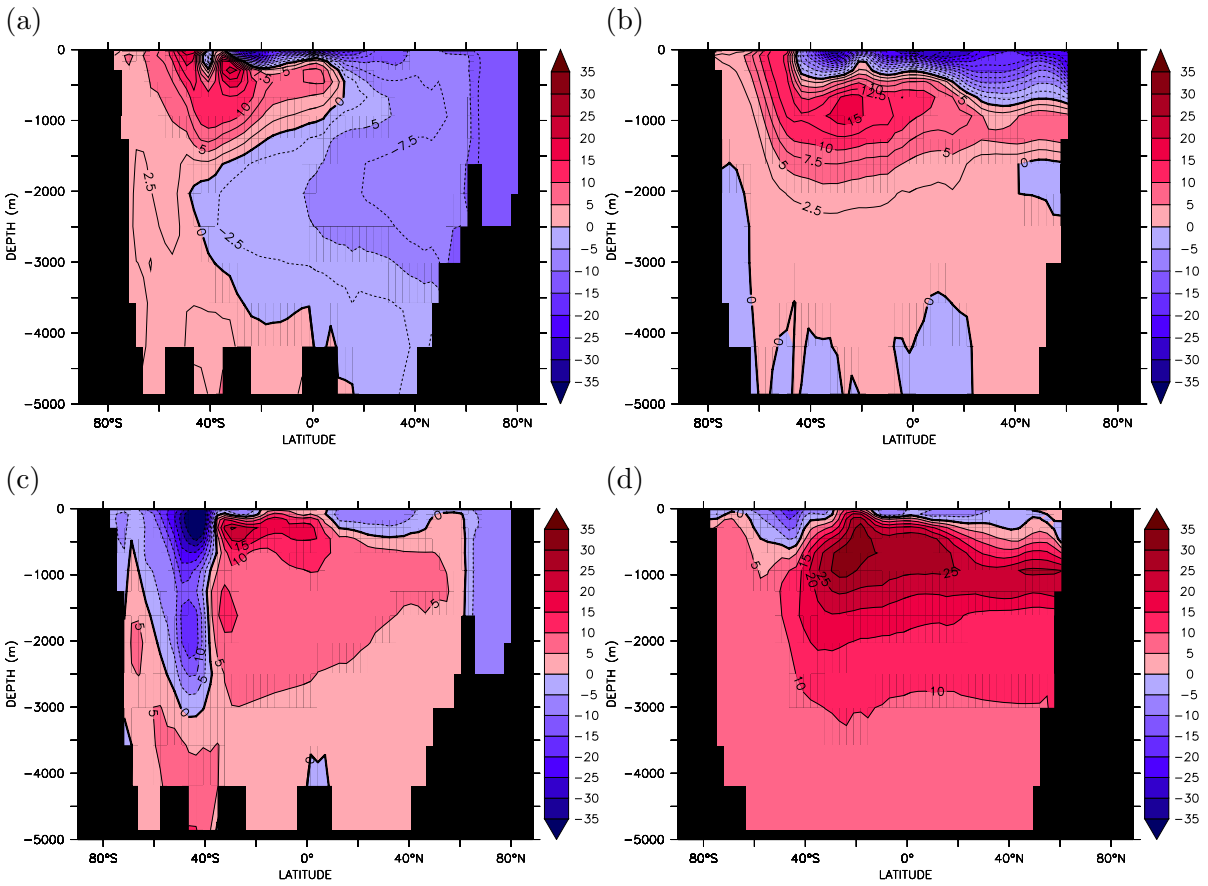

Figure 4.23: Equilibrium MITgcm output for the southward-shifted wind stress perturbation. Meridional sections in the Atlantic (left column) and Indo-Pacific Oceans (right column) of (a and b) anomalies of the quasiconservative tracer $C_{gas\ exch}$ (mmol C m^{-3}) calculated using Equation 2.37 and (c and d) air-sea disequilibrium concentration of Dissolved Inorganic Carbon anomaly at the time interior water masses were last at the surface, diagnosed using control "preindustrial" concentrations after "correction" for the effects of organic carbon remineralisation and calcium carbonate dissolution (Equation 2.36) .

associated with the vigorous Southern Hemisphere gyre circulation downwelling water masses at 40°S before they have reached equilibrium with the atmosphere.

4.3 Additional perturbations to Southern Hemisphere wind stress magnitude

Finally, four wind stress perturbations were realised to determine the effects of a shift north or south coupled with an increase or decrease in strength of the Southern Hemisphere westerlies.

1. A northward shift and 50% increased wind stress increased atmospheric CO_2 by 26.3 µatm to 304.4 µatm compared to the control, which is an extra 18.3 µatm released from the ocean with northward-shifted wind stress alone. Stronger westerly wind stress actually spins up both the Southern Ocean overturning cells to 50.75 Sv in the northern circulation and the counter-rotating deep southern circulation to 19.97 Sv resulting in a larger advective supply of macronutrients to the southern subtropical gyres and the entire Atlantic and an associated increase in global rate of primary production of 0.92 Gt C yr^{-1}. However, the more energetic circulation results in increased subduction of unutilised phosphate into the ocean interior and although the concentration of biologically fixed, regenerated phosphate increases in the Southern Hemisphere, the efficiency of the biological pump is reduced to 34.2%, which promotes the outgassing of 55.86 Gt C from intermediate and mode waters originating in the Southern Ocean, intensifying the anomaly in the distribution of the gas exchange pump. Furthermore, the disequilibrium concentration of DIC in Southern Ocean increased but is offset in the global integral of −28.44 Gt C by a further reduction in disequilibrium in lower latitudes, enhancing the pattern associated with a simple northward shift.

2. Decreasing the magnitude of a northward-shifted wind by 50% acts to slightly draw down atmospheric CO_2 levels to 272.0 µatm, which is 14.1 µatm lower than with northward-shifted wind stress alone. Weaker, northward-shifted westerlies reduced the strength of the Southern Ocean overturning cells, with the northern cell reduced by more than a third to 7.50 Sv and the depth of the cell decreasing to 500 m while the southern overturning cell is reduced slightly to −14.45 Sv. The net reduction in upwelling around 40°S decreases the concentration of upwelled macronutrients, which are largely consumed at the same rate *in situ* between 20–40°S, leading to a decline in supply by advection to the Atlantic so that phosphate limitation increases. Since low-latitude isopycnals shoal instead of being depressed by intense Southern Ocean thermocline water production, Indo-Pacific nutrient stress is reduced by an increase in diapycnal nutrient supply from below the pycnocline. The balance between southern subtropical and northern hemisphere production leads to an increase of the globally integrated rate of primary production by 0.27 Gt C yr^{-1} with more complete nutrient utilisation leading to a decrease in preformed phosphate, with a concomitant increase in regenerated phosphate and slight increase in the efficiency of the soft tissue pump to 36.4%, which promotes CO_2 uptake from the atmosphere. Indeed, reduced upwelling around 40°S results in significantly reduced outgassing in the southern Indo-Atlantic with

an actual increase in uptake in the South Pacific, south of 60°S thus leading to a net accumulation of 12.83 Gt C in the ocean, stored in the region around 40°S and 1500 m diagnosed from anomalies of the gas exchange pump concentrations, which also contain an increased concentration of 23.23 Gt C disequilibrium DIC, while the waters having last outgassed at the surface in the Southern Ocean are confined to the upper 1000 m at low-latitudes.

3. For the 10° south shift in wind stress, the same pattern emerges. With increased Southern Hemisphere westerlies there is a slight net increase in atmospheric CO_2 of 1.6 µatm to 279.6 µatm which is 11.2 µatm higher than with the southern shift alone. This results from a more intense Southern Ocean overturning (21.86 Sv) that draws a greater volume of carbon and nutrient rich deep waters to the surface south of 60°S with net outgassing of 3.32 Gt C to the atmosphere compared to the control. However, because of limitation by iron and/ or light in the southern reaches of the ACC, these upwelled nutrients are not utilised for primary production and are injected back into the ocean interior instigating a decrease in the efficiency of the biological pump to 31.2%. Nevertheless, a slight increase in the adjacent Southern Hemisphere subtropical gyre increases the volume of upwelled nutrients at low-latitudes, leading to an increase of the global rate of primary production by 0.29 Gt C yr^{-1} fueled by biological activity in all northern basins, again, breaking the bimodal productivity pattern seen previously. Ultimately, although there is still significant CO_2 taken up from the atmosphere in intermediate waters formed in the Southern Ocean as noted before, there is a weaker but widespread loss of CO_2 vented from water masses entering the abyssal ocean that counterbalances the uptake with south shifted wind stress alone, as diagnosed from $C_{gas\ exch}$ distributions. Of course, offsetting the loss of carbon dioxide to the atmosphere due to more rapid circulation is an increase of disequilibrium DIC content of 186.90 Gt C compared to the control, or roughly 50 Gt C more than the standard south shifted case.

4. Finally, a decrease in the magnitude of the southward-shifted westerlies precipitates a further decrease in atmospheric CO_2 to 257.1 µatm that is ~21 µatm lower than the preindustrial control state and 11.3 µatm lower than solely shifting the wind stress south achieves. Again, this is attained by reducing the strength of the Southern Ocean meridional overturning cell, in this case to 4.60 Sv which is confined to the very surface layer. This all but halts the upwelling of deep waters in the Southern Ocean and decreases the concentration of macronutrients south

of 40°S, however this has little local effect on biological productivity, but causes a slight decrease in primary production in the Atlantic. Yet, in general, Northern Hemisphere productivity continues at a similar rate, compared to when the climatological wind stress is shifted southward, fed by nutrients that are mixed through the pycnocline and by nutrients upwelled directly by the strong and fairly deep reaching Southern Hemisphere subtropical gyres. Therefore, on balance, the globally integrated rate of biological production increases $0.18\,\mathrm{Gt\,C\,yr^{-1}}$ relative to the control run, but remains approximately equal to the south shift alone. In terms of the efficiency of the soft tissue pump there is an increase to 36.8%, instead of a small decline in efficiency, due to the reduced concentration of unutilised nutrients being subducted into the ocean interior as preformed phosphate from the Southern Ocean. There is a greater concentration of atmospheric CO_2 taken up in the region of the diminished Southern Ocean overturning circulation between 40–60°S that totals $44.60\,\mathrm{Gt\,C}$ over the control state and this intensifies the distribution of the anomaly of $C_{gas\ exch}$, with an increase in the uptake in the Southern Ocean and advection to intermediate depths further north. Indeed, slowing of the overturning results in a halving of the disequilibrium concentration of DIC compared to the south shifted case.

4.4 Summary

After 5000 years with a northward shift in the Southern Hemisphere winds, atmospheric CO_2 concentration increased by $8.0\,\mu\mathrm{atm}$ to $286.1\,\mu\mathrm{atm}$. The location of maximum northward Ekman transport migrated north as did the compensating eddy circulation and the core of the ACC particularly in the Atlantic and Indian sectors with little latitudinal shift in the Pacific sector. This slightly increased the strength of the "Deacon cell" overturning in the Southern Ocean because of the reduction in the Coriolis parameter but profoundly affected the depth from which waters were upwelled, reducing its reach to the upper 1500 m with direct geostrophic compensation occurring below the northward Ekman flow associated with the intensification of surface pressure gradients by the westerlies and the subsequent establishment of a Southern Hemisphere subpolar "supergyre" that strongly connects the South Atlantic and South Indian Oceans with a smaller extension into the South Pacific. Expansion of Southern Hemisphere easterlies creates an anticyclonic circulatory cell adjacent to Antarctica with southward flow across the unbounded latitudes of Drake Passage that is partially compensated by an

eddy induced circulation with southerly flow at the surface around 60°S. The residual of this southern cell is just as energetic as the cyclonic overturning in the control Southern Ocean, thus upwelling in this region continues to draw carbon and nutrient rich deep waters to the surface. However this is supplemented by the shallower subpolar Southern Ocean overturning that draws waters from at or just below the nutricline, that are nevertheless relatively enriched in macronutrients and DIC, to the surface. Subsurface isopycnal displacement aligns the region of maximum isopycnal slope with the peak in wind stress, however surface temperature and salinity restoring prevent a significant increase in Southern Ocean isopycnal outcrop area.

Enhanced surface northward Ekman transport delivers upwelled nutrients into the Atlantic basin to the detriment of the Indian and Pacific basins, creating the productivity dipole that reflects the differing nutrient supply mechanisms between the two regions observed previously. In this instance, the decline in biological productivity in the Indo-Pacific dominated the global net decline of $0.26\,\mathrm{Gt\,C\,yr^{-1}}$ but despite this decrease, the efficiency of the soft tissue pump actually increased slightly. The majority of the $17.07\,\mathrm{Gt\,C}$ expelled from the ocean to the atmosphere primarily through the Southern Ocean at 40°S may have been due to a net decrease of $12.67\,\mathrm{Gt\,C}$ in the ocean-atmosphere CO_2 disequilibrium concentration. There is an increase in disequilibrium concentration in the region of the northern cell of the Southern Ocean circulation, which has nearly doubled in strength compared to the Southern Ocean overturning cell in the control run. However, because the waters that are upwelled have a lower concentration of DIC compared to water masses upwelled from the abyssal ocean, whilst still being enriched compared to surface waters, when these waters are subducted into the ocean interior and exported north, they are much closer to equilibrium with the atmosphere carrying a reduced disequilibrium concentration. Indeed, tracing the air-sea exchange flux into the interior as $C_{gas\ exch}$ shows negative anomalies indicative of outgassing in these same regions. To the south of the ACC, there is also decreased disequilibrium, but this is coupled to an increase in uptake of CO_2 from the atmosphere, with some suggestion of deep ocean CO_2 uptake particularly in the Indian and Pacific Oceans.

Shifting the Southern Hemisphere winds to the south produced a southward shift in northward Ekman transport and the core of the ACC, however the maximum eddy driven overturning remained roughly stationary leading to more complete compensation in the residual circulation, reducing the volume of thermocline waters produced in the Southern Ocean and leading to shoaling of the low-latitude pycnocline. In the place of the shallow, intense subpolar circulation under northward-shifted winds in the

Indo-Pacific is an intense negative cell with southward flow at the surface that promotes convergence and downwelling in the Southern Ocean, causing decreased nutrient supply and biological productivity, and upwelling at low-latitudes, with subtropical upwelling even in the Atlantic Ocean that leads to increased nutrient supply and biological productivity in the surface of all three basins in a departure from the Atlantic/Indo-Pacific see-saw and increasing global net primary production rates by $0.16\,\mathrm{Gt\,C\,yr^{-1}}$. However, despite this increase, there is a marginal decline in the efficiency of the soft tissue pump. Yet ultimately, atmospheric CO_2 concentration decreased by 9.6 µatm to 268.4 µatm by oceanic uptake of 20.43 Gt C mostly through the Southern Ocean around 40°S. Oceanic circulation appears to prevent an astonishing 138.3 Gt C from escaping to the atmosphere, trapping it mainly in the abyss.

Combining these shifts with a perturbation to westerly wind stress magnitude results in an almost linear combination of effects, with the north-shifted winds causing slight increased sensitivity of atmospheric CO_2 to residual overturning due to the combined effects of the two overturning cells in the Southern Ocean. An increase in wind stress, with the maximum shifted either north or south, leads to outgassing of a further 11–18 µatm from the ocean due to increased Southern Ocean overturning, while decreasing wind stress magnitude, either shifted north or south, results in a further decrease of atmospheric CO_2 of 11–14 µatm.

Chapter 5

Response of the Global Carbon Cycle to Aeolian Dust Deposition

A key feature of the observed surface macronutrient distribution captured by this configuration of MITgcm is that the concentration of phosphate in the Southern Ocean is significantly higher than the remainder of the ocean due to upwelling that brings nutrient-rich deep waters to the surface along upwardly sloping isopycnals. Yet levels of biological productivity, particularly south of 60°S are low. In these so-called High Nutrient Low Chlorophyll (HNLC) regions, numerous *in vitro* (bottle incubation) and *in situ* experiments [reviewed by *de Baar et al.*, 2005] have indicated that addition of dissolved Fe stimulates the growth of phytoplankton, in particular siliceous diatoms, and a concomitant drawdown of CO_2. In an extension of this, *Martin* [1990] suggested that glacial pCO_2 may have been lower due to a 50-fold (2–5x globally) increase in atmospheric dust supply to the Southern Ocean during the LGM. By relieving the Fe limitation, phytoplankton growth may have been greatly enhanced and larger amounts of upwelled nutrients may have been utilised, preventing the escape of upwelled concentrations of CO_2, causing atmospheric CO_2 drawdown and also increasing the efficiency of the soft tissue pump by reducing the concentration of unutilised nutrients being subducted into the ocean interior.

However, the range of possible atmospheric responses to perturbations in aeolian iron deposition in a variety of box models and GCMs (40–8 µatm, [*Archer et al.*, 2000; *Bopp et al.*, 2003; *Dutkiewicz et al.*, 2005a; *Parekh et al.*, 2006b; *Watson et al.*, 2000]) and the incomplete picture provided by paleoceanographic proxy evidence revealing more

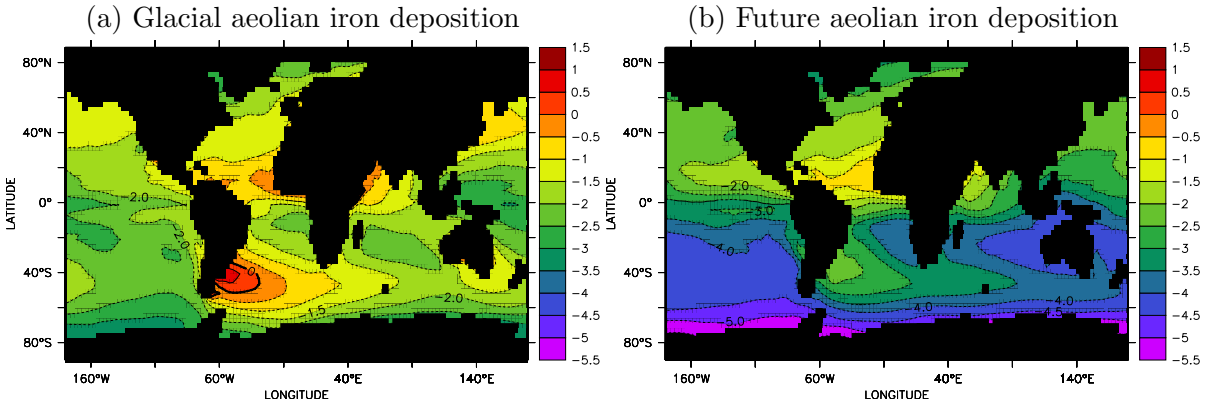

Figure 5.1: Perturbed aeolian iron deposition fields derived from *Mahowald et al.* [2006a,b]. Annual average of (a) monthly glacial aeolian iron deposition and (b) monthly aeolian iron deposition under CO_2 doubling (log_{10}nmol Fe m^{-2} s^{-1}).

regional changes in productivity [*Kohfeld et al.*, 2005] and nutrient utilisation [*Archer et al.*, 2000; *Sigman and Boyle*, 2000] whose interpretation is complicated by multiple other processes and environmental factors [*Kohfeld et al.*, 2005], warrants further investigation.

Furthermore, while glacial increased aeolian dust deposition in the Southern Ocean has been recorded in Antarctic ice cores [*Petit et al.*, 1999] supposedly due to more arid and dustier conditions, possible future changes in climate may result in a more vigorous hydrological cycle, a more humid atmosphere and reduced atmospheric dust loading [e.g. *Parekh et al.*, 2006a]. To examine the sensitivity of atmospheric CO_2 concentration to iron deposition, and test the iron fertilisation hypothesis, the modern monthly aeolian iron deposition field used in the control run (Figure 2.4a) was substituted for the "best guess" LGM field (Figure 5.1a) of *Mahowald et al.* [2006a,b], which is approximately four times greater globally than the control field and ~40 times greater in the Southern Hemisphere (158 times more south of 40°S), and integrated until a new steady state was reached. In a further perturbation, the monthly deposition field is substituted for the simulated dust distribution under a doubling of carbon dioxide (Figure 5.1b) that deposits approximately 2.5 times less iron globally than the control forcing per year and half as much iron in the Southern Hemisphere (~3 times less south of 40°S). After 3000 years of increased glacial dust deposition, atmospheric CO_2 decreased 2.43 µatm to 275.64 µatm while under decreased future dust deposition atmospheric CO_2 rose 4.75 µatm to 282.84 µatm.

5.1 Glacial aeolian iron deposition

Since there are no alterations to the physical circulation, anomalies in the biogeochemical tracers reflect changing patterns of biological productivity mediated by altered micronutrient concentrations. As expected, greater atmospheric iron deposition increases surface dissolved iron concentrations globally (Figure 5.2a compared to Figure 2.8b) and this signal is exported into the ocean interior through the conduits of deep water formation particularly increasing the iron concentrations in the Southern Hemisphere where the largest increase in input occurs.

The globally integrated rate of productivity responds to the global increase in micronutrient concentrations sequestering an additional $0.35\,\mathrm{Gt\,C\,yr^{-1}}$ but despite the blanket increase in surface dissolved iron, the primary production increase is confined to the Southern Hemisphere (Figure 5.2b) because much of the Northern Hemisphere, particularly the North Atlantic, is already micronutrient replete being limited instead by light or the concentration of macronutrients [*Dutkiewicz et al.*, 2006; *Parekh et al.*, 2006a].

In the South Pacific subtropical gyre, a region of particularly high iron stress in this model as it is remote and does not benefit from the upwelled supply of dissolved Fe as in the Southern Ocean or equatorial Pacific, the level of macronutrients is almost completely drawn down yet south of 60°S substantial quantities of macronutrients remain as a result of continuing limitation by other factors, especially photosynthetically active radiation due to deep mixed layers and sea-ice cover [*Dutkiewicz et al.*, 2006; *Mitchell et al.*, 1991; *van Oijen et al.*, 2004]. The role of the organic ligand is also somewhat unknown in the real ocean [*Parekh et al.*, 2005]. If the concentration of the ligand-iron complex that protects the free iron from scavenging in the ocean interior becomes saturated then the bioavailible dissolved iron concentration peaks and therefore no further increase in the supply of micronutrients to Fe limited upwelling regimes can occur. *Parekh et al.* [2006a,b] find that a doubling of the ligand concentration almost doubles the drawdown of atmospheric CO_2.

There is also a small but widespread decrease in productivity in the remaining regions of the photic zone probably in reaction to enhanced macronutrient utilisation in the south. The Southern Ocean is a key source region of nutrients to the surface ocean in the tightly interconnected nutrient supply chain, also displayed in other perturbations, upwelling nutrient rich deep waters and exporting them to the north [*Dutkiewicz et al.*,

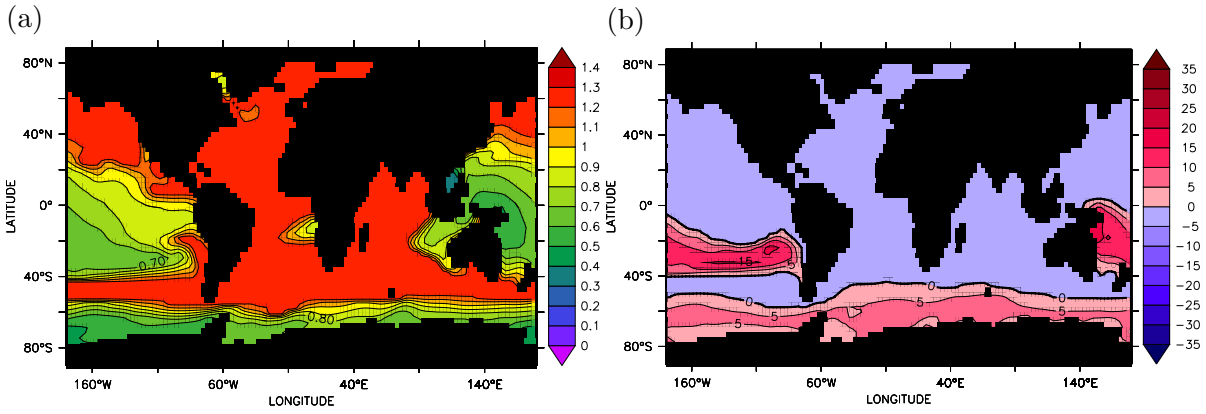

Figure 5.2: Equilibrium MITgcm output for the glacial aeolian iron deposition perturbation. (a) Sea surface dissolved iron concentration ($\mu mol\,m^{-3}$) and (b) biological productivity anomaly ($mmol\,C\,m^{-3}$)

2005a; *Sarmiento et al.*, 2004; *Williams and Follows*, 1998]. Thus *in situ* use of nutrients here ultimately reduces the supply by lateral advection to the remainder of the ocean.

Tracing the fate of the additional biological production using the regenerated phosphate concentration (Equation 2.29) uncovers the accumulation of production from south of 60°S in the deep Southern Ocean (Figure 5.3a and b), which is not captured in the physical experiments previously because this region consistently shows little or no change in biological activity despite changes in macronutrient concentration, highlighting the region's iron stress. There is also a noticable increase in local remineralisation in the surface layer of the subtropical South Pacific where biological production was enhanced the most. This perhaps explains the particularly small change in atmospheric CO_2 concentration because a smaller quantity of carbon dioxide is actually trapped in the deep ocean whilst the remainder is recycled and released back to the atmosphere. Overall, the efficiency of the soft tissue pump increases marginally from 35.70% in the control to 36.30% mainly due to reduced concentrations of preformed nutrients due to increased consumption anomaly being subducted into the ocean interior (Figure 5.3c and d).

Uptake of CO_2 from the atmosphere occurs in the regions of biological uptake, but there is also a slight increase in outgassing in the Pacific Ocean at around 40°S possibly due to the escape of the locally remineralised iron-fertilised biologically-fixed carbon, which appears to erase much of the effect of increased subtropical South Pacific production. Also there is a slight net outgassing across the remainder of the surface ocean caused by the slight decrease in productivity associated with decreased nutrient supply from

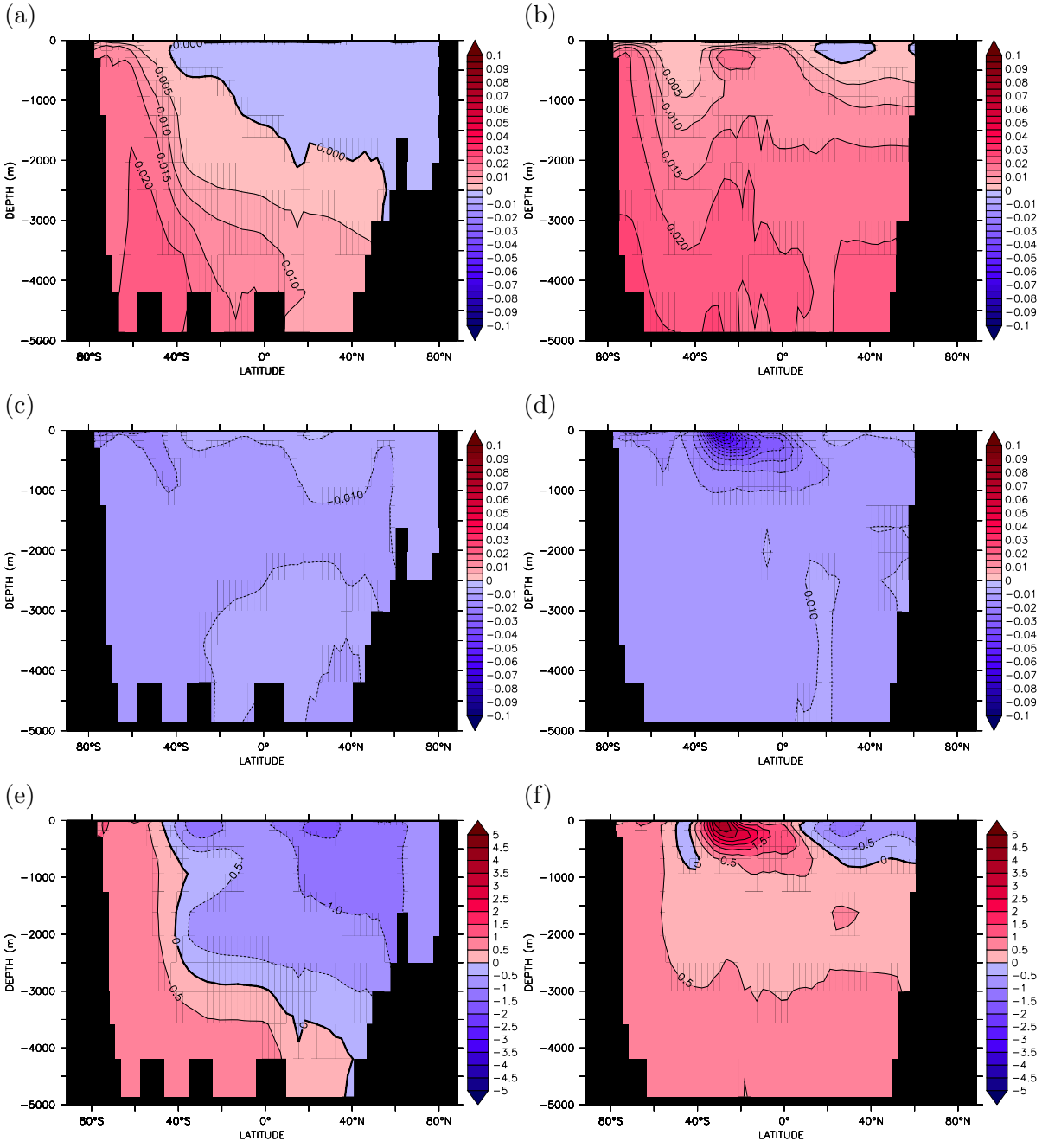

Figure 5.3: MITgcm output for the glacial aeolian iron deposition perturbation. Meridional sections of tracer anomaly in the Atlantic Ocean (left column) and in the Indo-Pacific Oceans (right column) for (a and b) regenerated phosphate anomaly (mmol P m^{-3}) calculated from Apparent Oxygen Utilisation using Equation 2.28 and Equation 2.29, (c and d) preformed phosphate anomaly (mmol P m^{-3}) calculated using the regenerated component and Equation 2.27, and (e and f) $C_{gas\ exch}$ anomaly (mmol C m^{-3}) calculated from Equation 2.37. Note the reduced scale.

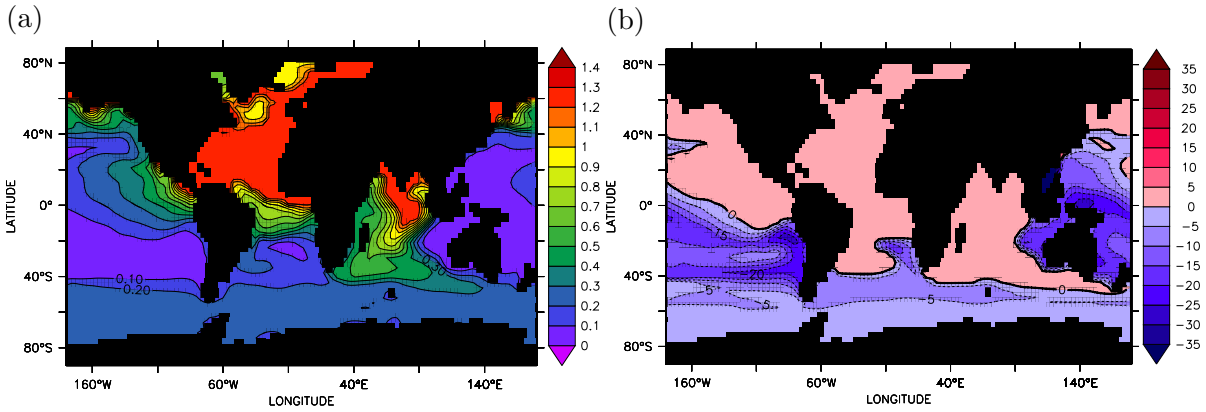

Figure 5.4: Equilibrium MITgcm output for the future aeolian iron deposition perturbation. (a) Sea surface dissolved iron concentration ($\mu mol\,m^{-3}$) and (b) biological productivity anomaly ($mmol\,C\,m^{-3}$)

the Southern Ocean and the decreased concentration of atmospheric CO_2 that lowers surface ocean equilibrium concentration. The globally integrated effect of net air-sea CO_2 fluxes is to remove 5.13 Gt C from the atmosphere before the atmosphere-ocean balance is restored. The water masses that are involved in this exchange, highlighted by anomalies in the quasiconservative tracer $C_{gas\ exch}$ (Figure 5.3e and f), show that AABW is a key player in the Atlantic and Indo-Pacific Oceans with a large volume, all be it of low concentration, taking up CO_2 from the atmosphere. The region of South Pacific uptake is also seen confined near to the upper 1000 m. Finally, especially in the North Atlantic, waters that were outgassing at the surface are observed being subducted into the deep ocean. Again, the net adjustment of $C_{gas\ exch}$ of 4.65 Gt C compares reasonably well with the net air-sea flux adjustment.

5.2 Future aeolian iron deposition

Under reduced aeolian iron deposition the atmospheric CO_2 perturbation is roughly twice as large as when significantly enhanced iron addition is applied. The Southern Hemisphere and particularly the remote South Pacific becomes increasingly iron limited (Figure 5.4a) and suffers a decline in biological productivity (Figure 5.4a). The relative importance of the upwelling source of iron to the Southern Ocean is highlighted by the smaller decrease in productivity there than in the subtropical South Pacific, which shows a particularly large decline in primary production. In opposition to the decline in productivity in the Southern Hemisphere and the Pacific Ocean, the regions of strong

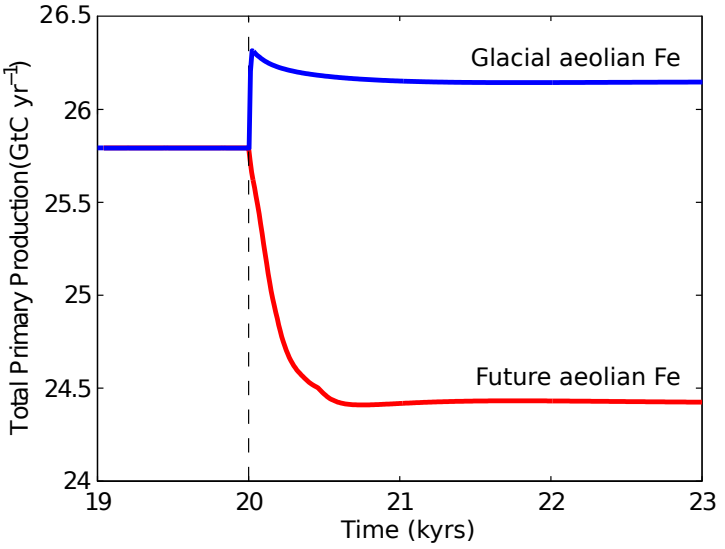

Figure 5.5: Equilibrium MITgcm output for perturbed aeolian iron fluxes. Timeseries of globally integrated primary production (Gt C yr^{-1}), starting from the control state when t=20 kyrs and applying increased, glacial aeolian iron fluxes (blue) and decreased future aeolian iron fluxes under CO_2 doubling (red).

dust deposition under the major plumes in the North Atlantic and North Indian Oceans (and to some extent along the western coast of North America) remain iron replete. Due to reduced macronutrient utilisation in the iron deficient upwelling regions and an increase in lateral supply of phosphate to the Northern Hemisphere results in a slight increase in biological production. The net effect of this is to temper the decrease in net global production rate to 1.37 Gt C yr^{-1} (see also Figure 5.5).

The concentration of regenerated phosphate (Figure 5.6a and b) is reduced in the Southern Hemisphere of all basins, with the Southern Ocean decreased productivity reflected in low regenerated nutrients in AABW that spreads to the north. There is also decreased influence of the soft tissue pump in the northern Indo-Pacific Oceans particularly just south of the Equator. Meanwhile, enhanced nutrient supply to the iron-replete North Atlantic results in slightly increased concentrations of regenerated phosphate. These decreases therefore lead to greater preformed nutrient concentrations (Figure 5.6c and d) injected into the ocean interior in southern source intermediate and mode waters and within the surface gyre circulation that reflect a 1.39% decrease in the efficiency of the soft tissue pump from 35.70% in the control to 34.31%. Ultimately this results in 10.12 Gt C being expelled from ocean to atmosphere. Anomalies of $C_{gas\ exch}$ show that the origin of much of this CO_2 is from surface and intermediate waters of the South Atlantic and Indo-Pacific Oceans, with increased uptake in the more productive North

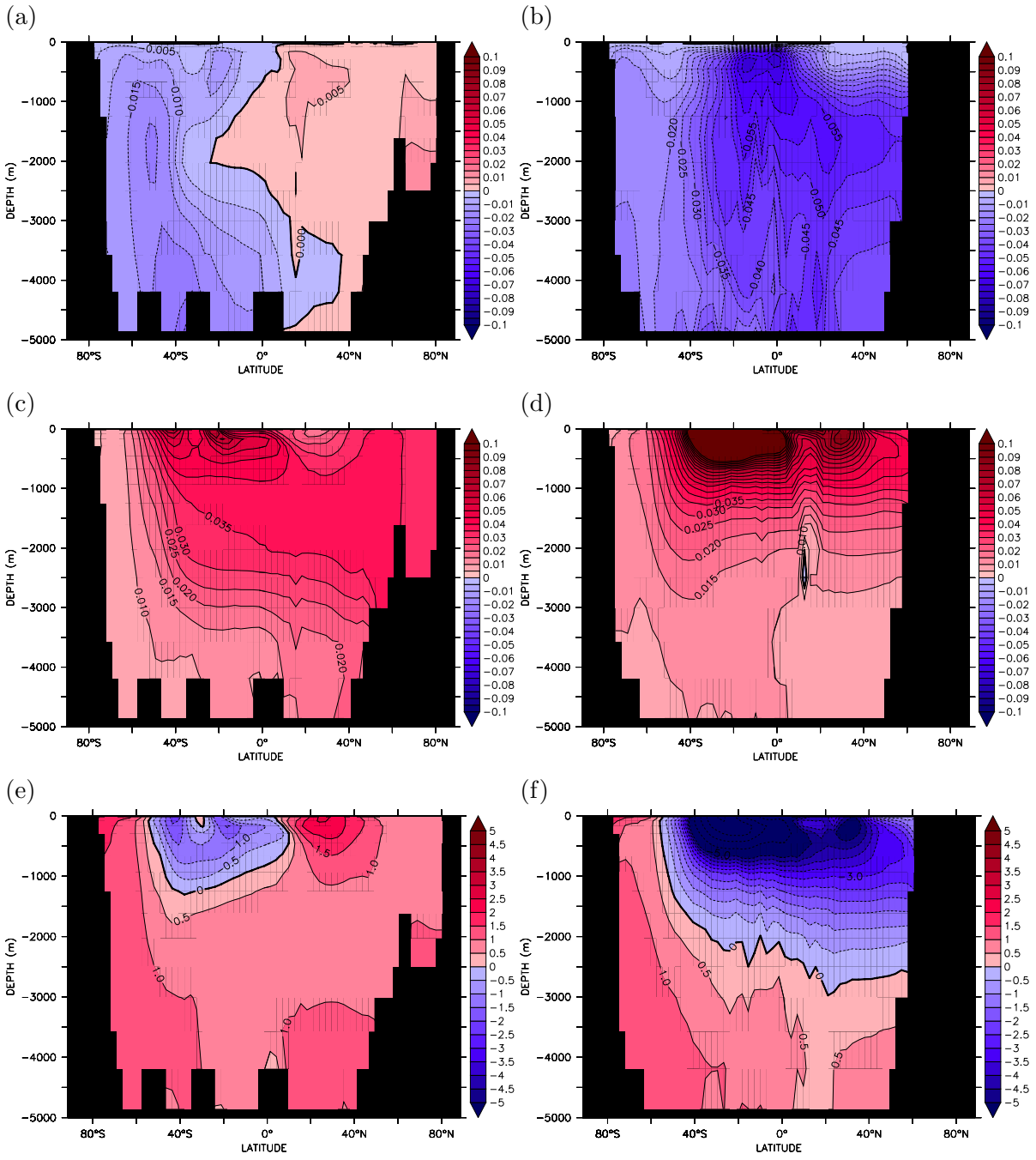

Figure 5.6: MITgcm output for the future aeolian iron deposition perturbation. Meridional sections of tracer anomaly in the Atlantic Ocean (left column) and in the Indo-Pacific Oceans (right column) for (a and b) regenerated phosphate anomaly (mmol P m^{-3}) calculated from Apparent Oxygen Utilisation using Equation 2.28 and Equation 2.29, (c and d) preformed phosphate anomaly (mmol P m^{-3}) calculated using the regenerated component and Equation 2.27, and (e and f) $C_{gas\ exch}$ anomaly (mmol C m^{-3}) calculated from Equation 2.37. Note the reduced scale.

Atlantic. However, despite decreased production in the Southern Ocean there is actually slightly increased CO_2 storage resulting from slightly reduced outgassing south of 40°S due to increased equilibrium concentration in response to elevated atmospheric CO_2, which is exported into the deep ocean via bottom water formation. The net adjustment of $C_{gas\ exch}$ is equivalent to oceanic loss of 10.60 Gt C to the atmosphere that is corroborated by the net global surface flux.

5.3 Summary

Increased aeolian iron deposition suggestive of the inputs experienced during the last glacial maximum resulted in a slight increase in primary production in the micronutrient limited regions of the Southern Ocean and the South Pacific subtropical gyre and a marginal increase in the efficiency of the soft tissue pump. Reduction in lateral macronutrient transfer to the parts of the Northern Hemisphere instigated a small but widespread decrease in biological productivity. Only a small decline in atmospheric CO_2 concentration was produced because of possible saturation of the deep ocean ligand concentration that protects the dissolved iron from scavenging. Upwelling of this protected iron is a major source of micronutrients in upwelling regions and thus saturation prevents increased aeolian iron effectively being delivered. Also, only a fraction of the Fe-fertilised production was exported to the deep ocean as concentrations of both regenerated phosphate and $C_{gas\ exch}$ suggest that the additional fixed carbon in the subtropical South Pacific was locally remineralised and susceptible to flushing back to the atmosphere.

Decreased aeolian iron deposition, which may be applicable to a more humid, warmer greenhouse climates and was on average a smaller perturbation than the glacial perturbation, resulted in a greater decline in biological productivity. A dramatic increase in surface iron limitation particularly in the South Pacific reduces primary production while the Southern Ocean, despite being fairly micronutrient limited, is not so badly affected due to the alternative supply of iron in upwelling waters. Decreased regenerated phosphate and decreased efficiency of the soft tissue pump lead to an approximately twice as large change in atmospheric CO_2 than with iron fertilisation.

Chapter 6

Response of the Global Carbon Cycle and the Southern Ocean Wind Stress Magnitude Experiments to Surface Buoyancy Forcing, Mesoscale Eddy Activity and Wind Speed.

In this chapter, several assumptions and simplifications made throughout Part II will be examined using the simple and well examined perturbation to Southern Hemisphere wind stress magnitude including the use of climatological sea surface temperature and salinity relaxation in Section 6.1, proportionally changing the activity of the mesoscale eddy field in Section 6.2 and the effect of Southern Ocean wind speed in Section 6.3, which is an assumption made for ease of interpretation but also a standing question regarding the rate of air-sea gas exchange.

6.1 Response of the global carbon cycle to surface heat and freshwater boundary conditions

Surface buoyancy fluxes are important in determining the balance between Eulerian-mean and eddy-induced circulations that contribute towards the residual circulation [*Karsten and Marshall*, 2002; *Marshall*, 1997]. At the depth of the mixed layer, $-h$, the net overturning circulation in the Southern Ocean, Ψ_{res}, forms a balance (Equation 6.1) with the net air-sea heat and freshwater fluxes combined as the buoyancy flux, B, scaled by the meridional gradient of buoyancy in the mixed layer, $\partial b/\partial y$, and modified by the vertical flux of buoyancy across the base of the mixed layer, which is probably small in the ocean and in this model determined by the values of diapycnal mixing, κ_z, (Table 2.2).

$$\Psi_{res}\frac{\partial b}{\partial y} = B - \kappa_z\frac{\partial b}{\partial z} \tag{6.1}$$

In the Southern Ocean, the meridional gradient of buoyancy is positive so that for a northward transport of water driven by the westerly surface wind stress over the ACC, the water must gain buoyancy from the atmosphere (and to a lesser extent from below the mixed layer) to become less dense [*Keeling and Stephens*, 2001; *Watson and Naveira Garabato*, 2006]. *Keeling and Stephens* [2001] suggest that the modern density decrease is achieved by net precipitation at the southern flank of the ACC, which contributes to form fresh AAIW, however *Karsten and Marshall* [2002] find net buoyancy gain is dominated by a small air-sea heat flux. Either way, the rapid buoyancy gain sustains a relatively vigorous contemporary residual circulation and associated upwelling of deep water. In previous chapters, the residual circulation was allowed to vary because the air-sea heat and freshwater fluxes contained a varying component due to climatological restoration. With increased upwelling of cold waters an increase in the net heat flux also occurs to restore the balance in Equation 6.1. *Watson and Naveira Garabato* [2006] hypothesised that during glacial periods the buoyancy flux would be increasingly dependent on the salinity balance and would therefore remain relatively constant, varying mainly with the formation and melting of sea-ice and linked with the production of AABW. Assuming a similar density gradient across the ACC then the invariable freshwater-driven buoyancy fluxes would have supported a reduced volume of deep ocean residual upwelling. Indeed, if a blanket cover of glacial sea ice protected the upwelling waters from atmospheric buoyancy input, with sea ice melt adding freshwater to the north of the ACC then the surface buoyancy gradient may have been

greater, or even reversed thus further inhibiting northward Ekman transport [*Keeling and Stephens*, 2001; *Watson and Naveira Garabato*, 2006].

A change in residual circulation in the Southern Ocean may have consequences for global and particularly Atlantic meridional overturning circulations if the formation of NADW is governed by Southern Hemisphere upwelling [*McDermott*, 1996; *Toggweiler and Samuels*, 1995, 1998] also described in Chapter 3. However, the relaxing conditions may also introduce additional responses to the perturbed wind stress forcing that may affect the sensitivity of the global ocean and carbon cycle to Southern Ocean processes. *Rahmstorf and England* [1997] attribute the linear response of NADW circulation and the Atlantic meridional overturning to the use of relaxing near surface boundary conditions as experiments with an ocean and simple atmospheric feedback model show an enhanced response to increased Southern Hemisphere winds but little change when wind stress was reduced. This is related to the North Atlantic buoyancy feedback whereby, under prognostic surface forcing, increased (decreased) wind stress in the Southern Hemisphere increases (decreases) North Atlantic Deep Water formation, driving an increase (decrease) in northward heat transport and an increase (decrease) in surface density which acts as a negative feedback to decrease (increase) North Atlantic Deep Water formation. Under relaxing conditions this feedback is almost completely damped and the North Atlantic overturning responds linearly to Southern Hemisphere wind perturbations.

6.1.1 Wind stress perturbations using fixed surface boundary conditions

To investigate the effect of climatological relaxation, the option of implementing alternative surface boundary conditions was encoded into the model. Monthly average temperature and salinity relaxation fields ($TRELAX$ and $SRELAX$) were diagnosed from the control run that maintain the control state without excessive drift in circulation or biogeochemistry. Relaxation was turned off and these surface fluxes were prescribed in addition to the climatological heat (Q_{net}) and freshwater ($E-P-R=-S_0\times F$) fluxes. Figure 6.1 shows the resultant zonally-averaged monthly and annual average buoyancy fluxes calculated from Equation 6.2, Where g is acceleration due to gravity, ρ_0 and C_p are the reference density and specific heat capacity of seawater respectively, α and β are typical thermal expansion and haline contraction coefficients respectively, F is a mass

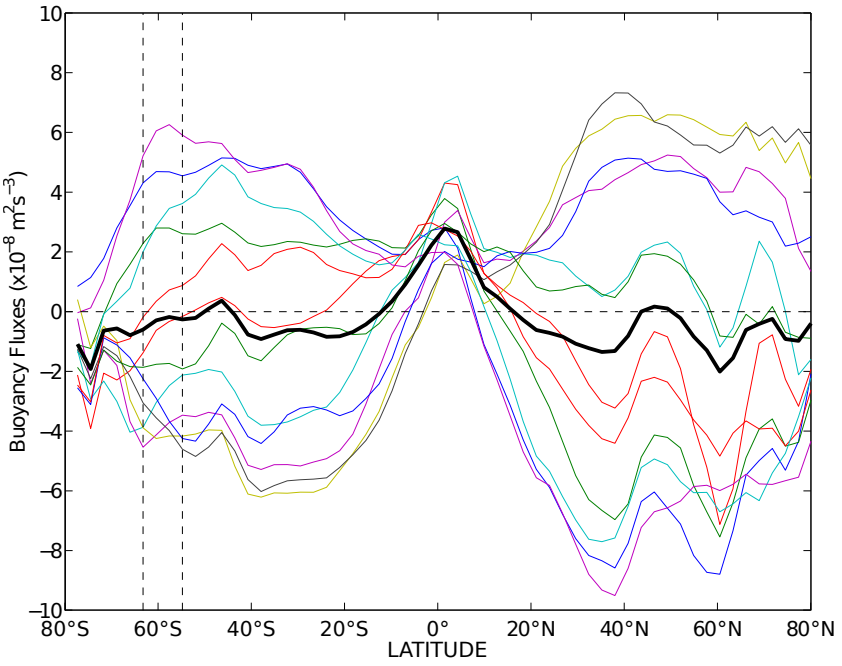

Figure 6.1: Monthly (thin coloured) and annual mean (thick black) buoyancy fluxes calculated with Equation 6.2 from the control heat and freshwater forcing and surface temperature and salinity relaxation used to drive the fixed surface boundary condition experiments. Dashed vertical lines denote the position of the unblocked latitudes at Drake Passage. Positive values indicate buoyancy gain (density loss) while negative values indicate buoyancy loss (density gain). Monthly variability is dominated by seasonally varying heat fluxes (of the order $1 \times 10^{-8}\,\mathrm{m^2\,s^{-3}}$) with smaller freshwater/salt fluxes (of the order $1 \times 10^{-10}\,\mathrm{m^2\,s^{-3}}$).

flux of freshwater and S_0 is a reference salinity, see Table 2.2 for constant values).

$$B(\mathrm{m^2\,s^{-3}}) = \frac{g\alpha}{\rho_0 C_p}(Q_{net} + TRELAX) - \frac{g\beta}{\rho_0}(E - P - R + SRELAX) \qquad (6.2)$$

The general pattern of buoyancy gain at the equator and buoyancy loss in the polar regions is modulated by buoyancy loss in midlatitudes due to excess evaporation over precipitation (see control flux components in Figure 2.3e). In particular in the Southern Hemisphere, south of 60°S there is buoyancy loss associated with southward transport of upwelled waters and bottom water formation, while to the north, buoyancy gain, in part due to freshwater input, aids the northward-flow of lighter upwelled waters across mean surface isopycnals in the Ekman layer associated with intermediate and mode water formation. The increased and decreased wind stress magnitude perturbations (Chapter 3, Figure 3.1) were repeated with this pattern of buoyancy fluxes held constant, with no climatological restoration. After 5000 years atmospheric CO_2 increased 16.58 µatm from 278.05 µatm to 294.63 µatm, a small difference with "fixed" surface

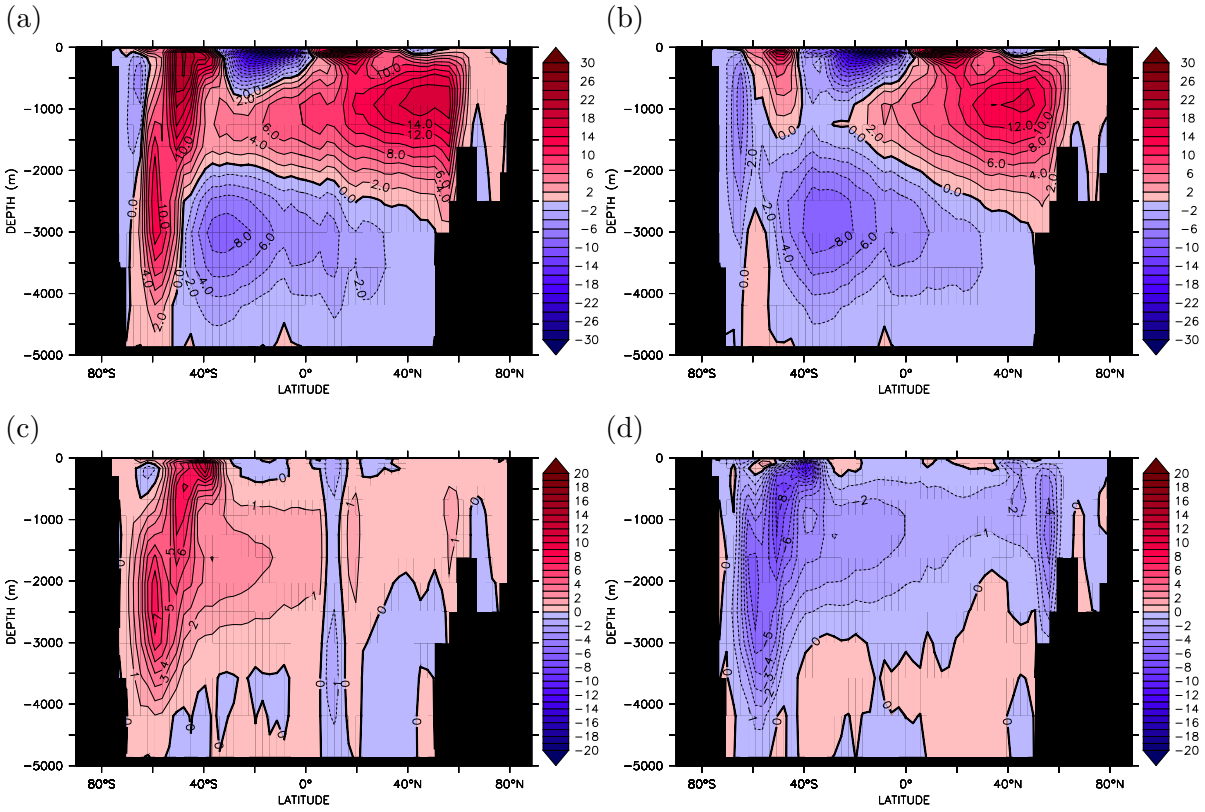

Figure 6.2: Equilibrium MITgcm output for the increased (left column) and decreased (right column) wind stress perturbations repeated with "fixed" surface boundary conditions. (a and b) show the residual overturning circulation (Sv) while (c and d) show the residual overturning anomaly compared to the control run (Sv).

boundary conditions compared with surface relaxing boundary conditions that achieved a change of 15.6 µatm. Atmospheric CO_2 content decreased 16.81 µatm to 261.87 µatm with decreased wind stress, which is roughly the same as seen previously, with decreased wind stress and surface relaxation resulting in a decrease of 16.3 µatm.

Compared to the control run, increased wind stress causes the same increase in Eulerian-mean circulation of ~60 Sv however the eddy return flow is more vigorous by just under 4.5 Sv due to steepened isopycnals south of 40°S as a result of the increased upwelling of denser deep waters to the south that are inhibited from flowing north at the surface by reduced buoyancy input, particularly between 40–60°S (see Figure 3.6e), under the new constant surface fluxes. This leads to an increase in the extent of compensation between the two components and reduction in the residual Southern Ocean overturning circulation to 22.5 Sv (Figure 6.2a and c) instead of 31.12 Sv observed in Chapter 3, but this change occurs in the upper ocean and therefore does not significantly affect the rate of deep ocean upwelling or water mass subduction. Although surface heat fluxes remained

constant, roughly $5\,W\,m^{-2}$ was added to the Southern Ocean at 60°S from the latent heat of fusion due to freezing of seawater at the surface that might aid the colder water held to the south in travelling northward down the buoyancy gradient. Furthermore, the diapycnal flux of buoyancy becomes more important. When forced with decreased wind stress there is a considerably stronger Southern Ocean residual overturning circulation (Figure 6.2b and d) of 15.44 Sv compared to the 3.84 Sv with relaxing to climatology, despite the almost complete compensation between the individual Eulerian-mean and eddy circulations, which are of a similar order to those in Chapter 3. The relative invariance of the residual circulation can be related to the balance in Equation 6.1 because the fixed fluxes applied in these experiments support the control circulation of ~16 Sv therefore when wind stress is decreased, the strong circulation is maintained by buoyancy fluxes alone and there is no increase in buoyancy loss between 40–60°S (see Figure 3.25). However, the major difference between the two realisations of the residual circulation (Figure 6.2a and b) is the vertical extent of the positive cell in the Southern Ocean, with the increased wind stress showing a vigorous deep reaching circulation while with decreased wind stress, although the circulation is of a similar magnitude to the control run, the depth that it reaches is greatly reduced to 1000–1500 m, similar to the reduction in extent seen previously in Chapter 4 under northward shifted winds.

In both cases, changes to wind stress in the Southern Hemisphere drive changes in the Atlantic meridional overturning circulation of 0.75 Sv and −1.92 Sv for the increased and decreased wind stress perturbations, which is 1.9 Sv and 0.9 Sv lower respectively than previously calculated for wind stress perturbations with surface relaxation. Furthermore, alteration to the abyssal circulation of AABW is reduced by 2.2 Sv and 1.4 Sv in the increased and decreased wind stress cases. Unlike the standard perturbation, increasing the wind stress using "fixed" surface boundary conditions greatly affects the stratification anomaly in the upper 1000 m (Figure 6.3). Instead of seeing a consistent decrease in the upper ocean, stratification is only reduced in the Southern Hemisphere while the top 500 m of the Northern Hemisphere becomes increasingly stratified. Similarly the global increase in stratification of the upper 1000 m with decreased wind stress and relaxing surface boundary conditions is altered so that only the Southern Hemisphere becomes more stratified with a widespread decrease in stratification in the Northern Hemisphere. The constant surface buoyancy fluxes set the mean upper ocean stratification and constrain it to remain similar to the control run. However, in both "fixed" and relaxing cases. deep ocean stratification still shows the same anomaly.

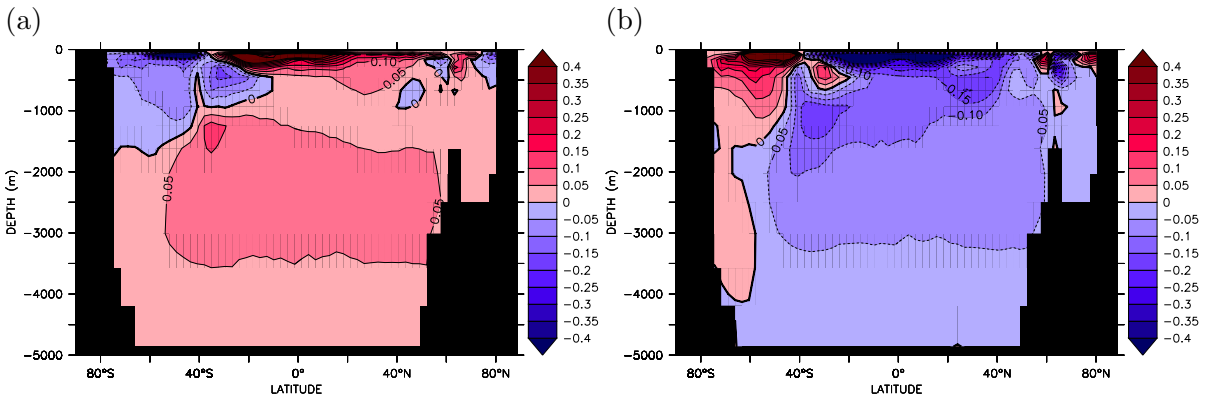

Figure 6.3: MITgcm output for the increased and decreased wind stress perturbations repeated with "fixed" surface boundary conditions. Globally-averaged meridional sections of stratification ($\partial\rho/\partial z$, $\mathrm{g\,m^{-4}}$) for (a) increased and (b) decreased wind stress.

Since the changes to the circulation in the Southern Ocean with "fixed" surface boundary conditions are less extreme compared to those using relaxing surface boundary conditions, the pattern of nutrient and primary production anomalies is the same but somewhat reduced in extent. For example, increased wind stress supplies upwelled nutrients into the South Atlantic at the expense of upwelling nutrients in the Indo-Pacific Oceans and vice versa with decreased wind stress. With surface relaxation, the rate of primary production changes by $0.58\,\mathrm{Gt\,C\,yr^{-1}}$ and $-0.10\,\mathrm{Gt\,C\,yr^{-1}}$ for the increased and decreased perturbations respectively, however with "fixed" surface boundary conditions these anomalies are reduced to $0.18\,\mathrm{Gt\,C\,yr^{-1}}$ and $-0.01\,\mathrm{Gt\,C\,yr^{-1}}$.

With increased wind stress, reduced upper ocean residual overturning circulation decreases the rate of upwelled nutrient export from the light and micronutrient limited Southern Ocean to the macronutrient limited regions to the north so the increase in biological production is not as great. With decreased wind stress, the stronger Southern Ocean overturning with "fixed" surface boundary conditions, although from a shallow depths supplies the surface ocean with a slightly higher concentration of macronutrients and therefore moderates the decreased biological activity in the Atlantic Ocean. In terms of efficiency of the soft tissue pump (see Figure 6.4) increased wind stress causes a reduction in the globally-averaged ratio of regenerated phosphate to total phosphate concentration by 3.7% from 35.7% to 32.0% while decreased wind stress causes and increase in efficiency of 4.2% to 39.9% instead of the previously seen anomalies of ~ ±2.5%, which reinforces the repartitioning of carbon dioxide between the atmosphere and ocean [*Ito and Follows*, 2005]. In common with the previous increased wind stress perturbation, spin up of the Southern Ocean overturning increases the concentration of unutilised,

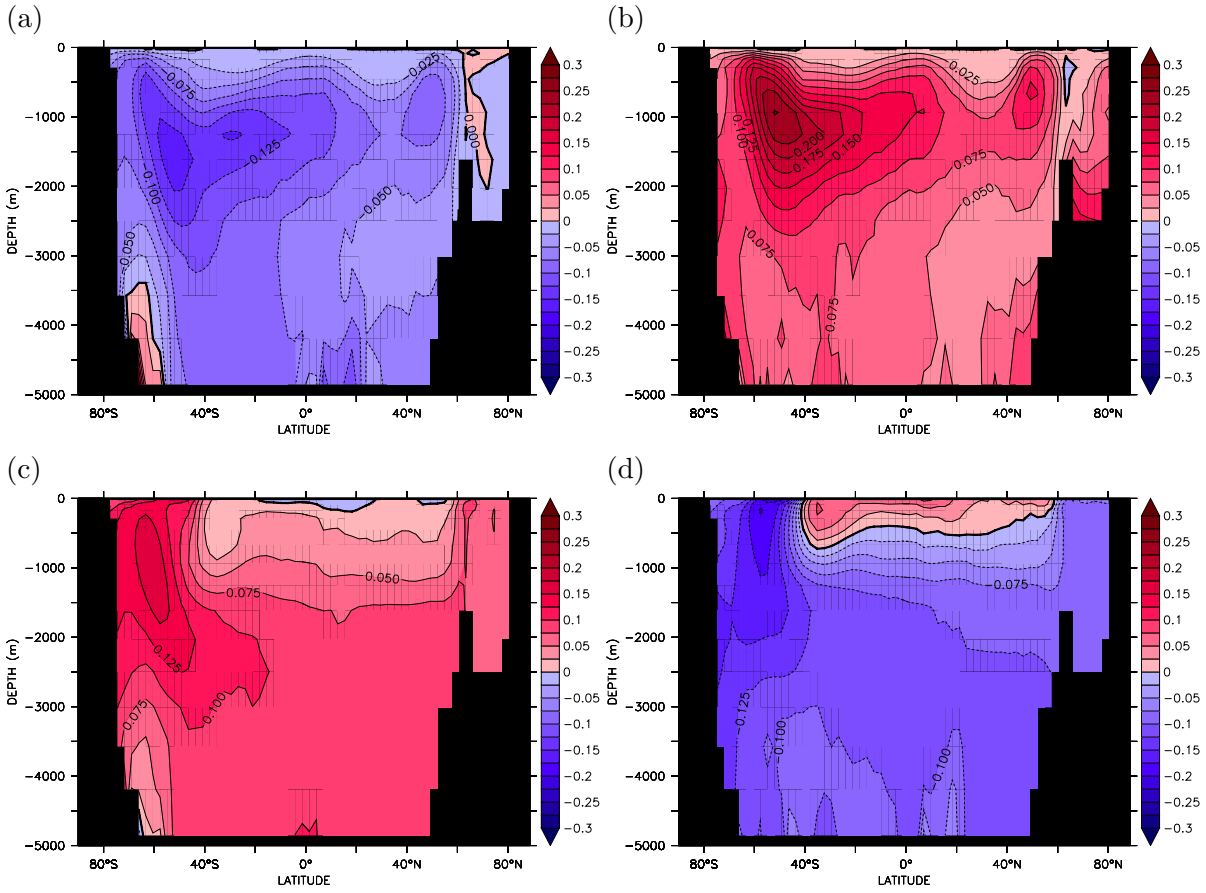

Figure 6.4: MITgcm output for the increased and decreased wind stress perturbations repeated with "fixed" surface boundary conditions. Globally-averaged meridional sections of tracer anomaly for increased (left column) and decreased (right column) wind stress for (a and b) regenerated phosphate anomaly (mmol P m^{-3}) calculated from Apparent Oxygen Utilisation using Equation 2.28 and Equation 2.29, and (c and d) preformed phosphate anomaly (mmol P m^{-3}) calculated using the regenerated component and Equation 2.27.

preformed nutrients (and dissolved oxygen) that are injected into the ocean interior thus reducing the concentration of nutrients returned to the ocean interior through the biological pathway as regenerated phosphate and therefore reducing the efficiency of the soft tissue pump. The relatively rapid, but shallower reaching circulation achieved with decreased wind stress reduces the ventilation of the deep ocean, while the reduced concentration of macronutrients that it upwells tempers Atlantic production decline, acting to decrease the concentrations of preformed phosphate that are subducted from the surface. An increase in the concentration of macronutrients returning to the ocean interior via the biological pathway therefore increases the efficiency of the soft tissue pump.

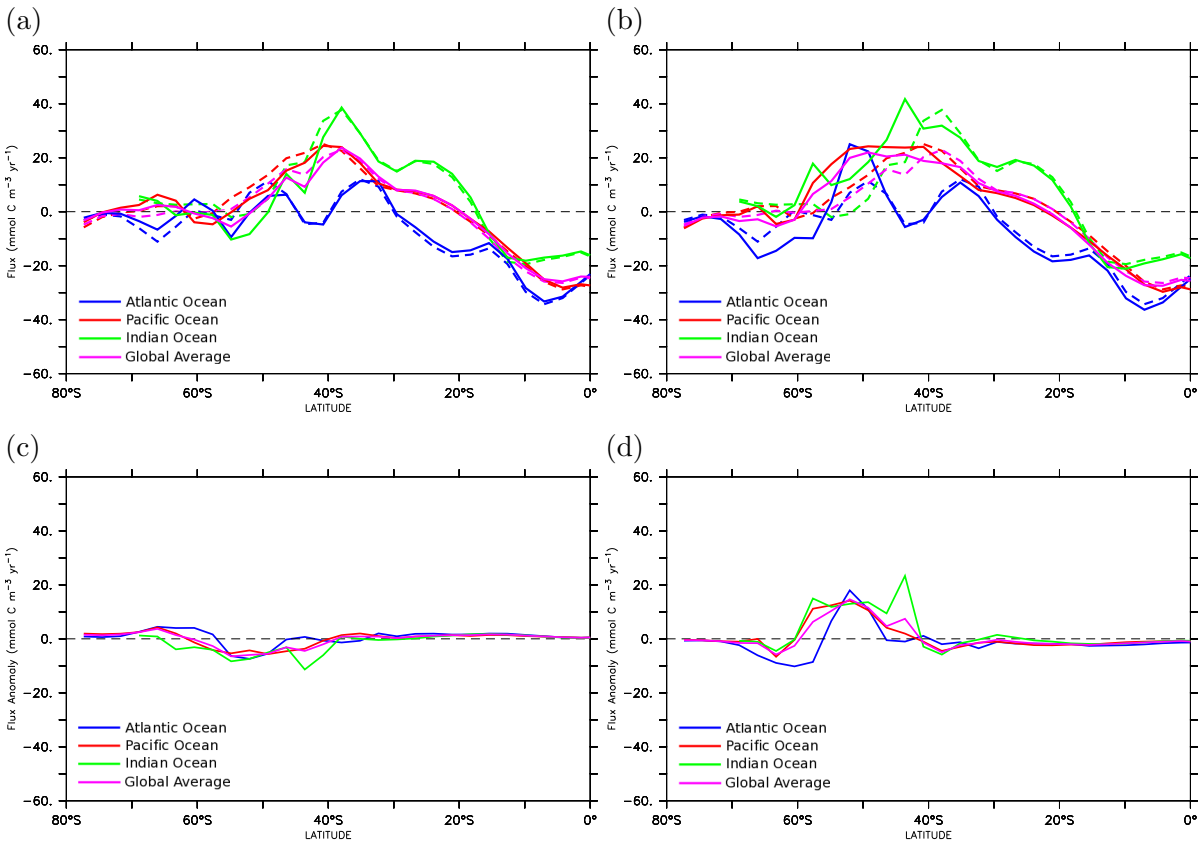

Figure 6.5: Equilibrium MITgcm output for the increased (left column) and decreased (right column) wind stress perturbations repeated with "fixed" surface boundary conditions. (a and b) Zonally averaged DIC concentration tendency due to air-sea exchange in the surface cell (mmol C m^{-3} yr^{-1}) and (c and d) their anomalies in the Atlantic (blue), Pacific (red) and Indian (green) sectors and the global zonal average (purple) for the control run (dashed, part (a and b) only) and near equilibrium after 5000 years (thick). Negative values indicate oceanic outgassing.

Air-sea fluxes of carbon dioxide (Figure 6.5) occur at a similar rate and in the same region, between 40–60°S, as in the standard perturbation. The greater volume of upwelling with increased wind stress draws carbon rich deep waters to the surface in the Southern Ocean causing the exhalation of 35.11 Gt C over the 5000 years of the integration, composed of strengthening of outgassing south of 55°S and reduced CO_2 uptake between 40–55°S. Despite little change in the strength of upwelling with decreased wind stress and "fixed" surface boundary conditions, the reduced depth from which the waters are brought to the surface contain a lower concentration of DIC than in the control run, driving increased atmospheric CO_2 uptake when at the surface, totaling 34.48 Gt C over the 5000 years of the integration before the surface flux balance is restored. These fluxes can be linked to the oceanic DIC distribution using $C_{gas\ exch}$ (Figure 6.6a and

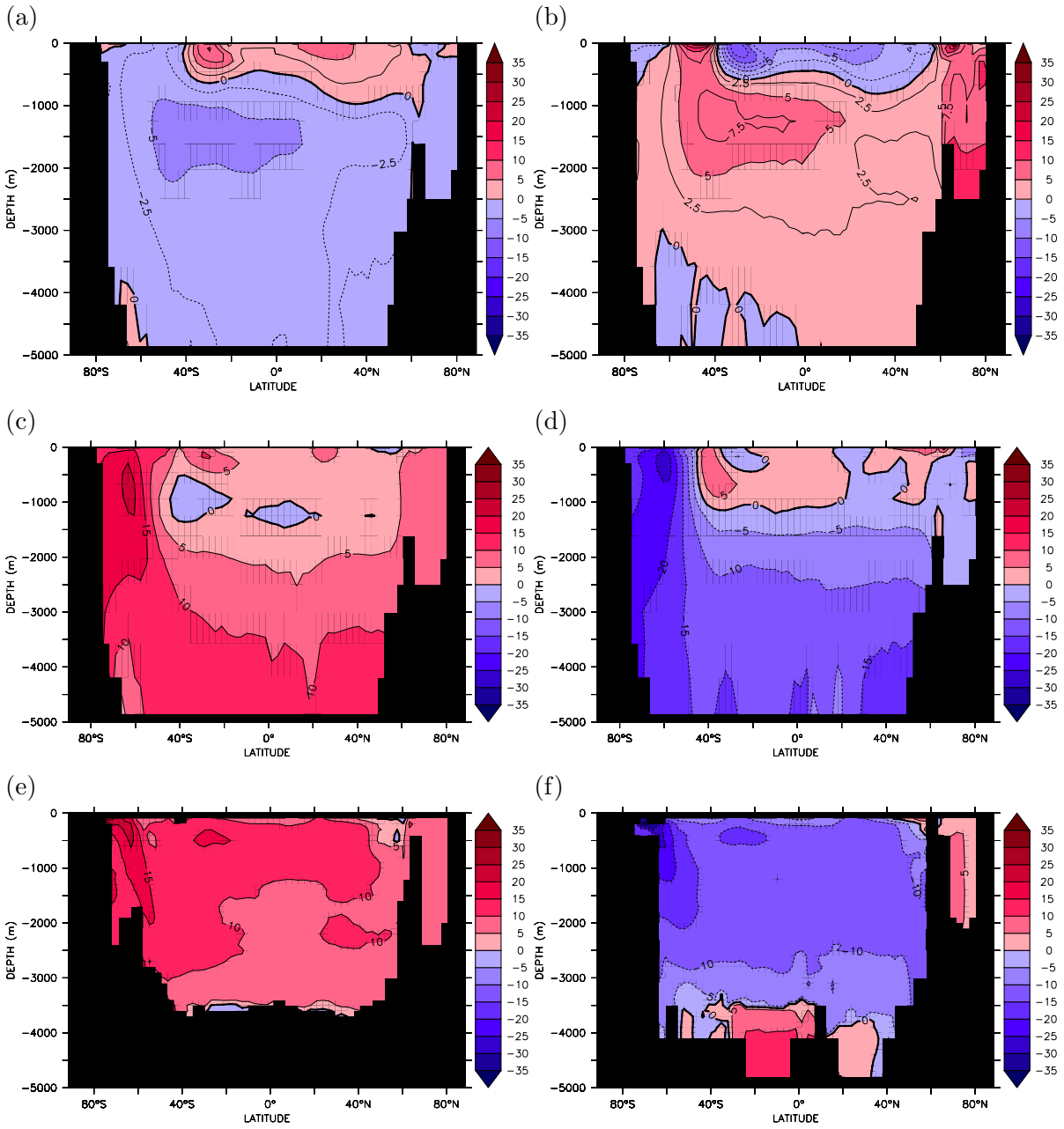

Figure 6.6: Equilibrium MITgcm output for the increased and decreased wind stress perturbations repeated with "fixed" surface boundary conditions. Globally-averaged meridional anomaly sections for increased (left column) and decreased (right column) wind stress perturbations of (a and b) anomalies of the quasiconservative tracer $C_{gas\ exch}$ (mmol C m^{-3}) calculated using Equation 2.37, and air-sea disequilibrium concentration of Dissolved Inorganic Carbon anomaly at the time interior water masses were last at the surface, diagnosed using control "preindustrial" concentrations after "correction" for the effects of organic carbon remineralisation and calcium carbonate dissolution (Equation 2.36) calculated and zonally-averaged in (c and d) depth coordinates and (e and f) density coordinates.

b), which shows that again, the intermediate depth waters at 1000 m originating from the Southern Ocean are responsible for communicating the atmospheric exchange signal into the ocean interior, losing 36.73 Gt C and gaining 33.60 Gt C for the increased and decreased wind stress perturbations respectively, with little atmospheric carbon trapped in the abyssal ocean. Indeed, the abyssal content of DIC follows the similar, positive correlation to atmospheric CO_2 content seen in Chapter 3 driven in part by more pronounced changes in the "preindustrial" disequilibrium concentration of DIC (Figure 6.6c to f) that oppose the outgassing of carbon dioxide from the ocean. Initially, viewed on depth levels the majority of this change in disequilibrium concentration appears to be accumulated in the abyssal ocean and to the south of 60°S, however when viewed in density coordinates the emphasis is shifted to intermediate depths, particularly in the Southern Hemisphere and at 1000 m. With increased wind stress and vigorous residual circulation, there is an accumulation of an additional 97.1 Gt C that is out of equilibrium with the atmosphere at the time interior water masses were last at the surface while 120.7 Gt C is released from disequilibrium forced by decreased wind stress due to shallower Southern Ocean overturning and reduced upwelling of deep ocean DIC.

6.1.2 Wind stress perturbations with mixed surface boundary conditions

A third set of boundary conditions were used in addition to the "fixed" surface forcing used previously in this chapter. "Mixed" or thermohaline surface boundary conditions, established using a combination of SST relaxation to climatology and prescribed freshwater fluxes with fixed relaxation fluxes diagnosed from the control run, were implemented and the increased and decreased wind stress magnitude perturbations using the perturbed fields of Figure 3.1 were repeated. Conceptually, when an anomalously warm or cold water mass is upwelled to the surface, then heat fluxes would naturally occur to restore the surface temperature to some equilibrium level that is constant in time [c.f. *Haney*, 1971], however an anomalously fresh or saline water mass would not necessarily provoke changes in evaporation or precipitation since surface freshwater exchanges are more likely a function of SST than SSS. Only a short integration of 500 years was used in order to capture the majority of the model adjustment since it is expected the equilibrium state will not deviate far from that of fully prescribed and freely relaxing surface boundary conditions.

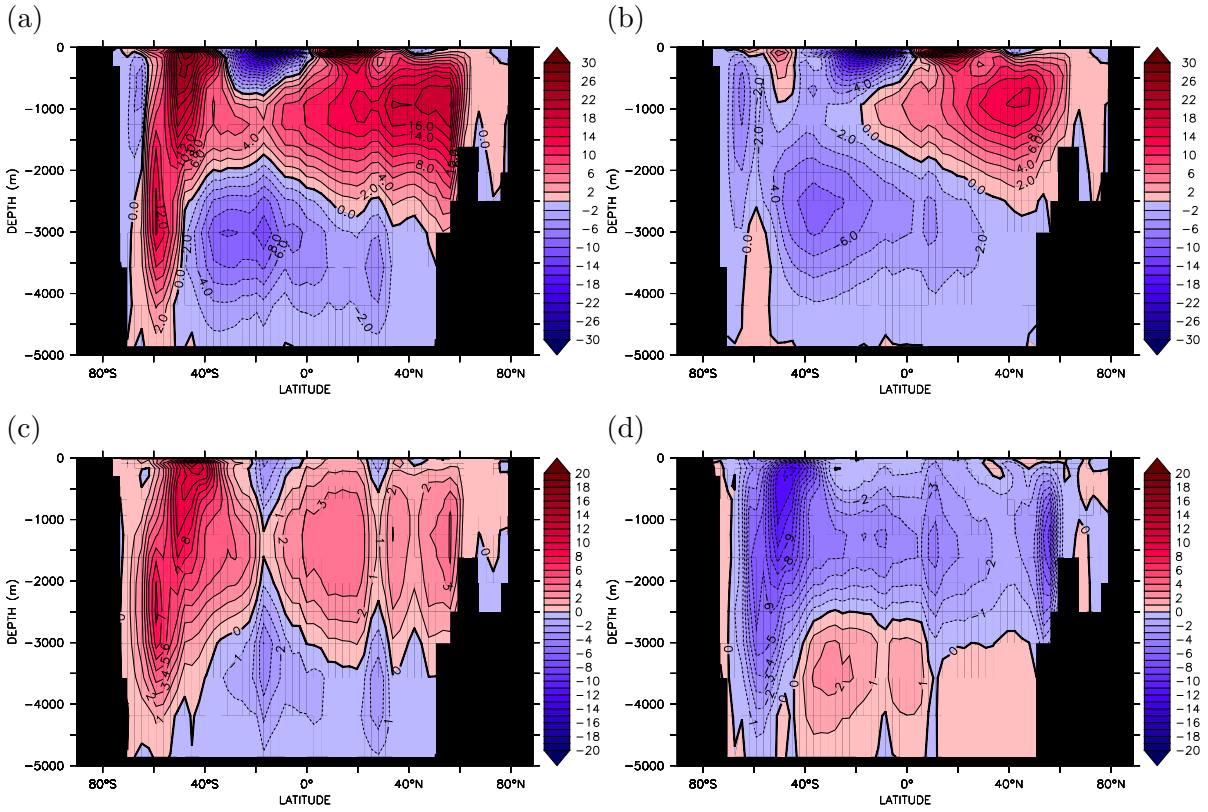

Figure 6.7: Equilibrium MITgcm output for the increased (left column) and decreased (right column) wind stress perturbations repeated with "mixed" surface boundary conditions. (a and b) show the residual overturning circulation (Sv) while (c and d) show the residual overturning anomaly compared to the control run (Sv).

After 500 years atmospheric CO_2 increased 14.02 µatm from 278.05 µatm to 292.07 µatm with increased wind stress, while atmospheric CO_2 content decreased 13.08 µatm to 264.97 µatm with decreased wind stress, which are roughly the same as seen with both previous surface boundary configurations.

Under increased wind stress and relaxing to SST, the residual circulation responds more to wind forcing (Figure 6.7a and c), increasing to 27.8 Sv, than with fixed temperature and salinity fluxes, as a result of the buoyancy fluxes associated with the surface temperature adjustment (Figure 6.8a). While the Eulerian-mean circulation remains similarly perturbed, the eddy induced circulation is increased ~4 Sv compared to the increased wind stress experiment with full relaxing boundary conditions but is approximately 2.5 Sv less intense than with "fixed" boundary conditions because the slope of isopycnals is greater than the former but shallower than the latter. A particular effect of the additional heat fluxes due to relaxation, but without SSS relaxation (Figure 6.8a) are to allow a stronger abyssal circulation of 11.5 Sv to occur which is greater than in

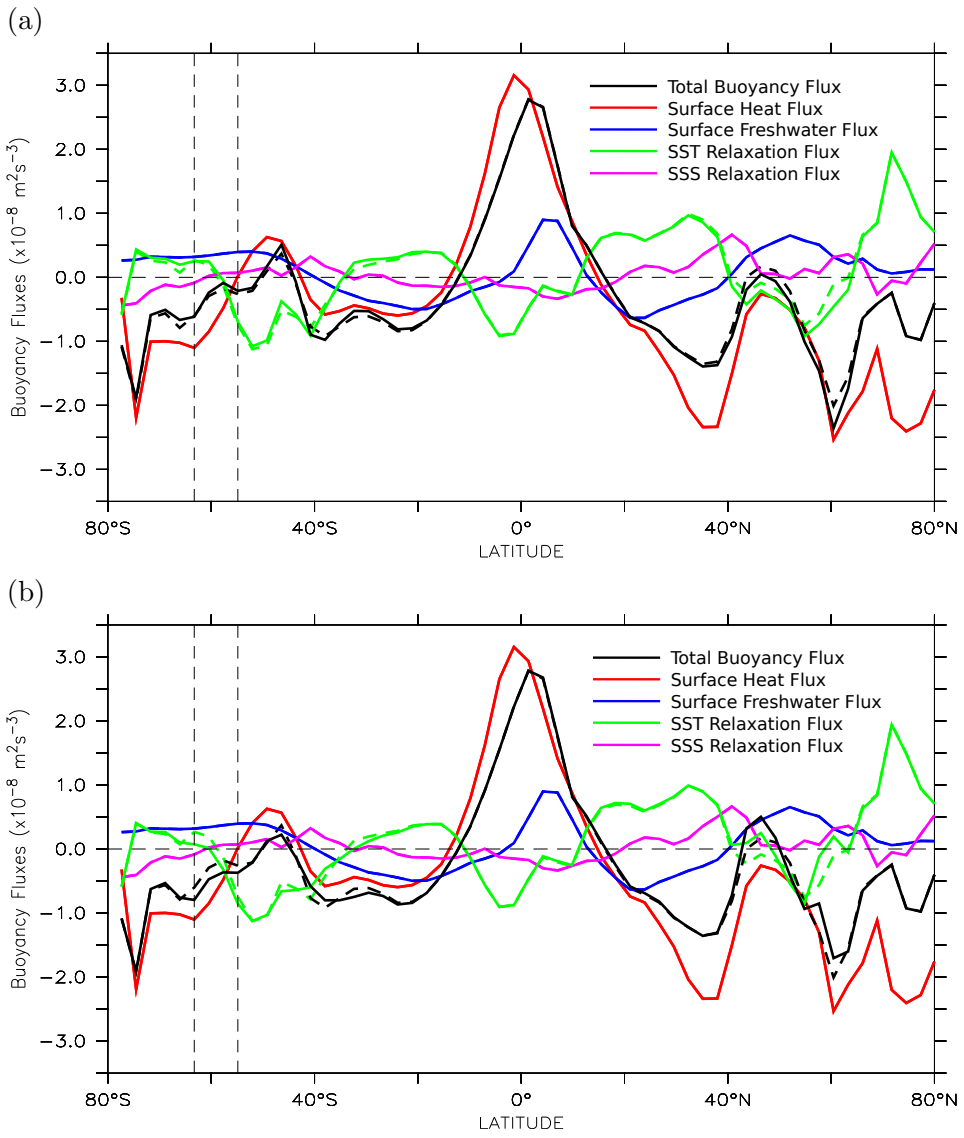

Figure 6.8: Equilibrium MITgcm output for Southern Ocean wind stress perturbations with "mixed" surface boundary conditions. Zonal average surface buoyancy flux ($m^2\,s^{-3}$) and its components (see Section 6.1 and Equation 6.2) for the perturbed (solid) and control (dashed) states. (a) under increased and (b) under decreased wind stress magnitude perturbations. Positive values indicate a gain of buoyancy (an increase in heat or freshwater/reduced salinity) while negative values indicate buoyancy loss (reduced heat or freshwater/increased salinity). Dashed vertical lines denote the position of the unblocked latitudes at Drake Passage.

either the control run or both previous surface boundary conditions under increased wind stress that actually decrease in strength relative to the control. This is because of the increase in sea surface salinity due to greater freshwater divergence in the Southern Ocean that would otherwise be damped by relaxing freshwater fluxes, therefore reducing surface stratification (Figure 6.9a) and increasing the rate of dense water convection. However the Atlantic meridional overturning circulation exhibits a similar increase to roughly 20 Sv as with increased wind stress and relaxation.

Decreased wind stress under thermohaline boundary conditions results in a residual overturning of 7.4 Sv (Figure 6.7b and d) that is a less extreme decrease than with relaxation to both SST and SSS, but weaker than with "fixed" surface fluxes, as a result of the balance in Equation 6.1 (Figure 6.8b). The Eulerian-mean circulation is similar to the previous experiments however the eddy circulation is around 1.6 Sv lower compared to the decreased wind stress, relaxing case. Despite the stronger residual circulation in this experiment compared to decreased wind stress alone, the depth of the cell still only reaches a depth of 1000 m, in common with the vigorous buoyancy-supported surface cell under fixed fluxes. In addition, the abyssal circulation cell is reduced in strength, opposing the previously derived trend of an increase with decreased winds, because of reduced freshwater divergence in the Southern Ocean that increases surface stratification and inhibits deep water formation (Figure 6.9b). The Atlantic meridional overturning circulation is also reduced, as would be anticipated for temperature relaxation and damping of the North Atlantic buoyancy feedback [*Rahmstorf and England*, 1997], although the NADW anomaly is still shy of that produced with SST and SSS relaxation for the same wind stress perturbation.

The perturbations to the physical circulation reproduce the bimodal distributions of nutrients and biological productivity with increased residual upwelling bringing nutrient rich deep waters to the surface fueling Atlantic production while reduced residual circulation reduces the supply of upwelled nutrients to the Atlantic and is substituted by upwelling in the Indo-Pacific supplying enhanced production there. With increased wind stress and "mixed" boundary conditions, the global rate of primary production increased 0.47 Gt C yr^{-1} whereas the rate of primary production decreased 0.52 Gt C yr^{-1} under reduced wind stress. Previous experiments have shown that the global rate of primary production adjusts over approximately 1000 years. Indeed, the distribution for both perturbations and mixed boundary conditions are similar to the relaxing boundary cases. For increased wind stress the magnitude may decline slightly in the Atlantic while for the decreased wind stress, production in the Indo-Pacific is somewhat low and

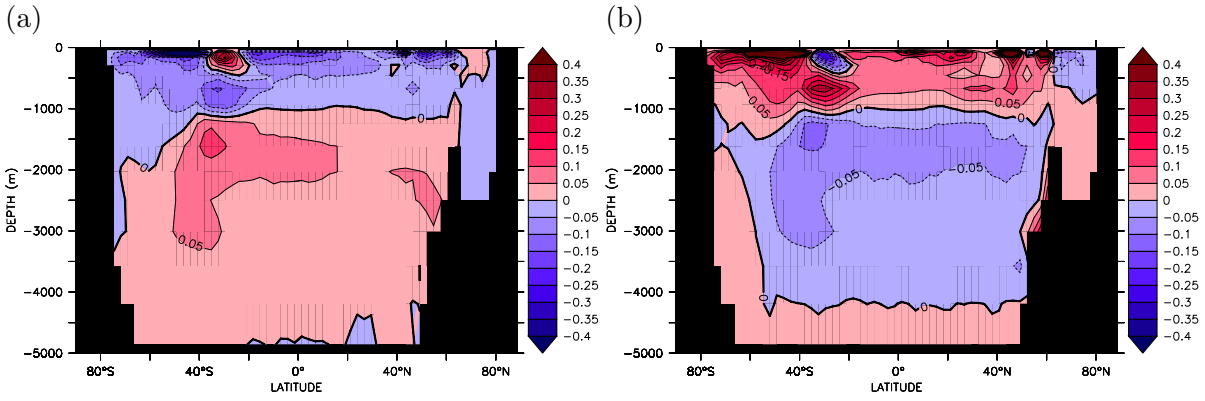

Figure 6.9: MITgcm output for the increased and decreased wind stress perturbations repeated with "fixed" surface boundary conditions. Zonally averaged stratification anomalies ($\partial\rho/\partial z$, $\mathrm{g\,m^{-4}}$) for (a) increased and (b) decreased wind stress magnitude perturbations.

should increase as the slow process of diapycnal diffusion supplies the surface with an enhanced supply of macronutrients. Efficiency of the soft tissue pump is also probably still adjusting but nevertheless decreased efficiency of 32.6% for increased wind stress and mixed surface fluxes and increased efficiency of 37.0% for decreased wind stress and mixed surface fluxes compare favourably to those seen for the alternative surface boundary conditions, depending mostly on the physical circulation redistributing phosphate than large changes in biological activity.

As well as the regular changes to regenerated and preformed concentrations of phosphate associated with the altered upper ocean overturning, the relatively large changes to the abyssal circulation that occur in opposition to the trends seen previously manifest in the regenerated phosphate concentrations (Figure 6.10a and b) with enhanced deep circulation in the increased wind stress case flushing regenerated phosphate out of the abyssal ocean while decreased deep circulation associated with decreased wind stress acts to store biologically partitioned phosphate, with such a defined separation between the upper and lower limbs unique to these flux conditions that is robust even when the effects of isopycnal heave are removed. Cumulatively, the increased wind stress over the Southern Ocean with fixed freshwater forcing and relaxation to SST causes atmospheric carbon content to increase by 29.97 Gt C through increased outgassing to the south of the ACC and reduced atmospheric CO_2 uptake to the north of the ACC. This signal is carried into the ocean interior causing a negative anomaly in the gas exchange pump tracer $C_{gas\ exch}$ (Figure 6.11a) below 1000 m. Furthermore, spin up of the Southern Hemisphere circulation causes an increase in the disequilibrium DIC content

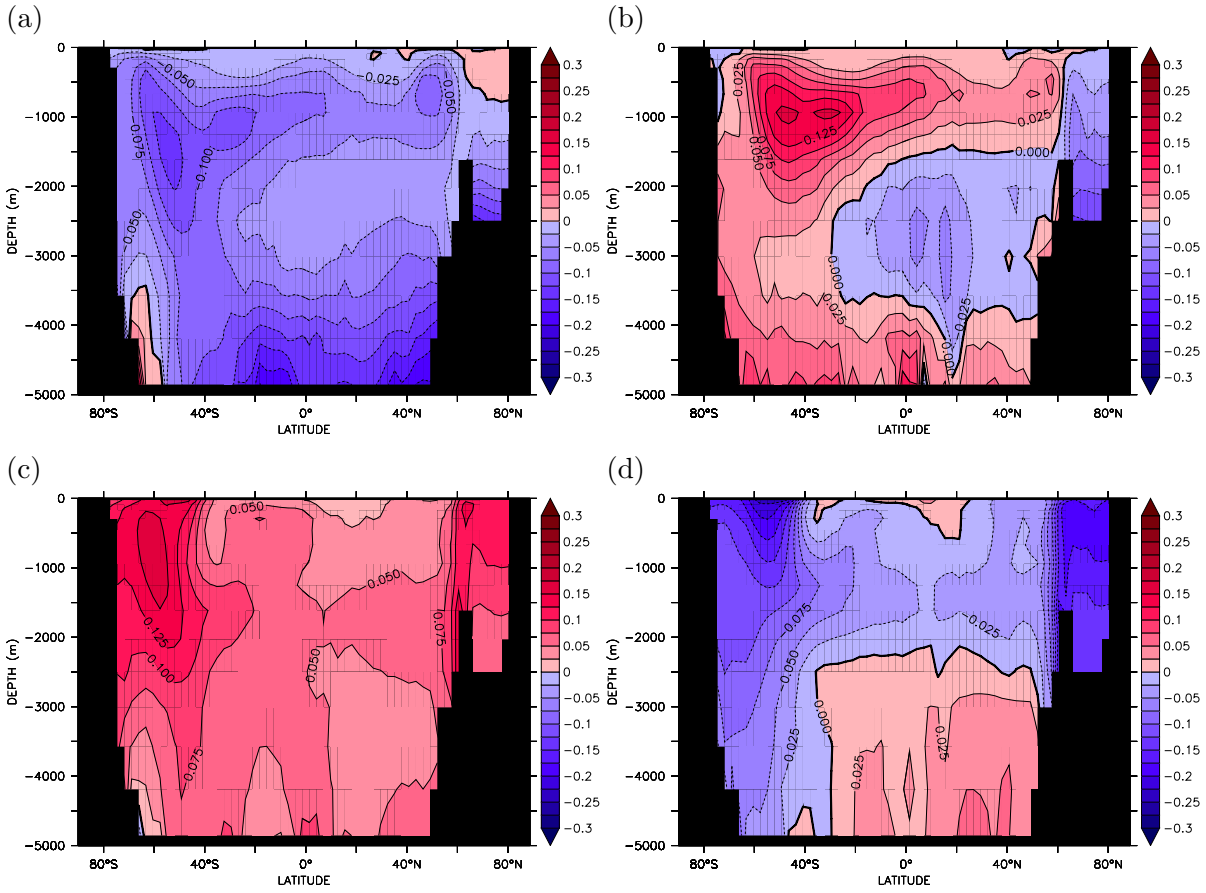

Figure 6.10: MITgcm output for the increased and decreased wind stress perturbations repeated with "mixed" surface boundary conditions. Globally-averaged meridional sections of tracer anomaly for increased (left column) and decreased (right column) wind stress for (a and b) regenerated phosphate anomaly (mmol P m^{-3}) calculated from Apparent Oxygen Utilisation using Equation 2.28 and Equation 2.29, and (c and d) preformed phosphate anomaly (mmol P m^{-3}) calculated using the regenerated component and Equation 2.27.

of 92.80 Gt C (Figure 6.11c) which is partially offset by a decrease in disequilibrium in the abyssal regions due to enhanced circulation, but is still of a comparable size to the same perturbation with fixed surface fluxes and three times as large as with additional relaxation to surface temperature and salinity. Likewise, with decreased wind stress and mixed surface boundary conditions, atmospheric carbon content decreased 27.59 Gt C due to increased CO_2 uptake between 40–60°S that creates a positive anomaly in the gas exchange pump at intermediate depths (Figure 6.11b). Furthermore, the more quiesent interior Southern Ocean becomes more in equilibrium with the atmosphere, reducing the disequilibrium concentration of DIC (Figure 6.11d), however the globally integrated adjustment of −8.49 Gt C is countered by in increase in disequilibrium associated with the decreased abyssal circulation trapping CO_2 in the deep sea.

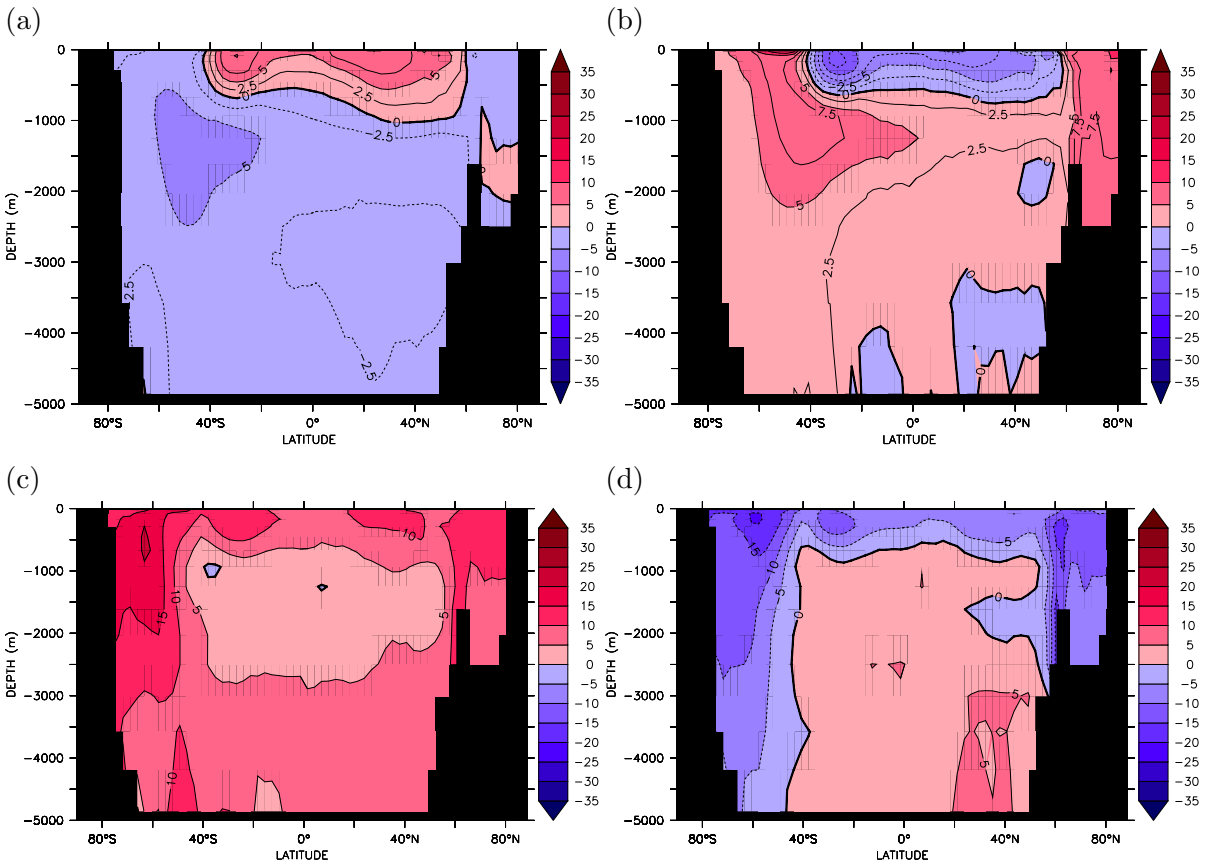

Figure 6.11: Equilibrium MITgcm output for the increased and decreased wind stress perturbations repeated with "mixed" surface boundary conditions. Globally-averaged meridional anomaly sections for increased (left column) and decreased (right column) wind stress perturbations of (a and b) anomalies of the quasiconservative tracer $C_{gas\ exch}$ ($\mathrm{mmol\,C\,m^{-3}}$) calculated using Equation 2.37, and (c and d) air-sea disequilibrium concentration of Dissolved Inorganic Carbon anomaly at the time interior water masses were last at the surface, diagnosed using control "preindustrial" concentrations after "correction" for the effects of organic carbon remineralisation and calcium carbonate dissolution (Equation 2.36) .

6.2 Response of the global carbon cycle to the coarse resolution parameterisation of eddies

Mesoscale eddy activity plays an important role in the momentum balance of the ACC [e.g. *Bryden and Cunningham*, 2003; *Johnson and Bryden*, 1989], compensating the northward flowing Ekman transport in the Southern Ocean, modulating deep upwelling and therefore directly affects the response of the global oceanic circulation and carbon cycle to changes in climate. The effect of eddies is under debate [*Farneti et al.*, 2010; *Hallberg and Gnanadesikan*, 2006; *Keeling and Visbeck*, 2001; *Sigman and Boyle*, 2001], not least because of the difficulty in successfully parameterising the effect of the eddy

induced circulation in coarse resolution ocean and climate models. Many of these models under future climate change scenarios produce large increases in northward Ekman and zonal ACC transports with predicted strengthening of the Southern Hemisphere westerlies [*Fyfe and Saenko*, 2005, 2006; *Gnanadesikan and Hallberg*, 2000] that are essentially recreated in the increased wind experiment in Chapter 3. Although there is some evidence that wind stress at the latitude band of Drake Passage is positively linked to ACC transport [*Gent et al.*, 2001; *Meredith et al.*, 2004], changes in the mesoscale eddy field, which would likely become intensified with increasing wind stress, as well as the possibility of the ACC being saturated with respect to the winds, with further increases instead invigorating the eddy field [*Hogg and Blundell*, 2006; *Meredith and Hogg*, 2006], would probably damp this response therefore also affecting the residual circulation and thus altering the sensitivity of atmospheic CO_2 to this perturbation [*Gnanadesikan and Hallberg*, 2000; *Hallberg and Gnanadesikan*, 2006; *Zickfeld et al.*, 2007]. These observations are not recreated in these results, because although the eddy circulation increases in response to the greater slope of isopycnals, the magnitude of the increase, indeed the entire circulation is dependent on a spatially uniform mixing coefficient and to some extent the scheme to limit spurious bolus circulation in regions of low stratification (see Chapter 2).

Since the eddy circulation under increased winds in coarse resolution models is somewhat inconsistent with fine resolution models and observations, results obtained with reduced wind forcing should be treated with caution. On the one hand a more stratified ocean in glacial times, with shallow sloping Southern Ocean isopycnals, would support a weaker eddy overturning which could result in a decrease of compensation and an increase of the residual circulation [*Keeling and Visbeck*, 2001], depending on the details of the wind stress. On the other hand, the eddy circulation forms a negative feedback mechanism [*Sigman and Boyle*, 2001] that would respond to the increased baroclinicity caused by greater Eulerian-mean upwelling tending to restore the stratification and residual circulation set by surface buoyancy fluxes [*Karsten and Marshall*, 2002; *Marshall*, 1997; *Watson and Naveira Garabato*, 2006] that was previously shown in Section 6.1 under "fixed" surface boundary conditions.

In this section, changes to the intensity of mesoscale eddy activity will be simulated in response to the simple wind stress magnitude perturbations made in Chapter 3 (Figure 3.1) and the response of Southern Ocean biogeochemical cycles and atmospheric CO_2 examined. To make resultant ACC transports under increasing IPCC SRES A2 winds in a coarse resolution climate model consistent with results from eddying ocean models

[*Hallberg and Gnanadesikan*, 2006], *Fyfe et al.* [2007] suggested that the intensity of the Southern Ocean eddy circulation could be modified by globally increasing the GM90 mixing coefficient, κ_{GM}, proportionally to the gradual increase in maximum zonally-average wind stress, $\overline{\tau_x(n)}$, between 1990–2100. This simple method of comparing the control ($t = 0$) and contemporary ($t = n$) fields (Equation 6.3, also employed by *Zickfeld et al.* [2007]) that plausibly captures the direct mesoscale eddy response to changing wind strength was applied to this configuration of MITgcm but $\kappa_{GM}(n)$ was calculated offline and specified as an input parameter rather than calculated prognostically in the model code since the wind stress forcing applied here does not evolve in time.

$$\frac{\overline{\tau_x(n)}}{\kappa_{GM}(n)} = \frac{\overline{\tau_x(0)}}{\kappa_{GM}(0)} \tag{6.3}$$

Despite further significant perturbations to Southern Ocean wind stress forcing and internal physics, circulation and atmospheric carbon dioxide levels showed only a modest response. After 5000 years forced with increased wind stress and an increased GM90 transfer coefficient of 1481.4 $m^2 s^{-1}$ atmospheric CO_2 increased by 9.24 µatm from 278.05 µatm to 287.31 µatm. However, a decrease in atmospheric CO_2 of 6.42 µatm from 278.05 µatm to 271.65 µatm was found forcing the model with decreased wind stress and a reduced GM90 transfer coefficient of 518.73 $m^2 s^{-1}$.

Despite the magnitude of the maximum resultant Eulerian-mean and eddy circulations remaining similar when forced with increased wind stress, the degree of compensation increases with elevated κ_{GM} so that the residual Southern Ocean overturning increases to 28 Sv instead of 31 Sv (Figure 6.12a and c). There is also a reduction in the perturbation to the Atlantic meridional overturning of ~1 Sv as opposed to ~3 Sv and a 1 Sv increase in the abyssal circulation of AABW, which decreased slightly with stronger winds and standard values of κ_{GM}. Surface buoyancy fluxes (Figure 6.13a) show greater buoyancy loss to the south of 60°S as a result of reduced surface temperature relaxation, while between 40–60°S, surface temperature relaxation increased presumably due to increased southward eddy diffusive heat fluxes. This deviates from the net buoyancy flux gain in the standard wind stress magnitude perturbation (Figure 3.6e).

With decreased wind stress and proportionally reduced GM90 isopycnal mixing coefficient the eddy circulation is reduced by roughly 50% however the degree of compensation at 3000 m is high so that the Southern Ocean overturning, which actually has a larger maximum overturning of 11.7 Sv compared to 3.8 Sv with control κ_{GM}, extends only just out of the upper ocean (Figure 6.12b and d). Surface buoyancy fluxes remain largely

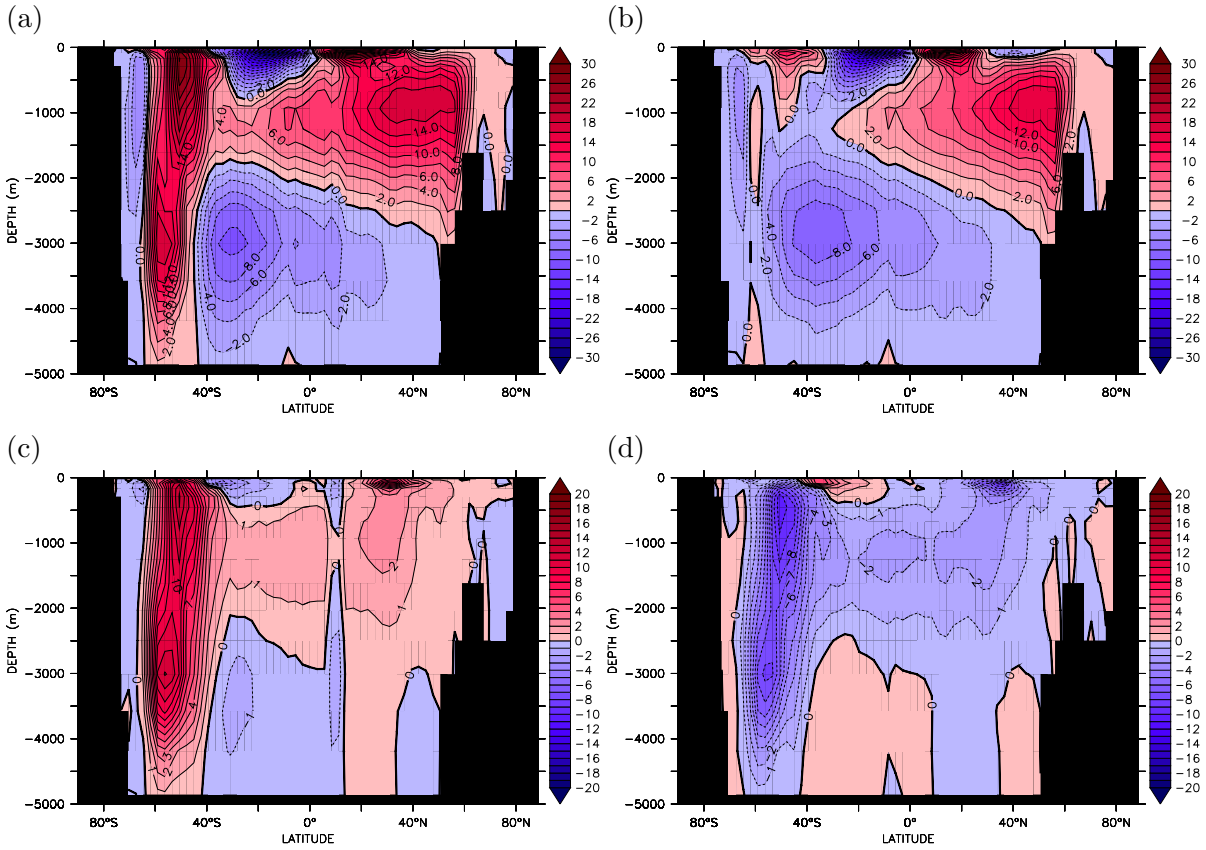

Figure 6.12: Equilibrium MITgcm output for the increased (left column) and decreased (right column) wind stress perturbations repeated with adjusted GM90 transfer coefficient. (a and b) show the residual overturning circulation (Sv) while (c and d) show the residual overturning anomaly compared to the control run (Sv).

unchanged from the control south of roughly 55°S, due to opposing negative salinity relaxation and postitive heat relaxation fluxes, unlike the enhanced buoyancy loss in the decreased wind stress perturbation with control κ_{GM} (Figure 3.25). However, reduced southward eddy heat transport necessitates greater surface temperature relaxation at approximately 40°S. Abyssal circulation is slightly reduced, as is the perturbation to the Atlantic meridional overturning circulation. Furthermore, while these perturbations to the residual circulation create shifts in isopycnal depth of ~100–150 m they are smaller compared to the isopycnal heave of 200–300 m seen previously, therefore leading to a smaller meridional density gradient anomalies and smaller anomalies in ACC transport through Drake Passage (25–35 Sv compared to ~55 Sv) that is somewhat more consistent with an eddy saturated regime.

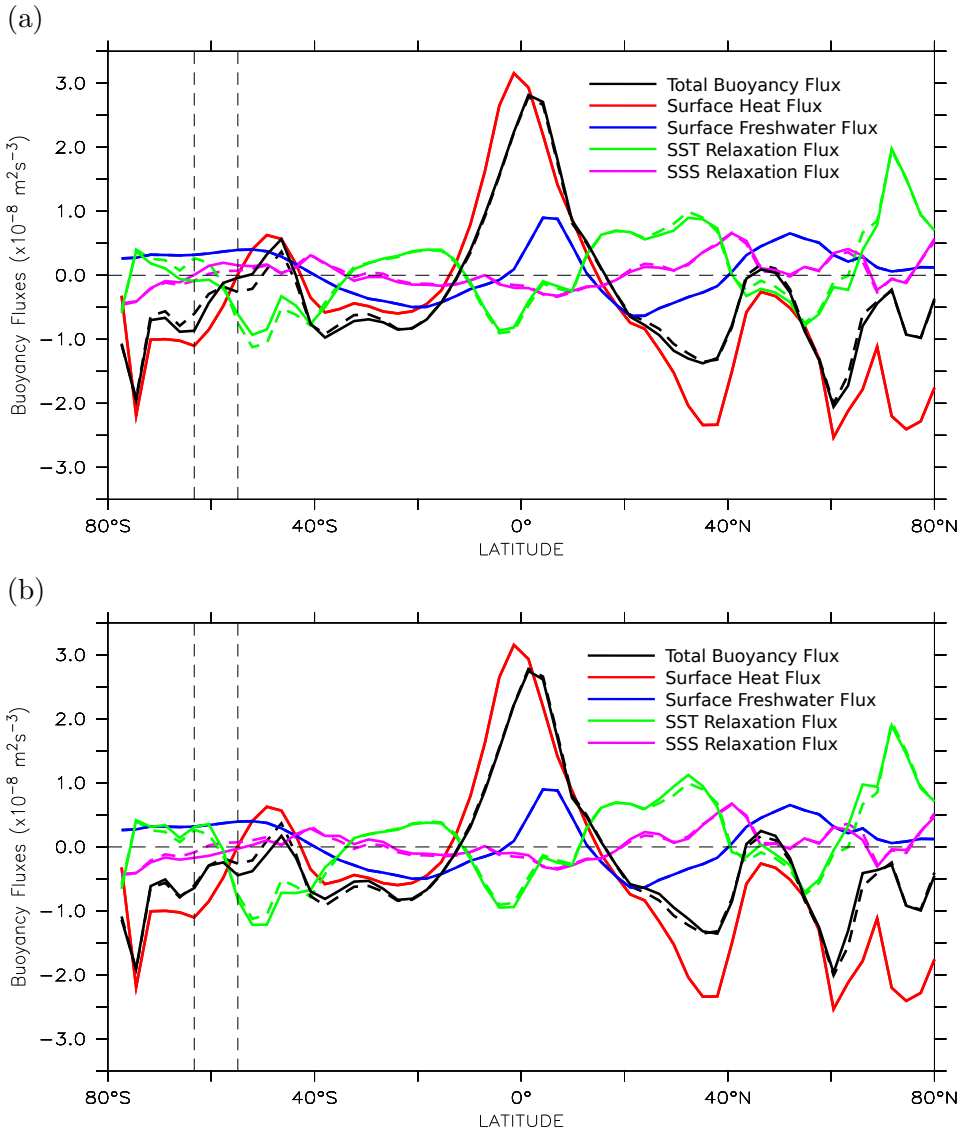

Figure 6.13: Equilibrium MITgcm output for the increased and decreased wind stress perturbations repeated with adjusted GM90 thickness coefficient. Zonal average surface buoyancy flux ($m^2\,s^{-3}$) and its components (see Section 6.1 and Equation 6.2) for the perturbed (solid) and control (dashed) states. (a) under increased and (b) under decreased wind stress magnitude perturbations. Positive values indicate a gain of buoyancy (an increase in heat or freshwater/ reduced salinity) while negative values indicate buoyancy loss (reduced heat or freshwater/ increased salinity). Dashed vertical lines denote the position of the unblocked latitudes at Drake Passage.

Interestingly net eddy upwelling/downwelling in the southeast Pacific and between 30–45°S in the Atlantic and Indian Sectors of the Southern Ocean dominate the residual vertical velocity anomaly and draw deeper waters to the surface with increased wind stress and κ_{GM} with the reverse seen with decreased wind stress and κ_{GM}. This produces the bimodal distribution of nutrient and primary production anomalies seen previously. With increased wind stress, the Atlantic Ocean is fed nutrients advected from the Southern Ocean in the northward surface Ekman and SAMW and AAIW flows with a reduction in vertical diffusive nutrient supply in the Indo-Pacific Oceans due to increased pycnocline depth. Because the magnitude of the perturbation to the residual circulation is weaker, this pattern is somewhat reduced and a proportionally reduced rate of primary production would be anticipated, however increased isopycnal ventilation and stirring acts to rapidly remove upwelled nutrients from the surface of the Southern Ocean resulting in a lower anomalous increase in surface macronutrient concentrations, reduced concentration of regenerated phosphate (Figure 6.14a), a larger concentration of unutilised, preformed phosphate (Figure 6.14c) and a smaller increase of the globally integrated rate of biological productivity than expected of $0.02\,\mathrm{Gt\,C\,yr^{-1}}$. This culminates in a large decrease in the efficiency of the soft tissue pump from 35.7% to 32.1%.

Similarly for decreased wind stress, reduced upwelling limits the concentrations of nutrients that are supplied to the Atlantic Basin by northward Ekman transport from the Southern Ocean and reduced AAIW and SAMW subduction into the thermocline thus decreasing productivity there, while shoaled isopycnals in the Indo-Pacific favour diapycnal upwelling of nutrients through the pycnocline, increasing biological productivity. On balance in the previous wind stress perturbations, the decreased production in the macronutrient limited Atlantic generally exceeds the increased production the Indo-Pacific to cause net reduction in globally integrated biological productivity. However, by reducing κ_{GM} and isopycnal ventilation, macronutrients are increasingly well utilised in the North Pacific and Indian Oceans, leading to an increase in the global rate of primary production of $0.38\,\mathrm{Gt\,C\,yr^{-1}}$, and returned to the ocean interior at midlatitudes causing increased regenerated nutrient concentration, decreased preformed nutrient concentration and a large increase in the efficiency of the soft tissue pump from 35.7% to 38.5% (Figure 6.14b and d).

Changes to the efficiency of the soft tissue pump under increased or decreased winds respectively act to promote or inhibit net oceanic outgassing or uptake of CO_2. With increased wind stress, there is enhanced outgassing south of approximately 55–60°S

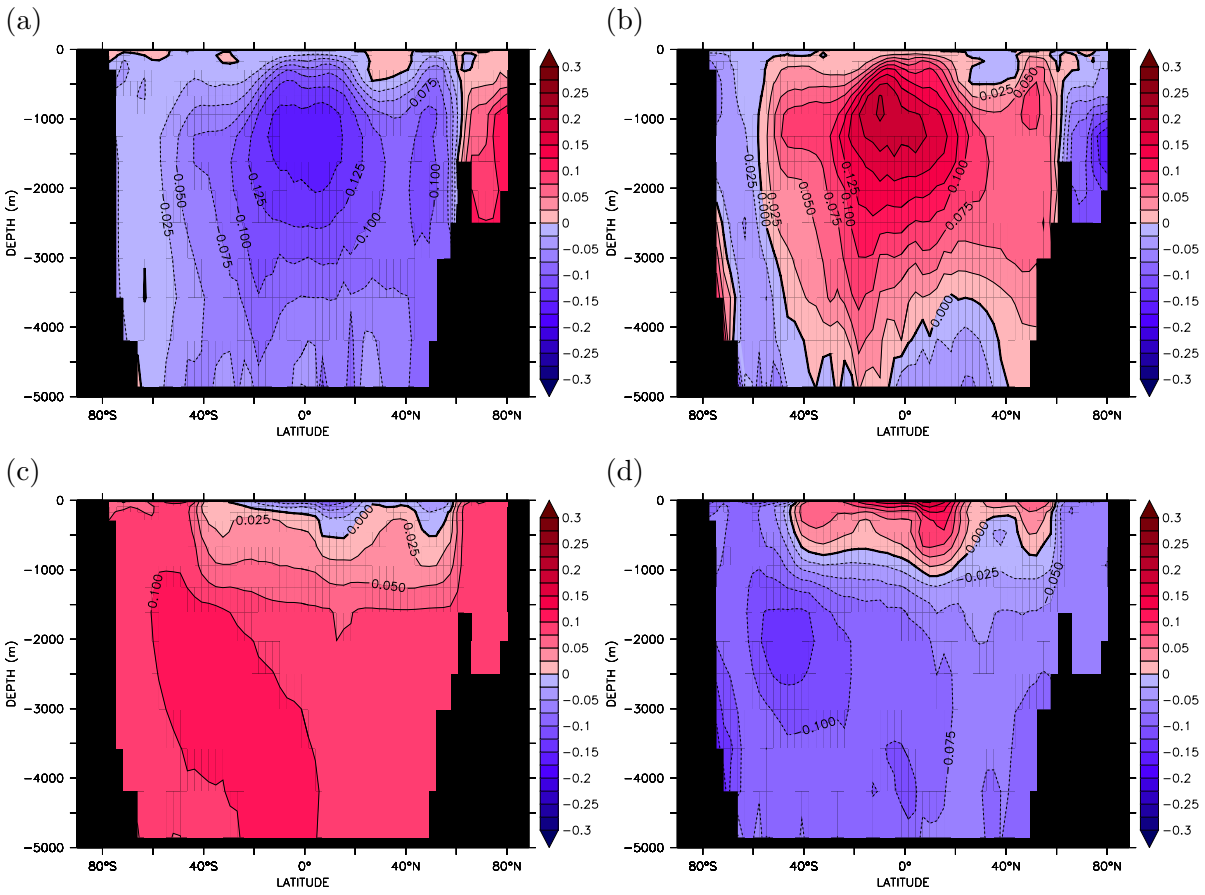

Figure 6.14: MITgcm output for the increased and decreased wind stress perturbations repeated with adjusted GM90 thickness coefficient. Globally-averaged meridional sections of tracer anomaly for increased (left column) and decreased (right column) wind stress for (a and b) regenerated phosphate anomaly (mmol P m^{-3}) calculated from Apparent Oxygen Utilisation using Equation 2.28 and Equation 2.29, and (c and d) preformed phosphate anomaly (mmol P m^{-3}) calculated using the regenerated component and Equation 2.27.

associated with increased upwelling of DIC rich deep waters, particularly in the Atlantic Sector and reduced uptake to the north between 55–40°S transferring 19.7 Gt C to the atmosphere. This results in a slightly reduced anomaly of the gas exchange pump tracer $C_{gas\ exch}$ (Figure 6.15a) with a similar distribution to previous perturbations. These fluxes are driven by both the increase in residual upwelling to the south and subduction to the north of the ACC. Also, enhanced isopycnal stirring increases surface water subduction to the interior before atmosphere-ocean equilibrium has been reached thus increasing the concentration of disequilibrium DIC by 106.3 Gt C, which is above and beyond that achieved by increasing wind stress and the Southern Ocean residual overturning circulation alone. Reducing wind stress with a concurrent decrease in κ_{GM} results in enhanced uptake between ~40–60°S of 13.6 Gt C from the atmosphere that is

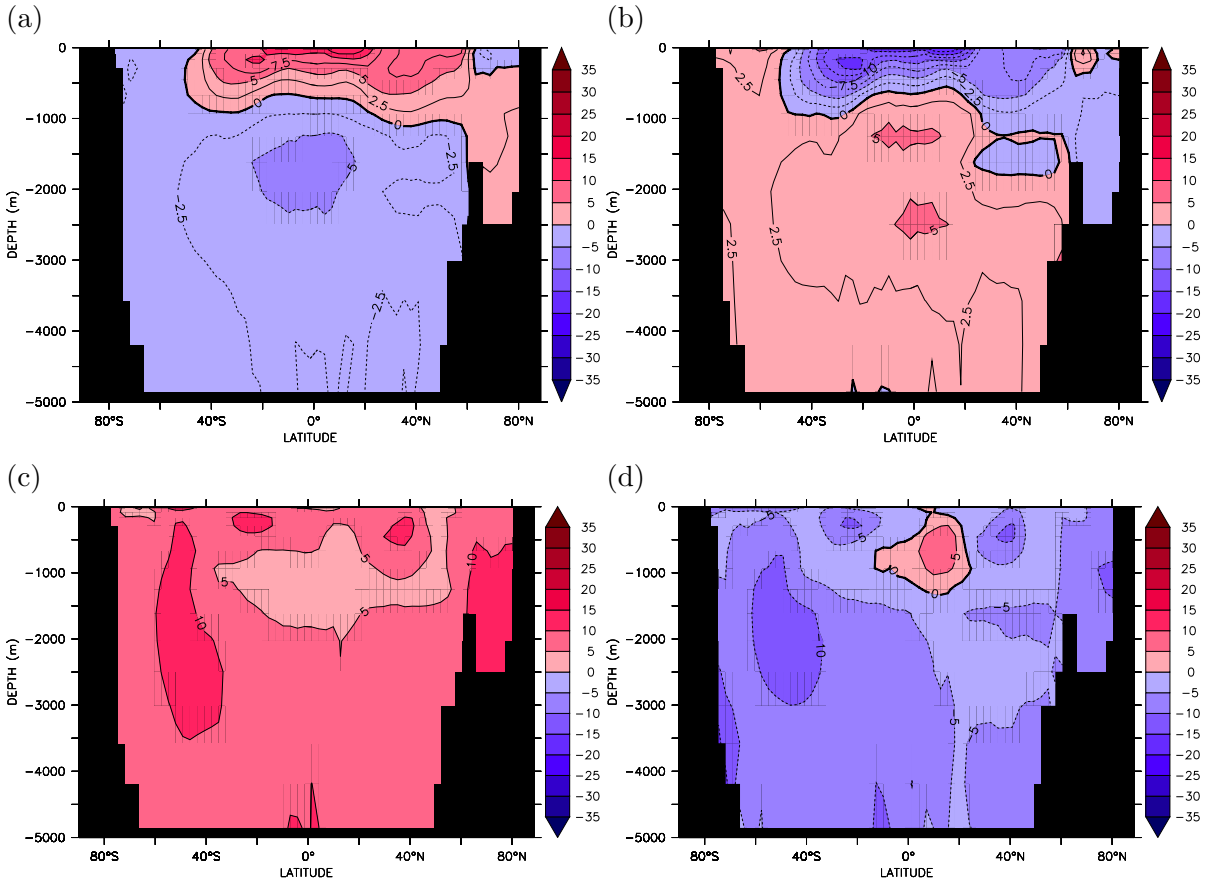

Figure 6.15: Equilibrium MITgcm output for the increased and decreased wind stress perturbations repeated with adjusted GM90 thickness coefficient. Globally-averaged meridional anomaly sections for increased (left column) and decreased (right column) wind stress perturbations of (a and b) anomalies of the quasiconservative tracer $C_{gas\ exch}$ ($\mathrm{mmol\,C\,m^{-3}}$) calculated using Equation 2.37, and (c and d) air-sea disequilibrium concentration of Dissolved Inorganic Carbon anomaly at the time interior water masses were last at the surface, diagnosed using control "preindustrial" concentrations after "correction" for the effects of organic carbon remineralisation and calcium carbonate dissolution (Equation 2.36).

sequestered at intermediate depths (Figure 6.15b) in common with other experiments. However, along with the reduced residual overturning circulation, decreasing isopycnal diffusion increases the residence time of waters in the surface layer of the Southern Ocean before they are stirred into the ocean interior, allowing the oceanic concentration of CO_2 to become more closely balanced with the atmosphere, decreasing the disequilibrium DIC concentration by 83.0 Gt C, which again is above and beyond that achieved by reducing wind stress and the Southern Ocean residual overturning circulation alone.

6.3 Response of the global carbon cycle to Southern Hemisphere westerly wind speed

In the above perturbations to wind stress, the effect of changing Southern Hemisphere westerly wind speed was ignored for simplicity since wind speed only interacts with the biogeochemistry package in calculation of the gas exchange coefficient (Equation 2.23, *Wanninkhof* [1992]) during determination of air-sea fluxes of carbon dioxide and oxygen and does not affect the physical model. However, since gas exchange does play a major role in the partitioning of CO_2 between the atmosphere and ocean, two further perturbations were conducted to quantify the effect of neglecting this term. Wind speed over the ACC was perturbed by ±50% , in the same region as the wind stress and then the model was integrated towards a new stable state. Here, the control wind stress was used. After 3000 years, atmospheric pCO_2 decreased by 0.21 µatm with increased Southern Ocean winds, while atmospheric pCO_2 increased by 1.4 µatm with decreased Southern Ocean winds. Increased wind speed enhances uptake of atmospheric CO_2 around 40°S but also increases the rate of outgassing around 60°S (Figure 6.16a) whereas reduced Southern Hemisphere wind speed does the opposite reducing the rate of CO_2 uptake from the atmosphere at 40°S and decreasing the outgassing at 60°S (Figure 6.16a). Crucially it is the perturbation on the northern flank of the ACC that affects the extent of exchange with newly forming Antarctic intermediate and mode waters as they travel northwards that controls atmospheric CO_2 in these experiments. Increased wind speed allows more CO_2 to be absorbed by these waters and subducted into the ocean interior in the upper 1000 m (Figure 6.16c and e) with slight enhancement of CO_2 loss to the atmosphere further south while decreased wind speed prevents AAIW and SAMW uptake of atmospheric CO_2 and reduces the flux to the atmosphere from waters south of 60°S. This asymmetry in the anomalies, due to surface area of the perturbed fluxes, may also explain the slight imbalance between the wind stress magnitude experiments for equal sized perturbations since the combined effects of increased wind stress and speed would produce an equilibrium atmospheric CO_2 anomaly of 15.39 µatm while combined decreased wind stress and speed would produce an equilibrium atmospheric CO_2 anomaly of −14.9 µatm. Nevertheless, these adjustments are small and do not alter the general interpretation of these wind stress perturbations.

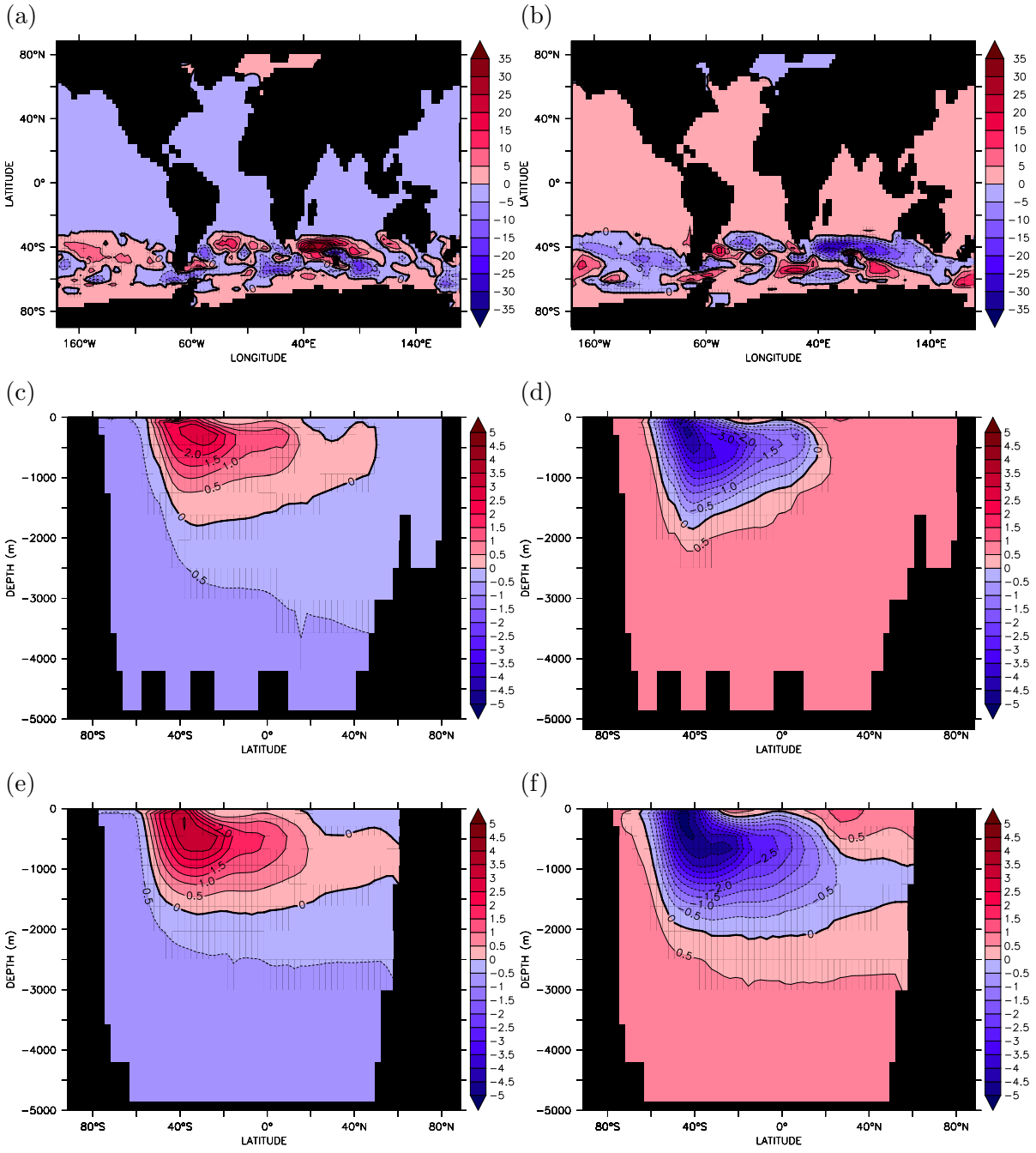

Figure 6.16: Equilibrium MITgcm output for the Southern Ocean wind speed perturbations. Anomalies for increased (left column) and decreased (right column) wind speeds for (a and b) the tendency of surface carbon concentration due to air-sea flux of CO_2 (mmol C m^3) and meridional anomalies of the quasiconservative tracer $C_{gas\ exch}$ (mmol C m^{-3}) in (c and d) the Atlantic and (e and f) Indo-Pacific Oceans. Note the reduced scale.

6.4 Summary

Although the modifications to forcing or physics made here are fairly significant, the results of the wind stress magnitude perturbations in Chapter 3 are relatively unchanged by surface buoyancy boundary conditions, mesoscale eddy activity or wind speed.

Holding surface temperature and salinity fluxes constant with no climatological relaxation made little difference to the end results of increased and decreased wind stress perturbations as changes in circulation, which were more moderate that with relaxing boundary conditions, were offset by opposing changes in efficiency of the biological pump and changes in air-sea disequilibrium. With thermohaline surface boundary conditions, that is fixed salinity fluxes and temperature relaxation, although the upper ocean overturning circulation responded in a similar way as the previous wind stress magnitude perturbations there was a marked pattern in the abyssal ocean overturning caused by changes in Southern Ocean freshwater divergence corresponding to the perturbations in wind stress. Increased wind stress and greater northward Ekman transport created an increase in Southern Ocean surface salinity that reduced surface ocean stratification and promoted bottom water formation, increasing the transfer of respired CO_2 from deep ocean to atmosphere. Alternatively, decreased wind stress and reduced northward Ekman transport caused Southern Ocean freshwater retention that increased surface stratification and inhibited bottom water formation, thus reducing the quantity of respired CO_2 escaping from the deep ocean.

The rate of mesoscale eddy circulation had a greater impact on the steady state quantity of CO_2 exchanged between ocean and atmosphere, however large changes to the rate of isopycnal ventilation and stirring still only introduced a small sensitivity to the wind stress perturbations with the same κ_{GM} as the preindustrial control. This effect was noticed in the altered the balance of Southern Ocean residual overturning circulation, leading to more modest changes in the rate of Southern Ocean upwelling, which again may have been opposed by greater changes in the efficiency of the soft tissue pump. Furthermore, larger κ_{GM} with increased wind stress resulted in faster export of nutrients out of the surface layer, limiting the action of the biological feedback and a coincident increase in the export of DIC rich surface waters with the result that in the globally integrated concentration of disequilibrium DIC was increased. Alternatively, reduced κ_{GM} with decreased wind stress resulted in longer occupancy of nutrients in the surface layer and enhanced biological consumption whilst also increasing the extent of ocean-atmosphere CO_2 equilibrium, thus decreasing the globally integrated concentration of

disequilibrium DIC and therefore reducing the sensitivity of atmospheric CO_2 to wind stress perturbations.

Finally, the assumption of maintaining control wind speed fields in the perturbations of Chapter 3 was shown to be small and mostly affected the concentration of atmospheric CO_2 contained in Antarctic intermediate and mode waters and also was the cause of slight asymmetry between the wind stress perturbations.

Part III

Implications for Past and Future Climates

Chapter 7

Discussion

Despite significant changes in Southern Ocean forcing and internal physics, the atmospheric concentration of carbon dioxide varied modestly, given the postulated importance of oceanic processes in glacial-interglacial CO_2 change, compared to the magnitude of CO_2 changes recorded in ice cores (explaining approximately 15% of the total change). It is clear that a combination of several processes, possibly acting in synergy, are necessary to explain such changes [e.g. *Archer et al.*, 2000; *Fischer et al.*, 2010; *Peacock et al.*, 2006] and indeed, if changes to ocean circulation need only account for the initial ~20–40 ppm then perturbations to Southern Ocean residual overturning circulation explain a considerable portion of these fluxes. A consistent series of relationships emerges from the individual perturbation experiments that explain the changes in atmospheric CO_2 levels in terms of forcing, circulation and biological activity that will be highlighted and elaborated on in this chapter. A comparison of the changes in atmospheric carbon dioxide brought about by perturbations to the physical and biogeochemical models presented in this thesis is shown in Figure 7.1. The preceding model investigations will also be compared to paleoceanographic observational data and other modelling studies in a discussion of the wider context of these results before outstanding questions and areas for ongoing research are identified in Chapter 8.

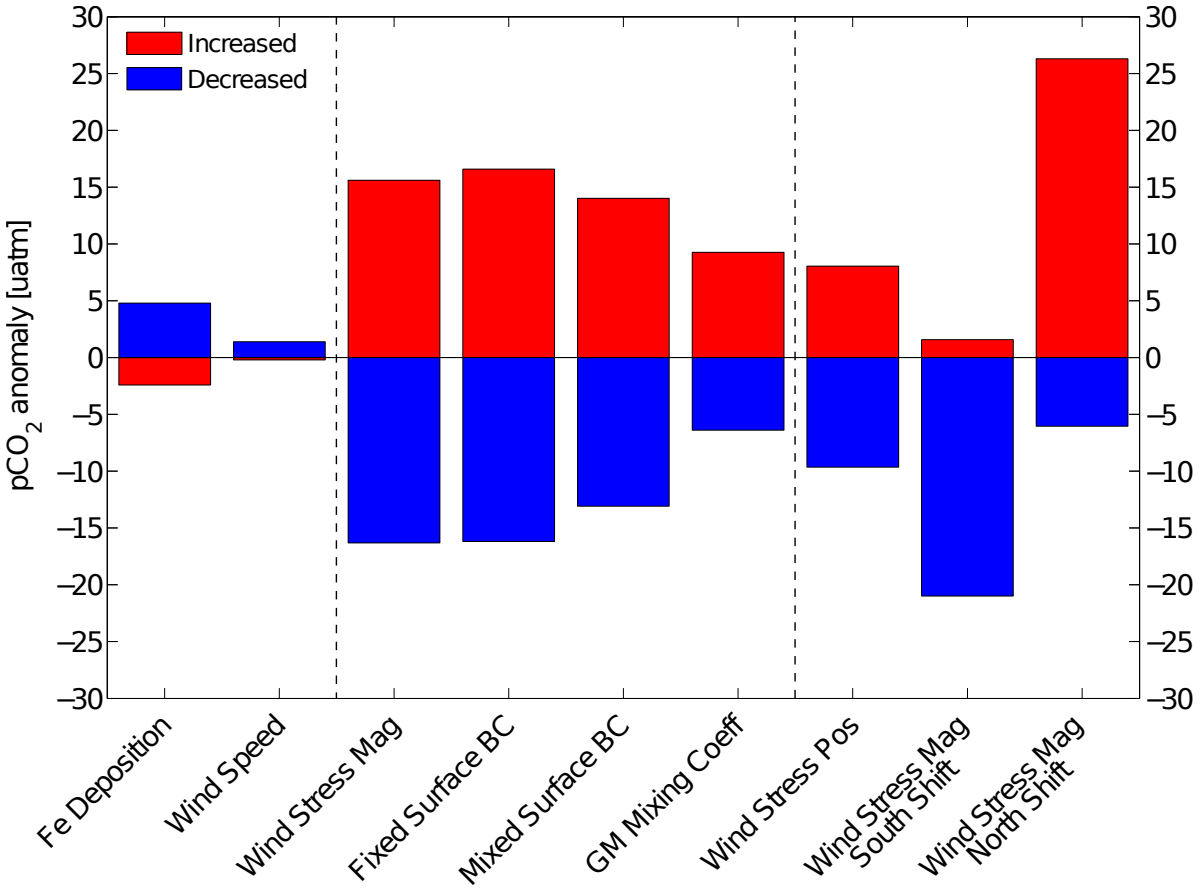

Figure 7.1: Comparison of atmospheric CO_2 anomalies achieved at steady state for the perturbations presented in Part II. Red bars indicate where a quantity or parameter was increased while blue bars indicate a decrease. "Fe Deposition" replaced the control aeolian deposition field for the increased LGM and decreased double CO_2 fields of *Mahowald et al.* [2006a,b], "Wind Speed" separately increased and decreased the Southern Hemisphere wind speed by ±50% to perturb gas exchange only, "Wind Stress Mag" increased and decreased the Southern Hemisphere extratropical westerly wind stress by ±50%, "Fixed Surface BC" increased and decreased the westerlies by ±50% with fixed surface buoyancy fluxes and no relaxation, "Mixed Surface BC" increased and decreased the westerlies by ±50% with fixed surface freshwater fluxes and surface temperature relaxation, "GM Mixing Coeff" repeated the ±50% westerly wind experiment with a corresponding change in the GM90 diffusion coefficient,"Wind Stress Pos" moved the peak Southern Hemisphere westerly wind stress by ±10°, "Wind Stress Mag, South Shift" increased the westerly winds in their southward-shifted position and "Wind Stress Mag, North Shift" increased the westerly winds in their northward-shifted position. To avoid like-with-like comparisons where they are not intended, the wind stress magnitude and position experiments have been seperated.

7.1 The role of aeolian iron deposition in atmospheric CO_2 change

A significant perturbation to the rate of aeolian iron deposition in section Chapter 5 produced only a small changes in atmospheric CO_2 levels. Previous attempts to simulate the response of oceanic biological activity to changes in aeolian iron deposition provide a range of possible responses, with up to 40 ppm drawdown achieved in the ocean-atmosphere carbon cycle box model of *Watson et al.* [2000] and 37 ppm in the Earth-system model of intermediate complexity (EMIC) of *Brovkin et al.* [2007], while OGCMs suggest a lower response, such as 26 ppm [which reduced to 12 ppm due to sediment interactions, *Archer et al.*, 2000], 15 ppm [*Bopp et al.*, 2003] and 8 ppm [also using MITgcm, *Parekh et al.*, 2006a,b]. The differences between box (and 2-D dynamic ocean/ EMIC) models and GCMs could be an artifact of enhanced vertical mixing and surface nutrient supply when using a z-coordinate primitive equation GCM, coupled with considerably differing iron and phytoplankton dynamics. The higher estimates [*Bopp et al.*, 2003; *Watson et al.*, 2000] both explicitly represent siliceous and non-siliceous phytoplankton groups with iron fertilisation favouring the siliceous diatoms, which also export carbon to the deep ocean quicker due to faster sinking rates. There may also be physiological effects of iron fertilisation such as more efficient use of silicate by diatoms in the Antarctic region [*Brzezinski et al.*, 2002; *Watson et al.*, 2000] with the excess nutrients then fertilising the Si-limited subantarctic region, equatorial Pacific and even northern Pacific. It is hard to tell if these indirect effects of iron fertilisation, leading to leakage of silicic acid from the Southern Ocean, actually occurred during the LGM because opal accumulation rates are not uniformly high in sediment records [*Ganeshram*, 2002] and there is no increase in export production south of the Polar Front (Figure 1.6) where the underutilised silicic acid pool should be created. *Parekh et al.* [2006b] point out the sensitivity of any solution to iron fertilisation is dependent on the details of a poorly understood iron cycle. In particular, they doubled the complexing ligand concentration, which protects free iron from scavenging, resulting in a doubling of the CO_2 response to LGM iron deposition to 14 ppm, but that is still considerably below other estimates.

The small response of the modelled Southern Ocean to increased aeolian iron deposition here also takes into account other factors that may be limiting phytoplankton productivity such as light availability and persistently deep mixed layer depth [*Mitchell et al.*, 1991; *van Oijen et al.*, 2004]. *Dutkiewicz et al.* [2006] demonstrated that primary

production in the Southern Ocean, particularly south of the Polar Front (~50°S) is principally limited by light in an adjoint study using a similar coarse resolution configuration of MITgcm. During autumn and winter at high-latitudes, low levels of insolation cause a dramatic decrease in primary production, therefore additional iron deposited during this time remains unutilised and may be scavenged or exported in its complexed form out of the euphotic zone. Even during the high-latitude summer, insolation is relatively diffuse and deep mixed layers can still cause light limitation. Indeed, the area most sensitive to continuous iron perturbations was found to be the subtropical south Pacific region [figure 1a, *Dutkiewicz et al.*, 2006] that also responded the most in Figure 5.2b due to a shallower mixed layer, favourable light conditions and available macronutrients laterally supplied from the Southern Ocean upwelling. This region has a minimal impact on atmospheric CO_2 levels however, because the majority of the extra production there is remineralised *in situ* resulting in little export of carbon from the surface to the deep ocean and flushing of sequestered carbon back into the atmosphere. Box models and EMICs have simplified physics or parameterised circulation and therefore may not capture the perturbation to the tightly coupled nutrient supply chain that leads to reduced biological activity in the oligotrophic gyres to the north when excess nutrients are consumed due to fertilisation in the upwelling regions to the south ("nutrient robbing"). Also, there is some debate over the importance of the aeolian source of iron compared to dissolved iron contained in upwelling waters [*Meskhidze et al.*, 2007; *Wagener et al.*, 2008], which agrees with the GCM studies where the primary source of iron to the Southern Ocean is from upwelling [*Bopp et al.*, 2003; *Parekh et al.*, 2006b].

The largest anomaly of regenerated phosphate and therefore biogenic carbon produced by direct iron fertilisation was in the deep Southern Ocean around 60°S below the band of slightly enhanced productivity, which confirms that this is the most efficient region for converting iron perturbations into oceanic carbon uptake even though the magnitude of the enhanced productivity is low [*Dutkiewicz et al.*, 2006]. Nevertheless, as it stands, this violates the observations of reduced export production south of the modern polar front [*Kohfeld et al.*, 2005; *Wolff et al.*, 2006]. This may be reconciled by considering that if the supply of upwelled iron and nutrients was probably reduced at the LGM but their ratio remained constant (or indeed lower due to enhanced scavenging on account of slower ventilation), then an external source of iron is necessary to produce the observed increase in nutrient utilisation, else the fraction of nutrients consumed would also remain constant or even decline due to iron limitation. As a matter of fact, in the reduced overturning plus LGM dust case of *Parekh et al.* [2006b], export production actually decreases around 60°S, compared to the LGM dust only case.

On the other hand, atmospheric CO_2 appeared roughly twice as sensitive to a similarly sized reduction in iron deposition that may result from a more intense hydrological cycle due to a doubling of CO_2 levels in the future[*Mahowald et al.*, 2006a,b]. This non-linearity was noticed by *Parekh et al.* [2006a] who decreased the magnitude of the modern aeolian dust deposition field by degrees until the dust flux was zero and observed the effect on atmospheric CO_2 in a similar model configuration. After 1000 years the atmospheric CO_2 concentration had increased 14 ppm with a 50% reduction in iron, 95 ppm with a 90% reduction and 181 ppm with no aeolian iron source. These results are more sensitive to the decline than those presented in Chapter 5, however iron deposition is not uniformly reduced in this case, for example future rates of deposition remain of a similar order of magnitude to LGM rates in the North Atlantic and eastern equatorial Pacific, allowing biological production to continue there. Indeed the release of CO_2 from the increasingly iron-depleted Southern Hemisphere due to reduced biological activity increases the lateral transfer of unutilised macronutrients into the oligotrophic gyres, particularly in the Atlantic Ocean resulting in slightly increased productivity and recapture of some outgassed CO_2.

However, while in the limit of global excess iron deposition "nutrient robbing" damps the integrated response of increased iron deposition, decreasing deposition towards zero has no such negative feedback. As the iron replete regions become increasingly micronutrient stressed and no longer able to make use of the increased preformed nutrient concentration, eventually the ocean becomes abiotic and the atmospheric CO_2 levels are determined by the solubility pump alone [*Gruber and Sarmiento*, 2002; *Knox and McElroy*, 1984; *Parekh et al.*, 2006a; *Sarmiento and Toggweiler*, 1984]. However, these models do not take into account other sources of iron to the ocean such as continental sediment sources, hydrothermal activity or lateral transport by ice bergs, which would maintain some degree of dissolved iron supply. *Bopp et al.* [2003] found only a small CO_2 increase (~3 ppm) when aeolian iron supply was completely removed, which is of comparable magnitude to the reduction in Chapter 5. However instead of the extensive scavenging and removal of free iron that occurs in the MITgcm biogeochemistry model [e.g. *Parekh et al.*, 2005, 2006a,b] on account of the thermodynamic equilibrium between free and complexed iron, their model scavenged toward a constant deep ocean concentration of 0.6 µmol Fe m^{-3} which is much greater than the ~0.2 µmol Fe m^{-3} upwelled to the surface in the Southern Hemisphere for the 2.5–3 times reduced iron source in Figure 5.4a. *Tagliabue et al.* [2010] estimate a hydrothermal input of around 9×10^8 mol Fe yr^{-1} resulting in a whole ocean average increase of dissolved iron of 0.12 µmol Fe m^{-3} compared

to a model forced with aeolian deposition alone, with the deep south Pacific and Southern Ocean augmented slightly more than the north Pacific or Atlantic Oceans, but even with this taken into account dissolved iron concentration is still shy of $0.6\,\mu mol\,Fe\,m^{-3}$.

These results add a further voice to the growing body of literature that suggests iron fertilisation cannot be considered a major driving force for the glacial-interglacial CO_2 changes recorded in ice cores. Indeed, the timing of changes of aeolian dust deposition and carbon dioxide changes indicate that during the last deglaciation, the majority of the CO_2 increase occurred after iron fluxes had already reached their interglacial levels, thus limiting their attributable effect to less that 30 ppm [*Wolff et al.*, 2006], while other rapid CO_2 changes were associated with no coincident dust fluxes [*Fischer et al.*, 2010]. Both perturbations presented in Chapter 5 question iron fertilisation as a method of geoengineering to mitigate future effects of anthropogenic carbon emissions, showing micronutrient deposition is not an efficient means of sequestering CO_2 from the atmosphere and locking it in the deep ocean. Significant and widespread aeolian iron deposition (although this might be somewhat reduced by fertilising only in the Austral summer) removed a net small volume of CO_2 from the atmosphere, a significant proportion of which is locally remineralised in the upper ocean and subject to return to the atmosphere on short timescales. The general decline in productivity of oligotrophic regions that are fuelled by lateral nutrient transfer also limits the efficiency of CO_2 uptake and highlights the need to consider the global, not just local effects of such a strategy [e.g. *Gnanadesikan and Marinov*, 2008]. Furthermore a reduction of aeolian iron input with a warmer, moister climate under doubling atmospheric CO_2 represents a positive feedback on climate [*Parekh et al.*, 2006a] that is not necessarily considered when discussing the geoengineering potential of iron fertilisation [e.g. *Royal Society*, 2009], which would necessitate widespread iron fertilisation to maintain the status quo.

7.2 The role of Southern Ocean ventilation in atmospheric CO_2 change

The consensus of many recent studies [e.g. *Fischer et al.*, 2010; *Keeling and Visbeck*, 2001; *Sigman et al.*, 2010; *Toggweiler et al.*, 2006; *Watson and Naveira Garabato*, 2006] is that atmospheric CO_2 is more sensitive to the rate of ventilation of the Southern Ocean and its stratification [*François et al.*, 1997], which is influenced by the rate of the residual mean overturning circulation and modulated by surface winds, buoyancy fluxes

and mesoscale eddies. In Chapter 3, westerly wind stress was increased and decreased by 50% relative to the control and in Chapter 4 the peak westerly wind stress in the Southern Hemisphere was shifted ~10° north and south in order to perturb the Southern Ocean overturning circulation. This resulted in modest changes in atmospheric pCO_2 of roughly 10–15 ppm (see Figure 7.1). *Parekh et al.* [2006b] doubled Southern Ocean wind stress and applied LGM dust fluxes in a coarse resolution OGCM to achieve a 25 ppm increase in atmospheric CO_2 relative to their preindustrial control. A 50% decrease in Southern Ocean westerlies with LGM dust fluxes achieved a 31 ppm decrease in atmospheric pCO_2. Using their LGM iron fertilisation with modern circulation as a guide, increased ventilation is responsible for a 33 ppm increase in atmospheric CO_2, while decreased ventilation is responsible for a 23 ppm draw down of atmospheric carbon giving a sensitivity of 3 ppm Sv^{-1}, which compares reasonably with wind stress anomalies in Figure 7.1, although with elevated sensitivity as experiments presented here reveal a sensitivity of just over 1 ppm Sv^{-1}. Differences are likely due to the use of different aeolian iron fluxes and the details of the perturbed wind stress climatologies. *Menviel et al.* [2008] recorded a ±5 ppm change in atmospheric CO_2 for a ~20–30% change in winds in an EMIC, which extrapolated linearly produces a similar, if slightly reduced, sensitivity. Using an ensemble of wind stress forcing and different configurations of a geostrophic-frictional balance model, *Tschumi et al.* [2008] found atmospheric CO_2 responses in the range of 20–40 ppm per 100% increase in Southern Hemisphere westerlies. Model configuration dependency is introduced when winds are decreased, resulting in a larger range of −2 to −55ppm for a fourfold decrease in wind stress. Again, these results compare well to previous estimates. Finally, *Toggweiler et al.* [2006] increased and decreased wind stress in a primitive equation GCM coupled to an energy balance model of the atmosphere resulting in the same positive correlation between wind stress and atmpospheric CO_2 levels. With wind stress held steady at 1.5 times greater than their original climatology, their model produced a series of 4000 year duration cycles of atmospheric CO_2 with an amplitude of ~35 ppm. Ultimately, these are an artifact of perfectly steady forcing that is unseen in nature but nevertheless demonstrate the effect of surface stratification, forming low salinity surface layers when bottom water formation is low and then breaking them when the deep ocean is warm and bottom water formation resumes.

Menviel et al. [2008] highlight *Toggweiler et al.* [2006]'s use of nutrient restoring [e.g. *Najjar and Orr*, 1998] to simulate biological productivity and lack of sea ice dynamics in obtaining such a large sensitivity to wind stress changes (with cycles that were 35 ppm in amplitude). Changing nutrient concentrations as a result of upwelling acts as a negative

feedback that, via biological production, counteracts the change in atmospheric carbon dioxide by modulating mid latitude CO_2 outgassing. *Menviel et al.* [2008]'s experiments with nutrient restoring reproduce an increased CO_2 sensitivity to Southern Hemisphere winds, implying that sea ice dynamics in their model is of secondary importance. Nevertheless, they neglect the effects of iron cycling that may result in their soft tissue pump being over active in its compensation to enhanced nutrient supply as the experiments in Chapter 3 demonstrate. Increased upwelling draws relatively macronutrient-rich, but iron-deficient waters to the surface that does illicit a response in biological activity, but this extra production is somewhat smaller than the ±7–14% simulated by *Menviel et al.* [2008] and leads to an elevated atmospheric CO_2 sensitivity. The extent of air-sea CO_2 equilibrium also affects the magnitude of the change in atmospheric CO_2, determined by circulation and the rate of gas exchange. Using the spatially variable parameterisation of *Wanninkhof* [1992] dependent on local values of squared wind speed results in a ±50% reduction in the quantity of CO_2 exchanged between the atmosphere and ocean compared to instantaneous air-sea exchange where the disequilibrium concentration is zero [*Marinov et al.*, 2008], highlighting the need to properly resolve gas exchange processes since spatially uniform piston velocities [e.g. *Toggweiler et al.*, 2006] would not resolve this simple, but important process.

Based on the results of their increased and decreased wind stress perturbations, *Toggweiler et al.* [2006] argue that shifting the Southern Hemisphere westerlies achieves the same pattern of changes to Southern Ocean overturning circulation, with a northward shift reducing the wind stress in the latitudes of Drake Passage, lowering the rate of Southern Ocean upwelling and therefore decreasing the escape of respired CO_2 into the atmosphere and vice versa for southward-shifted winds. However, results for nominal 10° shifts presented in Chapter 4 clearly oppose this supposition: northward shifted winds result in increased atmospheric CO_2 concentration while more southerly winds cause decreased atmospheric pCO_2. *Tschumi et al.* [2008]'s results for a 5° shift in their simplified physics model are also the antithesis of *Toggweiler et al.* [2006]'s. This behaviour, which was not explicitly tested in the model of *Toggweiler et al.* [2006], likely stems from an assumption about what measure of wind stress determines ACC transport and Southern Ocean overturning circulation. If the ACC is dependent only on wind stress in the latitude band of Drake Passage [e.g. *Russell et al.*, 2006; *Toggweiler and Samuels*, 1995, 1998] then latitudinal migration will scale like a change in magnitude of the wind stress because the peak Southern Hemisphere westerlies lies at the northern edge of the unblocked latitudes of Drake Passage, so a northward migration will reduce Drake Passage wind stress, while a southward migration will move the peak into the

Drake Passage band and increase westerly wind stress. But if the Southern Ocean overturning circulation is dependent on wind stress outside the latitude of Drake Passage [*Allison*, 2009; *Allison et al.*, 2010] then the response would be different, as has been found.

Explicitly changing the latitude of the wind stress maximum not only alters the area of deep ocean isopycnal outcrop at the surface [*Tschumi et al.*, 2008], with a greater outcrop area and increased outgassing of respired carbon dioxide from the deep ocean with northward-shifted winds and vice versa for a southward shift, but also adjusts the Southern Ocean overturning circulation (see Chapter 4). Shifting the extratropical Southern Hemisphere westerlies reduces the momentum imparted by the winds into the ACC and diverts it into either the subpolar supergyre for a north shift or the Ross and Weddell Sea gyres for a south shift [*Allison*, 2009; *Allison et al.*, 2010]. Indeed, integrated momentum input is also dependent on the surface area on which the wind stress acts, with a greater area when winds are shifted to the north and a reduced surface area when the winds are moved southward. Both shifts also exhibit substantial circulation changes in the Southern Hemisphere mid latitudes. With northward shifted winds, greater Ekman transport generated by a lower value of the Coriolis parameter brings a larger volume of relatively nutrient and carbon rich intermediate depth waters to the surface in a stronger but shallower Deacon cell that augments the continued level of deep water upwelling in the Southern Ocean due to the expanded circulation forced by the Antarctic easterly winds. The atmosphere and ocean also become closer to equilibrium due to the reduced enrichment of upwelled waters that are converted to intermediate and mode waters and subducted into the interior compared to the control run, driving "trapped" CO_2 from the ocean to the atmosphere. On the other hand, a southward shift induces weaker Ekman transport due to a larger value of the Coriolis parameter and the Deacon cell is more strongly compensated by return eddy flow leading to reduced upwelling of carbon rich deep waters. Increased Southern Hemisphere subtropical gyre circulation driven by expanded tropical easterlies enhances downwelling at the subtropical convergence zone that augments reduced upwelling of carbon-rich deep waters in the Southern Ocean and leads to increased low latitude divergence/ upwelling. Air-sea CO_2 disequilibrium increases substantially isolating a greater volume of CO_2 from the atmosphere. When the magnitude of the shifted Southern Hemisphere westerlies is also perturbed, then the change in atmospheric CO_2 concentration is an almost linear combination of shift and magnitude experiments, with increased wind stress causing increased CO_2 outgassing with either north- or southward-shifted winds,

while decreased wind stress increased CO_2 uptake for north- or southward-shifted winds due to additional spin up/down of overturning circulations in the Southern Ocean.

For increased Southern Ocean winds, these findings suggest that future atmospheric pCO_2 may stabilise at a higher level than predicted by carbon chemistry alone because those estimates do not take into account the physical responses of the carbon cycle to changes in forcing [*Le Quéré et al.*, 2007; *Lenton and Matear*, 2007; *Lovenduski et al.*, 2007, 2008; *Wetzel et al.*, 2005] even with the associated increase in biological productivity that upwelling of nutrients stimulates [*Lovenduski and Gruber*, 2005; *Menviel et al.*, 2008]. However, if these winds are shifted south [e.g. *Gillet and Thompson*, 2003] then for more temperate changes in magnitude a slight net strengthening of the Southern Ocean natural CO_2 sink may occur in the long term. However, as the stratospheric ozone hole repairs, if the tropospheric Southern Hemisphere westerlies migrates to a more northern position [*Perlwitz et al.*, 2008] then a net weakening of the Southern Hemisphere CO_2 sink may be a more likely outcome.

Although these results may be somewhat dependent on the details of the perturbed wind stress fields, replication of the results of the shift perturbations using a primitive equation GCM forced by monthly varying modified climatological wind stress (this study) and an ocean model of intermediate complexity forced by temporally constant zonally-averaged analytical wind stress [*Tschumi et al.*, 2008] is cause for some confidence in the qualitative patterns derived from these idealised simulations. The perturbed magnitude simulations were also relatively insensitive to the surface heat and freshwater boundary conditions (Chapter 6.1), save modifications to circulation and primary production that act antagonistically, and changes in the rate of air-sea gas exchange due to perturbations to prescribed wind speed (Chapter 6.3). Crudely taking account of possible responses of mesoscale eddy activity to Southern Hemisphere wind perturbations (Chapter 6.2) had a greater impact through altering the balance of Southern Ocean residual overturning, which was countered by the negative productivity feedback [*Menviel et al.*, 2008], but also by changes in isopycnal stirring and ventilation. Increasing κ_{GM} with increased wind stress resulted in the more rapid subduction of nutrients out of the surface layer in the Southern Ocean, limiting the action of the biological feedback and a coincident increase in the export of DIC rich surface waters. Hence the globally integrated concentration of disequilibrium DIC was increased and therefore the global carbon inventory above that suggested by the nutrient field alone [e.g. *Gnanadesikan and Marinov*, 2008]. Alternatively, decreasing κ_{GM} with decreased wind stress resulted in a greater residency

of nutrients in the surface layer and enhanced biological consumption whilst also increasing the extent of ocean-atmosphere CO_2 equilibrium, thus decreasing the globally integrated concentration of "trapped" DIC and therefore reducing the sensitivity of atmospheric CO_2 to wind stress perturbations by reducing the global carbon inventory below that suggested by the nutrient field alone.

Paleoceanographic reconstructions of ocean circulation suggest that the overall pattern of stratification and hydrography of the Southern Ocean and thus meridional overturning circulation at the LGM was similar to today [*Matsumoto et al.*, 2001] with continued upwelling of CDW, northward surface Ekman transport and intermediate and mode water formation [*Pahnke and Zahn*, 2005; *Pahnke et al.*, 2008]. The perturbations in Part II are consistent with this view, with none of these perturbation totally reorganising the global meridional overturning circulation. Even the seemingly major circulation changes associated with the latitudinal shift in the Southern Hemisphere winds remain reminiscent of the control overturning, with a density structure that largely resembles the isopycnal configuration of the control run apart from minor adjustments to isopycnal gradients and location. Indeed, the resultant density anomalies for scenarios with decreased atmospheric CO_2 are consistent with proxy records that suggest a shoaling of the AMOC and decreasing NADW formation rate [e.g. *Duplessy et al.*, 1988; *Rahmstorf*, 2002] and shallower depth of the pycnocline with increased upper ocean stratification [*Sigman and Boyle*, 2000] associated with reduced AAIW formation [*Pahnke and Zahn*, 2005; *Pahnke et al.*, 2008]. On the other hand, the model does not reproduce evidence that suggests no significant migration of the ACC, although 5–7° shifts in the opal production belt [*François et al.*, 1997; *Matsumoto et al.*, 2001] associated with the Polar Front might dispute this. Neither does the model create denser, saltier AABW in the Southern Ocean [*Adkins et al.*, 2002; *Govin et al.*, 2009], although this is unsurprising given that the configuration of MITgcm does not have interactive sea ice and so the possible effects of changing wind forcing and residual overturning on sea ice formation and brine rejection are not captured [*Cai and Baines*, 1996; *Menviel et al.*, 2008].

7.3 The link between biological activity, ocean circulation and atmospheric CO_2

The general pattern of biological productivity associated with increasing and decreasing Southern Ocean overturning and subsequent changes to nutrient supply results in two

possible states. In the first, associated with increased northward residual transport at the surface, upwelled nutrients from the Southern Ocean are laterally supplied to adjacent subtropical gyres and along the length of the Atlantic Ocean [*Dutkiewicz et al.*, 2005a; *Parekh et al.*, 2005, 2006b; *Sarmiento et al.*, 2004; *Williams and Follows*, 1998]. Upwelling of deep nutrients, which is the primary supply into the Pacific and Indian Ocean surface layer, is reduced by increased volume of intermediate and mode waters exported from the Southern Ocean and deepening the low latitude pycnocline [*Dutkiewicz et al.*, 2005a; *Levermann and Fürst*, 2010; *Parekh et al.*, 2005, 2006b], therefore resulting in increased Atlantic, but decreased Indo-Pacific productivity. The reverse occurs for reduced residual flow in the upper part of the Southern Ocean that limits the supply of nutrients to the Atlantic, but enhances the diapycnal upwelling flux to the surface of the Indian and Pacific Oceans due to shallower pycnocline depth, leading to increased Indo-Pacific Ocean productivity but reduced Atlantic productivity. Such a distinct bimodal distribution should be captured in proxies of export production (e.g. Figure 1.6, *Kohfeld et al.* [2005]) that show a widespread increase in the southern and mid latitude Atlantic, but are ambiguous elsewhere due to paucity of data with relatively confident increases in the north Indian Ocean and off Madagascar and in the north west Pacific and off the coast of Chile. Given that the data are inconclusive, the only perturbation that produced increased productivity in the majority of the Northern Hemisphere was the 10° southward shift (Figure 4.18d), even the glacial iron fertilisation experiment suppressed biological activity in this region.

Changes in primary production are weakly positively correlated to atmospheric CO_2 (Figure 7.2a), which is counterintuitive considering that biological hypotheses for glacial-interglacial CO_2 call for a negative correlation to exist. However, because these changes are stimulated by changes to Southern Hemisphere circulation-induced nutrient supply, a stronger relationship is found between the rate of biological activity and Southern Ocean Eulerian-mean and residual overturning circulations (not shown), although there remains considerable scatter associated with low latitude upwelling and changes in oceanic CO_2 storage associated with the extent of ocean-atmosphere equilibration. *Parekh et al.* [2006b] found that primary production actually increased after 1000 years with increased and decreased winds and this is captured in the sequence of snapshots of primary production in Figure 3.32. Biological activity is elevated at 1000 years after decreasing wind stress thanks to upwelling of nutrients in the Indo-Pacific basins, but as the ocean circulation has not quite reached steady state (see Figure 3.32d), the upwelling

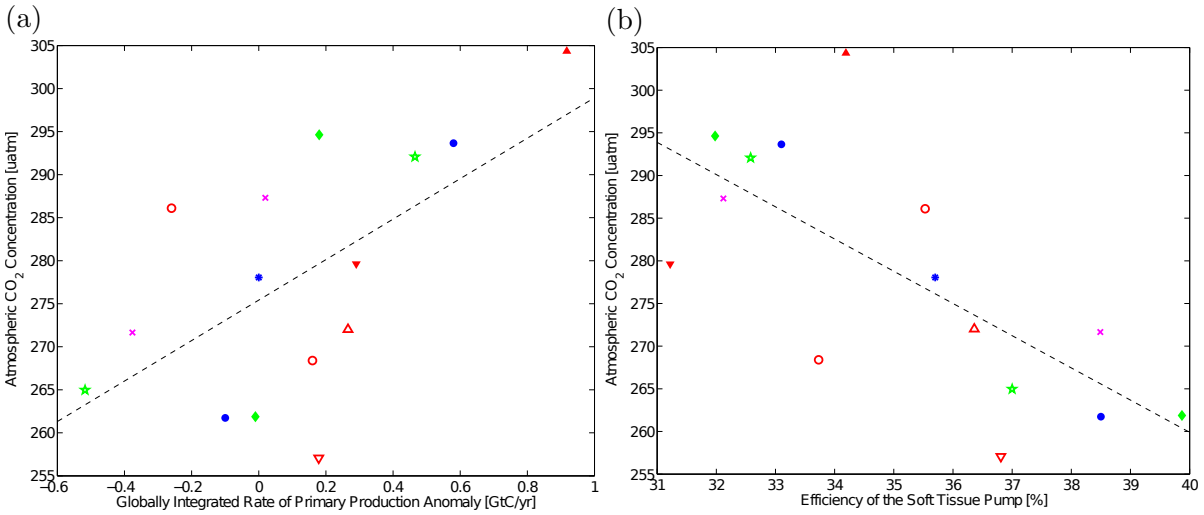

Figure 7.2: Steady state atmospheric CO_2 concentration from each experiment against (a) global rate of primary production ($\mathrm{Gt\,C\,yr^{-1}}$, R^2 = 0.37) and (b) global average efficiency of the soft tissue pump (%, R^2 = −0.50) for the control run (∗), wind stress magnitude (●), wind stress position (○), south shift increased wind stress magnitude (▾), north shift increased wind stress magnitude (▴), south shift decreased wind stress magnitude (▿), north shift decreased wind stress magnitude (▵), wind stress magnitude with varied κ_{GM} (×), wind stress magnitude with fixed surface heat and freshwater boundary conditions (◆) and wind stress magnitude with mixed surface heat and freshwater boundary conditions experiments (☆).

flux diminishes slightly and the Atlantic Ocean becomes increasingly macronutrient limited leading to an eventual reduction of globally integrated biological activity after 5000 years. Nevertheless, the globally integrated rate of primary production is not necessarily a good measure of the ability of ocean biology to determine atmospheric CO_2 levels, relating to early explanations of glacial-interglacial climate changes that suggested an increase in biological activity to draw down CO_2 levels. While increased Southern Ocean meridional overturning results in a greater supply of remineralised nutrients to the surface ocean and stimulates productivity, combined with the low efficiency of Southern Ocean nutrient utilisation leads to a greater volume of the upper ocean being ventilated by intermediate and mode waters with high preformed nutrient concentrations, which promotes net outgassing of carbon to the atmosphere [*Ito and Follows*, 2005], given no change in the disequilibrium concentration of DIC [*Gnanadesikan and Marinov*, 2008; *Marinov et al.*, 2008]. Thus a better metric is the ratio of globally-averaged regenerated phosphate concentration against total phosphate concentration that captures both changes in productivity and circulation, showing increased CO_2 levels with decreased soft tissue pump efficiency and alternatively lower CO_2 levels with increased soft tissue pump efficiency (Figure 7.2b, *Ito and Follows* [2005]). Efficiency of the soft tissue pump is inversely proportional to the strength of Eulerian-mean Southern Ocean overturning

as this sets the globally-averaged concentration of preformed nutrients, while a positive correlation is displayed with the strength of the Southern Ocean eddy-induced overturning circulation, which again demonstrates the importance of mesoscale eddies in influencing global ocean nutrient supply and atmospheric CO_2 concentrations.

Intriguingly, the major source/sink of carbon to the atmosphere in the perturbations to Southern Ocean residual overturning was not the deep ocean and bottom waters, as in the LGM iron perturbation or suggested elsewhere [e.g. *Toggweiler et al.*, 2006], but more intermediate depth waters centred at ~1000–1500 m, with the deep ocean below this depth generally displaying an opposing change in concentration. Anomalous phosphate concentration closely mirrors this pattern, the majority of which is accounted for by isopycnal heave and altered depth of the low latitude pycnocline associated with the changing volume of water masses formed in the Southern Ocean and exported to the north. A depression of the low latitude pycnocline brings low DIC and macronutrient depleted waters into regions of elevated concentrations, thus causing a negative anomaly on depth coordinates, while shoaling of the low latitude pycnocline raises relatively enriched DIC and macronutrient waters towards the surface thus causing positive anomalies on depth levels. This is also the case in the deep North Atlantic where altered strength of the AMOC changes the depth of the NADW/AABW boundary and since NADW has relatively low nutrient and CO_2 concentrations because it is freshly ventilated, the pattern of heave anomalies is the same as for shifting the pycnocline. However, tracing the CO_2 associated with air-sea gas exchange using the quasi-conservative tracer $C_{gas\ exch}$ reveals that the intermediate-depth waters also carry the climatic signals that relate to changing atmospheric CO_2 levels, with an increase of $C_{gas\ exch}$ here when atmospheric CO_2 declines and a decrease in $C_{gas\ exch}$ when atmospheric CO_2 rises, indicating that when these waters were last at the surface, they were responsible for the outgassing/ uptake fluxes.

$\delta^{13}C$ in fossil foraminifera can be linked to nutrient concentration [e.g. *Curry et al.*, 1988; *Duplessy et al.*, 1988; *Oppo and Fairbanks*, 1990] since biological activity in the upper ocean preferentially consumes light isotopes of carbon and nutrients and then exports them to depth where remineralisation occurs establishing a gradient with depth where surface waters are low in nutrients and enriched in heavy carbon isotopes (positive $\delta^{13}C$) while abyssal waters have high nutrient concentrations and are enriched in light carbon isotopes (negative $\delta^{13}C$). This first order relationship is complicated by gas exchange fractionation, carbon release from the terrestrial biosphere and sediment dissolution. However taking account of these factors, *Toggweiler et al.* [2006] show a

meridional section in the Atlantic showing the difference in δ^{13}C between the glacial and modern Atlantic Ocean, with a clear negative anomaly (i.e. greater enrichment of light carbon isotopes, implying greater nutrient concentration of roughly 0.5 mmol m^{-3}) below ~2500 m and a positive anomaly above (i.e. greater enrichment of heavy carbon isotopes, implying reduced nutrient concentration), which compared to anomalies of carbon and nutrients in the Atlantic for perturbations where CO_2 in the atmosphere declined (Figure 3.30 for decreased magnitude and Figure 4.19 for southward shifted wind stress) produces the inverse pattern with a smaller magnitude. However, *Ninnemann and Charles* [2002] suggest that this distribution of anomalies is instead due to deep ocean circulation changes and an increase in AABW volume, filling the deep ocean to roughly 2500 m. Also there is evidence of competition at intermediate depths due to the formation of Glacial North Atlantic Intermediate Water [GNAIW, e.g. *Keeling and Stephens*, 2001; *Rahmstorf*, 2002], which would have injected nutrient depleted waters (enriched values of δ^{13}C) from the North Atlantic into the ocean interior and displacing high nutrient AAIW downwards in the water column. *Brovkin et al.* [2007] simulate such a reorganisation of water masses and generate δ^{13}C anomalies of approximately $-0.5‰$ in the deep ocean of an EMIC using glacial physical and biogeochemical boundary conditions that compare well with the paleoceanographic record [*Duplessy et al.*, 1988]. Furthermore, *Pahnke and Zahn* [2005] suggested that glacial δ^{13}C concentrations from a core in the southwest Pacific Ocean at roughtly 1500 m show low AAIW production during glacial periods and intensified AAIW production during interglacials. Although this model does not take account of variability of AABW formation, except where thermohaline surface boundary conditions capture the altered Southern Ocean freshwater balance with perturbed wind stress and therefore will not reproduce the abyssal ocean changes, increased upper ocean stratification due to the reduction of intermediate depth water mass formation in the Southern Ocean is consistent with the patterns of Southern Ocean residual overturning circulation and atmospheric CO_2 presented in this thesis.

Changes to overturning circulation in the Southern Ocean correlate well with anomalies of atmospheric CO_2 (Figure 7.3), particularly with changes in Eulerian-mean overturning circulation that controls the rate that carbon and nutrient-rich deep waters are upwelled and exposed to atmospheric interactions and to the compensating effects of mesoscale eddy transport that opposes it. The relationship between CO_2 and eddies is also somewhat counterintuitive because a stronger eddy circulation should flatten isopycnals and reduce outgassing, while weak mesoscale eddy activity allows steeper sloping isopycnals, upwelling and CO_2 outgassing. In this case, isopycnal steepening by the Eulerian-mean circulation forced by the change in wind stress is driving the changes in

eddy overturning, therefore producing the observed correlation. Interestingly, pCO_2 is also well correlated to the strength of the AMOC [e.g. *Parekh et al.*, 2006b; *Toggweiler and Samuels*, 1995, 1998] through the "Drake Passage" effect and the dependence of the rate of NADW formation on the depth of the global pycnocline in a regime of low vertical diffusivity [*Gnanadesikan*, 1999] even with altered surface heat and freshwater boundary conditions [e.g. *de Boer et al.*, 2008]. However, for the reasons suggested above, due to the lack of interactive sea ice formation and brine rejection, atmospheric CO_2 shows no strong relationship with the abyssal circulation of AABW. This is interesting because it suggests that the "biologically productive northern circuit" of the meridional overturning circulation [*Marinov et al.*, 2006, 2008; *Toggweiler et al.*, 2006] does have significant impact on atmospheric carbon dioxide, probably in addition to the "unproductive Southern Ocean circuit". Not only may CO_2 be drawn out of the atmosphere by biological production stimulated by the nutrients carried in AAIW and SAMW as suggested by *Toggweiler et al.* [2006], which in this case was found to be fairly inefficient, but CO_2 is also directly sequestered from the atmosphere and subducted to intermediate depths at lower latitudes [*Caldeira and Duffy*, 2000; *Sabine et al.*, 2004].

The perturbations in Part II recreate another important relationship, seen in proxy data suggesting enhanced nutrient utilisation, between atmospheric CO_2 and stratification that relates back to the early box model experiments and the Harvardton Bears' suggestion of lowering atmospheric CO_2 through decreased vertical mixing [*Knox and McElroy*, 1984; *Sarmiento and Toggweiler*, 1984; *Siegenthaler and Wenk*, 1984]. Figures 7.4a and 7.4b show the relationship between atmospheric CO_2 concentration and two measures of the change in upper ocean stratification, the former is the anomaly in the top 1000 m of the global ocean while the latter is the anomaly in the upper 1000 m in the region south of 40°S only. Both show a negative correlation, with enhanced stratification associated with lower atmospheric CO_2 and reduced stratification associated with higher atmospheric CO_2 as deduced from the paleoceanographic record [*François et al.*, 1997; *Sigman and Boyle*, 2000; *Toggweiler*, 1999] and glacial modelling studies [*de Boer et al.*, 2010; *Tschumi et al.*, 2010]. The global stratification anomaly with perturbed wind stress magnitude and fixed surface boundary conditions is particularly small in relation to the change in pCO_2 because the surface buoyancy fluxes derived from the control steady state constrains the average surface density structure leading to their plotted locations at the end of the integration lying significantly away from the rest of the experiments. When only Southern Ocean stratification is considered then even the fixed buoyancy flux experiments show a much closer relationship between

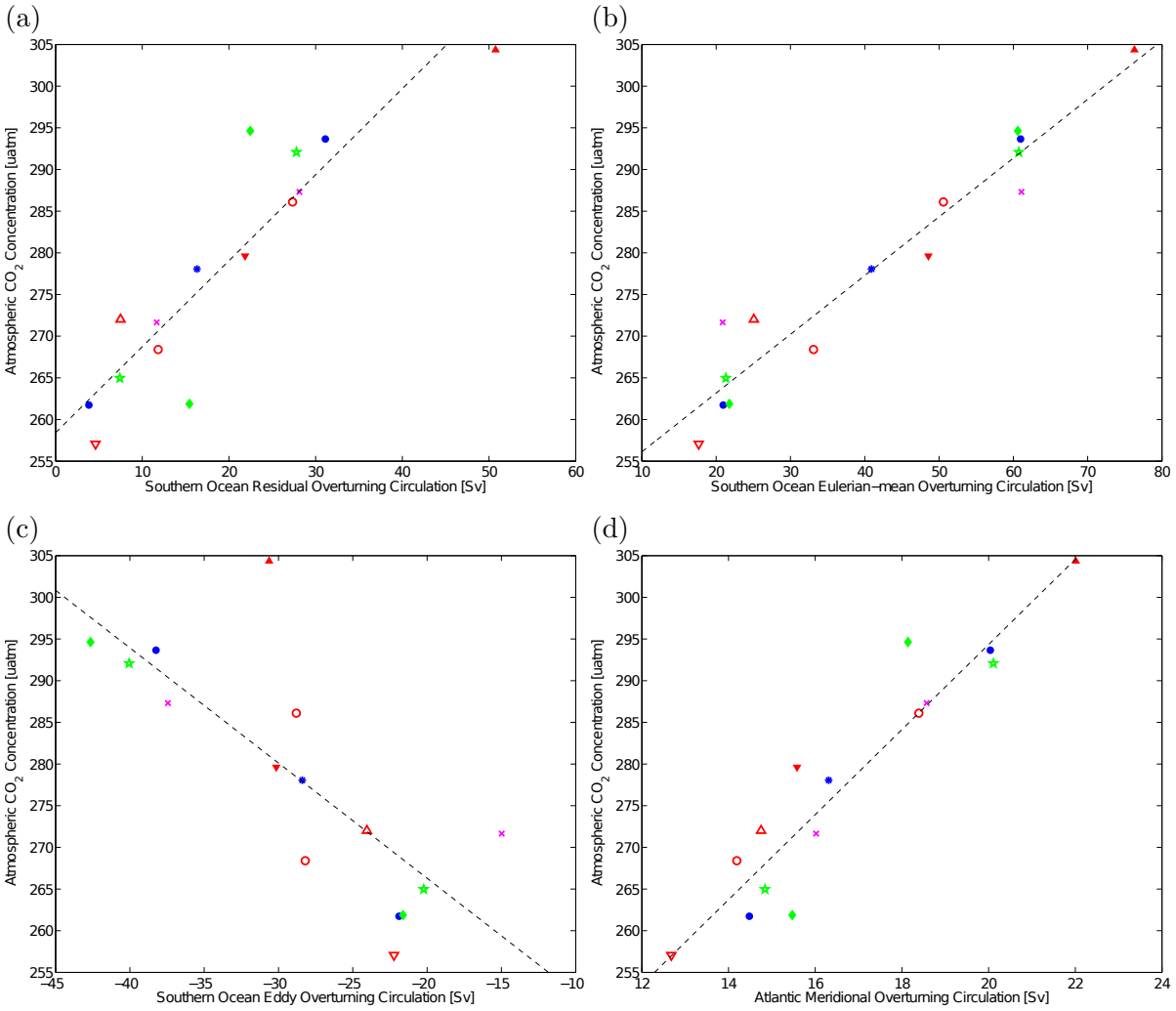

Figure 7.3: Steady state atmospheric CO_2 concentration from each experiment against (a) maximum Southern Ocean residual meridional overturning circulation (Sv, R^2 = 0.83), (b) maximum Southern Ocean Eulerian-mean meridional overturning circulation (Sv, R^2 = 0.93), (c) maximum Southern Ocean eddy meridional overturning circulation (Sv, R^2 = −0.61) and (d) maximum North Atlantic meridional overturning circulation (Sv, R^2 = 0.88) for the control run (∗), wind stress magnitude (●), wind stress position (○), south shift increased wind stress magnitude (▾), north shift increased wind stress magnitude (▴), south shift decreased wind stress magnitude (▿), north shift decreased wind stress magnitude (▵), wind stress magnitude with varied κ_{GM} (×), wind stress magnitude with fixed surface heat and freshwater boundary conditions (◆) and wind stress magnitude with mixed surface heat and freshwater boundary conditions experiments (☆).

stratification and CO_2 concentration in the atmosphere. A positive correlation between stratification below 1000 m and atmospheric CO_2 (not shown) is probably again related to the suspected deficiencies in the representation of sea-ice in AABW formation, and may also be driven by variations in the strength of the AMOC, with stronger NADW formation depressing the AABW/NADW boundary and compressing deep isopycnals

and vice versa. Also, the change in strength and location of Southern Hemisphere Ekman convergence and divergence probably also influenced the observed changes in deep ocean stratification.

Southern Ocean stratification, as with the efficiency of the soft tissue pump, is largely determined by Southern Ocean overturning circulation. Having prescribed the perturbations to the wind stress in order to create such alterations to Southern Ocean circulation it is useful to derive a metric that encompases changes to the wind stress fields and describes the oceanic response that leads to atmospheric carbon dioxide uptake or outgassing. Since the Eulerian-mean circulation determines the rate of upwelling of carbon and nutrient rich waters and therefore influences atmospheric CO_2, efficiency of the soft tissue pump and upper ocean stratification, Figure 7.4c shows the relationship between the root mean squared value of zonal wind stress that is directly linked to the strength of the Southern Ocean Deacon cell through northward Ekman transport, against atmospheric CO_2 concentration, and displays a good positive correlation with increasing average wind stress driving increasing atmospheric CO_2 via enhanced Eulerian-mean overturning circulation. However, this is no more instructive than looking at the circulation fields in the Southern Hemisphere, other than a compact description of the applied perturbation to surface forcing. It is imperceptive to factors that influence oceanic carbon content such as internal ocean processes or processes that are not local to the altered wind stress region. For example, the same modified wind stress is used for several different perturbation experiments, including modifications to internal eddy circulation strength and surface buoyancy conditions that produce different steady state pCO_2 and circulation results leading to a spread in the data in Figure 7.4c of approximately 10 ppm. In order to take these shortcomings into account, the globally integrated input of energy from the work done by the wind on the oceanic general circulation (W) may be diagnosed [Equation 7.1 *Wunsch*, 1998]:

$$W = \int (\tau \cdot \mathbf{v}_g) dA \tag{7.1}$$

that includes both wind stress forcing (τ) and changes to large scale geostropic ocean circulation at the sea surface ($\mathbf{v}_g = (u_g, v_g)$) over the sea surface area (A). The prognostically-computed model surface velocity field was used, removing the wind-driven Ekman flows by calculating the Ekman velocity at the sea surface [e.g. *Wang and Huang*, 2004] from

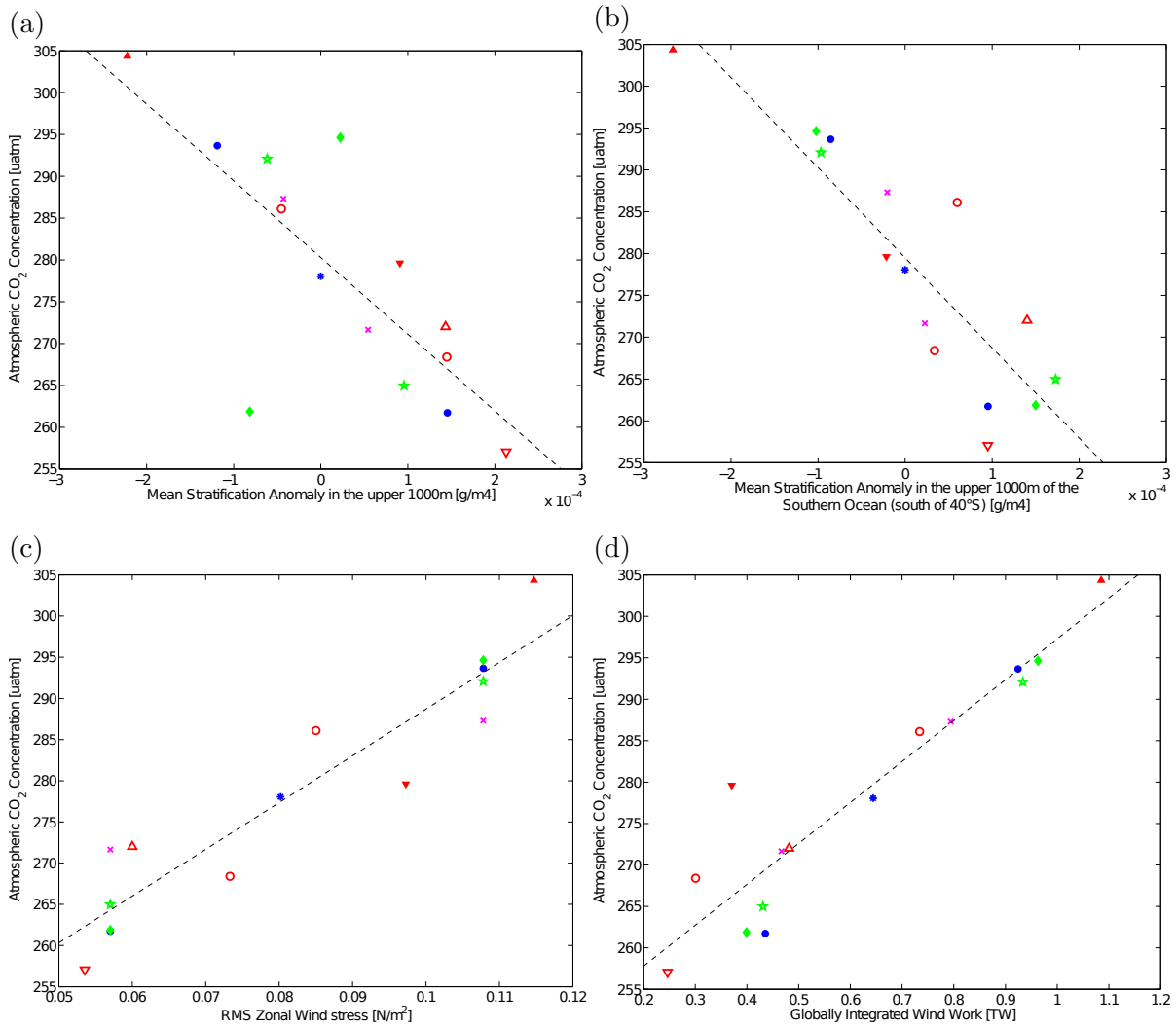

Figure 7.4: Steady state atmospheric CO_2 concentration from each experiment against (a) anomaly of stratification in the upper 1000 m of the global ocean (Sv, $R^2 = 0.58$), (b) stratification anomaly in the upper 1000 m of the Southern Ocean south of 40°S ($g\,m^{-4}$, $R^2 = 0.78$), (c) root mean squared average zonal wind stress ($N\,m^{-2}$, $R^2 = 0.88$) and (d) globally integrated wind work calculated using Equation 7.1 (TW, $R^2 = 0.88$) for the control run (∗), wind stress magnitude (●), wind stress position (○), south shift increased wind stress magnitude (▾), north shift increased wind stress magnitude (▴), south shift decreased wind stress magnitude (▿), north shift decreased wind stress magnitude (▵), wind stress magnitude with varied κ_{GM} (×), wind stress magnitude with fixed surface heat and freshwater boundary conditions (♦) and wind stress magnitude with mixed surface heat and freshwater boundary conditions experiments (☆).

the classical Ekman spiral solution (Equation 7.2):

$$\mathbf{U}_0 = \frac{\sqrt{2}\tau}{\rho_w f D_E} e^{-i\pi/4} \tag{7.2}$$

where ρ_w is the density of seawater, f is the Coriolis parameter and D_E is the depth

of frictional influence determined using the scaling of *Wimbush and Munk* [1970] where $D_E = 0.4u^*/f$ and $u^* = \sqrt{\tau/\rho_w}$ is the frictional velocity.

The globally integrated wind work in Figure 7.4d is dominated by input of energy into the Southern Ocean by the Southern Hemisphere westerlies. Values for the control run of 0.64 TW compare relatively well with the estimates of 0.88 TW derived from altimetry and NCEP winds by *Wunsch* [1998] (0.84 TW if the time varying components are neglected) and 0.76 TW derived from QuiKSCAT winds and altimetry by *Hughes and Wilson* [2008]. By including variations in forcing and the subsequent oceanic response, even in remote regions such as the North Atlantic due to changes in energy input into the western boundary currents, this representation indeed takes into account variations in ocean processes such as mesoscale eddy activity and surface heat and freshwater fluxes that lead to changes in sensitivity of atmospheric CO_2 to the same pattern of wind perturbations. There is only a small change in wind work in the three perturbations where the Southern Hemisphere winds are migrated south, which may be explained by the reduced surface area of the globe over which the wind energy is applied to the surface, reducing its contribution to the global integral, with the reverse also true for the large changes in wind work in the three experiments with northward-shifted winds. Interestingly, the experiments at low wind work are slightly more scattered than those at elevated energy input, which may be an artifact of the model vertical diffusivity being set independently of the wind energy input [e.g. *de Boer et al.*, 2008]. However the work done by the wind does convert mechanical energy into available potential energy stored in sloping isopycnals.

Indeed, an estimated ~2 TW of mechanical energy is needed to maintain the observed global ocean stratification [*Munk and Wunsch*, 1998; *Wunsch and Ferrari*, 2004], with approximately 0.6–1.2 TW of this derived from the winds [*Munk and Wunsch*, 1998] and assuming a conversion efficiency to turbulent mixing of 20%. The calculated decrease in wind work for scenarios that result in decreased atmospheric CO_2 and increased surface ocean stratification and the increase in wind energy input for scenarios with increased atmospheric CO_2 and decreased surface stratification suggest that the amount of energy imparted by the winds into the oceanic general circulation is of considerable importance in driving the ACC and Southern Ocean residual overturning circulation. Furthermore, changes to the amount of work done by the winds of the order of 50% can alter the observed oceanic stratification, nutrient supply, efficiency of the soft tissue pump and therfore drive variations in the concentration of atmospheric CO_2. If upwelling around Antarctica is forced by the extratropical Southern Hemisphere westerlies [e.g. *Toggweiler*

and Samuels, 1995, 1998] then a reduction in the rate of energy input by the winds into the ocean, by a decrease in magnitude or a southward shift, reduces the energy available to sustain a vigorous circulation and therefore results in reduced overturning and increased upper ocean stratification and in turn reduces surface nutrient supply from the Southern Ocean resulting in decreased productivity but more efficient utilisation of available resources leading to a more efficient biological pump. The combination of reduced deep upwelling and outgassing of respired CO_2, increased surface stratification and an efficient biological pump trap carbon in the ocean, while continued intermediate and mode water formation sequesters additional CO_2 from the atmosphere. An increase in oceanic energy input leads to a more vigorous ocean circulation, with reduced surface stratification, greater deep upwelling and outgassing in the Southern Ocean and more plentiful supply of nutrients that increases productivity, but a larger concentration of preformed nutrients leads to a decrease in the efficiency of the soft tissue pump combining to promote carbon transfer from the ocean to the atmosphere. A similar sequence of events has been postulated from a number of paleoceanographic indices such as changes in opal accumulation [*Anderson et al.*, 2009], $\delta^{13}C$ of intermediate waters [*Spero and Lea*, 2002] and reduction of $\delta^{14}C$ in the upper ocean and atmosphere [*Marchitto et al.*, 2007; *Skinner et al.*, 2010].

These results, while providing an interesting insight into the mechanisms that may regulate atmospheric CO_2 concentration on climatic timescales, are not supposed to accurately recreate conditions found in these altered climate states. They represent idealised perturbations, in a consistent modelling framework, that explore the interactions between physical and biogeochemical processes and forcing and include some strong assumptions regarding (1) a closed ocean–atmosphere carbon system that does not include the effects of carbonate compensation by sediment interaction and resultant changes in alkalinity, which directly affects CO_2 solubility [e.g. *Archer et al.*, 2000; *Sigman and Boyle*, 2000] that can enhance changes in atmospheric CO_2 by ~10 ppm over 15–50 kyr [*Tschumi et al.*, 2010], which is an exceptionally expensive process to capture with this class of model, (2) a simple representation of biological activity that does not consider changing nutrient utilisation ratios under different conditions, nor different phyoplankton groups that have different nutrient requirements or higher trophic levels [e.g. *Dutkiewicz et al.*, 2005a] and a parameterisation of a poorly understood iron cycle [*Parekh et al.*, 2005, 2006b] that only represents aeolian iron inputs [e.g. *Tagliabue et al.*, 2010]. Furthermore, the additional phosphate tracers make assumptions regarding surface oxygen saturation while the disquilibrium and gas exchange tracers contain assumptions about the extent to which the soft tissue and carbonate pumps can

be successfully removed from the DIC field, (3) absence of thermodynamic/interactive sea ice that has a great impact on the correct representation of AABW formation and Southern Ocean circulation as a whole [e.g. *Cai and Baines*, 1996; *Gent et al.*, 2001] and may contribute to trapping respired CO_2 in the ocean by limiting atmospheric contact and gas exchange [*Keeling and Stephens*, 2001; *Stephens and Keeling*, 2000], and (4) mesoscale eddy parameterisation, since the computational cost of performing such perturbations at fine enough resolution to resolve such features at a global scale is too great.

These assumptions have noticeable effects in the results such as acceleration and deceleration of the ACC with increased/decreased wind stress. Although there is evidence that wind stress at the latitude band of Drake Passage is positively linked to ACC transport [*Gent et al.*, 2001; *Meredith et al.*, 2004], changes in the mesoscale eddy field, which would likely become intensified with increasing wind stress, as well as the possibility of the ACC being saturated with respect to the winds would probably damp this response and may also affect other aspects such as the overturning circulation and thus alter the sensitivity of atmospheric CO_2 to this perturbation [*Gnanadesikan and Hallberg*, 2000; *Hallberg and Gnanadesikan*, 2006; *Zickfeld et al.*, 2007].

Nevertheless these idealised experiments did not seek to exactly recreate conditions in the past or predict the future state of the ocean system but to probe the mechanisms involving ocean circulation, nutrient redistribution, biological activity and air-sea exchange that might be responsible for millennial scale changes in the concentration of atmospheric CO_2. Future changes in the strength of the Southern Ocean natural CO_2 sink depend on the eventual position and strength of the Southern Hemisphere extratropical westerlies. Southward-shifted and intensified winds may lead to a net strengthening of the Southern Ocean natural CO_2 sink in the long term. However, if the winds return to a more northward location [*Perlwitz et al.*, 2008] with reduction in the size of the ozone hole and anomalous photochemical cooling over Antarctica, then a net weakening of the Southern Hemisphere CO_2 sink may be a more likely outcome. For past changes in climate, assuming that physical processes need only account for the initial change of CO_2 in to or out of an ice age [e.g. *Peacock et al.*, 2006], after which other processes that are slower in action or constrained by the timing of sea level or ice-sheet changes come into play, processes that are totally neglected in this model, then these results actually represent a significant fraction of the estimated 20–40 ppm attributed to "physical changes" [*Bopp et al.*, 2003; *Brovkin et al.*, 2007; *Fischer et al.*, 2010; *Gildor et al.*, 2002; *Köhler and Fischer*, 2006; *Peacock et al.*, 2006; *Toggweiler*,

1999], before alterations in ocean mean properties are considered. Nevertheless, the robust nature of the relationship between Southern Ocean residual overturning circulation and atmospheric CO_2, even after significant alterations to surface heat and freshwater boundary conditions and mesoscale eddy activity illustrates that the upper limb of the Southern Ocean overturning is as important in determining atmospheric CO_2 levels. The upper limb [*Marinov et al.*, 2006; *Toggweiler et al.*, 2006] should not be neglected in discussions of changes in the Earth and Ocean system.

Chapter 8

Conclusions and Future Work

8.1 Conclusions

In this thesis were presented a series of idealised perturbation experiments to the forcing and internal physics of the Southern Ocean in a primitive equation ocean general circulation model in order to examine and explain the subsequent response of global ocean circulation, biogeochemical cycles, primary productivity, air-sea exchange and atmospheric CO_2 levels in order to discover more about the response of the ocean to past, present and future changes in climate. The outcomes of this thesis are namely that:

- Perturbations to Southern Hemisphere westerly wind stress illustrate the new mechanism through which changes in the rate or spatial pattern of the Southern Ocean residual overturning circulation, driven by the work done on the ocean by the winds, result in alteration of stratification in the Southern Ocean. In glacial times there may have been less wind energy available to drive the Southern Ocean overturning circulation therefore increasing the ability of the ocean to isolate CO_2 from the atmosphere for extended periods of time.
- Alteration of the Southern Ocean residual overturning subsequently impacts the rate and depth that relatively carbon and nutrient-rich deep waters are upwelled to the surface and their residence time in the surface layer, during which atmosphere ocean interaction occurs and surface waters are imprinted with the pattern of air-sea gas exchange.

- Water masses formed in the Southern Ocean carry these climatically important signals into the ocean interior indicating the loss/gain of CO_2 to/from the atmosphere, at intermediate depths in these experiments, not abyssal depths, illustrating that the upper limb of the Southern Ocean overturning circulation is important in determining atmospheric CO_2 levels [c.f. *Marinov et al.*, 2006; *Toggweiler et al.*, 2006]. The rate of intermediate water formation and subduction affects upper ocean stratification with isopycnal heave enhancing mid depth anomalies. Lower (but non-zero) AAIW production in scenarios with reduced atmospheric CO_2 levels and intensified AAIW production in scenarios with elevated atmospheric CO_2 levels conforms with the proxy record [*Pahnke and Zahn*, 2005; *Pahnke et al.*, 2008].

- In new experiments using a primitive equation OGCM where the maximum of the Southern Hemisphere westerlies are explicitly shifted reveals that response of the Southern Ocean overturning circulation does not scale like a simple change in magnitude of the wind stress in Drake Passage [e.g. *Toggweiler et al.*, 2006]. On the contrary, with the maximum shifted north the expanded polar easterlies drive deep upwelling while the westerlies drive a vigorous upper ocean overturning, due to latitude and increased surface area, of relatively carbon and nutrient-rich intermediate waters that augment net upwelling in the Southern Ocean causing outgassing. Alternatively a southward-shift in the westerlies reduces the rate of Southern Ocean net upwelling, due to latitude and reduced surface area, while increased area of subtropical easterlies promotes convergence and downwelling in the Southern Ocean causing enhanced CO_2 uptake.

- Shifting the westerlies to the south, which stimulates biological productivity in the entire Northern Hemisphere and is reminiscent of export production estimates from the LGM [*Kohfeld et al.*, 2005] does not conform to the bimodal export patterns in which increased upwelling of macronutrients from below the surface layer in the Southern Ocean stimulates primary production in the adjacent subtropical gyres and in the Atlantic Ocean by lateral supply. However, increased depth of the pycnocline reduces nutrient supply by diapycnal mixing and therefore biological activity in the Pacific and Indian Oceans. Similarly, decreased Southern Ocean upwelling and lateral advective supply of macronutrients reduces productivity in the Atlantic Ocean but increases vertical diapycnal supply in the Pacific and Indian Oceans [e.g. *Parekh et al.*, 2006b].

- The balance between Atlantic and Indo-Pacific productivity results in globally increased production with energetic upwelling and decreased production with reduced upwelling. However, changes in ventilation of the ocean interior by intermediate depth waters carrying macronutrient anomalies leads to the opposite result with a greater concentration of preformed nutrients indicating reduced efficiency of the soft tissue pump, which promotes oceanic CO_2 outgassing while a reduced concentration of preformed nutrients increases the efficiency of the soft tissue pump, which promotes oceanic CO_2 uptake [*Ito and Follows*, 2005].

- These perturbation experiments emphasise that the quantity of CO_2 transferred between oceanic and atmospheric reservoirs during gas exchange is further modulated by the air-sea CO_2 equilibration time compared to the residence time of waters in the surface ocean. Vigorous Southern Ocean residual overturning circulation generally results in an increase in air-sea disequilibrium and prevents the total escape of CO_2 from the ocean to the atmosphere while sluggish overturning circulation increases the extent of atmosphere-ocean equilibrium resulting in the release of previously trapped CO_2. Therefore the change in atmospheric CO_2 levels are lower than would be expected using instantaneous or spatially constant gas exchange rates.

- These experiments do not capture the effect of changing Antarctic Bottom Water formation and circulation and therefore demonstrates that the upper limb of the Southern Ocean overturning circulation is important in determining atmospheric CO_2 levels [c.f. *Marinov et al.*, 2006; *Toggweiler et al.*, 2006]. This is due to surface salinity relaxation that prevent accumulation of salt or freshwater in the Southern Ocean in response to variations in northward Ekman transport that was revealed implementing mixed, or thermohaline surface boundary conditions. However the net result of the Southern Ocean overturning circulation, even using fixed surface heat and freshwater fluxes, was negligible.

- Changes to mesoscale eddy activity, parameterised due to the model's coarse resolution had a slightly larger effect on the Southern Ocean residual overturning circulation, compared to the wind stress magnitude perturbations where the isopycnal mixing coefficient remained at the control value, through greater compensation of the Eulerian-mean wind-driven overturning and through isopycnal ventilation rates that affected both nutrient utilisation and the efficiency of the soft tissue pump, and the extent of atmosphere-ocean CO_2 equilibrium.

- Rates of gas exchange due to alterations in the magnitude of Southern Hemisphere westerly wind speed also had a minor effect on atmospheric CO_2 concentrations and the signal carried into the ocean at intermediate depths, that has not been explicitly demonstrated before, although reducing the rate of the air-sea CO_2 flux did somewhat prevent Southern Ocean CO_2 uptake from the atmosphere.

Although these idealised experiments did not seek to exactly recreate conditions in the past or predict the future state of the ocean system it is possible to make inferences about how the results of this thesis relate to changes in the concentration of atmospheric CO_2. For projected future climates, these findings suggest that future atmospheric pCO_2 may stabilise at a higher level than predicted by carbon chemistry alone under intensified Southern Ocean winds, due to the increased outgassing of natural carbon [*Le Quéré et al.*, 2007; *Lenton and Matear*, 2007; *Lovenduski et al.*, 2007, 2008; *Wetzel et al.*, 2005] even with the associated increase in biological productivity that consequent upwelling of nutrients stimulates [*Lovenduski and Gruber*, 2005; *Menviel et al.*, 2008]. However, if these winds are shifted south [e.g. *Gillet and Thompson*, 2003] then a slight net strengthening of the Southern Ocean natural CO_2 sink may occur in the long term, but as the stratospheric ozone hole repairs, if the tropospheric Southern Hemisphere westerlies migrates to a more northern position [*Perlwitz et al.*, 2008] then a net weakening of the Southern Hemisphere CO_2 sink may be a more likely outcome. The small changes in atmospheric CO_2 achieved with significant additional aeolian iron fluxes question iron fertilisation as a method of geoengineering to mitigate future effects of anthropogenic carbon emissions with considerable local remineralisation in the upper ocean and CO_2 return to the atmosphere on short timescales. Increased new production results in "nutrient robbing" from regions downstream in the nutrient supply chain, leading to non-local reduction in biological activity in micronutrient-replete but macronutrient-limited regions such as the Atlantic Ocean and highlights the need to consider the global effects of such a strategy [e.g. *Gnanadesikan and Marinov*, 2008]. Furthermore a reduction of aeolian iron input with a warmer, moister climate under doubling atmospheric CO_2 represents a positive feedback on climate [*Parekh et al.*, 2006a] that is not necessarily considered when discussing the geoengineering potential of iron fertilisation [e.g. *Royal Society*, 2009].

For past changes in climate, these idealised simulations may account for a significant fraction of the change in glacial-interglacial CO_2, considering that they neglect other important processes that are reasonably well understood such as change in mean ocean temperature, salinity and collapse of the terrestrial biosphere [e.g. *Archer et al.*, 2000;

Sigman and Boyle, 2000]. Indeed, if changes in ocean circulation need only account for the initial change of CO_2 in to or out of an ice age [e.g. *Peacock et al.*, 2006] before other processes that are slower in action or constrained by the timing of sea level or ice-sheet changes come into play, then these results, that are robust to significant alterations to surface heat and freshwater boundary conditions and mesoscale eddy activity, actually represent a significant proportion of the change in CO_2 generated by altered ocean circulation[*Bopp et al.*, 2003; *Brovkin et al.*, 2007; *Fischer et al.*, 2010; *Gildor et al.*, 2002; *Köhler and Fischer*, 2006; *Peacock et al.*, 2006; *Toggweiler*, 1999] and shows that the upper limb of the Southern Ocean overturning circulation is important in determining atmospheric CO_2 levels [c.f. *Marinov et al.*, 2006; *Toggweiler et al.*, 2006].

8.2 Future Work

To this point, zonal wind stress has been used in a quasimechanistic sense as a tuning dial for the Southern Ocean residual overturning circulation without a significant impact on the formation and circulation of abyssal water masses. The fixed surface buoyancy forcing configuration could be employed to investigate the effects of changing buoyancy fluxes on the upper and lower limbs of the Southern Ocean overturning simultaneously by simulating the effects of increased sea-ice formation and brine rejection adjacent to Antarctica and export of freshwater to the north, representing an increase of the buoyancy gradient, or even a reversal. Of course an interactive, prognostic sea ice model could be used, however this adds a further level of complexity and additional computational expense that would not necessarily be needed for such an idealised series of experiments. An interesting set of diagnostics that could be added to these and other experiments would be to explicitly carry paleoceanographic tracers such as $\Delta^{14}C$ and $\delta^{13}C$ to allow direct comparison of model simulations with the proxy record.

A more sophisticated, rigorous and exhaustive assessment of the connections and sensitivities between the carbon cycle and Southern Ocean physical processes could be pursued by using MITgcm's adjoint code [e.g. *Dutkiewicz et al.*, 2006], novel modelling technology not yet applied to this problem. An objective cost function is evaluated during a forward model run with a subsequent reverse integration of the adjoint model that returns the gradient/sensitivity of the cost function with respect to a set of control variables at each grid point. This exercise is the equivalent to conducting tens of thousands of continuous perturbation experiments at each grid point and evaluating the

global response, yet increasing the computational cost by only a factor of $\mathbf{O}(5)$ relative to a single perturbation experiment.

A notable sensitivity of these results was found when mesoscale eddy activity was perturbed in concert with the magnitude of the Southern Ocean wind stress as suggested by [*Fyfe et al.*, 2007; *Zickfeld et al.*, 2007] guided by eddy resolving modelling results [*Hallberg and Gnanadesikan*, 2006]. But how would the eddy-induced circulation change, for example, in the buoyancy experiments suggested above? How much should κ_{GM} be altered? The GM90 scheme assumes that the transfer constant, κ_{GM}, is constant in time and space but several proposals have been made for a more flexible parameterisation of global mesoscale eddy fluxes. Inspired by linear baroclinic instability analysis of the atmosphere, *Visbeck et al.* [1997] described the coefficient as a function of the eady growth rate, which is related to the slope of isopycnals and the stratification averaged over the water column, allowing κ_{GM} to vary in space and time in a manner dependent on the large-scale density field [*Visbeck et al.*, 1997]. Such a scheme for online evaluation of κ_{GM} as a function of time and space and in response to oceanic perturbations, already implimented in the MITgcm code, is a relatively simple and computationally efficient way of plausibly representing not only the change in eddy-induced circulation with respect to wind stress-induced changes to the density field in a possible eddy-saturated regime, but any external or internal forcing. Of course, [*Hallberg and Gnanadesikan*, 2006] demonstrate in their hierarchy of models with increasingly fine resolutions that the best way to capture eddy dynamics is to resolve them. At $1/6°$, there is a considerably weaker response of the deep water to intermediate water overturning cell in the Southern Ocean for increased wind stress, however [*Hallberg and Gnanadesikan*, 2006]'s weak wind stress experiment shows a more consistent response between resolutions because the resolved eddies are weaker and less able to compensate the Eulerian-mean circulation *Hallberg and Gnanadesikan* [2001, 2006] and it is speculated that the "real" ocean might exhibit even greater asymmetry. Thus the results for weaker wind stress cases may be more reliable than those for stronger wind stress cases. It might still be difficult to apply a fine, eddy resolving ocean model to climate scale problems since many eddy-interaction studies employ simplified basin geometry such as channel models [*Hallberg and Gnanadesikan*, 2001] or have "sponges" at low latitudes to avoid the cost of a global integration. These results place emphasis on resolving the entire global ocean, although it would be interesting to explore the prospect of a fine-resolution Southern Ocean model nested within a coarser resolution global model. An emerging area of research regards processes in the "submesoscales" that require resolutions of the order of 1 km to capture, and play an important role in mixing properties in the upper ocean, significantly

enhancing vertical nutrient supply, exchange of dissolved gasses with the atmosphere and restratification of the surface layer [*Thomas et al.*, 2008]. The importance of such processes in conjunction with their larger-scale cousins could radically alter our view of the Southern Ocean's role in the global carbon cycle and atmospheric CO_2 change.

Considering the experiments in Part II and references within this thesis supports the notion that the search for the "Holy Grail" of a single elegant mechanism that describes the entire change in glacial-interglacial climate and associated paleoceanographic record is unlikely, but precluding the use of an Earth system model of extreme complexity in which mechanisms for milennial scale climate cannot be disentangled, by undertaking process related studies and idealised perturbation experiments it will be possible to increasingly understand facets of the proxy data or consequences of mechanisms inferred from elsewhere in order to explain past, present and future changes in the Earth and Ocean system.

Bibliography

Adcroft, A., C. Hill, and J. Marshall, Representation of topography by shaved cells in a height coordinate ocean model, *Monthly Weather Review*, pp. 2293–2315, 1997.

Adcroft, A., J.-M. Campin, S. Dutkiewicz, C. Evangelinos, D. Ferreira, G. Forget, B. Fox-Kemper, P. Heimbach, C. Hill, E. Hill, H. Hill, O. Jahn, M. Losch, J. Marshall, G. Maze, D. Menemenlis, and A. Molod, *MITgcm User Manual*, Massachusetts Institute of Technology Department of Earth, Atmosphere and Planetary Science, 77 Massachusetts Ave, Cambridge, MA, USA, 2009.

Adkins, J., K. McIntyre, and D. Schrag, The salinity, temperature and delta O–18 of the glacial deep ocean, *Science*, *298*, 1769–1773, 2002.

Allison, L., Spin-up and adjustment of the Antarctic Circumpolar Current and the global pycnocline, Ph.D. thesis, Department of Meteorology, University of Reading, 2009.

Allison, L., H. Johnson, D. Marshall, and D. Munday, Where do winds drive the Antarctic Circumpolar Current?, *Geophysical Research Letters*, *37*, L12,605, doi:10.1029/2010GL043355, 2010.

Altabet, M., M. Higginson, and D. Murray, The effect of millenial-scale changes in Arabian Sea denitrification on atmospheric CO_2, *Nature*, *415*, 159–162, 2002.

Anderson, L., and J. L. Sarmiento, Redfield rations of remineralization determined by nutrient data analysis, *Global Biogeochemical Cycles*, *8*, 65–80, 1994.

Anderson, R., and M. Carr, Uncorking the Southern Ocean's vintage CO_2, *Science*, *328*, 1117–1118, 2010.

Anderson, R., S. Ali, L. Bradtmiller, S. Nielsen, M. Fleisher, B. Anderson, and L. Burckle, Wind-driven upwelling in the Southern Ocean and the deglacial rise in atmospheric CO_2, *Science*, *323*, 1443–1448, doi:10.1126/science.1167441, 2009.

Arakawa, A., and V. Lamb, Computational design of the basic dynamical processes of the UCLA general circulation model., in *Methods in Computational Physics*, vol. 17, pp. 174–267, Academic Press, 1977.

Archer, D., A. Winguth, D. Lea, and N. Mahowald, What caused the glacial/interglacial atmospheric pCO_2 cycles?, *Reviews of Geophysics*, *38*, 159–189, 2000.

Bindoff, N., and J. Church, Warming of the water column in the south-west Pacific, *Nature*, *357*, 1992.

Bindoff, N., and T. McDougall, Diagnosing climate change and ocean ventilation using hydrographic data, *Journal of Physical Oceanography*, *24*, 1137–1152, 1994.

Bindoff, N., J. Willebrand, V. Artale, A. Cazenave, J. Gregory, S. Gulev, K. Hanawa, C. Le Quéré, S. Levitus, Y. Nojiri, C. Shum, L. Talley, and A. Unnikrishnan, Observations: oceanic climate change and sea level, in *Climate Change 2007: The Physical Science Basis. Contribution of Working Group I to the Climate Change 2007: The Physical Science Basis. Contribution of Working Group I to the Fourth Assessment Report of the Intergovernmental Panel on Climate Change*, edited by S. Solomon, D. Qin, M. Manning, Z. Chen, M. Marquis, K. Averyt, M. Tignor, and H. Miller, chap. 5, pp. 386–432, Cambridge University Press, Cambridge, United Kingdom and New York, NY, USA., 2007.

Böning, C., A. Dispert, M. Visbeck, S. Rintoul, and F. Schwartzkopf, The response of the Antarctic Circmpolar Current to recent climate change, *Nature Geoscience*, *1*, 864–869, doi:10.1038/ngeo362, 2008.

Bopp, L., K. Kohfeld, and C. Le Quéré, Dust impact on marine biota and atmospheric CO_2 during glacial periods, *Paleoceanography*, *18*, doi:10.1029/2002PA000810, 2003.

Borowski, D., R. Gerdes, and D. Olbers, Thermohaline and wind forcing of a circumpolar channel with blocked geostrophic contours, *Journal of Physical Oceanography*, *32*, 2520–2540, 2002.

Boyd, P. W., A. J. Watson, C. S. Law, E. R. Abraham, T. Trull, R. Murdoch, D. C. E. Bakker, A. R. Bowie, K. O. Buesseler, H. Chang, M. Charette, P. Croot, K. Downing, R. Frew, M. Gall, M. Hadfield, J. Hall, M. Harvey, G. Jameson, J. LaRoche, M. Liddicoat, R. Ling, M. T. Maldonado, R. M. McKay, S. Nodder, S. Pickmere, R. Pridmore, S. Rintoul, K. Safi, P. Sutton, R. Strzepek, K. Tanneberger, S. Turner, A. Waite, and J. Zeldis, A mesoscale phytoplankton bloom in the polar southern ocean stimulated by iron fertilization, *Nature*, *407*, 695–702, 2000.

Boyer, T., C. Stephens, J. Antonov, M. Conkright, R. Locarnini, T. O'Brien, and H. Garcia, World ocean atlas 2001, volume 2: Salinity, in *NOAA Atlas NESDIS 50*, edited by S. Levitus, p. 165, U.S. Government Printing Office, Washington, D.C., 2002.

Broecker, W., NO: A conservative water-mass tracer, *Earth and Planetary Science Letters*, *23*, 100–107, 1974.

Broecker, W., Glacial to interglacial changes in ocean chemistry, *Progress in Oceanography*, *11*, 151–197, 1982.

Broecker, W., and E. Clark, Search for a glacial-age ^{14}c-depleted ocean reservoir, *Geophysical Research Letters*, *37*, doi:10.1029/2010GL043969, 2010.

Broecker, W., and G. Henderson, The sequece of events surrounding Termination II and their implications for the cause of glacial-interglacial CO_2 changes, *Paleoceanography*, *13*, 352–364, 1998.

Brovkin, V., A. Ganapolski, D. Archer, and S. Rahmstorf, Lowering of glacial atmospheric CO_2 in response to changes in oceanic circulation and marin biogeochemistry, *Paleoceanography*, *22*, PA4202, doi:10.1029/2006PA001380, 2007.

Bryden, H., and S. A. Cunningham, How wind forcing and air-sea heat exchange determine the meridional temperature gradient and stratification for the Antarctic Circumpolar Current, *Journal of Geophysical Research*, *108*, 10.1029/2001JC001296, 2003.

Brzezinski, M. A., C. J. Pride, V. M. Franck, D. Sigman, J. L. Sarmiento, K. Matsumoto, N. Gruber, G. H. Rau, and K. H. Coale, A switch from $Si(OH)_4$ to NO_3^- depletion in the glacial Southern Ocean, *Geophysical Research Letters*, *29*, doi:10.1029/2001GL014349, 2002.

Cai, W., and P. Baines, Interactions between thermohaline- and wind-driven circulations and their relevance to the dynamics of the Antarctic Circumpolar Current, in a coarse-resolution global ocean general circulation model, *Journal of Geophysical Research*, *101*, 14,073–14,093, 1996.

Caillon, N., J. Severinghaus, J. Jouzel, J.-M. Barnola, J. Kang, and V. Lipenkov, Timing of atmospheric CO_2 and Antarctic temperature changes across Termination III, *Science*, *299*, 1728–1731, 2003.

Caldeira, K., and P. Duffy, The role of the Southern Ocean in uptake and storage of anthropogenic carbon dioxide, *Science*, *287*, 620–622, 2000.

Campin, J.-M., A. Adcroft, C. Hill, and J. Marshall, Conservation of properties in a free-surface model, *Ocean Modelling*, *6*, 221—244, 2004.

Church, J., J. Godfrey, D. Jackett, and T. McDougall, A model of sea level rise caused by ocean thermal expansion, *Journal of Climate*, *4*, 438–456, 1991.

Conkright, M. E., H. E. Garcia, T. D. O'Brien, R. Locarnini, T. P. Boyer, C. Stephens, and J. I. Antonov, World ocean atlas 2001, volume 4: Nutrients, in *NOAA Atlas NESDIS 52*, edited by S. Levis, p. 392, U.S. Government Printing Office, Washington, D.C., 2002.

Cox, M. D., An idealised model of the world ocean. part 1: The global-scale water masses, *Journal of Physical Oceanography*, *19*, 1730–1752, 1989.

Crosta, X., J. Pichon, and L. Burckle, Reappraisal of Antarctic seasonal sea-ice at the Last Glacial Maximum, *Geophysical Research Letters*, *25*, 2703–2706, 1998.

Cunningham, S. A., S. G. Alderson, B. A. King, and M. A. Brandon, Transport and variability of the Antarctic Circumpolar Current in Drake Passage, *Journal of Geophysical Research*, *108*, doi:10.1029/2001JC001147, 2003.

Curry, W., J. Duplessy, L. Labeyrie, and N. Shackleton, Changes in the distribution of δ^{13}C of deepwater ΣCO_2 between the last glaciation and the Holocene, *Paleoceanography*, *3*, 317–341, doi:10.1029/PA003i003p00317, 1988.

Danabasoglu, G., and J. McWilliams, Sensitivity of the global ocean circulation to parameterisations of mesoscale tracer transports, *Journal of Climate*, *8*, 2967–2987, 1995.

de Baar, H., P. Boyd, K. Coale, M. Landry, A. Tsuda, P. Assmy, D. Bakker, Y. Bozec, R. Barber, M. Brzezinski, K. Buesseler, M. Boyé, P. Croot, F. Gervais, M. Gorbunov, P. Harrison, W. Hiscock, P. Laan, C. Lancelot, C. Law, M. Levasseur, A. Marchetti, F. Millero, J. Nishioka, Y. Nojiri, T. van Oijen, U. Riebesell, M. Rijkenberg, H. Saito, S. Takeda, K. Timmermans, M. Veldhuis, A. Waite, and C.-S. Wong, Synthesis of iron fertilization experiments: From the iron age in the age of enlightenment, *Journal of Geophysical Research*, *110*, doi:10.1029/2004JC002601, 2005.

de Boer, A., J. R. Toggweiler, and D. Sigman, Atlantic dominance of the meridional overturning circulation, *Journal of Physical Oceanography*, *38*, 435–450, doi:10.1175/2007JPO3731.1, 2008.

de Boer, A., A. J. Watson, N. Edwards, and K. Oliver, A comprehensive, multi-process box-model approach to glacial-interglacial carbon cycling, *Climates of the Past Discussions*, *6*, 867–903, doi:10.5194/cpd-6-867-2010, 2010.

De Pol-Holz, R., L. Keigwin, J. Southon, D. Hebbeln, and M. Mohtadi, No signature of abyssal carbon in Antarctic Intermediate Water off Chile during deglaciation, *Nature Geoscience*, *3*, 192–195, doi:10.1038/NGEO745, 2010.

Devol, A., Getting cool with nitrogen, *Nature*, *415*, 131–132, 2002.

Dong, B., and P. Valdes, Simulations of the Last Glacial Maximum climates using a general circulation model: prescribed versus computed sea surface temperatures, *Climate Dynamics*, *14*, 571–591, 1998.

Döös, K., and D. Webb, The Deacon cell and other meridional cells in the Southern Ocean, *Journal of Physical Oceanography*, *24*, 429–442, 1994.

Duplessy, J., N. Shackleton, R. Fairbanks, L. Labeyrie, D. Oppo, and N. Kallel, Deepwater source variations during the last climatic cycle and their impact on the global deepwater circulation, *Paleoceanography*, *3*, doi:10.1029/PA003i003p00343, 1988.

Dutkiewicz, S., M. Follows, and P. Parekh, Interactions of the iron and phosphorus cycles: A three dimensional model study, *Global Biogeochemical Cycles*, *19*, doi:10.1029/2004GB002342, 2005a.

Dutkiewicz, S., A. Sokolov, J. Scott, and P. Stone, A three-dimensional ocean-seaice-carbon cycle model and its coupling to a two-dimensional atmospheric model: Uses in climate change studies., *Tech. Rep. Report 122*, Joint Program of the Science and Policy of Global Change, M.I.T., Cambridge, MA., 2005b.

Dutkiewicz, S., M. Follows, P. Heimbach, and J. Marshall, Controls on ocean productvity and air–sea carbon flux: An adjoint model sensitivity study, *Geophysical Research Letters*, *33*, doi:10.1029/2005GL024987, 2006.

Egbert, G., R. Ray, and B. Bills, Numerical modelling of the global semidiurnal tide in the present day and the last glacial maximum, *Journal of Geophysical Research*, *109*, doi:10.1029/2003JC001973, 2004.

Elderfield, H., and R. Rickaby, Oceanic Cd/P ratio and nutrient utilisation in the glacial Southern Ocean, *Nature*, *405*, 305–310, 2000.

Falkowski, P., Evolution of the Nitrogen Cycle and its influence on the biological sequestration of CO_2 in the ocean, *Nature*, *387*, 1997.

Farneti, R., T. R. Delworth, A. J. Rosati, S. Griffies, and F. Zeng, The role of mesoscale eddies in the rectification of the Southern Ocean respose to climate change, *Journal of Physical Oceanography*, *in press*, doi: 10.1175/2010JPO4353.1, 2010.

Fischer, H., M. Wahlen, J. Smith, D. Mastroianni, and B. Deck, Ice core records of atmospheric CO_2 around the last three glacial terminations, *Science*, *283*, 1712–1714, doi:10.1126/science.283.5408.1712, 1999.

Fischer, H., J. Schmitt, D. Lüthi, T. F. Stocker, T. Tschumi, P. Parekh, F. Joos, P. Köhler, C. Völker, R. Gersonde, C. Barbante, M. L. Floch, D. Raynaud, and E. Wolff, The role of southern ocean processes in orbital and millennial co2 variations - a synthesis, *Quaternary Science Reviews*, *29*, 193–205, doi:10.1016/j.quascirev.2009.06.007, 2010.

Follows, M., T. Ito, and S. Dutkiewicz, On the solution of the carbonate chemistry system in ocean biogeochemistry models, *Ocean Modelling*, *12*, 290–301, 2006.

François, R., M. Altabet, E.-F. Yu, D. Sigman, M. Bacon, M. Frank, G. Bohrmann, G. Bareille, and L. Labeyrie, Contribution of Southern Ocean surface-water stratification to low atmospheric CO_2 concentrations during the last glacial period, *Nature*, *389*, 929–935, 1997.

Fučkar, N., and G. Vallis, Interhemispheric influece of surface buoyancy conditions on a circumpolar current, *Geophysical Research Letters*, *34*, L14,605, doi:10.1029/2007GL030379, 2007.

Fyfe, J., and O. Saenko, Human-induced changes in the Antarctic Circumpolar Current, *Journal of Climate*, *18*, 3068–3073, 2005.

Fyfe, J., and O. Saenko, Simulated changes in the extratropical southern hemisphere winds and currents, *Geophysical Research Letters*, *33*, doi:10.1029/2005GL025332, 2006.

Fyfe, J., O. Saenko, K. Zickfeld, M. Eby, and A. Weaver, The role of poleward-intensifying winds on Southern Ocean warming, *Journal of Climate*, *20*, 5391–5400, doi:10.1175/2007JCLI1764.1, 2007.

Ganachaud, A., and C. Wunsch, Improved estimates of global ocean circulation, heat transport and mixing from hydrographic data, *Nature*, *408*, 453–457, 2000.

Ganeshram, R., Oceanic action at a distance, *Nature*, *419*, 123–124, 2002.

Ganeshram, R., T. Pederson, S. Calvert, G. McNeill, and M. Fontugne, Glacial-interglacial variability in denitrification in the world's oceans: causes and consequences, *Paleoceanography*, *15*, 361–376, 2000.

Ganeshram, R., T. Pederson, S. Calvert, and R. François, Reduced N_2-fixation in the glacial ocean inferred from changes in marine nitrogen and phosphorus inventories, *Nature*, *415*, 156–159, 2002.

Geider, R., and J. La Roche, Redfield revisited: variability of the C:N:P in marine microalgae and its biochemical basis, *European Jouurnal of Phycology*, *37*, 1–17, 2002.

Gent, P., and J. McWilliams, Isopycnal mixing in ocean circulation models, *Journal of Physical Oceanography*, *20*, 150–155, 1990.

Gent, P., W. Large, and F. Bryan, What sets the mean transport through Drake Passage?, *Journal of Geophysical Research*, *106*, 2693–2712, 2001.

Gerdes, R., C. Köberle, and J. Willebrand, The influence of numerical advection schemes on the results of ocean general circulation models, *Climate Dynamics*, *5*, 211–226, 1991.

Gildor, H., and E. Tziperman, Physical mechanisms behind biogeochemical glacial-interglacial CO_2 variations, *Geophysical Research Letters*, *12*, 2421–2424, doi:10.1029/2000GL012571, 2001.

Gildor, H., E. Tziperman, and J. R. Toggweiler, Sea ice switch mechanism and glacial-interglacial CO_2 variations, *Global Biogeochemical Cycles*, *16*, 1032, doi:10.1029/2001GB001446, 2002.

Gill, A. E., and K. Bryan, Effects of geometry on the circulation of a three-dimensional southern-hemisphere ocean model, *Deep-Sea Research*, *18*, 685–721, 1971.

Gille, S., Warming of the Southern Ocean sind the 1950s, *Science*, *295*, 1275–1277, 2002.

Gillet, N., and D. Thompson, Simulation of recent Southern Hemisphere climate change, *Science*, *302*, 273–275, doi:10.1126/science.1087440, 2003.

Gloor, M., N. Gruber, J. L. Sarmiento, C. L. Sabine, R. A. Feely, and C. Rödenbeck, A first estimate of present and preindustrial air-sea CO_2 fluxes based on ocean interior carbon measurements and models, *Geophysical Research Letters*, *30*, doi:10.1029/2002GL015594, 2003.

Gnanadesikan, A., A simple predictive model for the structure of the oceanic pycnocline, *Science*, *283*, 2077–2079, doi:10.1126/science.283.5410.2077, 1999.

Gnanadesikan, A., and R. Hallberg, On the relationship of the circumpolar current to southern hemisphere winds in coarse-resolution ocean models, *Journal of Physical Oceanography*, *30*, 2013–2034, 2000.

Gnanadesikan, A., and I. Marinov, Export is not enough: nutrient cycling and carbon sequestration, *Marine Ecology Progress Series*, *364*, 289–294, doi:10.3354/meps07550, 2008.

Goodwin, P., R. Williams, A. J. Ridgwell, and M. Follows, Climate sensitivity to the carbon cycle modulated by past and future changes in ocean chemistry, *Nature Geoscience*, *2*, 145–150, doi:10.1038ngeo416, 2009.

Govin, A., E. Michel, L. Labeyrie, C. Waelbroeck, F. Dewilde, and E. Jansen, Evidence for northward expansion of Antarctic Bottom Water in the Southern Ocean during the Last Glacial Maximum, *Paleoceanography*, *24*, PA1202, doi:10.1029/2008PA001603, 2009.

Gregg, M., Diapycnal mixing in the thermocline: a review, *Journal of Geophysical Research*, *92*, 5249–5286, 1987.

Griffies, S., A. Gnanadesikan, R. Pacanowski, V. Larichev, J. Dukowicz, and R. Smith, Isoneutral diffusion in a z-coordinate ocean model, *Journal of Physical Oceanography*, *28*, 805–830, 1998.

Gruber, N., and J. L. Sarmiento, Biogeochemical/physical interactions in elemental cycles, in *The Sea: Biological-Physical interactions in the oceans*, edited by A. Robinson, J. McCarthy, and B. Rothschild, vol. 12, pp. 337–399, John Wiley, Hoboken, N.J., 2002.

Gruber, N., J. L. Sarmiento, and T. F. Stocker, An improved method for detecting anthropogenic CO_2 in the oceans, *Global Biogeochemical Cycles*, *10*, 809–837, 1996.

Gruber, N., M. Gloor, S. Mikaloff Fletcher, S. Doney, S. Dutkiewicz, M. Follows, M. Gerber, A. Jacobson, F. Joos, K. Lindsay, D. Menemenlis, A. Mouchet, S. Müller, J. L. Sarmiento, and T. Takahashi, Oceanic sources, sinks and transport of atmospheric CO_2, *Global Biogeochemical Cycles*, *23*, doi:10.1029/2008GB003349, 2009.

Hallberg, R., and A. Gnanadesikan, An exploration of the role of transient eddies in determining the transport of a zonally reentrant current, *Journal of Physical Oceanography*, *31*, 3312–3330, 2001.

Hallberg, R., and A. Gnanadesikan, The role of eddies in determining the structure and response of the wind-driven southern hemisphere overturning: Results from the modeling eddies in the Southern Ocean (MESO) project, *Journal of Physical Oceanography*, *36*, 2232–2252, 2006.

Haney, R., Surface thermal boundary conditions for ocean circulation models, *Journal of Physical Oceanography*, *1*, 241–248, 1971.

Hegerl, G., F. W. Zwiers, P. Braconnot, N. Gillett, Y. Luo, J. M. Orsini, N. Nicholls, J. Penner, and P. Stott, Understanding and attributing climate change, in *Climate Change 2007: The Physical Science Basis. Contribution of Working Group I to the Climate Change 2007: The Physical Science Basis. Contribution of Working Group I to the Fourth Assessment Report of the Intergovernmental Panel on Climate Change*, edited by S. Solomon, D. Qin, M. Manning, Z. Chen, M. Marquis, K. Averyt, M. Tignor, and H. Miller, chap. 9, pp. 664–745, Cambridge University Press, Cambridge, United Kingdom and New York, NY, USA., 2007.

Heinze, C., Assessing the importance of the Southern Ocean for natural atmospheric pCO_2 variations with a global biogeochemical general circulation model, *Deep-Sea Research, Part II*, *49*, 3105–3125, 2002.

Heywood, K., A. C. Naveira Garabato, and D. Stevens, High mixing rates in the abyssal Southern Ocean, *Nature*, *415*, 1011–1014, 2002.

Hogg, A., and J. Blundell, Interdecadal variability of the Southern Ocean, *Journal of Physical Oceanography*, *36*, 1626–1645, 2006.

Hogg, A., M. Meredith, J. Blundell, and C. Wilson, Eddy heat flux in the Southern Ocean: response to variable wind forcing, *Journal of Climate*, *21*, 608–620, 2008.

Hughes, C., and C. Wilson, Wind work on the geostrophic circulation: an observational study of the effect of small scales in the wind stress, *Journal of Geophysical Research*, *113*, C02,016, doi:10.1029/2007JC004371, 2008.

Imbrie, J., E. A. Boyle, S. C. Clemens, A. Duffy, W. R. Howard, G. Kukla, J. Kutzbach, D. G. Martinson, A. McIntyre, A. C. Mix, B. Molfino, J. J. Morley, L. C. Peterson, N. G. Pisias, W. L. Prell, M. E. Raymo, N. J. Shackleton, and J. R. Toggweiler, On the structure and origin of major glaciation cycles 1. linear responses to Milankovitch forcing, *Paleoceanography*, *7*, 701–738, 1992.

Ito, T., and M. Follows, Upper ocean control on the solubility pump of CO_2, *Journal of Marine Research*, *61*, 465–489, 2003.

Ito, T., and M. Follows, Preformed phosphate, soft tissue pump and atmospheric CO_2, *Journal of Marine Research*, *63*, 813–839, 2005.

Ito, T., M. Follows, and E. Boyle, Is AOU a good measure of respiration in the oceans?, *Geophysical Research Letters*, *31*, doi:10.1029/2004GL020900, 2004a.

Ito, T., J. Marshall, and M. Follows, What controls the uptake of transient tracers in the Southern Ocean?, *Global Biogeochemical Cycles*, *18*, doi:10.1029/2003GB002103, 2004b.

Ito, T., P. Parekh, S. Dutkiewicz, and M. Follows, The Antarctic circumpolar productivity belt, *Geophysical Research Letters*, *32*, doi:10.11029/2005GL023021, 2005.

Jansen, E., J. Overpeck, K. Briffa, J.-C. Duplessy, F. Joos, V. Masson-Delmotte, D. Olago, B. Otto-Bliesner, W. Peltier, S. Rahmstorf, R. Ramesh, D. Raynaud, D. Rind, O. Solomina, R. Villalba, and D. Zhang, Palaeoclimate, in *Climate Change 2007: The Physical Science Basis. Contribution of Working Group I to the Climate Change 2007: The Physical Science Basis. Contribution of Working Group I to the Fourth Assessment Report of the Intergovernmental Panel on Climate Change*, edited by S. Solomon, D. Qin, M. Manning, Z. Chen, M. Marquis, K. Averyt, M. Tignor, and H. Miller, chap. 6, pp. 434–497, Cambridge University Press, Cambridge, United Kingdom and New York, NY, USA., 2007.

Jiang, S., P. Stone, and P. Malanotte-Rizzoli, An assessment of the Geophysical Fluid Dynamics Laboratory ocean model with coarse resolution: Annual-mean climatology, *Journal of Geophysical Research*, *104*, 25,623–25,645, 1999.

Johnson, G., and H. Bryden, On the size of the Antarctic Circumpolar Current, *Deep-Sea Research*, *36*, 39–53, 1989.

Karsten, R., and J. Marshall, Constructing the residual circulation of the ACC from observations, *Journal of Physical Oceanography*, pp. 3315–3327, 2002.

Keeling, R., and B. Stephens, Antarctic sea ice and the control of Pleistocene climate instability, *Paleoceanography*, *16*, 112–131, 2001.

Keeling, R., and M. Visbeck, Antarctic stratification and glacial pCO_2, *Nature*, *412*, 605–606, 2001.

Key, R. M., A. Kozyr, C. L. Sabine, K. Lee, R. Wanninkhof, J. L. Bullister, R. A. Feely, F. J. Millero, C. Mordy, and T. H. Peng, A global ocean carbon climatology: Results from the global data analysis project GLODAP, *Global Biogeochemical Cycles*, *18*, doi:10.1029/2004GB002247, 2004.

Kim, S.-J., G. Flato, and G. Boer, A coupled climate model simulation of the Last Glacial Maximum, part 2: approach to equilibrum, *Climate Dynamics*, *20*, 635–661, doi:10.1007/s00382-002-0292-2, 2003.

Kitoh, A., S. Murakami, and H. Koide, A simulation of the Last Glacial Maximum with a coupled atmosphere-ocean GCM, *Geophysical Research Letters*, *28*, 2221–2224, doi:10.1029/2000GL012271, 2001.

Knox, F., and M. B. McElroy, Changes in atmospheric CO_2: Influence of the marine biota at high latitude, *Journal of Geophysical Research*, *89*, 4629–4637, 1984.

Kohfeld, K., C. Le Quéré, S. Harrison, and R. Anderson, Role of marine biology in glacial-interglacial CO_2 cycles, *Science*, *308*, 74–78, 2005.

Köhler, P., and H. Fischer, Simulating low frequency changes in atmospheric CO_2 during the last 740,000 years, *Climates of the Past*, *2*, 57–78, 2006.

Krupitsky, A., and M. Cane, On topographic pressure drag in a zonal channel, *Journal of Marine Research*, *52*, 1–23, 1994.

Kuhlbrodt, T., G. Griesel, M. Montoya, A. Levermann, M. Hofmann, and S. Rahmstorf, On the driving processes of the Atlantic meridional overturning circulation, *Reviews of Geophysics*, *45*, doi:10.1029/2004RG000166, 2007.

Law, R., R. Matear, and R. Francey, Comment on "saturation of the Southern Ocean CO_2 sink due to recent climate change", *Science*, *319*, 570a, doi:10.1126/science.1149077, 2008.

Le Quéré, C., C. Rödenbeck, E. Buitenhuis, T. Conway, R. Langenfelds, A. Gomez, C. Labuschagne, M. Ramonet, T. Nakazawa, N. Metzl, N. Gillet, and M. Heimann, Saturation of the Southern Ocean CO_2 sink due to recent climate change, *Science*, *316*, 1735–1738, 2007.

Le Quéré, C., C. Rödenbeck, E. Buitenhuis, T. Conway, R. Langenfelds, A. Gomez, C. Labuschagne, M. Ramonet, T. Nakazawa, N. Metzl, N. Gillet, and M. Heimann, Response to comments on "saturation of the Southern Ocean CO_2 sink due to recent climate change", *Science*, *319*, 570c, doi:10.1126/science.1147315, 2008.

Ledwell, J., A. J. Watson, and C. S. Law, Evidence for slow mixing across the pycnocline from an open ocean tracer-release experiment, *Nature*, *364*, 701–703, 1993.

Lenn, Y.-D., and T. Chereskin, Observations of ekman currents in the Southern Ocean, *Journal of Physical Oceanography*, *39*, 768–779, 2009.

Lenton, A., and R. Matear, role of the Southern Annular Mode (SAM) in Southern Ocean CO_2 uptake, *Global Biogeochemical Cycles*, *21*, GB2016, doi:10.1029/2006GB002714, 2007.

Levermann, A., and J. J. Fürst, Atlantic pycnocline theory scrutinized using a coupled climate model, *Geophysical Research Letters*, *37*, doi:10.1029/2010GL044180, 2010.

Levitus, S., and T. Boyer, World ocean atlas 1994, volume 3: Salinity, *Tech. rep.*, NOAA Atlas NESDIS 3, U.S. Department of Commerce, Washinton, D.C., 1994a.

Levitus, S., and T. Boyer, World ocean atlas 1994, volume 4: Temperature, *Tech. rep.*, NOAA Atlas NESDIS 4, U.S. Department of Commerce, Washinton, D.C., 1994b.

Locarnini, R. A., T. D. O'Brien, H. E. Garcia, J. I. Antonov, T. P. Boyer, M. E. Conkright, and C. Stephens, World ocean atlas 2001, volume 3: Oxygen, in *NOAA Atlas NESDIS 51*, edited by S. Levitus, p. 286, U.S. Government Printing Office, Washington, D.C., 2002.

Lovenduski, N., and N. Gruber, Impact of the Southern Annular Mode on Southern Ocean circulation and biology, *Geophysical Research Letters*, *32*, L11,603, doi:10.1029/2005GL022727, 2005.

Lovenduski, N., N. Gruber, S. Doney, and I. Lima, Enhanced CO_2 outgassing in the Southern Ocean from a positive phase of the Southern Annular Mode., *Global Biogeochemical Cycles*, *21*, GB2026, doi:10.1029/2006GB002900, 2007.

Lovenduski, N., N. Gruber, and S. Doney, Toward a mechanistic understanding of the decadal trends in the Southern Ocean carbon sink, *Global Biogeochemical Cycles*, *22*, GB3016, doi:10.1029/2007GB003139, 2008.

Lumpkin, R., and K. Speer, Global ocean meridional overturning, *Journal of Physical Oceanography*, *37*, 2550–2562, doi:10.1175/JPO3130.1, 2007.

Mahowald, N., Y. Masaru, W. Collins, A. Conley, D. Fillmore, and D. Coleman, Climate respone and radiative forcing from mineral aerosols during the last glacial maximum, pre–industrial, current and doubled–carbon dioxide climates, *Geophysical Research Letters*, *33*, doi:10.1029/2006/GL026126, 2006a.

Mahowald, N., D. Muhs, S. Levis, P. Rasch, M. Yoshioka, C. Zender, and C. Luo, Change in atmospheric mineral aerosols in response to climate: Last glacial period, preindustrial, modern and doubled carbon dioxide climates, *Journal of Geophysical Research*, *111*, doi:10.1029/2005JD006653, 2006b.

Marchitto, T., S. Lehman, J. Ortiz, J. Flückiger, and A. van Geen, Marine radiocarbon evidence for the mechanism of deglacial atmospheric CO_2 rise, *Science*, *316*, 1456–1459, doi:10.1126/science.1138679, 2007.

Marinov, I., A. Gnanadesikan, J. R. Toggweiler, and J. L. Sarmiento, The Southern Ocean biogeochemical divide, *Nature*, *441*, 964–967, doi:10.1038/nature04883, 2006.

Marinov, I., M. Follows, A. Gnanadesikan, J. L. Sarmiento, and R. Slater, How does ocean biology affect atmospheric pCO_2? theory and models., *Journal of Geophysical Research*, *113*, C07,032, doi:10.1029/2007JC004598, 2008.

Marshall, D., Subduction of water masses in an eddying ocean, *Journal of Marine Research*, *55*, 201–222, 1997.

Marshall, J., and T. Radko, Residual mean solutions for the Antarctic Circumpolar Current and its associated overturning circulation, *Journal of Physical Oceanography*, *33*, 2341–2354, 2003.

Marshall, J., A. Adcroft, C. Hill, L. Perelman, and C. Heisey, A finite-volume, incompressible navier stokes model for studies of the ocean on parallel computers, *Journal of Geophysical Research*, *102*, 5753–5766, 1997a.

Marshall, J., C. Hill, L. Perelman, and A. Adcroft, Hydrostatic, quasi-hydrostatic, and nonhydrostatic ocean modeling, *Journal of Geophysical Research*, *102*, 5733–5752, 1997b.

Martin, J., Glacial–interglacial CO_2 change: the iron hypothesis, *Paleoceanography*, *5*, 1–13, 1990.

Martin, J., G. Knauer, D. Karl, and W. Broenkow, Vertex: carbon cycling in the northeast pacific, *Deep-Sea Research*, *34*, 1987.

Matsumoto, K., J. Lynch-Stieglitz, and R. Anderson, Similar glacial and Holocene Southern Ocean hydrography, *Paleoceanography*, *16*, 445–454, 2001.

Matsumoto, K., J. L. Sarmiento, and M. A. Brzezinski, Silicic acid leakage from the Southern Ocean: A possible explanation for glacial atmospheric pCO_2, *Global Biogeochemical Cycles*, *16*, doi:10.1029/2001GB001442, 2002.

McCulloch, R., M. Bentley, R. Purves, N. Hulton, D. Sugden, and C. Clapperton, Climatic inferences from glacial and palaeoecological evidence at the last glacial termination, southern South America, *Journal of Quaternary Science*, *15*, 409–417, 2000.

McDermott, D., The regulation of northern overturning by southern hemisphere winds, *Journal of Physical Oceanography*, *26*, 1234–1255, 1996.

Menviel, L., A. Timmerman, A. Mouchet, and O. Timm, Climate and marine carbon response to changes in the strength of the Southern Hemispheric westerlies, *Paleoceanography*, *33*, doi:10.1029/2008PA001604, 2008.

Meredith, M., and A. Hogg, Circumpolar response of Southern Ocean eddy activity to a change in the Southern Annular Mode, *Geophysical Research Letters*, *35*, doi:10.1029/2006GL026499, 2006.

Meredith, M., P. Woodworth, C. Hughes, and V. Stepanov, Changes in the ocean transport through Drake Passage during the 1980s and 1990s, forced by changes in the Southern Annular Mode, *Geophysical Research Letters*, *31*, doi:10.1029/2004GL021169, 2004.

Meskhidze, N., A. Nenes, W. Chameides, C. Luo, and N. Mahowald, Atlantic Southern Ocean productivity: Fertilisation from above or below?, *Global Biogeochemical Cycles*, *21*, doi:10.1029/2006GB002711, 2007.

Mignone, B., A. Gnanadesikan, J. L. Sarmiento, and R. Slater, Central role of Southern Hemisphere winds and eddies in modulating the oceanic uptake of anthropogenic carbon, *Geophysical Research Letters*, *33*, L01,604, doi:10.1029/2005GL024464, 2006.

Mikaloff Fletcher, S., N. Gruber, A. Jacobson, M. Gloor, S. Doney, S. Dutkiewicz, M. Gerber, M. Follows, F. Joos, K. Lindsay, D. Menemenlis, A. Mouchet, S. Müller, and J. L. Sarmiento, Inverse estimates of the oceanic sources and sinks of natural CO_2 and the implied oceanic carbon transport, *Global Biogeochemical Cycles*, *21*, doi:10.1029/2006GB002751, 2007.

Mitchell, B., E. Brody, O. Holm-Hansen, C. McClain, and J. Bishop, Light limitation of phytoplankton biomass and macronutrient utilization in the southern ocean, *Limnology and Oceanography*, *36*, 1662–1677, 1991.

Monnin, E., Atmospheric CO_2 concentrations over the last glacial maximum, *Science*, *291*, 112–114, 2001.

Moreno, P., T. Lowell, G. Jackobson Jr, and G. Denton, Abrupt vegetation and climate changes during the Last Glacial Maximum and last termination in the Chilean Lake District: A case study from Canal de la Puntilla (41°s), *Geografiska Annaler Series A*, *81*, 285–311, 1999.

Munk, W., Abyssal recipes, *Deep-Sea Research*, *13*, 707–730, 1966.

Munk, W., and E. Palmén, Note on the dynamics of the Antarctic Circumpolar Current, *Tellus*, *3*, 472–474, 1951.

Munk, W., and C. Wunsch, Abyssal recipes ii: Energetics of tidal and wind mixing, *Deep-Sea Research, Part I*, *45*, 1977–2010, 1998.

Muratli, J., Z. Chase, A. Mix, and J. McManus, Increase in glacial age ventilation of the Chilean margin by Antarctic Intermediate Water, *Nature Geoscience*, *3*, 23–26, doi:10.1038/ngeo0715, 2010.

Najjar, R., and J. Orr, Design of OCMIP-2 simulations of chlorofluorocarbons, the solubility pump and common biogeochemistry, 1998, http://www.ipsl.jussieu.fr/OCMIP/phase2/simulations/design.ps.

Naveira Garabato, A. C., K. Polzin, B. King, and M. Heywood, K.J. andVisbeck, Widespread intense turbulent mixing in the Southern Ocean, *Science*, *303*, 210–213, 2004.

Naveira Garabato, A. C., D. Stevens, A. J. Watson, and W. Roether, Short-circuiting of the overturning circulation in the Antarctic Circumpolar Current, *Nature*, *447*, 194–197, 2007.

Naveira Garabato, A. C., L. Jullion, D. Stevens, K. Heywood, and B. King, Variability of Subantarctic Mode Water and Antarctic Intermediate Water in the Drake Passage during the late-twentieth and early twenty-first centuries, *Journal of Climate*, *22*, 3661–3688, doi:10.1175/2006JCLI2621.1, 2009.

Ninnemann, U., and C. Charles, Changes in the mode of Southern Ocean circulation over the last glacial cycle revealed by foraminiferal stable isotope variability, *Earth and Planetary Science Letters*, *201*, 383–396, 2002.

Nowlin, W., and J. Klinck, The physics of the Antarctic Circumpolar Current, *Reviews of Geophysics*, *24*, 469–491, 1986.

Olbers, D., D. Borowski, C. Völker, and J.-A. Wölff, The dynamical balance, transport and circulation of the Antarctic Circumpolar Current, *Antarctic Science*, *16*, 439–470, doi:10.1017/S0954102004002252, 2004.

Oliver, K., and N. Edwards, Location of potential energy sources and the export of dense water from the Atlantic Ocean, *Geophysical Research Letters*, *35*, L22,604, doi:10.1029/2008GL035537, 2008.

Oppo, D., and R. Fairbanks, Atlantic ocean thermohaline circulation of the last 150,000 years: relationship to climate and atmospheric CO_2, *Paleoceanography*, *5*, 277–288, 1990.

Orsi, A., T. Whitworth III, and W. Nowlin Jr, On the meridional extent and fronts of the Antarctic Circumpolar Current, *Deep-Sea Research*, *42*, 641–673, 1995.

Otto-Bliesner, B., E. Brady, G. Clauzet, R. Tomas, S. Levis, and Z. Kothavala, Last Glacial Maximum and Holocene climate in CCSM3, *Journal of Climate*, *19*, 2526–2544, 2006.

Pahnke, K., and R. Zahn, Southern Hemisphere water mass conversion linked with North Atlantic climate varibility, *Science*, *307*, 1741–1746, doi:10.1126/science.1102163, 2005.

Pahnke, K., S. Goldstein, and S. Hemming, Abrupt changes in Antarctic Intermediate Water circulation over the past 25,000 years, *Nature Geoscience*, *1*, 870–874, 2008.

Parekh, P., M. Follows, and E. Boyle, Decoupling of iron and phosphate in the global ocean, *Global Biogeochemical Cycles*, *19*, doi:10.1029/2004GB002280, 2005.

Parekh, P., S. Dutkiewicz, M. Follows, and T. Ito, Atmospheric carbon dioxide in a less dusty world, *Geophysical Research Letters*, *33*, doi:10.1029/2005GL025098, 2006a.

Parekh, P., M. Follows, S. Dutkiewicz, and T. Ito, Physical and biological regulation of the soft tissue carbon pump, *Paleoceanography*, *21*, doi:10.1026/2005PA001258, 2006b.

Peacock, S., E. Lane, and J. Restrepo, A possible sequence of events for the generalized glacial-interglacial cycle., *Global Biogeochemical Cycles*, *20*, GB2010, doi:10.1029/2005GB002448, 2006.

Perlwitz, J., S. Pawson, R. Fogt, J. Nielsen, and W. Neff, Impact of stratospheric ozone hole recovery on Antarctic climate, *Geophysical Research Letters*, *35*, L08,714, doi:10.1029/2008GL033317, 2008.

Petit, J., J. Jouzel, D. Raynaud, N. Barkov, J.-M. Barnola, I. Basile, M. Bender, J. Chappellaz, M. Davis, G. Delaygue, M. Delmotte, V. Kotlyakov, M. Legrand, V. Lipenkov, C. Lorius, L. Pépin, C. Ritz, E. Saltzman, and M. Stievenard, Climate and the atmospheric history of the past 420,000 years from the Vostok ice core, Antarctica, *Nature*, *399*, 429–436, 1999.

Poisson, A., and C. T. A. Chen, Why is there little anthropogenic CO_2 in Antarctic Bottom Water, *Deep-Sea Research*, *34*, 1255–1275, 1987.

Polzin, K., J. Toole, J. Ledwell, and R. Schmitt, Spatial variability of turbulent mixing in the abyssal ocean, *Science*, *276*, 93–96, doi:10.1126/science.276.5309.93, 1997.

Rahmstorf, S., Ocean circulation during the past 120,000 years, *Nature*, *419*, 207–214, 2002.

Rahmstorf, S., and M. England, Influence of Southern Hemisphere winds on North Atlantic Deep Water flow, *Journal of Physical Oceanography*, *27*, 2040–2054, 1997.

Redi, M., Oceanic isopycnal mixing by coordinate rotation, *Journal of Physical Oceanography*, *12*, 1154–1158, 1982.

Ridgway, K. R., and J. R. Dunn, Observational evidence for a Southern Hemisphere oceanic supergyre, *Geophysical Research Letters*, *34*, doi:10.1029/2007GL030392, 2007.

Rintoul, S., The global influence of the Southern Ocean circulation, in *Proceedings of the eigth International Conference of Southern Hemisphere Meteorology and Oceanography (ICSHMO)*, pp. 1349–1354, 2006.

Rintoul, S., C. Hughes, and D. Olbers, The Antarctic circumpolar current system, in *Ocean Circulation and Climate: Observing and Modelling the Global Ocean*, edited by G. Siedler, J. Church, and J. Gould, chap. 4.6, pp. 271–302, Academic Press, 2001.

Royal Society, Geoengineering the climate: Science, governance and uncertainty, *Science Policy Report 10/09 RS1636*, Science Policy Centre, The Royal Society, London, UK, 2009.

Russell, J. L., K. Dixon, A. Gnanadesikan, R. Stouffer, and J. R. Toggweiler, The Southern Hemisphere westerlies in a warming world: propping open the door to the deep ocean, *Journal of Climate*, *19*, 6382–6390, 2006.

Sabine, C. L., R. A. Feely, N. Gruber, R. M. Key, K. Lee, J. L. Bullister, R. Wanninkhof, C. S. Wong, D. W. R. Wallace, B. Tilbrook, F. J. Millero, T. H. Peng, A. Kozyr, T. Ono, and A. F. Rios, The oceanic sink for anthropogenic CO_2, *Science*, *305*, 367–371, doi:10.1126/science.1097403, 2004.

Saenko, O., J. Gregory, A. Weaver, and M. Eby, Distinguishing the influence of heat, freshwater and momentum fluxes on ocean circulation and climate, *Journal of Climate*, *15*, 2002.

Saenko, O., J. Fyfe, and M. England, On the response of the oceanic wind-driven circulation to atmospheric CO_2 increase, *Climate Dynamics*, *25*, 415–426, 2005.

Sarmiento, J. L., and J. R. Toggweiler, A new model for the role of the oceans in determining atmospheric pCO_2, *Nature*, *308*, 621–624, 1984.

Sarmiento, J. L., N. Gruber, M. A. Brzezinski, and J. P. Dunne, High latitude controls of thermocline nutrients and low latitude biological productivity, *Nature*, *427*, 56–60, 2004.

Schmittner, A., and E. Galbraith, Glacial greenhouse gas fluctuations controlled by ocean circulation changes, *Nature*, *456*, 373–376, 2008.

Schmitz, W., On the interbasin-scale thermohaline circulation, *Reviews of Geophysics*, *32*, 151–173, 1995.

Schmitz, W., On the world ocean circulation: Volume 1, some global features and the north atlantic circulation, *Woods Hole Oceanographic Institution Tech. Rept. WHOI-96-03*, Woods Hole Oceanographic Institution, 1996a.

Schmitz, W., On the world ocean circulation: Volume 2, the Pacific and Indian oceans and a global update, *Woods Hole Oceanographic Institution Tech. Rept. WHOI-96-08*, Woods Hole Oceanographic Institution, 1996b.

Shin, S.-I., Z. Liu, B. Otto-Bliesner, E. Brady, J. Kutzbach, and S. Harrison, A simulation of the Last Glacial Maximum climate using the NCAR-CCSM, *Climate Dynamics*, *20*, 127–151, 2003.

Shulmeister, J., I. Goodwin, J. Renwick, K. Harle, L. Armand, M. McGlone, E. Cook, J. Dodson, P. Hesse, P. Mayewski, and M. Curran, The Southern Hemisphere westerlies in the Australasian sector over the last glacial cycle: a synthesis, *Quaternary International*, *118–119*, 23–53, doi:10.1016/S1040-6182(03)00129-0, 2004.

Siegenthaler, U., and T. Wenk, Rapid atmospheric CO_2 variations and ocean circulation, *Nature*, *308*, 624–626, 1984.

Sigman, D., and E. Boyle, Glacial/interglacial variations in atmospheric carbon dioxide, *Nature*, *407*, 859–869, 2000.

Sigman, D., and E. Boyle, Antarctic stratification and glacial pCO_2, *Nature*, *412*, 606, 2001.

Sigman, D., M. Hain, and G. Haug, The polar ocean and glacial cycles in atmospheric CO_2 concentration, *Nature*, *466*, 47–55, doi:10.1038/nature09149, 2010.

Sime, L., K. Kohfeld, C. Le Quéré, E. Wolff, A. de Boer, and L. Bopp, Strengthening of the Southern Hemisphere westerlies during glaciations, 2010, in preparation.

Skinner, L., S. Fallon, C. Waelbroeck, E. Michel, and S. Barker, Ventilation of the deep Southern Ocean and deglacial CO_2 rise, *Science*, *328*, 1147–1151, 2010.

Sloyan, B., and S. Rintoul, Circulation, renewal and modification of Antarctic mode and intermediate water, *Journal of Physical Oceanography*, *31*, 1005–1030, 2001.

Speer, K., S. Rintoul, and B. Sloyan, The diabatic Deacon cell, *Journal of Physical Oceanography*, *30*, 3212–3222, 2000.

Speich, S., B. Blanke, and W. Cai, Atlantic meridional overturning circulation and the Southern Hemisphere supergyre, *Geophysical Research Letters*, *34*, doi:10.1029/2007GL031583, 2007.

Spero, H., and D. Lea, The cause of carbon isotope minimum events on glacial terminations, *Science*, *296*, 522–525, 2002.

Stephens, B. B., and R. F. Keeling, The influence of Antarctic sea ice on glacial-interglacial CO_2 variations, *Nature*, *404*, 171–174, 2000.

Stephens, C., J. Antonov, T. Boyer, M. Conkright, R. Locarnini, T. O'Brien, and H. Garcia, World ocean atlas 2001, volume 1: Temperature, in *NOAA Atlas NESDIS 49*, edited by S. Levitus, p. 167, U.S. Government Printing Office, Washington, D.C., 2002.

Stevens, D., and V. Ivchenko, The zonal momentum balance in an eddy-resolving general-circulation model of the Southern Ocean, *Quarterly Journal of the Royal Meteorological Society*, *123*, 929–951, 1997.

Tagliabue, A., L. Bopp, J.-C. Dutay, A. R. Bowie, F. Chever, P. Jean-Baptiste, E. Bucciarelli, D. Lannuzel, T. Remenyi, G. Sarthou, O. Aumont, M. Gehlen, and C. Jeandel, Hydrothermal contribution to the oceanic dissolved iron inventory, *Nature Geoscience*, *3*, 252–256, doi:10.1038/ngeo818, 2010.

Takahashi, T., S. Sutherland, C. Sweeney, A. Poisson, N. Metzl, B. Tilbrook, N. Bates, R. Wanninkhof, R. Feely, C. Sabine, J. Olafsson, and Y. Nojiri, Global sea-air CO_2 flux based on climatological surface ocean pCO_2 and seasonal biological and temperature effects, *Deep-Sea Research, Part II*, *49*, 1601–1622, 2002.

Thomas, L., A. Tandon, and A. Mahadevan, Sub-mesoscale processes and dynamics, in *Ocean Modeling in an Eddying Regime*, edited by M. Hecht and H. Hasumi, vol. 177 of *Geophysical Monograph Series*, pp. 17–38, American Geophysical Union, Washington DC, 2008.

Thompson, D., and S. Solomon, Interpretation of recent Southern Hemisphere climate change, *Science*, *296*, 895–899, doi:10.1126/science.1069270, 2002.

Toggweiler, J. R., Variation of atmospheric CO_2 by ventilation of the ocean's deepest water, *Paleoceanography*, *14*, 571–588, 1999.

Toggweiler, J. R., Origin of the 100,000 year timescale in Antarctic temperatures and atmospheric CO_2, *Paleoceanography*, *23*, PA2211, doi:10.1029/2006PA001405, 2008.

Toggweiler, J. R., and B. L. Samuels, Effect of Drake Passage on the global thermohaline circulation, *Deep-Sea Research, Part I*, *42*, 477–500, 1995.

Toggweiler, J. R., and B. L. Samuels, On the ocean's large-scale circulation near the limit of no vertical mixing, *Journal of Physical Oceanography*, *28*, 1832–1852, 1998.

Toggweiler, J. R., J. L. Russel, and S. R. Carson, Midlatitude westerlies, atmospheric CO_2 and climate change during the ice ages, *Paleoceanography*, *21*, doi:10.1029/2005PA001154, 2006.

Tomczak, M., and J. Godfrey, Regional oceanography: An introduction, `http://www.es.flinders.edu.au/~mattom/regoc/pdfversion.html`, 2005.

Trenberth, K., J. Olson, and W. Large, A global wind stress climatology based on ECMWF analyses, *Tech. rep.*, NCAR/TN-338+STR, National Centre for Atmospheric Research, Boulder, Colorado, 1989.

Tschumi, T., F. Joos, and P. Parekh, How important are the Southern Hemisphere wind changes for low glacial carbon dioxide?, *Paleoceanography*, *34*, PA4208, doi:10.1029/2008PA001592, 2008.

Tschumi, T., F. Joos, M. Gehlen, and C. Heinze, Deep ocean ventilation, carbon isotopes, marine sedimentation and the deglacial CO_2 rise, *Climates of the Past Disussions*, *6*, 1895–1958, 10.5194/cpd-6-1895-2010, 2010.

Tyrrell, T., The relative influences of nitrogen and phosphorus on oceanic primary production, *Nature*, *400*, 525–531, 1999.

van Oijen, J., M. van Leeuwe, E. Granum, F. Weissing, R. Bellerby, W. Gieskes, and H. de Baar, Light rather than iron controls photosynthate production and allocation in southern ocean phytoplankton populations during austral autumn, *Journal of Plankton Research*, *26*, 885–900, 2004.

Varma, V., M. Prange, F. Lamy, U. Merkel, and M. Schulz, Solar-forced shifts of Southern Hemisphere westerlies during the late Holocene, *Climates of the Past Disussions*, *6*, 369–384, 2010.

Verdy, A., S. Dutkiewicz, M. Follows, J. Marshall, and A. Czaja, Carbon dioxide and oxygen fluxes in the Southern Ocean: mechanisms of interannual variability, *Global Biogeochemical Cycles*, *21*, GB2020, doi:10.1029/2006GB002916, 2007.

Visbeck, M., J. Marshall, T. Haine, and M. Spall, Specification of eddy transfer coefficients in coarse-resolution ocean circulation models, *Journal of Physical Oceanography*, *27*, 381–402, 1997.

Volk, T., and M. I. Hoffert, Ocean carbon pumps: Analysis of relative strengths and efficiencies in ocean-driven atmospheric CO_2 changes, in *The Carbon cycle and atmospheric CO_2: Natural variations Archean to present.*, edited by T. Sundquist and W. Broecker, vol. 32 of *Geophysical monograph series*, pp. 99–110, American Geophysical Union, Washington, D.C., 1985.

Wagener, T., C. Guieu, R. Losno, S. Bonnet, and N. Mahowald, Revisiting atmospheric dust export to the Southern Hemisphere ocean: biogeochemical implications, *Global Biogeochemical Cycles*, *22*, doi:10.1029/2007GB002984, 2008.

Wang, L., and R. Huang, A linear homogenous of wind-driven circulation in a β-plane channel, *Journal of Physical Oceanography*, *25*, 587–603, 1995.

Wang, W., and R. Huang, Wind energy input into the Ekman layer, *Journal of Physical Oceanography*, *34*, 1267–1275, 2004.

Wanninkhof, R., Relationship between wind speed and gas exchange over the ocean, *Journal of Geophysical Research*, *97*, 7373–7382, 1992.

Watson, A. J., and A. C. Naveira Garabato, The role of Southern Ocean mixing and upwelling in glacial-interglacial atmospheric CO_2 change, *Tellus*, *58b*, 73–87, 2006.

Watson, A. J., D. C. E. Bakker, A. J. Ridgwell, P. W. Boyd, and C. S. Law, Effect of iron supply on Southern Ocean CO_2 uptake and implications for glacial atmospheric CO_2, *Nature*, *407*, 730–733, 2000.

Weaver, A., O. Saenko, P. Clark, and J. Mitrovica, Meltwater pulse 1a from Antarctica as a trigger of the Bølling-Allerød warm interval, *Science*, *299*, 1709–1713, doi:10.1126/science.1081002, 2003.

Wetzel, P., A. Winguth, and E. Maier-Reimer, Sea-to-air CO_2 flux from 1948–2003: a model study, *Global Biogeochemical Cycles*, *19*, GB2005, doi:10.1029/2004GB002339, 2005.

Williams, G., and K. Bryan, Ice age winds: an aquaplanet model, *Journal of Climate*, *19*, 1709–1715, 2006.

Williams, R., and M. Follows, The Ekman transfer of nutrients and maintenance of new production over the North Atlantic, *Deep-Sea Research, Part I*, *45*, 461–489, 1998.

Wimbush, M., and W. Munk, The benthic boundary layer, in *The Sea: New concepts of seafloor evolution, part II: regional observations and concepts*, edited by M. Hill, vol. 4, pp. 731–758, Wiley and sons, 1970.

Wolff, E. W., H. Fischer, F. Fundel, U. Ruth, B. Twarloh, G. C. Littot, R. Mulvaney, R. R othlisberger, M. de Angelis, C. F. Boutron, M. Hansson, U. Jonsell, M. A. Hutterli, F. Lambert, P. Kaufmann, B. Stauffer, T. F. Stocker, J. P. Steffensen, M. Bigler, M. L. Siggaard-Andersen, R. Udisti, S. Becagli, E. Castellano, M. Severi, D. Wagenbach, C. Barbante, P. Gabrielli, and V. Gaspari, Southern Ocean sea-ice extent, productivity and iron flux over the past eight glacial cycles, *Nature*, *440*, 491–496, 2006.

Wunsch, C., The work done by the wind on the oceanic general circulation, *Journal of Physical Oceanography*, *28*, 2332–2340, 1998.

Wunsch, C., and R. Ferrari, Vertical mixing, energy and the general circulation of the oceans., *Annual Review of Fluid Mechanics*, *36*, 281–314, doi:10.1146/annurev.fluid.36.050802.122121, 2004.

Yamanaka, Y., and E. Tajika, Role of dissolved organic matter in the marine biogeochemical cycle: Studies using an ocean biogeochemical general circulation model, *Global Biogeochemical Cycles*, *11*, 599–612, 1997.

Zickfeld, K., J. Fyfe, O. Saenko, M. Eby, and A. Weaver, Response of the global carbon cycle to human–induced changes in Southern Hemisphere winds, *Geophysical Research Letters*, *34*, doi:10.1029/2006GL028797, 2007.

Zickfeld, K., J. Fyfe, M. Eby, and A. Weaver, Comment on "saturation of the Southern Ocean CO_2 sink due to recent climate change", *Science*, *319*, 570b, doi:10.1126/science.1146886, 2008.